

# Sheffield Hallam University

*Studies on cadmium sulphide nanoparticles formed by the Langmuir-Blodgett technique.*

IWANTONO.,

Available from the Sheffield Hallam University Research Archive (SHURA) at:

<http://shura.shu.ac.uk/20169/>

## A Sheffield Hallam University thesis

This thesis is protected by copyright which belongs to the author.

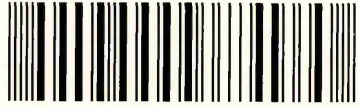
The content must not be changed in any way or sold commercially in any format or medium without the formal permission of the author.

When referring to this work, full bibliographic details including the author, title, awarding institution and date of the thesis must be given.

Please visit <http://shura.shu.ac.uk/20169/> and <http://shura.shu.ac.uk/information.html> for further details about copyright and re-use permissions.

CITY CAMPUS, HOWARD STREET  
SHEFFIELD S1 1WB

101 715 895 9



**REFERENCE**

ProQuest Number: 10699997

All rights reserved

INFORMATION TO ALL USERS

The quality of this reproduction is dependent upon the quality of the copy submitted.

In the unlikely event that the author did not send a complete manuscript and there are missing pages, these will be noted. Also, if material had to be removed, a note will indicate the deletion.



ProQuest 10699997

Published by ProQuest LLC (2017). Copyright of the Dissertation is held by the Author.

All rights reserved.

This work is protected against unauthorized copying under Title 17, United States Code  
Microform Edition © ProQuest LLC.

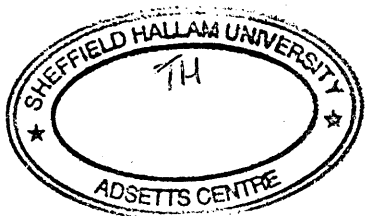
ProQuest LLC.  
789 East Eisenhower Parkway  
P.O. Box 1346  
Ann Arbor, MI 48106 – 1346

**STUDIES ON CADMIUM SULPHIDE  
NANOPARTICLES FORMED BY  
THE LANGMUIR-BLODGETT TECHNIQUE**

**IWANTONO**

**A thesis submitted in partial fulfilment of the requirements of  
Sheffield Hallam University  
for the degree of Doctor of Philosophy**

**July 2003**



## **Declaration**

I hereby declare that this thesis submitted for the degree of Ph.D is the result of my own research and that this thesis has not been submitted for a higher degree to any other university or institution.

Signed

**Iwantono**

# DEDICATION

To my parents,

H. Barnawi Naim Ratihardja and Hj. Saidah Asikin

To my beloved wife,

Yulianty Yunus

To my dearest sons,

Ilham Fauzi Iwantono and Taufiqurrahman Iwantono

To my brothers and sisters,

Irianto, Ibnu Sholeh, Inayati, Irawati, Itartati, Irmayanti and their families

## ABSTRACT

In this project, the formation and characterisation of CdS nanoparticles embedded within Langmuir-Blodgett (LB) films have been studied systematically. CdS nanoparticles were formed within calix[8]arene (CA) and stearic acid (SA) Cd-salt LB films by exposure to H<sub>2</sub>S gas at room temperature.

The AFM images of the treated SA and CA bilayers show CdS clusters with lateral dimensions in the range of 20-30 nm and 10-15 nm, respectively. These particles are pseudo two-dimensional and have a shape of hexagonal platelets which is most likely consequence of their wurtzite structure. Calculations of the cluster thickness  $L_z$  yield the value of 2 nm (Photoluminescence excitation-PLE) and 1.9 nm (UV-visible) for CdS clusters in SA matrix and two values of 1.2 nm and 1.6 nm (PLE) and 1.08 nm and 1.42 nm (UV-visible) for CA LB films. The PL spectra demonstrate a large Stokes shift, indicating the formation of "dark excitons" in the platelet CdS clusters.

The transformations of the absorption spectra caused by ageing yield a monotonic increase in CdS cluster size with the tendency of saturation. This behaviour can be explained by the model of two dimensional (2D) diffusion. According to this model, CdS molecules in the SA films, initially evenly distributed within each LB bilayer, aggregate and form "large" particles with an average size of 1.9 nm and smaller particles with their size distributed over a wide range down to single molecules.

The Surface Plasmon Resonance (SPR) and ellipsometry measurements confirmed that the H<sub>2</sub>S treatment to the LB films results both in the increase in thickness and refractive index of the LB films due to formation of CdS nanoparticles inside. SPR kinetics measurements during H<sub>2</sub>S treatment show that the formation of CdS clusters happened very fast and almost reached the saturation in about 30 minutes.

The I-V characteristics of the sandwich structures of Aluminium/LB films/Aluminium show exponential behaviour and weak temperature dependence, indicating a combination of electron-tunnelling and hopping mechanism. The formation of CdS clusters in the film matrix did not result in either an enhancement of the electron transfer or an additional polarisation at a small (50 mV) AC signal. Most likely, the observed changes in DC conductivity and AC impedance are caused by the film disorder introduced by CdS nanoparticles.

# ACKNOWLEDGEMENTS

First of all, I would like to express my sincere thanks to my director of studies, Dr. Alexei Nabok for his excellent supervision, guidance and support during the last three years, and for his excellent discussion of various aspects of science, experimental procedures and the results obtained.

My special appreciations and thanks go to my supervisor Professor Asim K. Ray for his advice, encouragement, assistance and help. I would also like to thank Dr. Aseel Hassan for his continuous encouragement, discussion, and advice. I would like to express my thanks to Dr. Tim Richardson of Physics Department, Sheffield University for his advice, discussion and suggestion.

My sincere thanks must go to Dr. Ivan Larkin (Physics Department, Sheffield University) for his help and collaboration with the modelling work. I must also thank Dr. Alexander Ruban from MBB Department, Sheffield University for his help with photoluminescence measurements. Many thanks are also due to Dr. Mike Simmonds of Materials Research Institute (MRI), Sheffield Hallam University for his essential help and discussion with the AFM measurements.

I would also like to thank all technical staff of the School of Engineering, especially Mr. Ken Duty for his special help. My thanks also go to Mr. Roger T. and Mr. Richard W. for preparing the masks for the electrical study.

I would like to take this opportunity to thank all my fellow Ph.D colleagues for their help, good humour and advice during the past three years: Syed Malik, Saharuddin Haron, Abbas, Najla, Allaister, Alan, Anna and Dr. Thomas Wilkop.

My special thanks also go to the LPIU-DUE Project of Riau University, Indonesia for their financial support.

I would like to express my special thanks to my mother, Saidah Asikin and my father Barnawi Naim Ratihardja for their continuing love, encouragement, advice and support. Many thanks must go to my bothers and sisters: Irianto, Ibnu Sholeih, Inayati, Irawati, Itartati, Irmayanti and their family.

Finally, my special thanks and love go to my lovely wife Yulianty and my sons Ilham fauzi and Taufiqurrahman for their patience, support and encouragement all the way through my Ph.D study.

# LIST OF PUBLICATIONS

## Journal Publications

1. "*Optical study on II-VI semiconductor nanoparticles in Langmuir-Blodgett films*", published in the IEEE Transactions on Nanotechnology, March 2003, Volume 2, Number 1, p44-49
2. "*Electrical characterisation of LB films containing CdS nanoparticles*", published in the Materials Science and Engineering C, 22 (2002), p355-358
3. "*Evolution of CdS nanoparticles self-assembled within two-dimensional Langmuir-Blodgett layers*", published in the Journal of Physics D: Applied Physics, 35 (2002), p1512-1515

## Conference Publications

1. "*Electrical characterisation of LB films containing CdS nanoparticles*", presented at the 8<sup>th</sup> European Conference on Organised Films, Otranto (Lecce), Italy, 3-7 September 2001.
2. "*Formation of nanoparticles by wet technology*", presented at the Half-day General-interest Meeting, The Future of Electronic Devices, 22 March 2002, The Institute of Physics, 76 Portland Place, London, UK
3. "*Optical study of CdS nanoparticles formed by LB film technique*", presented at the Postgraduate Research in electronics, Photonics, Communications and Software (PREP) Conference, 17-19 April 2002, East Midlands Conference Centre, University of Nottingham, Nottingham, UK
4. "*II-VI Semiconductor Nanoparticles Formed by Langmuir-Blodgett Film Technique: Optical Study*", presented at The Second Conference on Nanotechnology (IEEE-NANO 2002), 26-28 August 2002, Hilton Crystal City at National Airport, Arlington, Washington DC, USA

5. *“Nanotechnology and Optical Study of Cadmium Sulfide Nanostructure”*, presented at the Indonesian Students Scientific Meeting (ISSM) in Europe 2001, 25-26 August 2001, UMIST, Manchester, UK.
6. *“Formation of nanoparticles by wet technology”*, presented at the Materials Congress 2002, 9-11 April 2002, Carlton House Terrace, London, UK
7. *“Combined Surface Plasmon Resonance (SPR) and Ellipsometry Study on II-VI Semiconductor nanoparticles Formed by Langmuir-Blodgett Film Technique”*, presented at the 7<sup>th</sup> International Indonesian Student’s Scientific Meeting (ISSM 2002), 4-6 October 2002, The Technology Centre Berlin, Berlin, Germany.
8. *“Photoluminescence Study on II-VI Semi-conductor Nanoparticles Formed by Langmuir-Blodgett Film Technique”*, presented at the 7<sup>th</sup> International Indonesian Student’s Scientific Meeting (ISSM 2002), 4-6 October 2002, The Technology Centre Berlin, Berlin, Germany.

# CONTENTS

<b>DEDICATION</b>	<b>i</b>
<b>ABSTRACT</b>	<b>ii</b>
<b>ACKNOWLEDGEMENTS</b>	<b>iii</b>
<b>LIST OF PUBLICATIONS</b>	<b>iv</b>
<b>CONTENTS</b>	<b>vi</b>
<b>LIST OF FIGURES</b>	<b>x</b>
<b>LIST OF TABLES</b>	<b>xvi</b>
<b>CHAPTER 1</b>	
<b>INTRODUCTION</b>	<b>1</b>
1.1. General Introduction	1
1.2. Aims and Objectives	4
1.3. Organisation of the Thesis	5
<b>CHAPTER 2</b>	
<b>PHYSICS OF SEMICONDUCTOR QUANTUM STRUCTURES</b>	<b>7</b>
2.1. Introduction to Semiconductors	7
2.1.1. Direct and Indirect Semiconductors	7
2.1.2. Excitons in Semiconductors	12
2.2. Physics of Bulk II-VI Semiconductors	15
2.2.1. Crystallographic Form of II-VI Compounds	15
2.2.2. Band Structures of II-VI Semiconductors	19
2.3. Physics of Semiconductor Nanostructures	22
2.3.1. Technology of Semiconductor Nanostructures	22
2.3.2. Excitons in Low-dimensional Systems	26
2.3.3. Quantum Confinement Effects	29
2.3.3.1. Theoretical Models of Quantum Confinement Effect	29
2.4. Review of Previous Works on CdS Quantum Structures	39
<b>CHAPTER 3</b>	
<b>PREPARATION OF THE SAMPLES</b>	<b>49</b>
3.1. Introduction	49

3.2. Principles of Langmuir-Blodgett Films	50
3.2.1. Langmuir Film – Monolayer	50
3.2.2. Surface Pressure of a Langmuir Layer	51
3.2.3. $\Pi$ -A Pressure-area isotherms	53
3.2.4. Monolayer Materials	58
3.2.4.1. Fatty Acids and related compounds	58
3.2.4.2. Calixarene derivatives	61
3.2.5. Langmuir-Blodgett Films – Multilayers	63
3.2.6. Langmuir-Blodgett Trough	66
3.3. Langmuir-Blodgett Film Deposition	68
3.3.1. Preparation of Langmuir Monolayer	69
3.3.2. Formation of Langmuir-Blodgett Films	72
3.4. Formation of II-VI Semiconductor Nanoparticles within LB films	73
3.5. Summary	77

## **CHAPTER 4**

### **STUDY OF MORPHOLOGY OF CADMIUM SULPHIDE (CdS)**

#### **NOPARTICLES FORMED WITHIN LB FILMS** 78

4.1. Introduction	78
4.2. Atomic Force Microscopy (AFM) Technique	79
4.3. Experimental Procedure	84
4.4. Results and Discussion	85
4.5. Summary	93

## **CHAPTER 5**

### **OPTICAL STUDY OF CADMIUM SULPHIDE (CdS) NANOPARTICLES**

#### **FORMED WITHIN LB FILMS** 94

5.1. Introduction	94
5.2. Theoretical Background	96
5.3. Review of Previous Work on Optical Study of II-VI Semiconductor Quantum Structures	108
5.3.1. Dark Excitons in II-VI Semiconductor Quantum Dots (QDs)	110
5.3.2. Optical Properties of CdS Particles in LB Films	111
5.3.3. Photoluminescence of CdS Nanoparticles	114

5.4. Details of the Experimental Technique	116
5.5. Results and Discussion	120
5.5.1. Analysis of the Absorption Spectra	120
5.5.2. Photoluminescence	132
5.5.3. Evolution of CdS particles within 2D LB Layers	135
5.5.3.1. Two-dimensional (2D) Diffusion Model	138
5.6. Summary	143
<b>CHAPTER 6</b>	
<b>SURFACE PLASMON RESONANCE AND ELLIPSOMETRY STUDIES OF LB FILMS CONTAINING CdS NANOPARTICLES</b>	<b>145</b>
6.1. Introduction	145
6.2. Principles of the Experimental Methods	147
6.2.1 Surface Plasmon Resonance (SPR)	147
6.2.2 Ellipsometry	156
6.3. Experimental Details	161
6.4. Experimental Results and Discussion	165
6.5. Summary	184
<b>CHAPTER 7</b>	
<b>THE STUDY OF ELECTRICAL PROPERTIES OF CdS NANOPARTICLES IN LB FILMS</b>	<b>185</b>
7.1. Introduction	185
7.2. Theoretical Background and Review of Previous Studies	186
7.3. Details of Experimental Technique	199
7.3.1. The Evaporation System	203
7.3.1.1. Evaporation Principles and Techniques	203
7.3.1.2. Evaporation Procedure for Deposition Electrodes	205
7.3.2. Electrical Measurements	208
7.4. Results and Discussion	212
7.4.1. DC I-V Characteristics	212
7.4.2. AC Measurements	227
7.5. Summary	231

<b>CHAPTER 8</b>	
<b>CONCLUSIONS AND FUTURE WORK</b>	<b>232</b>
8.1. Thesis Conclusions	232
8.2. Suggestion for Future Work	236
<b>REFERENCES</b>	<b>237</b>

## LIST OF FIGURES

Figure 2.1. Direct electron transitions in a direct band semiconductor with accompanying photon emission	10
Figure 2.2. Indirect electron transitions in an indirect semiconductor via a defect level	11
Figure 2.3. Schematic representation of the excitons, where $E_g$ is the energy gap	12
Figure 2.4. Tetrahedral sites for a compound: (a) bases of tetrahedra parallel and in line vertically; (b) bases of tetrahedra parallel and $60^\circ$ out of line vertically [after Ray, 1969]	16
Figure 2.5. Wurtzite structure formed from tetrahedral site	16
Figure 2.6. Crystallographic lattice of zinc blende structure	18
Figure 2.7. Energy bands for wurtzite CdS along the $\Gamma$ -A axis [after Segall, 1967]	20
Figure 2.8. Energy band structure of wurtzite CdS in the region of the $\Gamma$ point with crystalline field and spin-orbit splitting effects present in the valence band structure [after Birman et al, 1961]	21
Figure 2.9. Illustrations representing system dimensionality d: (a) bulk semiconductors, 3D; (b) thin films, layer structures, quantum wells, 2D; (c) linear chain structures, quantum wires, 1D; (d) clusters, colloids, nanocrystallites, quantum dots, 0D.	27
Figure 2.10. Densities $N(E)$ of states for ideal cases of (a) 3D, (b) 2D, (c) 1D and (d) 0D systems [after Yoffe, 1993]	27
Figure 2.11. Band structure of a zinc blende CdS spherical cluster having $R = 15 \text{ \AA}$ near the top of the valence band [after Rama Krishna and Friesner, 1991]	38
Figure 2.12. Allowed electronic levels of wurtzite CdS spherical cluster having $R = 15 \text{ \AA}$ [after Tomasula and Rama Krishna, 1996]	38
Figure 3.1. Wilhelmy plate used to measure the surface pressure of a monolayer	52
Figure 3.2. $\pi$ -A compression isotherm of stearic acid showing the gas, liquid and solid phases. Extrapolation of the solid phase a predicted area per molecule of $21 \text{ \AA}^2$ [after Martin and Szablewski, 1999]	56
Figure 3.3. Schematic representation of the three phases seen in the $\pi$ -A isotherm of stearic acid	56
Figure 3.4. Stages of collapse of a monolayer, going from the top to the bottom diagram	57

Figure 3.5. Schematic diagram of an amphiphilic molecule	59
Figure 3.6. Chemical formula for stearic acid (n-octadecanoic acid)	60
Figure 3.7. Chemical structure for calixarene	62
Figure 3.8. Space-filling model of calix[8]arene	62
Figure 3.9. Langmuir-Blodgett films deposition onto a hydrophobic substrate	65
Figure 3.10. Schematic comparison of Langmuir-Blodgett film deposition type; (a) Y-type, (b) X-type, (c) Z-type and (d) alternate type depositions	65
Figure 3.11. Schematic representation of the Langmuir trough used in this research	67
Figure 3.12. Formation of LB films of Cd-salt stearic acid	69
Figure 3.13. Area per molecule of stearic acid monolayer	71
Figure 3.14. $\Pi$ -A pressure isotherm of calix[8]arene carboxylic acids derivatives: (a) tbC[8]A-1, (b) tbC[8]A-3 and (c) tbC[8]A-5	71
Figure 3.15. Segregation of small clusters of CdS in LB films (a) a group of a few molecules of CdS (b) CdS molecules interact each other in order to reduce their surface energy	75
Figure 3.16. Formation of CdS nanoparticles inside each bilayer of the LB films of stearic acid. The structure of the films changes due to formation of the CdS particles	75
Figure 3.17. Formation of CdS nanoparticles inside LB films of Cd-salt calixarene. Much smaller CdS particles were formed within CA films due to CdS aggregation limited by calixarene cavities	76
Figure 4.1. Schematic illustration of the method of operation of an AFM	83
Figure 4.2. Photograph of AFM instrument	84
Figure 4.3. AFM image of SA LB films before H <sub>2</sub> S treatment	86
Figure 4.4. AFM image of CdS nanoparticles in SA LB films	86
Figure 4.5. AFM image of Cd-salt SA LB films after H <sub>2</sub> S treatment	87
Figure 4.6. Three-dimensional AFM image of CdS nanoparticles in SA LB films	87
Figure 4.7. AFM image of CdS nanoparticles in SA LB films	88
Figure 4.8. Small scale AFM image of CdS nanoparticles in SA LB films	88
Figure 4.9. Schematical hexagonal shape of CdS nanoparticles in SA LB films	90

Figure 4.10. AFM image (1.00 x 1.00 $\mu\text{m}$ ) of CA bilayer after $\text{H}_2\text{S}$ treatment	90
Figure 4.11. 400 x 400 nm scale of AFM image of CdS clusters in CA bilayer	91
Figure 4.12. AFM image (1.00 x 1.00 $\mu\text{m}$ ) of untreated CA bilayer	91
Figure 5.1. Absorption transitions between impurities and bands: (a) donor to conduction band; (b) valence band to acceptor; (c) valence band to donor; and (d) acceptor to conduction band [after Pankove, 1971]	99
Figure 5.2. Schematic diagram of the photoluminescence process in a semiconductor	102
Figure 5.3. Exciton recombination: (a) direct, (b) indirect	104
Figure 5.4. Direct exciton recombination with (a) one optical phonon emission, (b) two optical phonon emission [after Pankove, 1971]	104
Figure 5.5. Direct band-to-band radiative transition [after Pankove, 1971]	106
Figure 5.6. Deep transitions: (a) band-to-impurity transitions and (b) donor-to-acceptor transition	107
Figure 5.7. Schematic illustration of “dark” exciton in semiconductor [after Yoffe, 2001]	113
Figure 5.8. Schematic diagram for absorption measurement set-up	118
Figure 5.9. Apparatus set-up used to perform the PL measurement	119
Figure 5.10. Absorption spectra of SA-LB Films, before and after the exposure of $\text{H}_2\text{S}$ gas (before and after $\text{H}_2\text{S}$ treatment)	121
Figure 5.11. Subtracted absorption spectra (before and after $\text{H}_2\text{S}$ gas treatment) of CdS nanoparticles formed in SA-LB Films. The number of LB layers is shown near respective curves	122
Figure 5.12. Absorption spectra of CdS nanoparticles in SA-LB Films near the absorption edge. The number of LB layers is shown near respective curves	123
Figure 5.13. Absorption spectra of CA-LB Films $\text{H}_2\text{S}$ gas (before and after the exposure of $\text{H}_2\text{S}$ gas)	125
Figure 5.14. Subtracted absorption spectra (before and after $\text{H}_2\text{S}$ gas treatment) of CdS nanoparticles formed in CA-LB Films. The number of LB layers is shown near respective curves	126
Figure 5.15. Photoluminescence emission (PL) and excitation (PLE) spectra of LB films of stearic acid containing CdS nanoparticles	130
Figure 5.16. Photoluminescence emission (PL) and excitation (PLE) spectra of CdS nanoparticles within the LB films of calixarene	131

Figure 5.17. Energy level diagram of bulk and nano semiconductors	133
Figure 5.18. Room temperature time dependencies of the size of CdS nanoparticles in LB films of stearic acid (SA) and calix[8]arene (CA1 and CA2), obtained from the first and the second peaks, respectively.	136
Figure 5.19. Time dependencies of the size of CdS nanoparticles in LB films of stearic acid (SA) and calix[8]arene (CA1 and CA2) at elevated temperatures	137
Figure 5.20. Numerical simulation of the equation (5.17) for CdS grains	141
Figure 5.21. Distribution function of the CdS particles: black bars relate to the SA film, grey bars relate to the CA film	142
Figure 6.1. Graphical representation of wavevector matching [after De Bruijn, 1991]	148
Figure 6.2. Kretschmann's prism arrangement [after De Bruijn, 1991]	151
Figure 6.3. Typical SPR curve of metal film, showing critical angle ( $\theta_c$ ) and angle of incidence minimum ( $\theta_0$ ).	152
Figure 6.4. Experimental SPR curves for gold film, and those of LB films of calix-4-resorcinarene coated on it. The number of monolayers is indicated on the corresponding curve. The inset presents the dependence of resonance shift ( $\Delta\theta_{SPR}$ ) on the thickness of the LB films [after Hassan et al, 1999].	154
Figure 6.5. SPR curves of LB film of calix-4-resorcinarene before (solid line) and during (broken line) exposure to ethylbenzene vapour. The inset shows the full measured SPR curve [after Hassan et al, 2001].	155
Figure 6.6. Numerical solution of the equation (6.5) for transparent film	159
Figure 6.7. An in-house made Kretschmann type experimental set-up used to obtain SPR	163
Figure 6.8. Experimental arrangement for an ellipsometry measurement	164
Figure 6.9. Experimental SPR curves obtained for bare gold film and overlayers of stearic acid LB films deposited on gold. The number of monolayers is indicated on the corresponding curves	166
Figure 6.10. Experimental SPR curves of gold films and over layers of calix[8]arene LB films deposited on bare gold. The number of monolayer is indicated on the corresponding curves	167
Figure 6.11. Resonance shift of SA LB overlayers with respect to Au SPR curve	168
Figure 6.12. Resonance shift of CA LB overlayers with respect to Au SPR curve	169

Figure 6.13. Dependence of the resonance shift ( $\Delta\theta_{\text{SPR}}$ ) on the thickness of the LB films (number of the LB layers)	169
Figure 6.14. Increase in film thickness with the number of LB films acquired from SPR	174
Figure 6.15. Dependence of thickness on the number of layer obtained from ellipsometry	174
Figure 6.16. Variation of refractive index with the number of LB films obtained from ellipsometry measurements	175
Figure 6.17. Changes in SPR curves of SA LB films (6 layers) due to formation of CdS nanoparticles: (1) initial curve, (2) after 18 minutes exposure to $\text{H}_2\text{S}$ , (3) after 36 minutes exposure to $\text{H}_2\text{S}$	177
Figure 6.18. Changes in SPR curves of CA LB films (6 layers) due to formation of CdS nanoparticles: (1) initial curve, (2) after 18 minutes exposure to $\text{H}_2\text{S}$ , (3) after 36 minutes exposure to $\text{H}_2\text{S}$	178
Figure 6.19. Kinetics of CdS nanoparticles formation in SA LB films (6 layers) measured at a fixed angle of incidence ( $\theta^*=46^\circ$ )	180
Figure 6.20. Kinetics of CdS nanoparticles formation in CA LB films (6 layers) measured at a fixed angle of incidence ( $\theta^*=45.2^\circ$ )	180
Figure 7.1. Two configurations often used for measuring electrical conductivity in LB films structures: (a) in-plane; (b) normal to the plane[after Petty, 1996]	189
Figure 7.2. Electrode arrangements for electrical measurements of (a) normal to the plane and (b) in-plane conductivities [after Petty, 1996]	190
Figure 7.3. Quantum mechanical tunnelling in: (a) thick barrier; (b) thin barrier [after Petty, 1996]	191
Figure 7.4. Models of electron tunnelling in different barriers: (a) rectangular barrier; (b) trapezoidal barrier; (c) triangular barrier	193
Figure 7.5. Al/LB monolayer/Al system was applied by Mann and Kuhn [1971] to measure the electrical transport through LB film	195
Figure 7.6. Hopping process in the multilayer system (Sugi, 1985). An electron moves about the system, sometimes along the interface, sometimes traversing the hydrocarbon barrier, to drift stochastically towards the positive electrodes [after Sugi, 1985]	196
Figure 7.7. Sandwich structure of Al/LB film/Al samples	201
Figure 7.8. Planar structure samples using interdigitated electrodes	202
Figure 7.9. Schematic diagram of the coating system of thermal evaporation	204

Figure 7.10. A specially design mask using to evaporate aluminium thin film on the glass slide for a bottom electrode	206
Figure 7.11. A specially design mask used to evaporate aluminium thin films for the top contact of the sandwich structures	207
Figure 7.12. A Liquid nitrogen cryostat used for electrical measurements on different temperatures	210
Figure 7.13. Schematic diagram of the electrical measurement system	211
Figure 7.14. I-V characteristics of 33 layers of SA LB films for both treated and untreated samples	214
Figure 7.15. I-V characteristics of 37 layers of CA LB film	215
Figure 7.16. Semi-logarithmic scale of I-V characteristics of 33 layers of SA LB films for both treated and untreated samples	216
Figure 7.17. Semi-logarithmic scale of I-V characteristics of 37 layers of CA LB films for both treated and untreated samples	217
Figure 7.18. Temperature dependence of conductivity of SA LB films: (1) after H <sub>2</sub> S at 0.5 V, (2) before H <sub>2</sub> S at 0.5 V, (3) after H <sub>2</sub> S at 2.5 V, (4) before H <sub>2</sub> S at 2.5 V.	219
Figure 7.19. Temperature dependence of I-V Characteristics of CA LB films (1) after H <sub>2</sub> S at 0.5 V, (2) after H <sub>2</sub> S at 2.5 V, (3) before H <sub>2</sub> S at 0.5 V, (4) before H <sub>2</sub> S at 2.5 V	220
Figure 7.20. Schematic diagram of the physical process of the electron transfer through a multilayered LB film	225
Figure 7.21. Energy model of the electron transfer through a multilayered LB film	226
Figure 7.22. AC capacitance of the sandwich structures containing LB films (33 layers) of SA (1,2) and 37 layers of CA (3,4) before (1,3) and after (2,4) H <sub>2</sub> S treatment	229
Figure 7.23. AC conductance of the sandwich structures containing LB films (33 layers) of SA (1,2) and 37 layers CA (3,4) before (1,3) and after (2,4) H <sub>2</sub> S treatment	230

## LIST OF TABLES

Table 3.1. Long chain fatty acids compounds used in monolayer work [after Petty, 1996]	60
Table 5.1. Characteristic energies for the luminescence of CdS nanoparticles in LB films	134
Table 6.1. Ellipsometry data for both SA and CA LB films before H <sub>2</sub> S treatment	172
Table 6.2. Optical parameters of LB films obtained from UV-visible absorption, ellipsometry and SPR measurements. Thickness per monolayer is given in nm	175
Table 6.3. The value of minimum angle of resonance and the minimum intensity of SPR curve of SA and CA LB films	179
Table 6.4. Ellipsometry data for both SA and CA LB films after H <sub>2</sub> S treatment	182
Table 6.5. Optical parameters of LB films obtained from the absorbance, ellipsometry and SPR measurements. Thickness is given in nm perlayer	183
Table 7.1. Interface density of states and exponential term of conductivity of treated and untreated LB films	223

# CHAPTER 1

## INTRODUCTION

### 1.1. General Introduction

The discovery that matter consists of discrete entities called atoms in the early nineteenth century stimulated a natural desire to be able to control the structure of matter atom by atom. In recent years, by using a scanning tunnelling microscope (STM), researchers have afforded to write bits of information utilizing a small number of atoms (even fewer than 100 atoms) [Edelstein and Cammarata, 1998].

The technological applications of nanomaterials have prompted research on such materials. The quantum confinement effect in small geometries of semiconductors conceives new energy levels and thus modifies the optoelectronic properties of the materials. In microelectronics, reducing the size of electronic components has been motivated by the necessity for increased memory, faster switching times and higher functionality. The decreasing size of conventional devices, such as field effect transistors, to around 100 nm is a clear way to the miniaturization of electronics with the related benefits. Quantum effect devices are of potential necessity for future electronic devices. The advance in memory technology is utilized in cost reduction and the

development of ever faster, more compact, and less power consuming memory systems, with bigger storage capacity. It is natural to expect that nanotechnology will eventually play a fundamental role since all of these benefits can be obtained by reducing the size of the basic storage cell. Therefore, it is believed that the inclusion of nanostructures will be necessary for revolutionary advances in electronics and related technologies.

Quantum-sized semiconductor materials has been an active area of research due to their unique electrical and optical properties [Nabok et al, 1997; Lin Song Li et al, 1997; and Erokhin et al, 1998]. A variety of chemical methods including Langmuir-Blodgett (LB) films have been used to prepare nanoparticles with their sizes in the range of 1 and 10 nm. The research has mostly focused on the preparation and characterisation of the quantum dots and quantum wells systems and different nanoparticles [Kortan et al, 1990; Mews, 1994 and Lin Song Li, et al, 1997].

Particles of different materials, such as CdS [Smotkin et al, 1988], PbS [Erokhin et al, 1991] and HgS [Zylberajch et al, 1989] were formed using Langmuir-Blodgett films of fatty acid salts (with Cd, Pb and Hg) by exposing them to an H<sub>2</sub>S gas. The technology of ordered organic films gives many opportunities to control the size of nanoparticles and form ordered organic-inorganic systems. For instance, this approach has been used by Nabok et al [1997] to produce much smaller CdS particles in calixarenes LB films. Some interesting phenomena namely blue shift in the optical absorbance [Smotkhin et al, 1988; Erokhin et al, 1994] and single-electron conductivity [Erokhin et al, 1995; Erokhin et al, 1996] were observed in such systems.

Erokhin et al [1994] has demonstrated that the fatty acid matrix can also be removed selectively, providing self-aggregation of semiconductor nanoparticles into a thin film at the substrate. The resulting material was polycrystalline, with an average thickness of around 0.6 nm per LB bilayer of the initial fatty acid salt. Such a resolution

in thickness can be reached by only a few available techniques. Molecular beam epitaxy (MBE) technology is the most powerful, but this technique uses expensive and complicated equipment as well as ultra pure materials. In 1998 Erokhin et al successfully produced semiconductor superlattices with alternating layers of different materials using nanoparticle aggregation.

The main goal of this research project is to study the formation and properties of the II-VI semiconductor quantum structures within organic films of different compounds (fatty acids and calixarenes). A number of organic film technologies (Langmuir-Blodgett (LB), spin coating, self-assembly and sol gel methods) can be used for the preparation of thin films. This project concentrates on the LB technique as a main method. These techniques have shown their potential for the formation of semiconductor quantum structures and superlattices in recent years, which provide a real alternative to costly MBE technology. These deposition techniques can be explored to optimise the control of electrical and optical properties of II-VI semiconductor and multi quantum well structures for application in nanoelectronics and optoelectronics. These technologies should potentially contribute to the development of advanced materials and nanoelectronic devices for many years to come.

## 1.2. Aims and Objectives

The aim of the present research is the formation and characterisation of II-VI semiconductor quantum structures prepared by Langmuir-Blodgett (LB) film technique. Optical and electrical properties of the deposited thin film layers will be investigated.

The objectives of this project are:

1. To produce CdS nanoparticles formed in LB films of different compounds (stearic acids and calix[8]arene).
2. To study the formation of II-VI semiconductor quantum structures, especially CdS nanoparticles formed inside LB films.
3. To study the optical properties of the produced quantum structures using UV-visible spectroscopy, photoluminescence emission (PL) and excitation (PLE), Surface Plasmon Resonance (SPR) and ellipsometry measurements.
4. To study the transformation in the size of CdS nanoparticles within two-dimensional LB layers.
5. To investigate the macroscopic electrical properties of the quantum structures with conductivity measurements and impedance measurements (dc and ac in both sandwich and lateral geometries)

## 1.3. Organisation of the Thesis

The thesis is organised into eight chapters. The current chapter presents a general introduction to the thesis.

Chapter 2 provides a summary of physics of II-VI semiconductor quantum structures. Technology of their formation and current applications are described, together with a review of their optical and electrical properties. The approach used in this thesis for selecting certain technologies and properties for investigation is explained.

Chapter 3 contains an introduction and detailed examination of the LB technique for deposition of thin monomolecular films onto solid substrates. A description of the method used in the current project is presented, with examples of the isotherms produced. Structural review of both stearic acid and calixarene compounds is presented. The remaining section covers preparation of nanoparticles in LB films concentrates on the formation of II-VI semiconductor nanoparticles in both LB films by the H<sub>2</sub>S treatment. The process of formation of II-VI semiconductor nanoparticles in LB films and the schematic structure of the nanoparticles are also presented.

Chapter 4 presents the study of morphology of Cadmium Sulphide (CdS) nanoparticles formed within LB films. The novel technique of Atomic Force Microscopy (AFM) was used in this study. An introduction, details of the experimental technique together with the results and their analysis are given.

Chapter 5 provides optical characterisation of Cadmium Sulphide (CdS) nanoparticles in LB films. Theoretical principles of the techniques used in this present research (UV-visible absorption spectroscopy and luminescence measurements) are

mentioned. Details of the experimental techniques and their results together with an analysis and discussion are also presented. This chapter also provides the study of the evolution of CdS nanoparticles in LB films. A theoretical model of two-dimensional diffusion of semiconductor nanoparticles in LB films is also given.

Chapter 6 is concerned with the studies of surface plasmon resonance (SPR) and ellipsometry of LB films containing CdS nanoparticles. Evaluation of optical parameters: film thickness ( $d$ ), refractive index ( $n$ ) and extinction coefficient ( $k$ ) of the LB films is also provided. The process of the formation of CdS nanoclusters in LB films was studied in situ by using SPR technique.

Chapter 7 contains the results of electrical study of the LB films containing CdS nanoparticles. The samples of LB films were studied in both planar (coated Pt interdigitated electrodes) and sandwich structures (Al/LB film/Al) before and after H<sub>2</sub>S treatment. Two types of electrical tests, DC I-V characteristics at different temperature (80-340K) and AC impedance measurements (capacitance and conductance) at different frequencies (20Hz-1MHz) and temperature (80-340K), were performed.

Chapter 8 summarises the thesis and brings together results from the different experiments. The final conclusions are made as well as suggestions for further work.

# CHAPTER 2

## PHYSICS OF SEMICONDUCTOR QUANTUM STRUCTURES

### 2.1. Introduction to Semiconductors

The energy band structure is responsible for electrical characteristics of materials. Semiconductor materials at low temperature (0 K) have an empty conduction band separated from a full valence band by a band gap having forbidden energy states. This band structure is similar to that of insulators. The relatively small value of energy gaps of semiconductors (as compared to those of insulators) permits electrons to excite from the valence band to the conduction band by certain amounts of thermal or optical energy.

#### 2.1.1. Direct and Indirect Semiconductors

According to the band structure, there are two types of semiconductor energy bands: direct and indirect band gaps (Figure 2.1). Direct band gap semiconductors have a minimum in the conduction band and a maximum in the valence band for the same  $\mathbf{k}$  value ( $\mathbf{k}=0$ ) in the  $(E, \mathbf{k})$  diagram, where  $E$  is the energy of an electron (or hole) and  $\mathbf{k}$  is the wavevector. On the other hand, indirect band gap semiconductors have their valence

band maximum at a different value of  $k$  than their conduction band minimum. Thus an electron making a smallest-energy transition from the conduction band to the valence band in the direct band gap materials can do so without a change in  $k$  value, while a transition from the minimum point of conduction in the indirect band gap materials to the maximum point of the valence band requires some change in  $k$  (requires a change of momentum for the electron).

As can be seen from Figure 2.1, in a direct semiconductor such as CdS, an electron in the conduction band can fall to an empty state in the valence band, emitting the energy difference  $E_g$  as a photon of light, in a process known as radiative recombination. The dispersion of the photon is given by  $k = \eta\omega/c$  (where  $\eta$  is the refractive index) and hence an optical photon has a wavevector which is relatively small in comparison to the Brillouin zone width  $\sim \pi/a_0$ . Thus, in order to conserve momentum, radiative recombination with the emission of only a photon can involve transitions for which  $\Delta k \approx 0$ . These transitions are vertical on an  $E$  vs  $k$  band diagram, and are known as direct transitions. Such materials are said to possess a direct band gap.

In contrast, an electron in the conduction band minimum of an indirect semiconductor such as PbS cannot fall directly to the valence band maximum but must undergo a momentum change as well as changing its energy. In this case radiative recombination cannot occur without the assistance of some  $k$ -conservation mechanism. Scattering processes, such as phonon or impurity scattering, may provide such a mechanism by allowing radiative recombination to take place via a virtual state ( $E_i$ ) in the forbidden gap, close to  $k = 0$ . In an indirect transition which involves a change in  $k$ , the energy is generally given up as heat to the lattice rather than as an emitted photon. However, irrespective of the recombination process, the transition probability for such indirect gap recombination is considerably smaller than that for direct gap

recombination. The radiative recombination time is increased and may become comparable to that of competing non-radiative processes. Hence, radiative emission is generally inefficient in indirect band gap semiconductors and, as a result these materials are usually of limited use in light emitting devices.

This difference between direct and indirect band structures is very important for deciding which semiconductors can be used in devices requiring light output. For example, semiconductor light emitters and lasers generally must be made of materials capable of direct band-to-band transitions or indirect materials with vertical transitions between defect states.

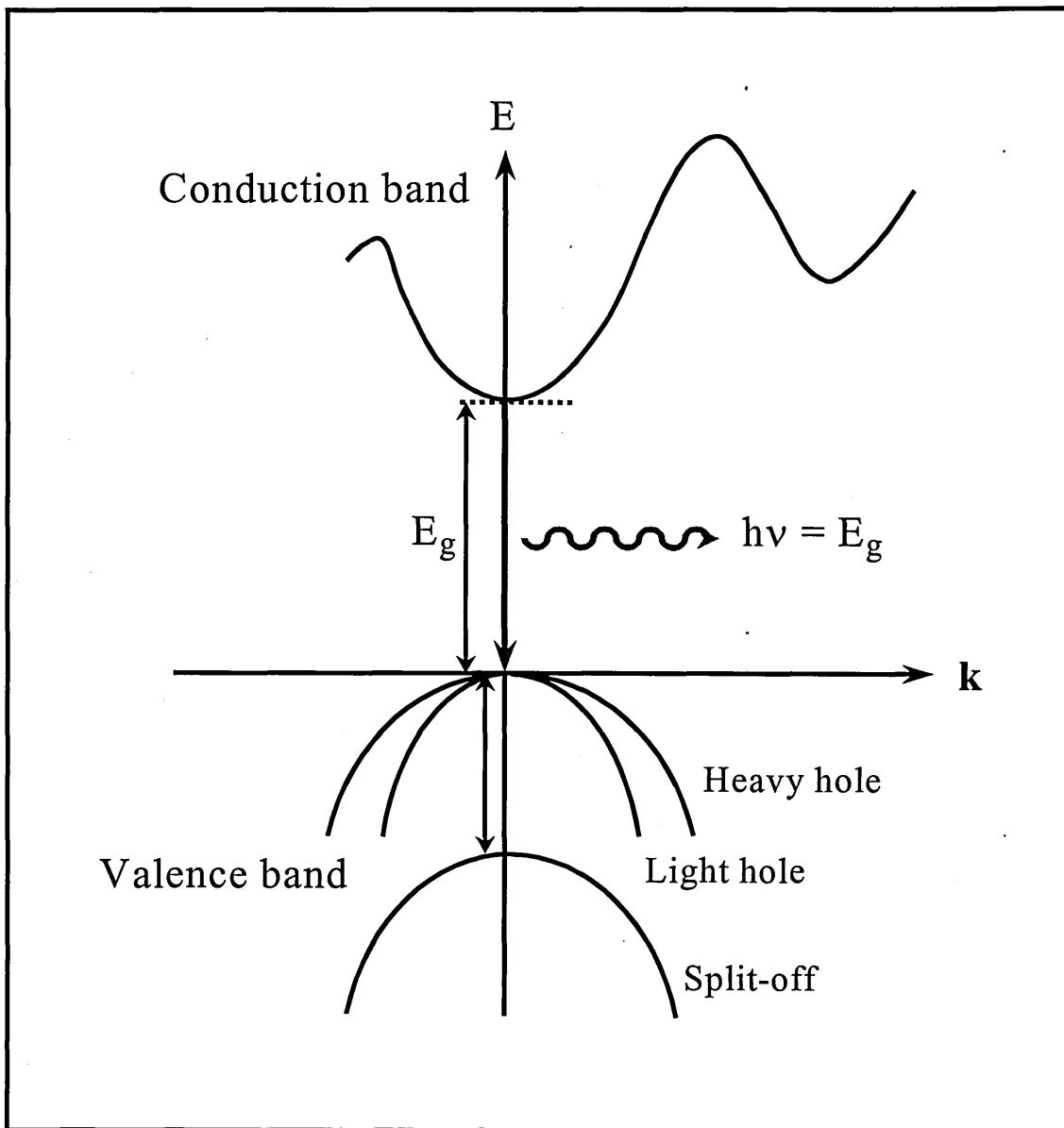


Figure 2.1. Direct electron transitions in a direct band semiconductor with accompanying photon emission

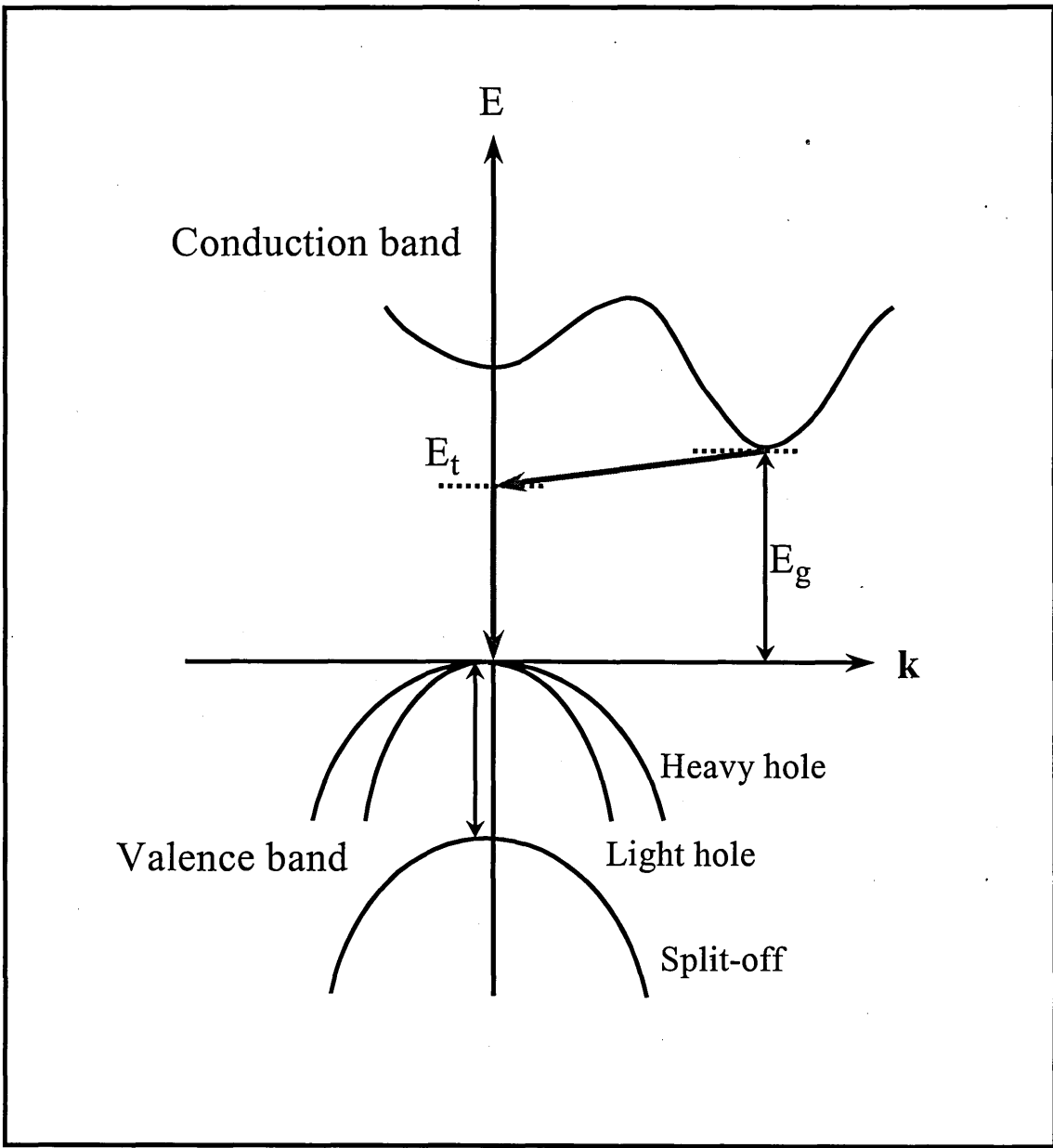


Figure 2.2. Indirect electron transitions in an indirect semiconductor via a defect level

## 2.1.2. Excitons in Semiconductors

Excitons are electron-hole pairs bound by their attractive coulomb interaction which can be described in terms of “hydrogenic” levels close to the conduction band. This is caused by the absorption of photons with the creation of the bound electron-hole pairs. Excitons can move through the crystal and transport energy. They do not transport charge because they are electrically neutral. The excitons form a series of hydrogenic-like states (discrete parabolic bands) below the energy level at the bottom of the conduction band ( $E_c$ ). Figure 2.3 shows the exciton levels in the simple case of a direct band gap semiconductor, such as the II-VI compounds, with energy gap  $E_g$  centred at  $k=0$  in the Brillouin zone.

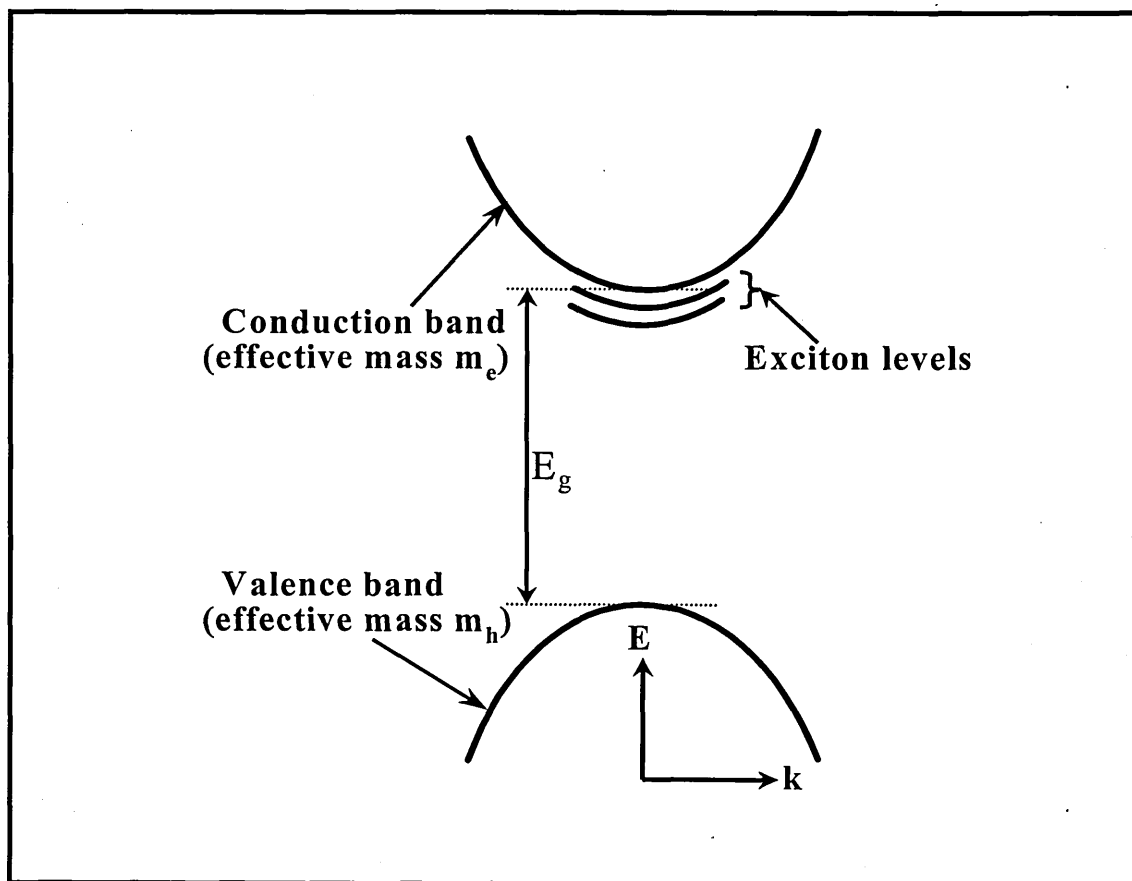


Figure 2.3. Schematic representation of the excitons, where  $E_g$  is the energy gap

Excitons can be split into two classes, one is the more localised exciton, which has a small electron-hole radius compared with the crystal lattice parameter. Such excitons are very tightly bound, these are known as Frenkel type excitons [Kittel, 1996]. The second one is Mott-Wannier type excitons, where electron and hole are more weakly bound, with the electron-hole radius significantly greater than the lattice parameter. In such excitons, the electron sees along with the associated hole, an average lattice potential. As a result of this it is possible to attribute the electron and hole with effective mass,  $m_e^*$  and  $m_h^*$ , which reflect the character of the valence and conduction bands within the crystal.

An electron in conduction band and a hole in the valence band may attract each other by the coulomb potential:

$$U(r) = -\frac{e^2}{\epsilon r} \quad (2.1)$$

where  $r$  is the distance between the particles and  $\epsilon$  is the appropriate dielectric constant. There will be bound states of the exciton system having total energies lower than the bottom of the conduction band.

The energy levels  $E_{n,K}$  of excitons created by the absorption of photons of appropriate wavelength are given by the simple hydrogenic model [Yoffe, 1993]:

$$E_{n,K} = E_g - \frac{\mu e^4}{2 \hbar^2 \epsilon^2 n^2} + \frac{\hbar^2 K^2}{2(m_e^* + m_h^*)} \quad (2.2)$$

where  $n$  is the exciton quantum number,  $E_g$  is the bulk energy gap,  $K = k_e - k_h$  and  $\mu$  is the reduced mass:

$$\frac{1}{\mu} = \frac{1}{m_e^*} + \frac{1}{m_h^*} \quad (2.3)$$

The second term in Equation (2.2) is associated with the exciton binding energy  $E_b$ . The ground state ( $n=1$ ) of the exciton binding energy can be expressed in various forms.

$$E_b = \frac{13.6\mu}{m_o \varepsilon_2^2} eV = \frac{e^2}{2\varepsilon_2 a_B} = \frac{\hbar^2}{2\mu a_B^2} \quad (2.4)$$

The general expressions for the exciton Bohr radii are

$$a_B(n) = \frac{\hbar^2 \varepsilon_2}{\mu e^2} n^2 = 0.53 \frac{\varepsilon_2}{\mu / m_o} n^2 \text{ \AA} = \frac{7.2}{\varepsilon_2 E_b(n=1)} n^2 \quad (2.5)$$

The third term in Equation (2.2) is the kinetic energy term related to the centre-of-mass motion of the exciton.

Equation (2.2) is commonly written in the simple form as

$$E(n) \approx E_g - \frac{E_b}{n^2}, \quad n = 1, 2, 3, \dots \quad (2.6)$$

The exciton may be free to move around the crystal, in which case it is termed a free exciton. Alternatively, the exciton may become bound by an impurity atom or localised at spatial potential fluctuations, caused by alloy composition fluctuations. The trapping of free excitons generally happens rapidly; frequently before free exciton recombination can occur. As a result, recombination of the free exciton state is observed only in high purity material.

## 2.2. Physics of Bulk II-VI Semiconductors

II-VI semiconductor materials have been and still are the subject of much intensive study. The feature of chemical stability of the higher energy gap materials at room temperature of these compounds offers an advantage over the unstable III-V compounds, such as III-V phosphides. The II-VI compounds in their broadest sense include compounds formed from elements of group II and group VI of the periodic table. A general character of the II-VI compounds is direct energy gaps with the exceptional of the semi-metals, HgTe and HgSe.

### 2.2.1. Crystallographic Form of II-VI Compounds

The tetrahedral lattice sites are usually formed by the combination of group II and VI elements, which gives on average four valence electrons per atom. In this situation, there is a tendency towards sharing rather than the transfer of electrons between atoms. Each atom A in a tetrahedral lattice site of AB compound is surrounded symmetrically by four nearest neighbouring B atoms. In order to form this structure, the B atoms should occupy the corners of a tetrahedron with the A atom sit at its geometrical centre. Two possible formations can be formed by the combination of the tetrahedral sites. Figure 2.4 (a) shows the formation when the base triangles of the interpenetrating tetrahedral are parallel and lined up normal to each other. The base triangles again parallel but rotated through  $60^\circ$  about the normal to each other is illustrated in Figure 2.4(b).

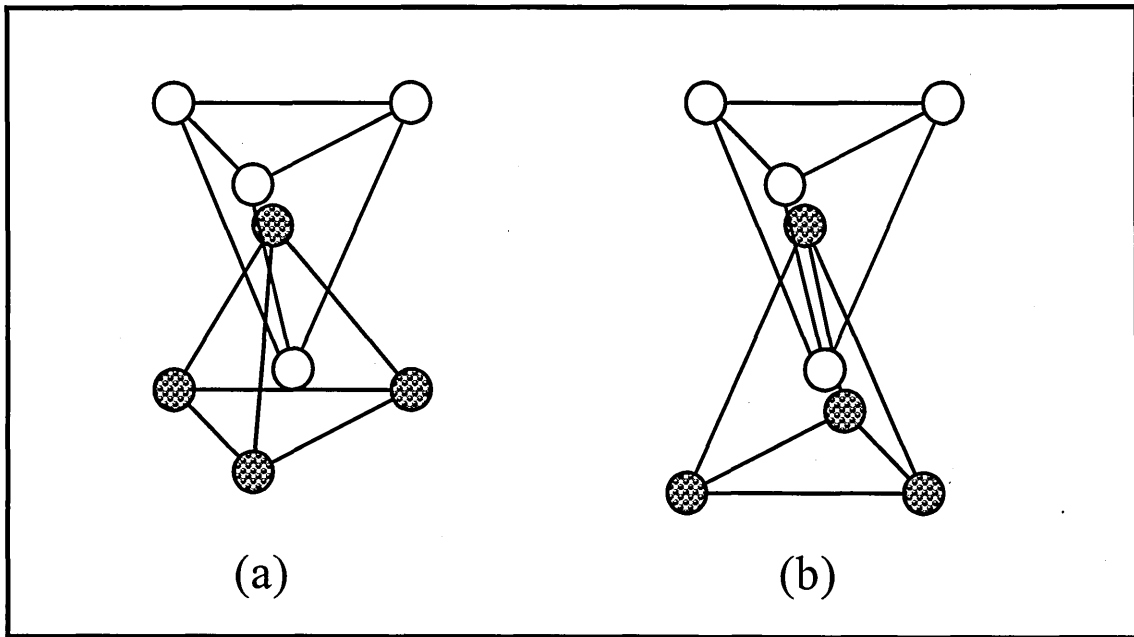


Figure 2.4. Tetrahedral sites for a compound: (a) bases of tetrahedra parallel and in line vertically; (b) bases of tetrahedra parallel and  $60^\circ$  out of line vertically [after Ray, 1969]

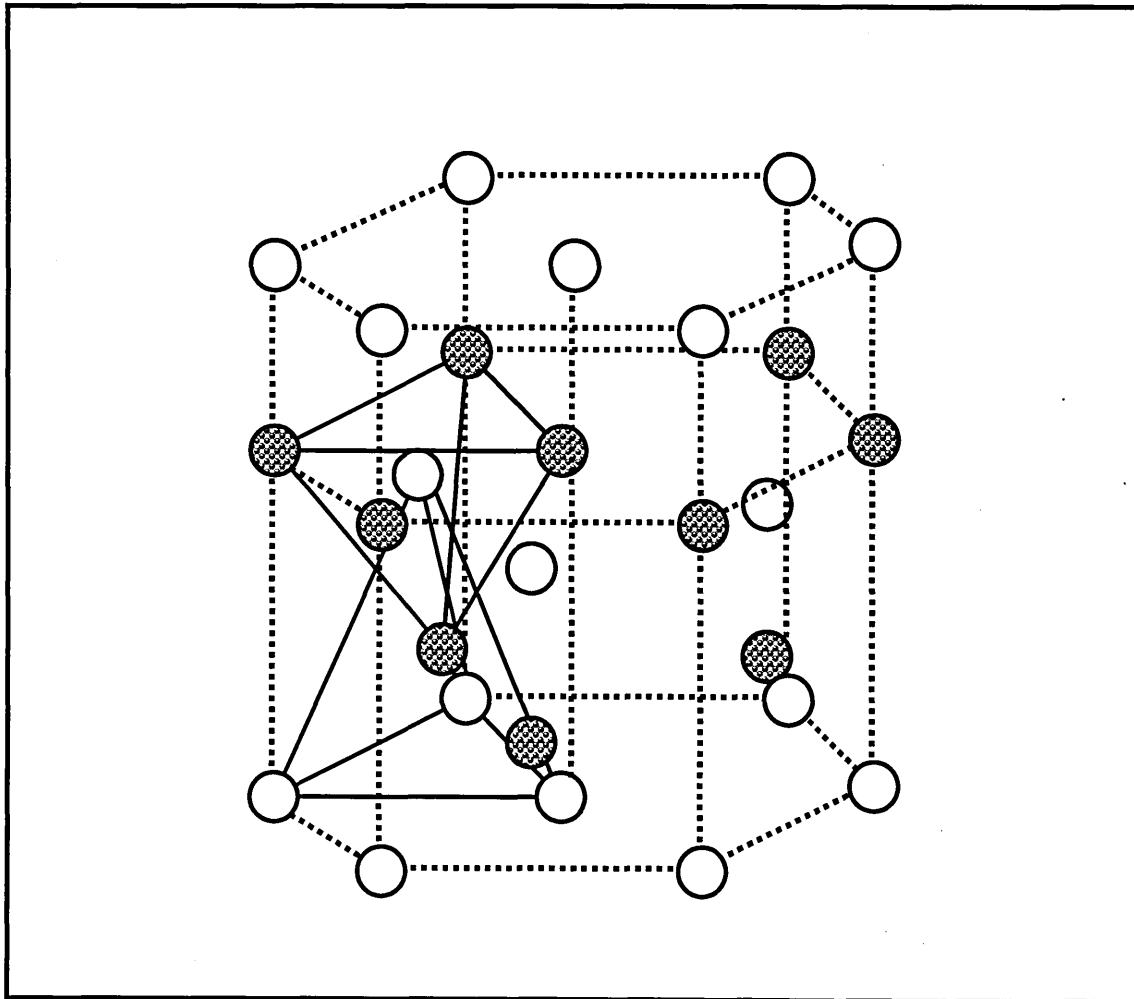
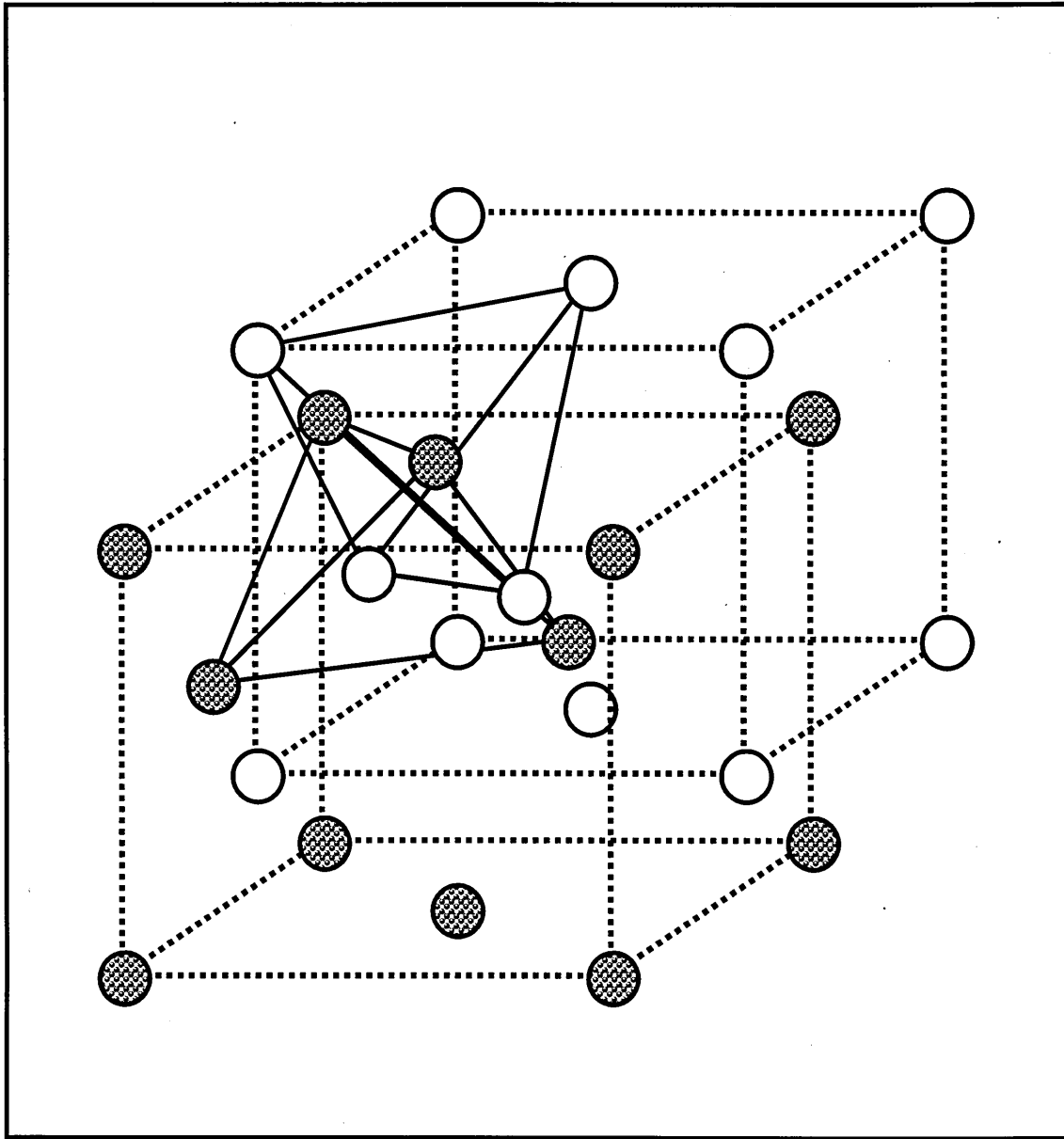


Figure 2.5. Wurtzite structure formed from tetrahedral site

The two crystal structures: wurtzite and zinc blende can be formed from these two combinations of the tetrahedral lattice sites. The wurtzite crystal structure is in hexagonal crystal class as illustrated in Figure 2.4 (a) has the combination of tetrahedral sites. This structure contains two interpenetrating close-packed hexagonal lattices, as shown in Figure 2.5, separated from each other by a distance  $3/8c$  along the hexagonal  $c$ -axis. Ideally in the wurtzite structure, the nearest neighbour distance is  $3/8c$  or  $\sqrt{3}/8a$ , which gives a  $c/a$  ratio of  $\sqrt{8/3} = 1.632$ . CdS, SdSe, ZnS, ZnSe, BeO, ZnO and MgTe have all been observed to take the wurtzite structure.

Figure 2.4(b) presents tetrahedral sites combination related to the zinc blende structure. This crystal structure is usually in cubic crystal class. This structure consists of two interpenetrating cubic close-packed lattices and derived from the diamond structure (Figure 2.6), displaced each other by  $1/4$  of the body diagonal. The nearest neighbour separation of this structure is  $\sqrt{3}/4a$ . The sulphides, selenides and tellurides of beryllium, zinc, cadmium and mercury have all been obtained with the zinc blende structure.



*Figure 2.6. Crystallographic lattice of zinc blende structure*

## 2.2.2. Band Structures of II-VI Semiconductors

The knowledge of band structure in the II-VI compounds has been derived from the semi-empirical pseudopotential method [Cohen and Bergstresser, 1967]. In this method, an approximated Schrödinger equation with a potential term is used. As mentioned above, the II-VI compounds can form both crystal structures: wurtzite and zinc blende. In case of CdS quantum structures, the wurtzite structure is more common. Figure 2.7 shows the band structure of the wurtzite CdS, one of the most studied II-VI compounds. It can be seen, the maxima of the uppermost valence bands are situated at the  $k = 0$  ( $\Gamma$ -point). The  $\Gamma$ -point valence band states are formed from p-like orbitals. The quadruply spin degenerate  $\Gamma_5$  band is split into  $\Gamma_9$ , upper  $\Gamma_7$  and lower  $\Gamma_7$  bands with separations related to the crystalline field  $\Delta_{cr}$  and spin-orbit splitting  $\Delta_{so}$  energies. The holes (and associated excitons) in these three valence bands are conventionally called A-, B-, and C-type holes or excitons. It is possible therefore to derive  $\Delta_{so}$  and  $\Delta_{cr}$  from the exciton spectrum in the wurtzite. At low temperatures the exciton absorption to the first excited state as well as the ground state is observed. The separation between the  $\Gamma_9$  level and the upper  $\Gamma_7$  and lower  $\Gamma_7$  levels are denoted by  $E'$  and  $E''$  and are related to the crystalline field and spin-orbit splitting energies by [Ray, 1969]:

$$E'(E'') = \frac{1}{2}(\Delta_{so} + \Delta_{cr})(\mp) \left[ \frac{1}{4}(\Delta_{so} + \Delta_{cr})^2 - \frac{2}{3}\Delta_{so}\Delta_{cr} \right]^{1/2} \quad (2.7)$$

The lowest energy conduction band state also occurs at the  $\Gamma$ -point in the wurtzite CdS ( $\Gamma_7$ ), and is formed from s-like orbitals. Most important for light emitters based on CdS is direct fundamental optical transition at or near the  $\Gamma$ -point ( $k = 0$ ). This transition is between the uppermost valence band states and the lowest conduction band minimum.

Figure 2.8 presents the energy band form of the wurtzite CdS which is centred about the  $\Gamma$  point. The diagram indicates the transitions, which occur for polarized radiation along with the two  $\Gamma_9$ - $\Gamma_7$  valence band separations.

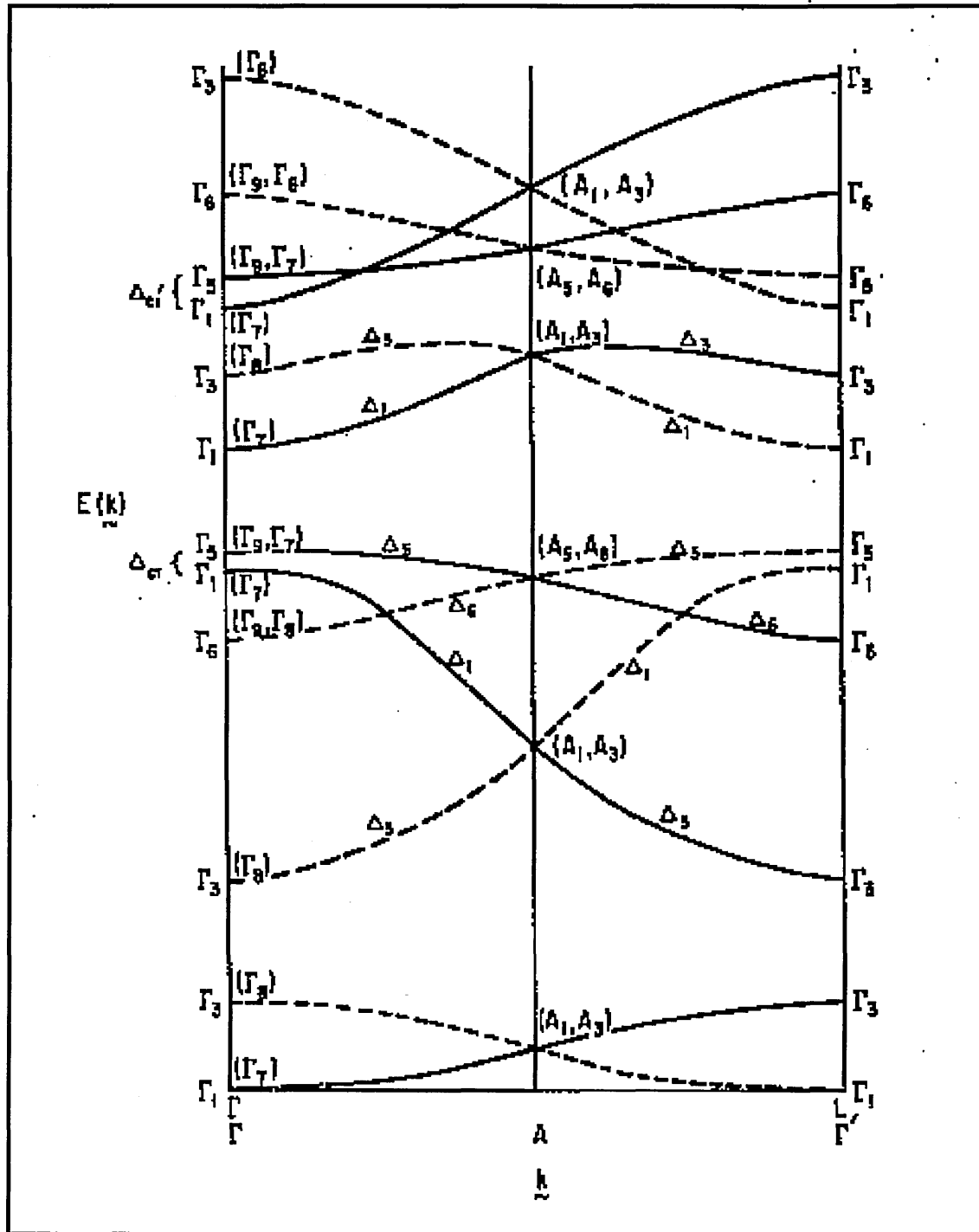


Figure 2.7. Energy bands for wurtzite CdS along the  $\Gamma$ -A axis [after Segall, 1967]

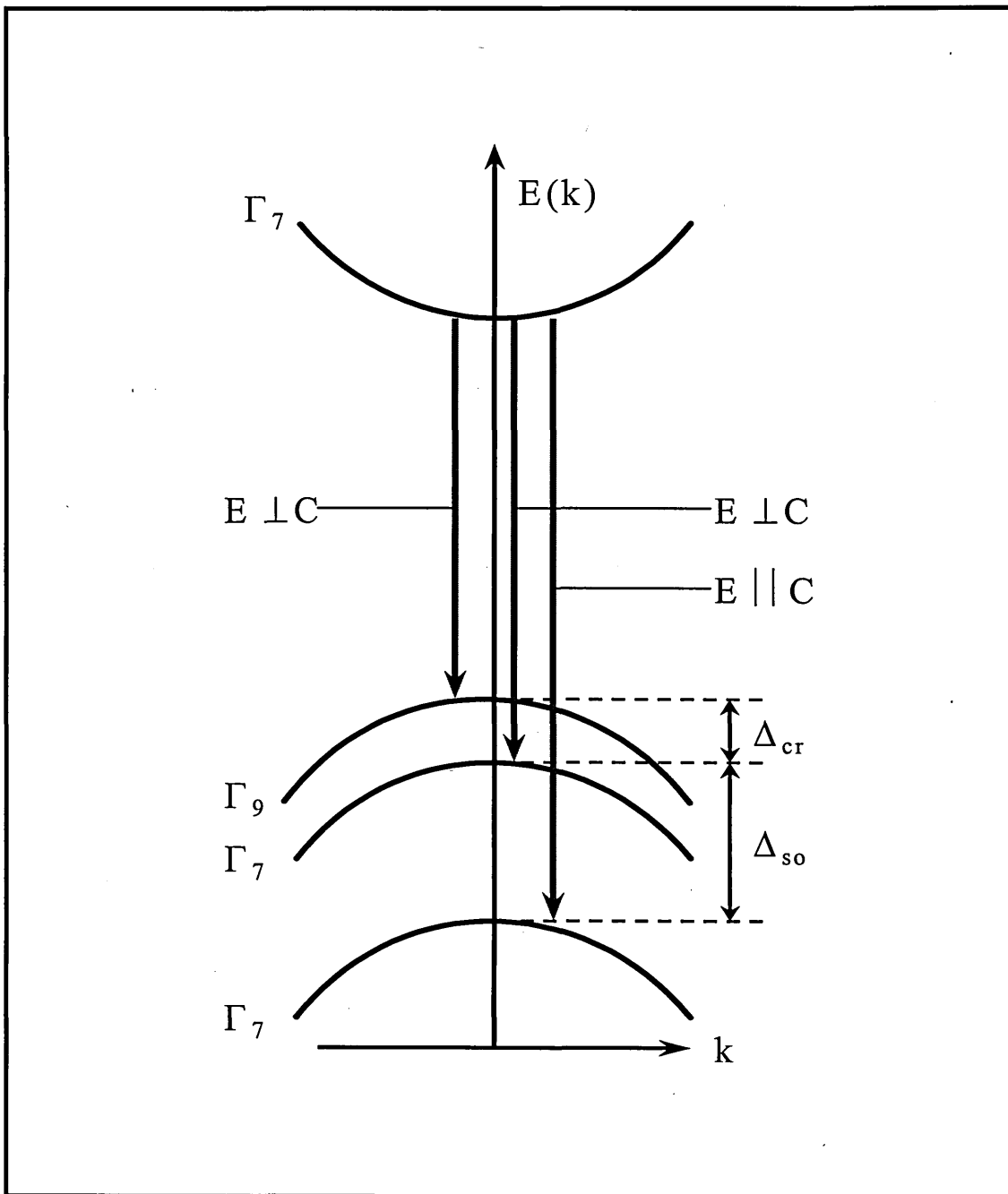


Figure 2.8. Energy band structure of wurtzite CdS in the region of the  $\Gamma$  point with crystalline field and spin-orbit splitting effects present in the valence band structure [after Birman et al, 1961]

## **2.3. Physics of Semiconductor Nanostructures**

Semiconductor nanostructures having unique electrical and optical properties, which differ from conventional bulk semiconductor, have been attracting much attention. In such materials, the carriers are confined in the nanometer regions. Their application is also expected to realize, high performance quantum functional devices.

One of the essential issues in studying and exploring the physics of semiconductor quantum structures and the possibility of their practical device applications, is how one can realize quantum structures which satisfy some requirements in their uniformity, electrical or optical quality, and so on. When these requirements are satisfied, the quantum effects arising from the wave nature of electrons can clearly be observed. This is partially proved in two-dimensional electron systems and quantum wells or superlattice structures. In such systems, the quantum mechanical confinement of electrons and holes are realized in one direction.

### **2.3.1. Technology of Semiconductor Nanostructures**

In recent years, several works on realisation of semiconductor quantum nanostructures have been reported. One of the approaches is to utilize nanofabrication techniques with lithography, etching and/or ion implantation. In this approach, quantum wells or heterostructures are used as starting materials for the nanofabrication. Lateral confinement in wire or dot structures are realized by etching after those patterns are defined by electron beam lithography. The limitation of the size by the lithography is one of the disadvantages of this approach. The other is that the process-induced can damage particularly at the etched-sidewalls. These two disadvantages are problematic for the quality of the devices. However, some of the unique electronic states and

transport properties in low-dimensional electron systems are disclosed [Asai et al, 1987].

The other approach for realization of semiconductor nanostructure is to use crystal growth technique. With this method semiconductor quantum nanostructures are directly formed during crystal growth by using molecular beam epitaxy (MBE) and metal organic vapour phase epitaxy (MOVPE) techniques. Such crystal growth techniques have realized a variety of quantum nanostructures, which can be classified as follows:

- (1) Quantum wire arrays utilizing atomic steps as templates for the lateral compositional or thickness modulation [Brasil et al, 1994; Nakata et al, 1995; Wu et al, 2002].
- (2) Quantum wire and quantum dots grown on selective area of substrates [Asai et al, 1987; Fukui et al, 1989; Galeuchet et al, 1991; Tsukamoto et al, 1993]
- (3) Growth on substrates with patterning, such as V-grooves or mesa-patterns [Kapon et al, 1989; Kojima et al, 1990; Isshiki et al, 1993; Wang et al, 1995]
- (4) Quantum dots formed by self-assembly, for examples, by droplet epitaxy [Chikyow and Koguchi, 1992, Petroff et al, 2001], by using islanding in Stranski-Krastanow growth mode in strained layer growth [Oshinowo et al, 1994; Kawabe et al, 1997], by self-organization of strained layer on high-index surfaces [Nötzel et al, 1994], or by strain-induced phase separation [Pearah et al, 1993; Kim et al, 1996].

These techniques can realize high-quality quantum nanostructures with small size. With these methods heterostructures in which electrons and holes confined can also be realized. Such methods of crystal growth are thought to be one of the most promising techniques for the formation of semiconductor nanostructures. In fact, several studies of one- and zero-dimensional properties of carriers in quantum wires and

quantum dots and their device applications with nanostructures formed by the above methods are reported [Kapon et al, 1989; Shoji, et al, 1995; Arakawa et al, 1996; Saito et al, 1996; Okada et al, 1997; Hara et al, 1998]. However, these methods have disadvantages that the techniques use expensive and complicated equipment as well as ultra pure materials.

Alternatively, a variety of chemical methods including Langmuir-Blodgett (LB) films have been used to prepare quantum nanostructures. The chemical synthesis of nanoscale materials from 1 to 20 nm in diameter (quantum dots, nanocrystals, or nanoparticles) is a rapidly expanding area of research, because of their low cost and many other advantages. In this size regime, the clusters possess short-range structures that are essentially the same as the bulk semiconductors, yet have optical and/or electronic properties which are different from the bulk [Efros and Efros, 1982; Wang and Herron, 1991].

In the chemical preparation of nanoscale particles with desired properties, the structural properties (crystalline or amorphous structure, size, shape, morphology), and chemical properties (composition of the bulk, interface, and surface) are important factors to be considered [Chow and Gonsalves, 1998]. Because of its advantages, the role of chemistry in materials science has been rapidly growing. Two kinds of approaches in the chemical techniques that can be applied to produce semiconductor nanostructures: colloid chemistry approach and ordered organic films technology.

### **(1) Colloid Chemistry Approach**

Nanomaterials can be prepared in the form of dispersed colloids or trapped and stabilized within micelles, polymers, zeolites, or glasses. In most cases, clusters prepared by these methods have poorly defined exterior surfaces and a relatively broad

size distribution of about 10-20 % [Herron and Wang, 1998]. The synthesis of single-sized clusters with well-defined surfaces remains a major goal in this field.

## **(2) Ordered Organic Films Technology**

A variety of ordered organic films technology including LB films, Spin Coating and self-assembled monolayers have been used to prepare nanoparticles with quantum sized of 1-10 nm. These techniques have shown potential application for the preparation of semiconductor quantum structures and superlattices in recent years and provided a real alternative for costly MBE technology. These deposition techniques can be explored to optimize the control of electrical and optical properties of semiconductor and quantum well structures for application in microelectronics and optoelectronics.

Langmuir-Blodgett (LB) technique has been used to form II-VI semiconductor nanoparticles of different materials [Smotkin et al, 1988; Erokhin et al, 1991; and Zylberajch et al, 1989]. One of the most important advantages using the technology of ordered organic films is the opportunity to control the size of nanoparticles and form ordered organic-inorganic systems. Nabok et al [1997] have used this approach to produce much smaller CdS particles formed in calixarenes LB films.

Erokhin et al [1994] has demonstrated that the fatty acid matrix can also be removed selectively, providing self-aggregation of semiconductor nanoparticles into a thin film at the substrate. The resulting material was polycrystalline, with an average thickness of around 0.6 nm per LB bilayer of the initial fatty acid salt. Such a resolution in thickness can be reached by only few available techniques. In 1998, Erokhin et al successfully produced semiconductor superlattices with alternating layers of different materials using nanoparticle aggregation. In this thesis, LB films method has been applied to produce II-VI semiconductors nanoparticles by using stearic acid and calixarenes as matrix materials.

## 2.3.2. Excitons in Low-dimensional Systems

Three categories of low dimensional systems that are usually considered:

- (1) The two-dimensional (2D) systems, which include thin films, layer structures, quantum wells and superlattices.
- (2) The one-dimensional (1D) systems, such as linear chain structures, quantum wires.
- (3) The zero-dimensional (0D) systems, such as clusters, quantum dots and colloids.

Figure 2.9 and 2.10 show the illustrations representing system dimensionality and densities of states of low-dimensional systems and bulk semiconductors.

As can be seen from Figure 2.9, the density  $N(E)$  of states changes from a continuous dependence  $N(E) \sim E^{1/2}$  in three dimensions to a step-like dependence in two dimensions. This transition has been studied by Dingle [1976] for the thin semiconductor layer in Figure 2.9 (b). This thin layer has a thickness  $L_z$ , with  $L_x, L_y \gg L_z$ . Carrier confinement (electrons, holes or excitons) occurs in a one-dimensional (1D) potential well. This phenomenon leads to quantization of particle motion in the thickness ( $z$ ) direction, while the carriers can move freely in the  $x$  and  $y$  directions. The optical absorption spectrum for a simple quantum well is shifted to higher energy with respect to the bulk semiconductor. Above the absorption edge, the spectrum is staircase like rather than smooth. These steps correspond to allowed transition between valence band states and conduction band states, while, sharp peaks appeared at each step, correspond to confined electron-hole pair states.

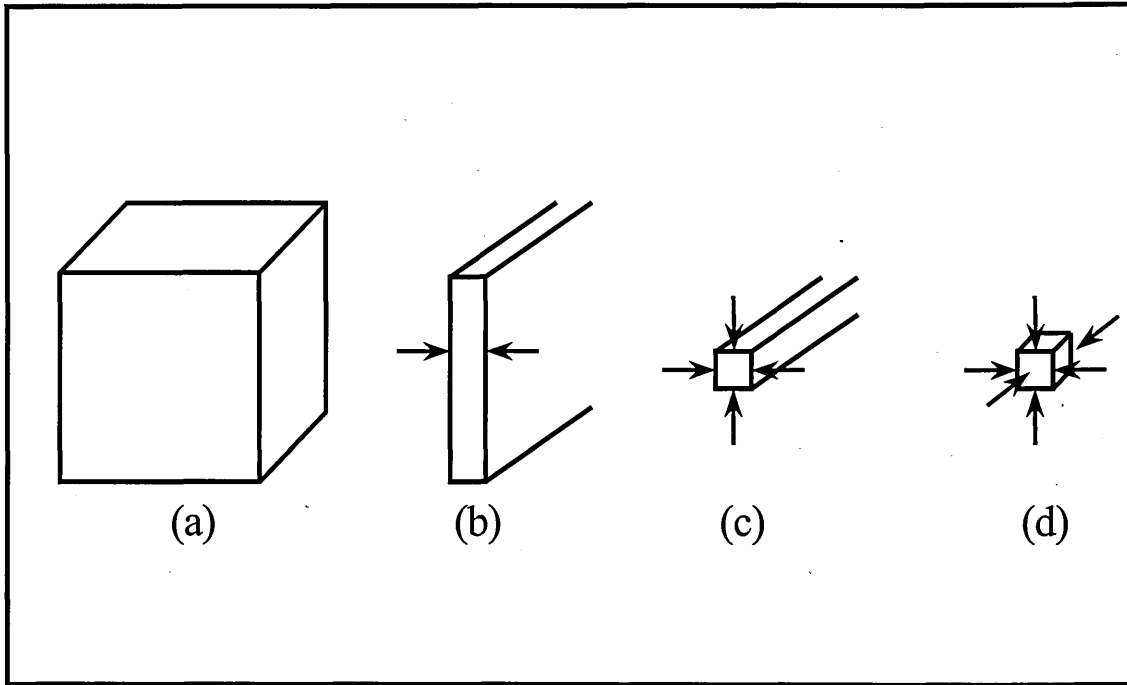


Figure 2.9. Illustrations representing system dimensionality  $d$ : (a) bulk semiconductors, 3D; (b) thin films, layer structures, quantum wells, 2D; (c) linear chain structures, quantum wires, 1D; (d) clusters, colloids, nanocrystallites, quantum dots, 0D.

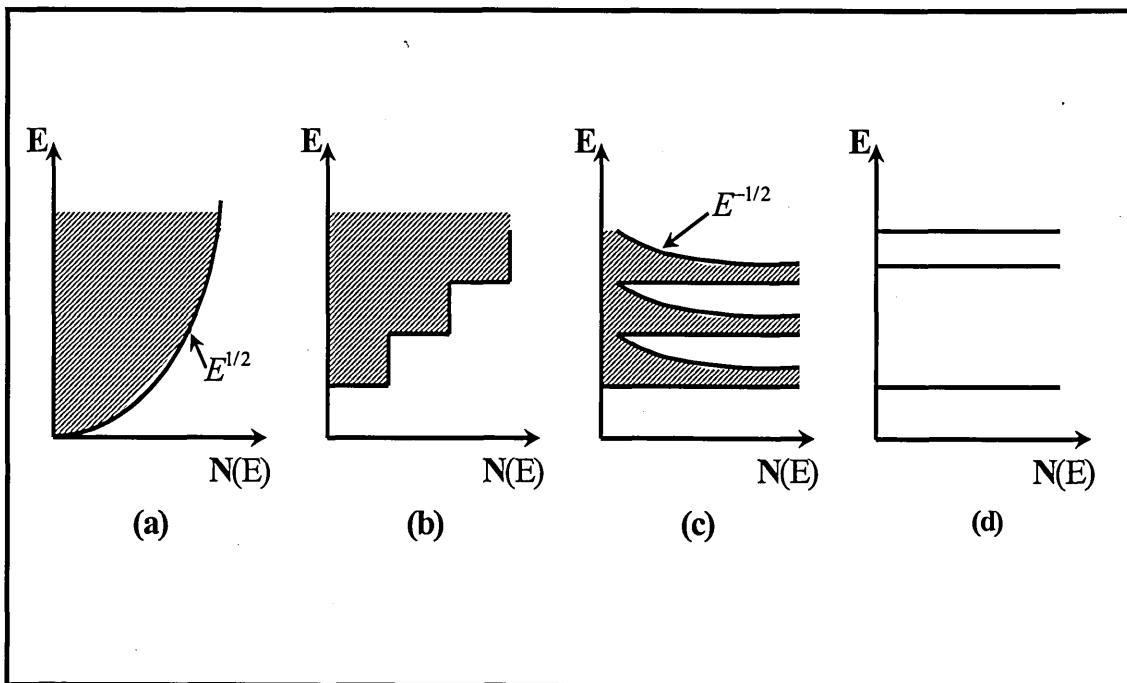


Figure 2.10. Densities  $N(E)$  of states for ideal cases of (a) 3D, (b) 2D, (c) 1D and (d) 0D systems [after Yoffe, 1993]

The energy for the transition to the quantized levels in two dimensions can be expressed [Elliot, 1957; and Ralph, 1965]

$$E_n = E_g - \frac{E_R}{(n + \frac{1}{2})^2}, n = 0, 1, 2, \dots, \quad (2.8)$$

where the exciton Rydberg  $E_R = E_b$ . The binding energy of the exciton series is

$$E_b(n) = \frac{E_b(n=0)}{(n + \frac{1}{2})^2} \quad (2.9)$$

The ground state binding energy for two-dimensional (2D) systems relative to three-dimensional (3D) systems is

$$E_b(n=0)(2D) = 4E_b(n=1)(3D) \quad (2.10)$$

Two-dimensional (2D) excitons in quantum wells with the larger binding energy are more stable than in the bulk crystals. Optical properties of two-dimensional systems can be dominated by exciton effects even at room temperature. These phenomena have been found by Greene and Bajaj [1983] on GaAs and by Pozina et al [1992] on CdTe. D'Andrea, et al [1990] calculated exciton binding energies of a slab (two dimensions), wire (one dimensions) and quantum dot (zero dimensions) for CdS in the cubic modification. They found that the exciton binding energy increased from two dimensions to zero dimensions.

### 2.3.3. Quantum Confinement Effects

If a simple model of a particle in a box is applied to a thin semiconductor film, it is expected that the energy gap will increase substantially (up to an electron volt or so) as the film thickness decreases. When these phenomena occur in excitons, the carriers will move to higher energies as a result of the quantum confinement effect. These effects have been observed since 1968 when Evans and Young investigated the confinement effects in the optical absorption spectra of the layered materials, the semiconducting transition metal dichalcogenides.

Ekimov and Onushchenko obtained the first experimental evidence of excitons confined in all three dimensions in 1981. They studied the quantum confinement effects in microcrystallites of CuCl dispersed in a silicate glass and found a blue shift of the main excitonic absorption feature. Ekimov [1991] also found the blue shift in position of exciton peaks for CuCl microcrystallites as the radius  $R$  changes from 310 Å to 20 Å.

#### 2.3.3.1. Theoretical Models of Quantum Confinement Effects

Four main procedures of the theoretical models of quantum confinement have been listed by Einevoll [1992].

##### (1) The effective-mass approximation (EMA) model

Efros and Efros [1982] developed the EMA model. They assumed parabolic bands and infinite potential barriers at the surface of a spherical microcrystallite. In order to denote the average crystallite radius as  $R$ , three regions involving  $R$  and  $a_B$  can be identified.

(a) *Weak confinement* ( $R \gg a_B$ , that is  $R \gg a_e$ ,  $a_h$  and  $a_B = a_e + a_h$ )

where  $a_B$  is the exciton Bohr radius of the bulk semiconductor,  $a_e$  and  $a_h$  are the electron and hole Bohr radii, respectively. In this weak confinement regime, the Coulomb term is the dominant energy. The exciton energy as the lowest-energy state is then shifted to higher energies by confinement and this shift is proportional to  $1/R^2$ . The energy shift of the ground-state exciton is given approximately by

$$\Delta E \approx \frac{\hbar^2 \pi^2}{2MR^2} \quad (2.11)$$

where  $M$ , the mass of the exciton, is given by  $M = m_e^* + m_h^*$ , with  $m_e^*$  and  $m_h^*$  are the effective masses of the electron and hole, respectively.

(b) *Medium confinement* ( $R \approx a_B$  and  $R \ll a_e$  but  $R \gg a_h$ )

This regime is the common condition for very small microcrystallites. In this case the electron is quantized and the hole interacts with it through the Coulomb potential.  $a_e$  and  $a_h$  are given as

$$a_e = \frac{\hbar^2 \epsilon_2}{m_e^* e^2} \quad (2.12)$$

$$a_h = \frac{\hbar^2 \epsilon_2}{m_h^* e^2} \quad (2.13)$$

where  $\epsilon_2$  is the background dielectric constant of the semiconductor materials and

$$a_B = \frac{\hbar^2 \epsilon_2}{\mu e^2} \quad (2.14)$$

(c) *Strong confinement* ( $R \ll a_B$  or  $R \ll a_h, a_e$ )

In this strong confinement regime, the Coulomb term is small and can be ignored or treated as a perturbation. Excitons are not formed in this regime, because the electrons

and holes can be thought of as confined independent particles. The simple model gives the shift in energy as a function of crystallite size as

$$\Delta E \approx \frac{\hbar^2 \pi^2}{2\mu R^2} \quad (2.15)$$

where  $M$  is replaced by the reduced exciton mass  $\mu$  where  $\frac{1}{\mu} = \frac{1}{m_e^*} + \frac{1}{m_h^*}$

In later treatment by Brus [1983, 1984, 1986] and Bawendi et al [1990], the small attractive Coulomb interactions between electrons and holes are taken into account. They developed a single-band effective-mass model with infinite confining potentials for the electrons and holes outside the clusters. The Coulomb interaction can be written as

$$V = \frac{-e^2}{\epsilon_2 |r_e - r_h|} + \text{small terms (polarization)} \quad (2.16)$$

Brus obtained an analytic approximation for the lowest 1s excited state as a function of cluster radius  $R$  for small  $R$  as [Brus, 1986]

$$E(R) = E_g + \frac{\hbar^2 \pi^2}{2\mu R^2} - \frac{1.8e^2}{\epsilon_2 R} + \text{small terms} \quad (2.17)$$

bulk energy gap	quantum conf. energy	Coulomb term	polarization term at surface
-----------------------	----------------------------	-----------------	------------------------------------

It is possible to analyse the importance of the various terms as a function of  $R$  by using above expression. For large  $R$ , exciton may form and the Coulomb term is more important than the kinetic energy. While in the small  $R$  case, the confinement term dominates. However, there are significant limitations to this approach, in particular the predictions made for small sizes in the range of about 18 Å are not reliable. One problem is the assumption of a constant effective mass.

Kayanuma [1986, 1988] has extended the treatment of Brus, especially for direct-bandgap semiconductors such as CdS and obtained quite reasonable agreement with the experiment for large clusters. For strong confinement the ground-state energy is derived as [Kayanuma, 1988]

$$E(R) = E_g + \frac{\hbar^2 \pi^2}{2\mu R^2} - \frac{1.786e^2}{\epsilon_2 R} - 0.248E_R \quad (2.18)$$

bulk	quantum	Coulomb	Correlation
energy	conf.; kine-	energy	energy
gap	tic energy		

where  $E_R = (13.606m_o / \mu\epsilon_2^2)$  is the value for the bulk semiconductor.

For strong confinement, Equation (2.18) gives a reasonable fit to the absorption spectra of CdS microcrystallite (with  $a_B \approx 30\text{\AA}$ ) dispersed in a silicate glass [Ekimov et al, 1985]. Other II-VI semiconductor such as CdSe is also suitable for this system.

## (2) Semi-empirical tight-binding calculations

This method uses fitting parameters, and this naturally leads to some measure of agreement with experimental results. Lippens and Lannoo [1989, 1990, 1991] provided the procedure for calculating energy levels for wide-bandgap clusters semiconductors such as CdS. The ground-state energy  $E(R)$  is taken as [Yoffe, 1993]

$$E(R) = E_g(R) + E_C(R) \quad (2.19)$$

where  $E_g(R)$  is the crystallite bandgap energy and is the dominant term, while  $E_C(R)$  is the Coulomb energy of the exciton and is a small correction term. The Coulomb energy for electron and hole in a spherical well of infinite depth ( $V_\infty$ ) is given by

$$E_C(R) = \frac{-e^2}{\epsilon_2 R} \left\langle \frac{R}{r} \right\rangle \quad (2.20)$$

where  $\langle R/r \rangle = 1.786$  according to Brus [1984], is the value of  $R/r$  averaged over the 1s wavefunctions. The average value of  $E_C(R)$  can be calculated numerically. Lippens and Lannoo [1991] have found a useful comparison of the calculated ground-state energies for the exciton of several II-VI semiconductors with zinc blende structures, using tight-binding and EMA procedures.

### **(3) Effective bond order model (EBOM)**

Einevoll [1992] determined energy levels for cubic modifications of the II-VI semiconductors such as CdS and ZnS using the effective bond order model (EBOM). This method has been used in an attempt to predict confined exciton energy levels in quantum dots in the diameter range 10-80 Å. In this model, a combination of two procedures was applied: the tight-binding model for the valence bands and the EMA for the conduction bands.

The clusters are assumed to be spherical, with finite potential barriers at the surfaces. The Coulomb energy is included in the calculation of the exciton energy levels. The calculated ground-state energies for the excitons for CdS clusters in the strong confinement regime and binding energies  $E_b$  are comparable with the experimental values taken from Ekimov et al [1985], Wang and Herron [1990]. However, the complicated procedure may be one of the limitations of this method.

### **(4) Empirical pseudo-potential method (EPM)**

The pseudo-potential method is well-established technique for calculating electronic structure of bulk semiconductors for many years. Rama Krishna and Friesner [1991] have used this method to calculate exciton energies, bandgap and band structure of II-VI (including CdS) and some III-V semiconductors quantum clusters. The exciton energies were calculated as a function of size, shape, crystal structure and lattice constants.

The energies of the electronic states in a crystal or clusters are described by the Schrödinger equation

$$H\Psi_{n,k}(r) = E_n(k)\Psi_{n,k}(r) \quad (2.22)$$

where  $H$  is the Hamiltonian,  $\Psi_{n,k}$  is the wavefunctions,  $E_n$  is the corresponding eigenvalues,  $k$  is the wavevector quantum numbers of the wavefunctions and  $n$  is the band index. For large clusters containing thousands of electrons, it is impossible to solve the Equation (2.22). Several approximations as a consequence are made to formulate this many body problem into a numerically form. The crystal field potential experienced by the valence electrons is replaced by the pseudo-potential  $V_p(r)$  to get the Hamiltonian

$$H = -\frac{\hbar^2}{2m}\nabla^2 + V_p(r) \quad (2.23)$$

and

$$V_p(r) = \sum_{R,j} v_j(r - R - d_j) \quad (2.24)$$

where  $v_j$  is the atomic pseudo-potential of the  $j$ th basis atom at a lattice site  $R$ ,  $d_j$  is the position vector of the  $j$ th basis atom relative to  $R$ , and the summation is over all lattice sites and all the basis atom  $j$  at each lattice site. The atomic potentials  $v_j$  may then be expanded as plane waves of the reciprocal lattice vector  $G$ ,  $V_p(r)$  can then be written as

$$V_p(r) = \frac{1}{Nn_a} \sum_G \sum_{R,j} v_j(G) e^{iG \cdot (r - R - d_j)} \quad (2.25)$$

where  $G$  is the reciprocal-lattice vector,  $N$  is the number of lattice sites in the samples, and  $n_a$  is the number of basis atoms at each lattice site. For zinc blende crystal structure,  $n_a = 2$ ,  $v_1(G) \neq v_2(G)$ , and an extension of the above procedure for this structure yields

$$V_p(r) = \sum_G [V_s(G)S_s(G) + iV_A(G)S_A(G)] e^{iG \cdot r} \quad (2.26)$$

where the symmetric ( $V_s$ ) and antisymmetric ( $V_A$ ) form factors are given by

$$V_s(G) = \frac{1}{2}[v_1(G) + v_2(G)] \text{ and } V_A = \frac{1}{2}[v_1(G) - v_2(G)] \quad (2.27)$$

and the symmetric ( $S_S$ ) and antisymmetric ( $S_A$ ) structure factors are given by

$$S_S(G) = \cos(G.t_1) \text{ and } S_A(G) = \sin(G.t_1) \quad (2.28)$$

with  $t_1 = (1, 1, 1)a_0/8$ ,  $a_0$  being the lattice constant.

In hexagonal (wurtzite) crystal, there are four basis atoms and two different types at each lattice site. For this case,  $n_a = 4$ , and since atoms 1 and 3, and 2 and 4 are identical in the hexagonal lattice, the Equation (2.26) with the structure functions defined as

$$S_S(G) = \cos(\sqrt{2}\pi G.t_2) \cos\left(\frac{2\pi u_0 G_z}{\sqrt{3}}\right) \quad (2.29a)$$

$$S_A(G) = \cos(\sqrt{2}\pi G.t_2) \sin\left(\frac{2\pi u_0 G_z}{\sqrt{3}}\right) \quad (2.29b)$$

where  $t_2 = \left(\frac{1}{\sqrt{48}}, \frac{1}{12}, \frac{1}{\sqrt{6}}\right)$  and  $u_0 = 0.375$

The form factors are determined by a fitting procedure to experimental optical data, and this introduces the empirical character to the calculation. It is possible to calculate the energy levels of the valence electrons as a function of  $k$  when  $V_p(r)$  is known.

In case of clusters, the energy levels do not form bands but can be represented as a collection of all the discrete quantized levels in the first Brillouin zone. For a cubic cluster, the physical dimensions are reduced from all sides to get a cube of side  $L$ . The wave vectors of the quantized energy levels of this shaped cluster can be represented as

$$k = \frac{\pi}{L}(n_x, n_y, n_z) \quad (2.30)$$

where  $n_x, n_y, n_z$  are the quantum numbers of a particle in a box with infinite potentials at the boundaries.

In a spherical cluster having radius  $R$ , the wave vectors for the quantized energy levels are given by

$$k = \frac{\pi}{\sqrt{3}R}(n_x, n_y, n_z) \quad (2.31)$$

It is now possible to calculate the band structure at allowed  $k$  states to obtain the energy levels of the clusters. These simple models of a cluster give an adequate understanding of the effect of quantum confinement on the electronic structure of the clusters.

Figure 2.11 and 2.12 show the results of the band structure calculations for zinc blende CdS in spherical cluster form having  $R = 15 \text{ \AA}$  and  $a_0 = 5.818 \text{ \AA}$ . The calculation results for a cubic CdS cluster of side  $L = 30 \text{ \AA}$  shows very similar to that given in Figure 2.12. Furthermore, for both models, the top of the valence and the bottom of the conduction bands lie at the smallest  $k$  given by  $(n_x, n_y, n_z) = 1$ .

In order to obtain the exciton energies,  $E_x$ , the treatments by Brus [1986] and Kayanuma [1988] are used, which is

$$E_x = E_g - \frac{1.786e^2}{\epsilon_2 R} - 0.248E_{Ry} \quad (2.32)$$

where  $E_{Ry} = \frac{\mu e^4}{2\epsilon_2^2 \hbar^2}$ . The third term in Equation (2.32), which is due to electron-hole correlation, is only 0.0171 eV and is of minor significance.

It is possible to estimate the number  $N$  of CdS molecules in the clusters using the calculated volumes of the unit cell and the cluster. With the volume of the unit cell is  $a_0^3$ , the volume of the cluster is  $4\pi R^3/3$ , and there are four CdS molecules in one conventional unit cell. Hence,

$$N = \frac{16\pi R^3}{3a_0^3} \quad (2.33)$$

For  $R = 5.0, 7.5, 10.0, 15.0,$  and  $30.0 \text{ \AA}$ , gives  $N = 13, 39, 89, 287$  and  $2297$ , respectively. It would therefore seem that the empirical pseudo-potentials method gives reasonable values for exciton energies, even for clusters containing as few as 13 molecules. However, this method cannot work well for clusters smaller than  $5.0 \text{ \AA}$ . The calculations of the excited states of very small clusters would have to be carried out according to the traditional methods of electronic structure theory.

The EPM is also used to calculate the exciton energy for both bulk and cluster of CdS with hexagonal symmetry and  $a_0 = 4.136 \text{ \AA}$ . The band gap of hexagonal CdS crystal is found to be  $2.52 \text{ eV}$  [Tomasulo and Rama Krishna, 1996], which is comparable to that of zinc blende CdS of  $2.44 \text{ eV}$  [Rama Krishna and Friesner, 1991] and in good agreement with the experimental value of  $2.50 \text{ eV}$  [Brus, 1986 and Kayanuma, 1988].

Figure 2.12 shows the discrete energy levels of a  $R = 15.0 \text{ \AA}$  wurtzite CdS cluster, modelled as a sphere of radius  $R$ . The exciton energies obtained using this calculation method are in agreement with experiment for large clusters. This result differs from that of zinc blende CdS for which both large and small clusters give good agreement with experimental data. This indicates that small CdS clusters are probably zinc blende structure, rather than hexagonal. These results also indicate that the exciton energies in small clusters are sensitive to the crystal structure. The shape effect study confirms that the shape has significant effect on the exciton energies. For zinc blende CdS clusters, the spherical shape gives better agreement with experiment for all cluster sizes, indicating that these crystallites are approximately spherical. The calculation results also confirm that the exciton energies are sensitive to the cluster shape.

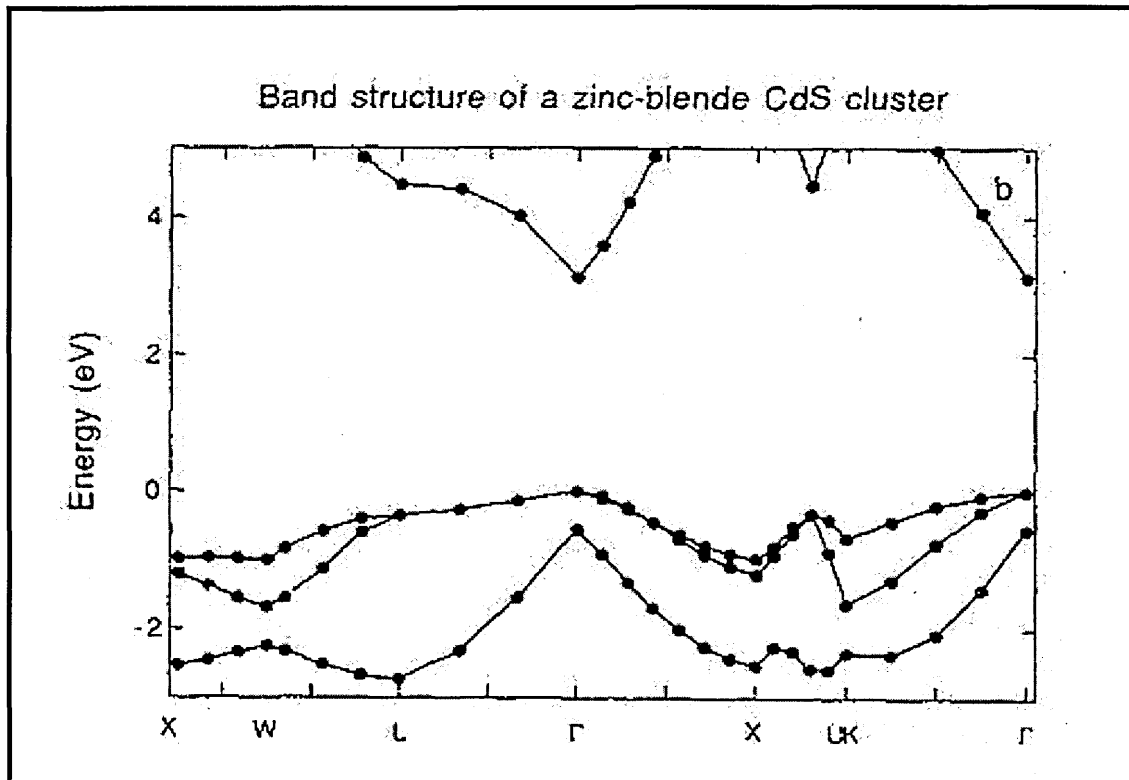


Figure 2.11. Band structure of a zinc blende CdS spherical cluster having  $R = 15 \text{ \AA}$  near the top of the valence band [after Rama Krishna and Friesner, 1991]

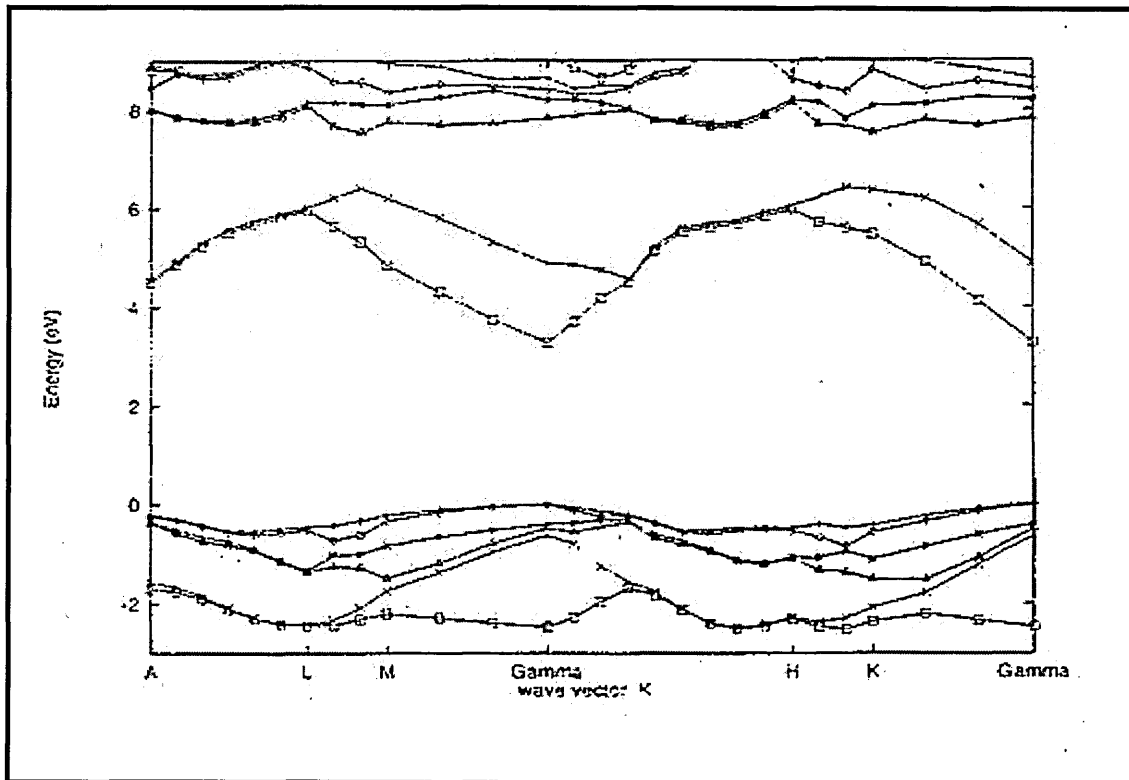


Figure 2.12. Allowed electronic levels of wurtzite CdS spherical cluster with  $R = 15 \text{ \AA}$  [after Tomasula and Rama Krishna, 1996]

## 2.4. Review of Previous Works on CdS Quantum Structures

II-VI semiconductor quantum structures have been studied very intensively in recent time due to their potential for various device applications. Most studied nanocrystalline semiconductors belong to the II-VI group, as they are relatively easy to synthesize and are generally prepared as particulates or in thin film form. Cadmium sulphide (CdS) has been one of the most studied materials among the II-VI compounds. Several groups [Nakamura et al, 2003; Aramoto et al, 2003 and Al Kuhaimi, 2000] have utilized CdS as a window layer in the thin film solar cells.

CdS quantum structures have been synthesized by several groups using various techniques, including ion implantation [Desnica et al, 2001; Desnica et al, 2002] aqueous colloid solutions [Salata et al, 1996; Sajinovic et al, 2000; Abdulkhadar and Thomas, 1998], precipitation technique [Nanda et al, 1998], electrochemical technique [Zhang et al, 2001], the reverse micelle method [Yu et al, 2001], magnetron sputtering technique [Gupta et al, 1995] and Langmuir-Blodgett (LB) films method.

Desnica et al [2001] studied CdS nanocrystals prepared by ion implantation. The blue shift with respect to bulk CdS in optical absorption spectra taken by UV-visible measurements reflects the quantum confinement of the charge carriers [Desnica et al, 2002]. The average size of CdS nanocrystals was estimated to be in the ranges from 3.5-4.5 nm to 10 nm, and depends on the ion dose and temperature of annealing post-treatment. X-ray diffraction (XRD) measurements performed on the samples after annealing post-treatment at 900°C identified the hexagonal phase of CdS.

Salata et al [1996] prepared nanoparticulate CdS films for optoelectronic device applications by aqueous colloidal solutions method. The samples were deposited on

ITO glass substrates utilizing a combination of the spin/dip coating techniques. The thickness of the CdS films varied from 50 to 200 nm. A typical diameter of the individual CdS nanoparticles was measured by high-resolution electron microscopy and it was found to be about 4 nm. Using similar technique, Sajinović et al [2000] also formed 50 Å CdS quantum dots in a polystyrene matrix. Absorption onset of the CdS-Q-dots was blue shifted about 0.2 eV, compared to bulk CdS material. Using effective mass approximation model, the radius of CdS Q-dots was found to be 2.5 nm. X-ray diffraction measurements applied on the same sample gave a 4.5 nm CdS diameter.

Nanda et al [1998] also successfully formed thin films of CdS nanoparticles of different crystalline sizes by a precipitation technique using precursors as CdSO<sub>4</sub>, thiourea and NH<sub>4</sub>OH. AFM analysis confirmed that the crystalline sizes of CdS nanoparticles were in the range of 11 to 13 nm and predicted the geometry of the nanoparticles was nonspherical. The room temperature optical absorption spectrum of the sample showed absorption maximum at 395 nm giving an estimation of band gap as 3.14 eV. This blue shift of 0.74 eV was due to quantum size effect in CdS nanoparticles. The optical absorption measurements also predicted the size of the particles to be in the range of 4 to 7.5 nm, although this value was different from that obtained from AFM measurements. They thought that the CdS nanoparticle has a nonspherical geometry and they expected a pancake structure with lateral diameter in the range of 11-13 nm and height of about 4-7.5 nm. XRD measurements of bulk CdS showed presence of mixed cubic and hexagonal phases, whereas the nanocrystalline sample showed predominantly cubic phase.

The electrochemical method was chosen by Zhang et al [2001] to produce CdS nanostructures. Porous silicon was used as a template/substrate. AFM measurements were then carried out on the samples. The CdS deposits appeared to be a dense grain-

like structure, each grain being  $\sim 100$  nm. They also observed aggregates of smaller particles of several nanometers. These small nanoparticles are passivated with oxides on the surface and are responsible for green colour luminescence band centred at  $\sim 530$  nm.

Yu et al [2001] synthesized CdS nanoparticles by using the reverse micelle method. TEM measurements showed that the CdS particles were about 4 nm in diameter with a narrow size distribution and had the cubic zinc blend structure. UV-visible absorption spectra of the CdS nanoparticles formed by the reverse micelle method showed their absorption edge around 400 nm. The general fluorescence spectra of the CdS nanoparticles exhibited broad emission bands at about 525 nm with the excitation source at 417 nm.

The dc high pressure magnetron sputtering technique was utilized by Gupta et al [1995] in order to deposit nanostructure CdS films onto glass and NaCl substrates. TEM observations were performed on the CdS nanostructures deposited on NaCl substrates having various temperatures in the range of 220 to 300 K. The average crystallite sizes were about 3 nm and did not vary considerably with change in substrate temperature. Variation of electrical conductivity measurements were carried out on the CdS nanostructures deposited on glass using the four-probe technique of van der Pauw in the temperature range of 80 to 350 K. Variable range hopping within the Coulomb gap, quantum mechanical tunnelling and thermionic emission found to dominate the electron conduction process as the temperature increased.

The concept of formation of CdS semiconductor nanoclusters inside Langmuir-Blodgett (LB) films of fatty acid derives from the work of Barraud and co-workers in 1980s [Ruau-del-Teixier et al, 1986; Zylberajch et al, 1988; 1989]. The unique properties of quantum-state semiconductor particles and the ability to control the thickness of LB films to the nanometer level make this technique promising for the formation of various

nanostructures for optoelectronics and nanoelectronics applications [Erokhin et al, 1996; Facci et al, 1996; Weller et al, 1998]. Later this approach was expanded for the other II-VI semiconductor nanoparticles, as well as for other types organic films.

II-VI semiconductor quantum structures, including CdS, PbS, and ZnS nanostructures were also successfully formed within Langmuir-Blodgett (LB) films. Several compounds have been used as matrix materials, such as oligomer: polymaleic acid octadecanol ester, PMAO [Li et al, 1997; Jin et al, 1998], a variety of fatty acids [Ruaudel-Teixier et al, 1986; Zylberajch et al, 1988; 1989; Erokhin et al, 1996; Facci et al, 1996; Weller et al, 1998; Smotkin et al, 1988; Moriguchi et al, 1991; Yang et al, 1998; Facci et al, 1994; Erokhin et al, 1997 & 1998; Nabok et al, 1997, 1998, 1999], calixarenes [Nabok et al, 1997, 1998, 1999, 2000].

An amphiphilic polymer (PMAO) with a large ratio of carboxylic group to hydrocarbon chain of 2.0 was synthesized and chosen by Li et al [1997] as a matrix material for LB film deposition. They believed that thermal and mechanical stabilities of the PMAO LB films should be better than those of fatty acid LB films, because PMAO is a polymer. Fourier transform infrared (FTIR) spectroscopy and XRD measurements showed that an ordered structure was obtained from the Pb PMAO LB films (Li et al, 1997). When such LB films of PMAO were reacted with H<sub>2</sub>S at lower pressure, CdS or PbS nanoparticulate multilayers were obtained. UV-vis absorption spectra of CdS and PbS formed within PMAO LB films showed a larger blue shift of absorption edge than those formed within the stearic acid LB films. They concluded that the size of the aggregate of the sulfides within PMAO LB films was smaller than those formed in stearic acid LB films, although they did not find the precise size of the nanoparticles. The calculated band gap energy (E<sub>g</sub>) of PbS within PMAO and stearic acid LB films was reported as 3.18 eV and 1.96 eV, respectively. Much smaller

quantum dots of CdS and PbS in PMAO LB films than in stearic acid LB films correlated to the aggregation of the sulfides was confined within a single PMAO molecule in the LB films.

Li et al [1998] reported the study of the formation and growth quantum dots-sized CdS particles using PMAO with different ratios (2:1, 3.7:1 and 6:1) between the carboxylic groups and the hydrocarbon chains. FTIR results showed that not all the Cd PMAO oligomers in the films were converted to PMAO after exposure to H<sub>2</sub>S gas. The UV-vis results indicated that CdS within PMAO LB films showed a larger blue shift of the optical absorption edge with the decrease of the ratio. The average size of CdS (less than 5 nm) was smaller than that in stearic acid LB films. Moreover, the size of the CdS nanoparticles increased with increasing ratio. This implied that the PMAO LB films provide the possibility of controlling the size of the particles by controlling the ratio between the carboxylic groups and the hydrocarbon chains. Jin et al [1998] reported on CdS nanoparticles stabilized with PMAO of different ratios in the form of reversed micelles. The monolayer of CdS nanoparticles was transferred onto various substrates and directly characterized by FTIR, small-angle XRD and UV-vis spectra. It was concluded that the size of the CdS particles could be efficiently controlled by changing the ratio.

Smotkin et al [1988] prepared layers of CdS quantum state particles (< 5nm) by LB films technique. The cadmium arachidate films were firstly transferred to glass slide at a constant pressure of 30 mN/m. The LB films were then exposed to an H<sub>2</sub>S atmosphere in order to yield CdS particles in a lattice of arachidic acid. The absorption onset for 1,2,3 or 7 layers of CdS LB films was about 450 nm (2.8 eV) blue shifted (0.4 eV) compared to bulk CdS. This shift in the LB layer of CdS would correspond to spherical particles with a 5 nm diameter and indicates no strong electronic interactions

between the particles. The ellipsometry measurements showed that exposure of the LB films of cadmium arachidic acid to  $H_2S$  gas results in an increase in thickness of about 0.3 nm per layer. The result of the ellipsometry measurements also gave a possibility of platelets shape of CdS.

Moriguchi et al [1991] synthesized CdS nanoparticles inside LB films of stearic acid. In order to form the CdS nanoparticles, the Cd-stearate LB films were exposed to  $H_2S$  gas at a pressure of 1 Torr. XRD measurement found that stearate molecules become less oriented with the formation and growth of CdS particles. In 1995, they also synthesized the size confined metal sulphides in LB films, including CdS, PbS and ZnS. The semiconductor nanostructures were formed by using the repeated processes of sulfidation, by exposing the metal ion-binding LB films to a flow of  $H_2S$  gas, and intercalation, by immersing the metal sulphide-bearing LB films into aqueous solution of the corresponding metal ion. Yang et al [1998] reported the formation of CdS nanoparticles inside the stearic acid LB films observed by atomic force microscopy (AFM) measurements. The surface of CdSt<sub>2</sub> LB films before being exposed to  $H_2S$  was homogeneous and the CdSt<sub>2</sub> molecules formed a well-ordered lattice structure on the molecular scale. After being exposed to  $H_2S$ , the ordered CdSt<sub>2</sub> molecules gradually changed into a disordered state and eventually the LB films surface became rough. This morphological change can be attributed to the aggregation of CdS nanoparticles within the LB films, which had been confirmed by UV-visible absorption spectra.

Facci et al [1994] formed semiconductor ultrathin films of CdS nanostructures on solid substrate by using CdS nanostructure aggregation. After exposing the LB films of cadmium arachidate to an atmosphere of  $H_2S$ , the fatty acid matrix was selectively removed from the LB films by immersing the samples in chloroform. X-ray measurement showed the changes in the film structure due to the formation of larger

CdS particles. Absorption spectra proved the presence of CdS nanoparticles before and after removing the fatty acid matrix. The spectrum before washing, showed as expected, a blue shift (85 nm) in the absorption onset of CdS (435 nm) with respect to the bulk CdS (520 nm). The effective size of the CdS particles was found to be about 3 nm. After washing with chloroform, the shift value decreased to 50 nm of the absorption onset (470 nm), revealing an increase in the effective size of the CdS particles of 4.4 nm. While STM imaging of the CdS particles gave the value of 2-2.5 nm and 4-5 nm, respectively for the particles size before and after washing procedure.

Erokhin et al [1997; 1998] studied CdS nanoparticles formed in LB films of arachidic acid using the same procedure as used by Facci et al [1994] for quantum devices application. The thickness of each bilayer of CdS thin films after washing process was about 0.6 nm. Electrical characterization produced the conductivity of the layers. Because the particles were in contact with each other, this resulted in a further increase of conductivity. Such CdS layers can be useful for preparing semiconductor devices and the thickness of the layer is a critical parameter. They also developed inorganic semiconductor superlattices from LB precursor [Erokhin et al, 1998]. Nanoparticles of different materials, including CdS, PbS and MgS were formed using alternating LB films technique. Thin semiconductor layers and superlattices were formed using particles aggregation of nanoparticles formed in the LB films. The scanning electron microscopy (SEM) results revealed that inorganic semiconductor superlattices (PbS-CdS-PbS and CdS-MgS-CdS-MgS-CdS) with different alternating layers were formed. The average thickness of each layer was about 50-60 nm for the superlattices from 100 bilayer LB films.

Formation of metal sulphide nanostructures within LB films of fatty acids has been extended by applying calixarene LB film as a matrix material [Nabok et al, 1997].

They successfully synthesized CdS nanoparticles within LB films of Cd-salts of calixarene (CA) by reaction with H<sub>2</sub>S gas. UV-visible absorption spectra confirmed the presence of much smaller CdS nanoparticles inside the LB films of calixarene compared to those formed in Cd-salts stearate LB films and other fatty acid LB films. The levels of size quantization were clearly resolved on the absorption spectra even at room temperature. The absorption edge of calixarene LB films was about 3.3 eV, while a lower absorption edge value of about 2.7 eV was found for the Cd-salts stearate films. The size of the CdS particles in LB films of calixarene and stearic acid was estimated from the position of absorption bands to be  $1.5 \pm 0.3$  nm and 3.3 nm, respectively. However, the size of CdS particles formed in CA LB films estimated from the position of the absorption edge was about 1.8 nm. It was shown that the particle size did not depend on the number of LB layers or on the dimensions of the calixarene but increased with increasing pH of the subphase. XPS study directly confirmed the formation of CdS particles in the LB films.

In order to derive the size of the CdS nanoparticles formed in the LB films of Cd-salts calixarene and stearic acid, Nabok et al [1998] performed further analysis of UV-visible absorption spectra. The absorption spectra of CdS formed in the calixarene LB films represented three clearly resolved absorption bands near the absorption edge. It was suggested that these bands are related to electron transitions between levels of size-quantization. However, Ekimov et al [1985] reported that such quantum behaviour was usually observed only at low temperature. To derive the size distribution of CdS nanoparticles in LB films of calixarene, the experimental absorption spectra were decomposed into three Gaussian bands. The size distribution of CdS clusters in CA LB films can be described well by a simple Gaussian error function. The size of the CdS clusters and their dispersion were found to be  $1.43 \pm 0.28$  nm and  $1.47 \pm 0.28$  nm, respectively for calix[4]arene and calix[8]arene LB films. The presence of very small

CdS particles in Cd-salts calixarene LB films did not affect their layer-by-layer film order. This fact was confirmed by small angle X-ray diffraction and ellipsometry measurements performed on the samples. While formation of larger CdS particles in Cd-salts stearate LB films nearly destroyed their periodicity. Much smaller CdS clusters formed in CA LB films as compared to those in fatty acid LB films were believed to be as a result of restriction of 2D aggregation of CdS within bilayers of the LB films caused by some CdS molecules were captured in calixarene cavities.

To study in more detail, the process of formation of CdS nanoclusters in Cd-salts calixarene LB films, Nabok et al [1999] formed and studied the CdS nanoclusters within different calixarene derivatives, possessing inner cavities of various sizes. Direct observation techniques such as AFM, TEM and electron diffraction were performed on the CdS/CA and CdS/SA LB films. AFM, TEM and electron diffraction directly confirmed the presence of CdS nanoparticles in Cd-stearate LB films. Such measurements also found that the CdS nanoclusters have zinc blende structure with the lattice parameter of 0.583 nm. This lattice parameter value is very close to that of bulk CdS materials. However, the results of AFM measurements on the calixarene LB films did not show the presence of CdS clusters. TEM measurements observed the small CdS clusters in calixarene LB films. The small clusters were possibly grown by stimulation of the electron beam itself. The CdS clusters also have zinc blende structure with a smaller lattice parameter of 0.567 nm. However, they believed that the observed behaviour showed the formation of two-dimensional (2D) CdS layers within each bilayer of calixarene LB films.

An in-situ study using TEM and electron diffraction was performed on the CdS nanoparticles in calixarene LB films by Nabok et al [2000]. In order to register changes of the optical parameters of calixarene LB films due to formation of CdS nanoparticles,

additional UV-visible absorption spectroscopy and surface plasmon resonance (SPR) measurements were carried out. The formation of either very small CdS nanoclusters with the size of about 1.5 nm or two-dimensional CdS planes with a thickness of around 1.7 nm within each calixarene bilayer interpreted the blue shift of absorption spectra obtained from UV-visible measurements. An increase in the extinction coefficient after exposure to H<sub>2</sub>S gas observed from SPR measurements of CA LB films was believed to be due to the presence of conductive (semiconductive) inclusions within the LB films. Neither TEM nor electron diffraction showed CdS clusters in fresh CA LB films, but they started to appear later under exposure to a focused electron beam. This fact was interpreted from aggregation of two-dimensional (2D) CdS planes and the formation of CdS nanoparticles stimulated by the electron beam.

The success of formation of two-dimensional II-VI semiconductor by various organic materials technology, including LB films technique opens the further research work towards the development of novel nanoelectronic and optoelectronic devices, such as tunnelling diodes and semiconductor lasers. Meanwhile, II-VI semiconductor nanoparticles or nanoclusters can be used to develop switching elements fabricated on the basis of single-electron transistors. Facii et al [1996] and Erokhin et al [1997] reported the development of an electronic junction based on single-electron phenomena that works at room temperature. This new electronic junction can be foreseen to display very low energy consumption, an ultra-high scale of integration and fast communication time. In order to realize the device, future efforts will be needed toward the development of nanowiring and nanolithography.

# CHAPTER 3

## PREPARATION OF THE SAMPLES

### 3.1. Introduction

This chapter describes the preparation procedure of the samples investigated in this thesis. The main technique used for the deposition of the samples was the Langmuir-Blodgett (LB) technique. As a result of the development of science in the 'nano' scale, LB films have been attracting more attention and are a promising technique for producing objects for nanotechnology. This elegant method for the formation of II-VI semiconductor nanostructures was first proposed in 1980s and has now become very promising for the formation of various nanostructures for optoelectronic and nanoelectronic applications. Details of this technique will be described later. Section 3.2 presents principles of LB films. Descriptions of deposition of LB films of fatty acid and calixarene are described in Section 3.3.

The formation of II-VI semiconductor nanostructures within LB films of stearic acid and calixarene will be presented in Section 3.4. Section 3.5 summarises the current chapter.

## 3.2. Principles of Langmuir-Blodgett Films

The Langmuir-Blodgett (LB) technique was first introduced by Irving Langmuir in 1917. Katharine Blodgett carried out the first study on deposition of multilayers of long chain carboxylic acid onto a solid substrate. They extensively characterised the properties of floating monolayers and found that the transfer of a monolayer to a solid surface could be achieved by drawing a substrate through the air-water interface. By applying this method monolayers and multilayers could be deposited onto the surface of the solid substrate. Such layers, or films, are now referred to as Langmuir-Blodgett films. Appealing aspects of Langmuir-Blodgett films are the high degree of molecular control and the ability to produce very thin films with the precise control of the film thickness.

### 3.2.1. Langmuir Film - Monolayer

Langmuir films consist of surface active materials or surfactants trapped at the interface between two dissimilar materials, either liquid-liquid or liquid-gas. At the interface between gas and liquid phases certain organic molecules will orient themselves to minimize their free energy. The resulting surface film is one molecule in thickness and is commonly called a monomolecular layer or simply a monolayer.

The Langmuir monolayer of any amphiphilic material is generally formed by dissolving this material in a suitable volatile solvent (e.g., chloroform, hexane, etc) and then spreading the solution on the clean water surface. However, some materials can spread spontaneously on water without using solvent. It is desirable that the solvent should be capable of dispersing the molecules of the film-forming surface at i.e. the air-

water interface and then evaporate completely, so that the film is not contaminated with the solvent. The solvent evaporates as the solution spreads over the entire surface, evenly distributing the molecules over the entire surface area.

When the material is applied to the surface of water, spreading will continue until the surface pressure reaches an equilibrium value. Once the solvent has completely evaporated, the molecules can be compressed by sweeping a barrier slowly over the surface of the water. The compression of the floating monolayer passes through different phases that can be viewed on a pressure-area isotherm. If this pressure is exceeded the equilibrium spreading pressure, the two-dimensional crystal phases started to form and deposition onto the solid substrate will start at these conditions.

### **3.2.2. Surface Pressure of a Langmuir Layer**

Any liquid always try to reduce its surface area known as “surface tension”. The less the surface tension of a liquid the higher it spreads out. The presence of a monolayer at the air-water interface lowers the interfacial surface tension as compared to pure water surface. This decrease arises due to the net repulsion of the molecules within the monolayer.

It is important to determine changes in the surface tension at the air-water interface with a monolayer present in comparison to a pure water surface. The Wilhelmy method lies in the measurement of the force (weight) of the plate in contact with the water surface (see Figure 3.1). The plate is suspended to a sensitive balance.

The net force acting on a rectangular plate of density  $\rho_p$ , immersed to a dept  $h$  into a liquid of density  $\rho_L$  is given by [Martin and Szablewski, 1999]

$$F = \rho_p g t w l + 2\gamma(t + w)\cos\theta - \rho_L g t w h \quad (3.1)$$

where  $l$ ,  $w$ , and  $t$  are the dimensions of the plate,  $\gamma$  is the surface tension at the interface,  $\theta$  the contact angle at a triple point plate-air-water and  $g$  the gravitational constant. It is assumed that the plate thickness ( $t$ ) is much smaller than other dimensions. The forces acting on the plate are seen to be due to the downward gravity force and the surface tension and upward force due to the buoyancy of the displaced water. Experimentally, the net force acting on the plate can be measured using a sensitive electromagnetic balance system. The change in the force on the plate when a monolayer is present at the interface is given by [Petty, 1996]

$$\Delta F = 2\Delta\gamma(t + w)\cos\theta \quad (3.2)$$

where  $\Delta\gamma$  is the change in the surface tension between the pure water surface ( $\gamma_0$ ) and the surface with the monolayer present ( $\gamma$ ).

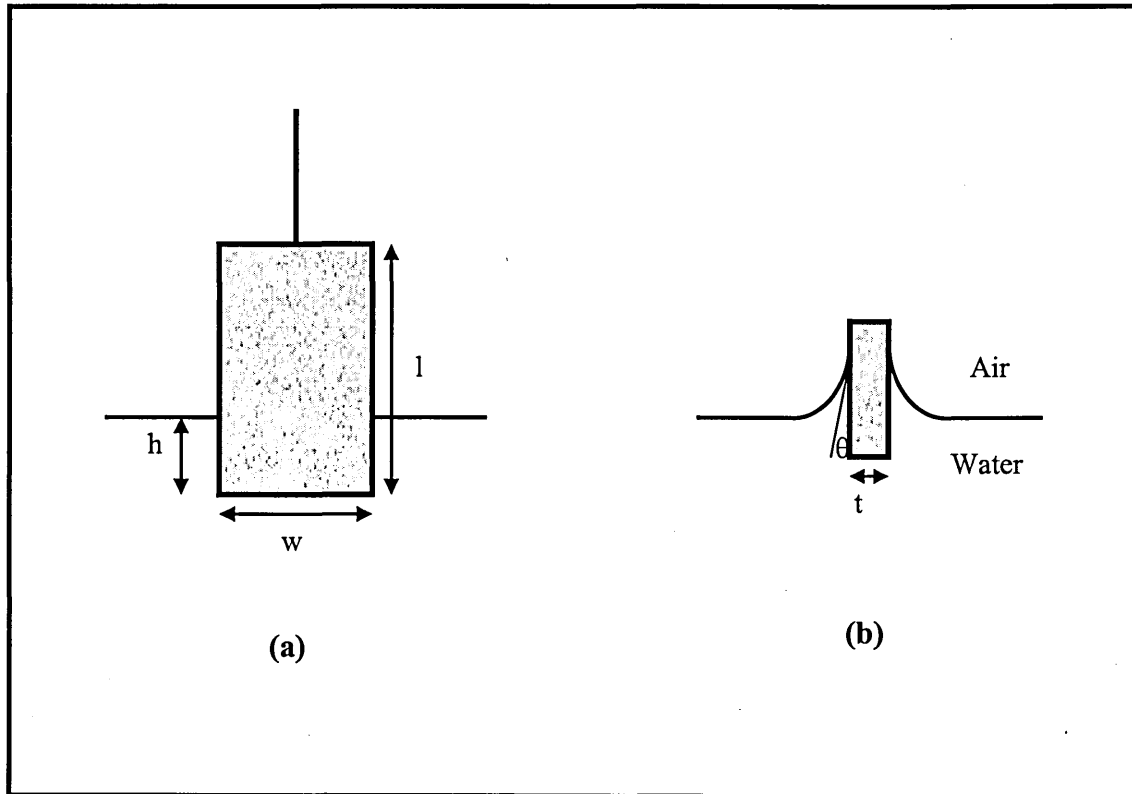


Figure 3.1. Wilhelmy plate used to measure the surface pressure of a monolayer

The contact angle is assumed to remain constant regardless of the presence of the monolayer. If the Wilhelmy plate is chosen to be constructed from a clean filter paper, Equation (3.2) can be simplified. For this material the contact angle can be taken to be zero and the thickness is small compared to the width ( $t \ll w$ ). Thus the change in surface tension of the interface due to the addition of the monolayer can be given by

$$\Delta\gamma = \frac{\Delta F}{2w} \quad (3.3)$$

The change in surface tension of the interface due to the monolayer can be determined from the measured change in force acting on a Wilhelmy plate of known width. Surface pressure is the inverse of surface tension. The surface pressure of the monolayer is defined from the measurement by

$$\pi = -\Delta\gamma \quad (3.4)$$

and is equal to the reduction of the pure water interface surface tension due to the monolayer. The surface tension is reduced in comparison to the pure water case as the confinement area of a Langmuir layer is reduced hence the surface pressure increases. The surface pressure of a monolayer is conceptually the best thought of as a two-dimensional equivalent to the well-known three-dimensional gas pressure.

### 3.2.3. $\Pi$ -A Pressure-area isotherms

Monitoring the surface pressure as the confinement area of the layer is reduced is the common characteristic technique used to determine the internal structure of a Langmuir layer. This is achieved by spreading a known concentration and volume ( $c$  and  $v$ , respectively) of the solution on the air-water interface and allowing the volatile solvent to evaporate. Whilst constantly measuring the surface pressure, the monolayer is then compressed at a constant rate and temperature. The area occupied by each

molecule (the area per molecule,  $A$ ) for a confinement area ( $a$ ), can be obtained at any moment of time from [Petty, 1996]

$$A = \frac{aM}{CN_a v} = \frac{a}{cN_a v} \quad (3.5)$$

where  $N_a$  is Avogadro's number,  $M$  is the molecular weight of the monolayer material,  $C$  is the concentration of the spreading solution in mass per unit volume,  $c$  is the specific molar concentration of the solution and  $v$  is its volume. A plot of measured surface pressure ( $\pi$ ) against the area per molecule ( $A$ ) is called as  $\pi$ - $A$  compression isotherm. It is usual to consider the case of a simple stearic acid to highlight the relationship between the  $\pi$ - $A$  compression isotherm and the internal structure of a Langmuir film.

Three distinct phases can be seen in the isotherm; these are the gas, liquid and solid phases as shown in the Figure 3.2. Figure 3.3 shows a schematic representation of the internal structure within the Langmuir film for these three phases. In the gas phase the molecules are far enough apart on the water surface that they exert little force on one another. The surface tension across the interface approximates to that of pure water and hence the surface pressure of the layer is close to zero. In the liquid phase the hydrocarbon chains will begin to interact as the confinement area and thus the area per molecule is reduced. The surface pressure starts to rise as the surface tension lowers due to the interaction between the molecules. The molecules take up a compact structure with long-range order as the area per molecule is reduced further. This is a solid phase. The layer is highly resistant to compression causing a sharp rise in the surface pressure for a small decrease in the area per molecule. If this phase is extrapolated to a zero pressure, as seen in Figure 3.3, the resulting area per molecule gives the hypothetical area each molecule would occupy in a solid state in the absence of an external pressure. For stearic acid the extrapolated area per molecule is measured as  $21 \text{ \AA}^2$ .

It is found that monolayers can be compressed to pressures considerably higher than the equilibrium spreading pressure. The increasing of surface pressure continues as surface area decreases until a point is reached. At this point, it is not possible to increase the pressure any further. If the pressure is kept constant, the area of the film decreases, or the pressure falls if the film is held at constant area. This is referred to as “collapse of monolayer”, which should be avoided. When collapse occurs, molecules are forced out of the monolayer and bilayer or multilayer structures are formed, as shown in figure 3.4.

It is known that the surface tension of pure water at 20°C is 73 mN/m and the surface pressure of a monolayer cannot theoretically exceed 73 mN/m. Experimentally, the surface pressure of a monolayer rarely exceeds 50 mN/m. In most monolayers, the collapse starts to occur below 40 mN/m. It is most likely due to the effect of vibrations and dust particles.

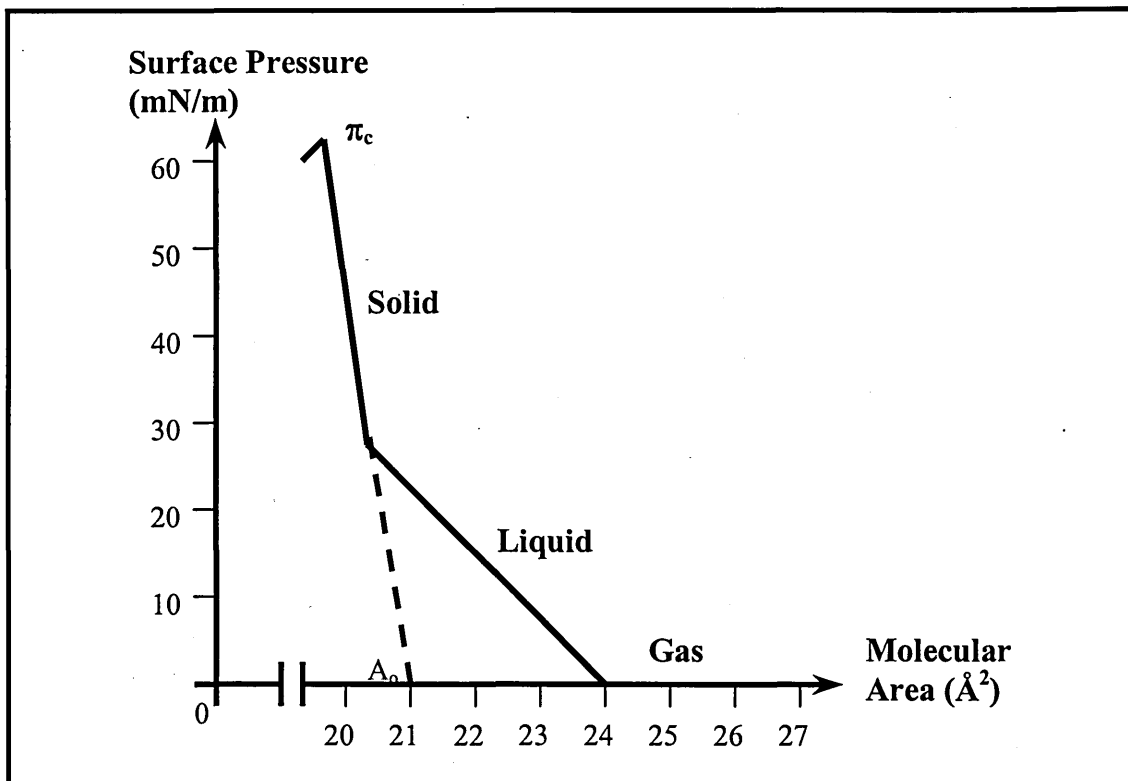


Figure 3.2.  $\pi$ - $A$  compression isotherm of stearic acid showing the gas, liquid and solid phases. Extrapolation of the solid phase a predicted area per molecule of  $21 \text{ \AA}^2$  [after Martin and Szablewski, 1999]

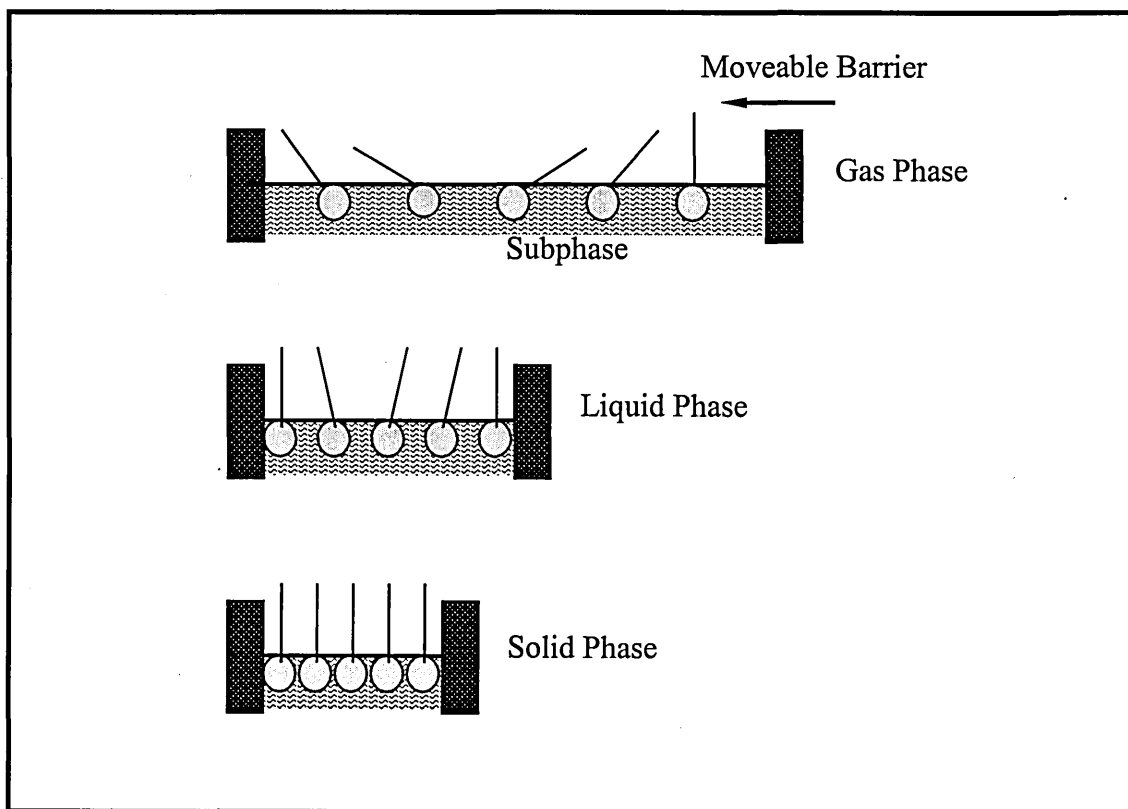


Figure 3.3. Schematic representation of the three phases seen in the  $\pi$ - $A$  isotherm of stearic acid

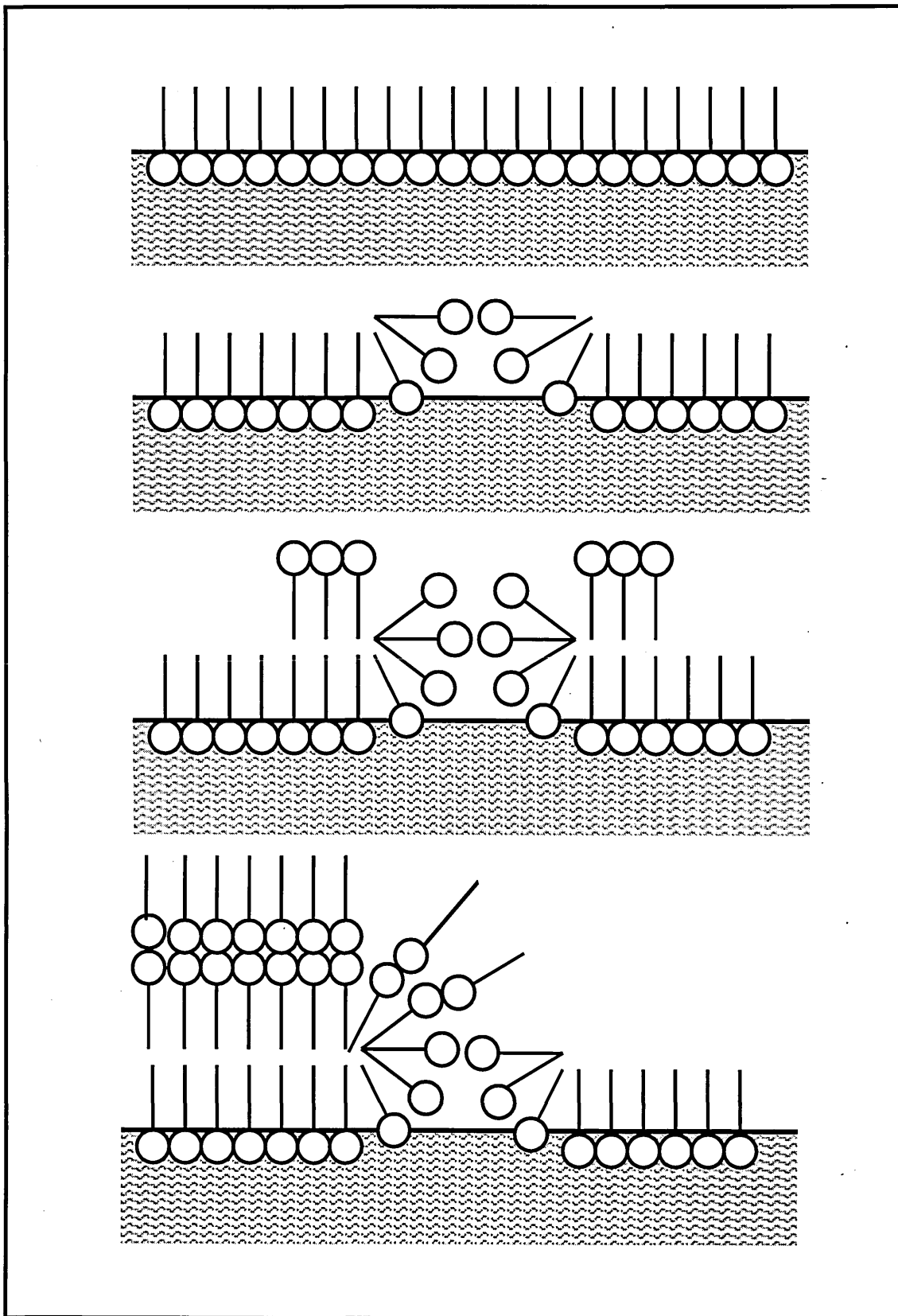


Figure 3.4. Stages of collapse of a monolayer, going from the top to the bottom diagram

### 3.2.4. Monolayer Materials

The molecules that can form a Langmuir monolayer, are called amphiphiles. The quality of Langmuir-Bodgett films is dependent upon the amphiphatic balance of the molecules, as the materials must be able to form a stable monolayer at the air-water interface. One part (hydrophilic) of these molecules is soluble in water and the forces acting upon them are predominantly coulomb type ( $1/r^2$ ), while the other part (hydrophobic) is insoluble and the forces acting upon them are predominantly Van der Waal's ( $1/r^6$  and  $1/r^{12}$ ). Being spread on the water surface, such molecule takes a preferential orientation with the hydrophilic part (also called the head), which usually consists of a polar COOH group immersed in water, while the hydrophobic part (also called the tail), which consists of a hydrocarbon chain, stays away from water (see Figure 3.5).

In order to form an insoluble monolayer the hydrophobic head and hydrophilic tail of the molecule must be in balance. A molecule with a short tail can be dissolved into the water. The length of the hydrocarbon chain required depends on the polarity of the molecule. The amphiphilic properties of a molecule depends on the balance between the hydrophilicity of the head group and the hydrophobicity of the tail, the latter depending on the chain length. These molecules are also commonly called surfactants.

#### 3.2.4.1. Fatty Acids and related compounds

The most common amphiphilic molecules are the long chain fatty acid, such as n-octadecanoic acid, commonly known as stearic acid ( $C_{17}H_{35}COOH$ ). This is one of a series of long chain fatty acids, with general chemical formula  $C_nH_{2n+1}COOH$ . The stearic acid molecule as shown in Figure 3.6 is cylindrical in the close pack form, with a

length of approximately 2.5 nm and a cross section of about 0.19 nm<sup>2</sup>. This molecule is flexible, since every CH<sub>2</sub> chain has got three stable configurations.

The 16 CH<sub>2</sub> groups of stearic acid form a long hydrocarbon chain (an alkyl chain) with methyl CH<sub>3</sub> group at one end (hydrophobic tail end), whilst a polar carboxylic acid COOH group forms the hydrophilic head at the other. The carboxylic acid COOH group confers water solubility while the hydrocarbon chain prevents it. An insoluble monolayer is formed at the air-water interface because of the balance between these two opposing forces. Any change in the nature of either the alkyl chain or the polar end group will effect the monolayer properties. The stability of the layer depends upon the polarity of the head group. The absence of a polar group or a weakly polar head will simply result in drops or lenses on the water surface. If the dipole moment associated with the head group is large then the compound becomes too soluble in the aqueous subphase.

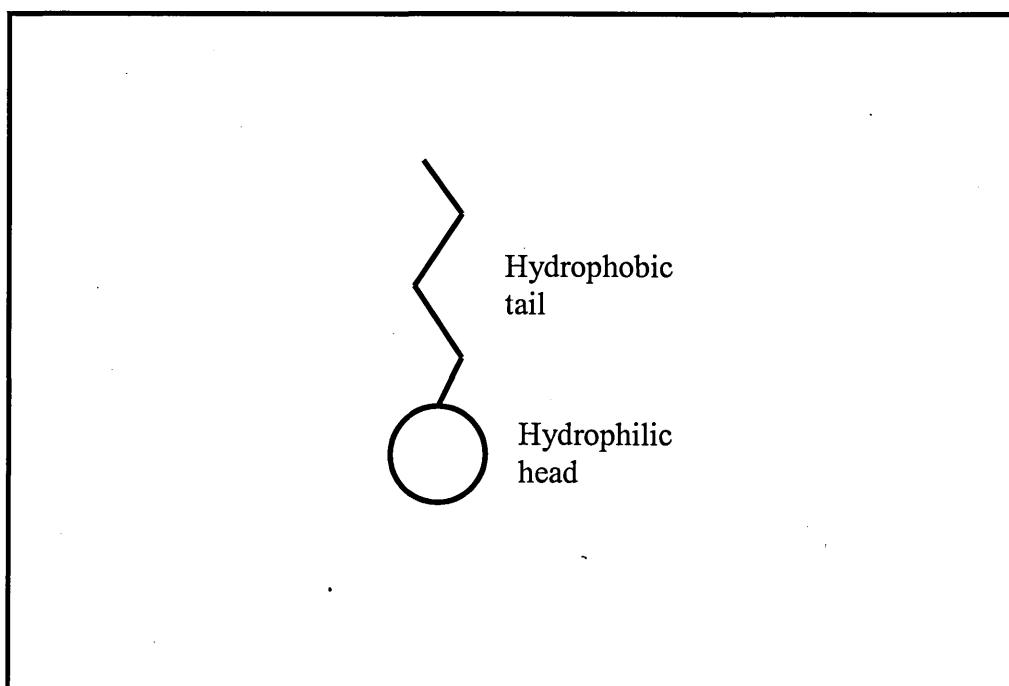


*Figure 3.5. Schematic diagram of an amphiphilic molecule*

If the length of the alkyl chain is increased the solubility of fatty acids in water decreases. The molecule must contain at least 12 carbon atoms to obtain an insoluble monolayer of a fatty acid. Lauric acid (n-dodecanoic acid –  $C_{11}H_{23}COOH$ ) for example forms a slightly soluble gaseous monolayer at low temperature. On the other hand, the additional of further carbon atoms results in the appearance of condensed monolayer phases. Table 3.1 lists some common fatty acids used for monolayer studies.

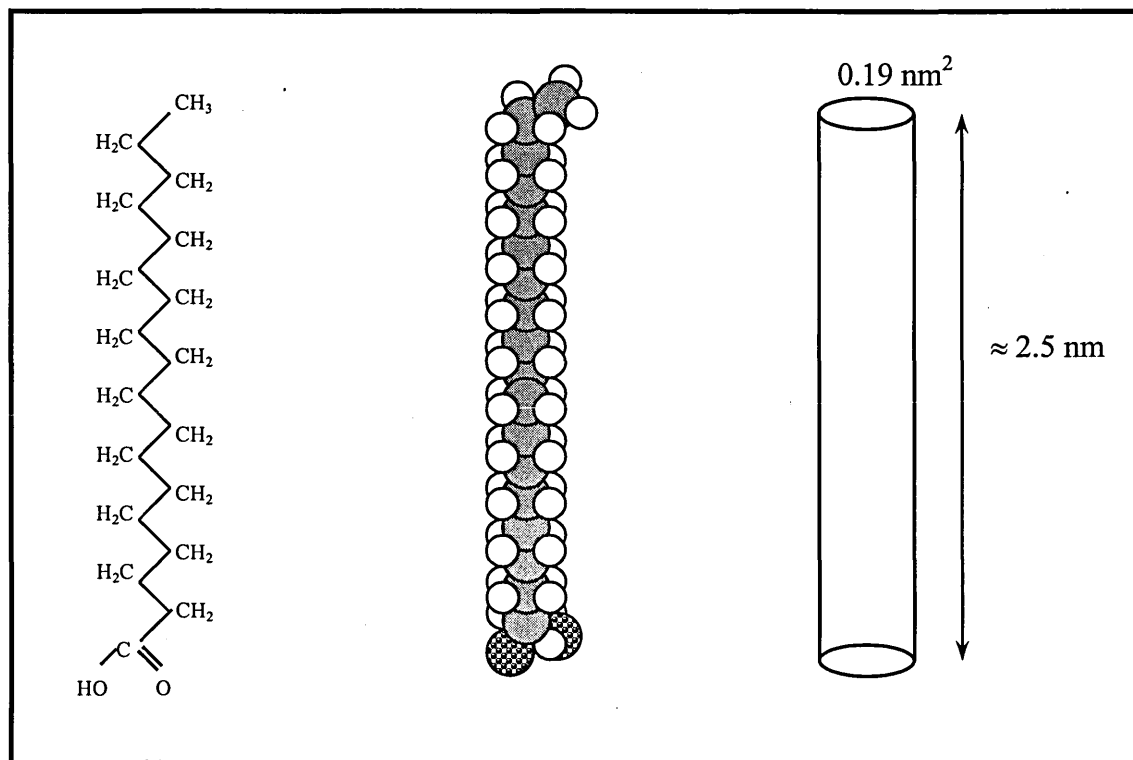


Figure 3.6. Chemical formula for stearic acid (*n*-octadecanoic acid)

Table 3.1. Long chain fatty acids compounds used in monolayer work [Petty, 1996]

Structure	Systematic name	Common name	Melting point, °C
$C_{13}H_{27}COOH$	n-tetradecanoic	Myristic	55
$C_{14}H_{29}COOH$	n-pentadecanoic		53
$C_{15}H_{31}COOH$	n-hexadecanoic	Palmitic	63
$C_{17}H_{35}COOH$	n-octadecanoic	Stearic	71
$C_{19}H_{39}COOH$	n-eicosanoic	Arachidic	77
$C_{21}H_{43}COOH$	n-docosanoic	Behenic	80
$C_{22}H_{45}COOH$	n-tricosanoic		79

### 3.2.4.2. Calixarene derivatives

The name 'calixarene' was originally coined by Gutsche to evoke the potential of these molecules to function as molecular cups or baskets for guest molecules or ions. [Seto, 1993]. Calixarenes have been termed molecular baskets owing to their ability to form complexes with a range of chemical species. The melting point of calixarenes is typically around 250°C which is very high when compared to 50-70°C for many other LB film-forming materials, such as fatty acids [McCartney et al., 1997]. Calixarenes possess an upper rim, defined by the *para*-substituents of the phenolic rings, and a lower rim defined by the phenolic hydroxy groups. Between the two lies a hydrophobic cavity whose boundaries are the inside  $\pi$ -surfaces of the constituent aromatic rings. By appropriate substitution at the hydroxy groups it is possible to extend the cavity on the lower rim. Similarly, attaching additional substituents to the *para*-positions a further extension of the cavity can be constructed on the upper rim.

Calixarene derivatives, having different substituting groups on the upper and lower rim, have been synthesised, and their chemical structures are shown in Figure 3.7. The short name of the compounds, i.e., tbC[8]A-1, tbC[8]A-3, tbC[8]A-5, and toctC[8]A-1, corresponded to  $m=1,3,5$ , respectively, are used throughout the text (tb and toct stand for tert-butyl and tert-octyl, respectively). Figure 3.8 shows the space-filling model of calix[8]arene.

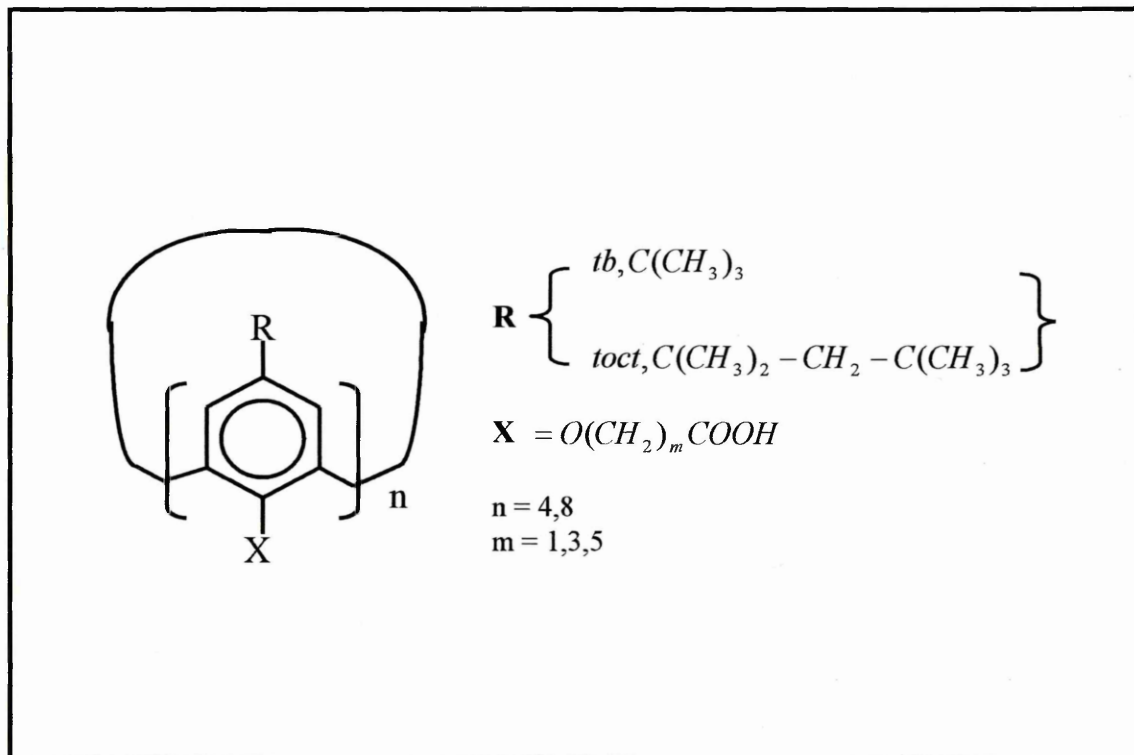


Figure 3.7. Chemical structure for calixarene

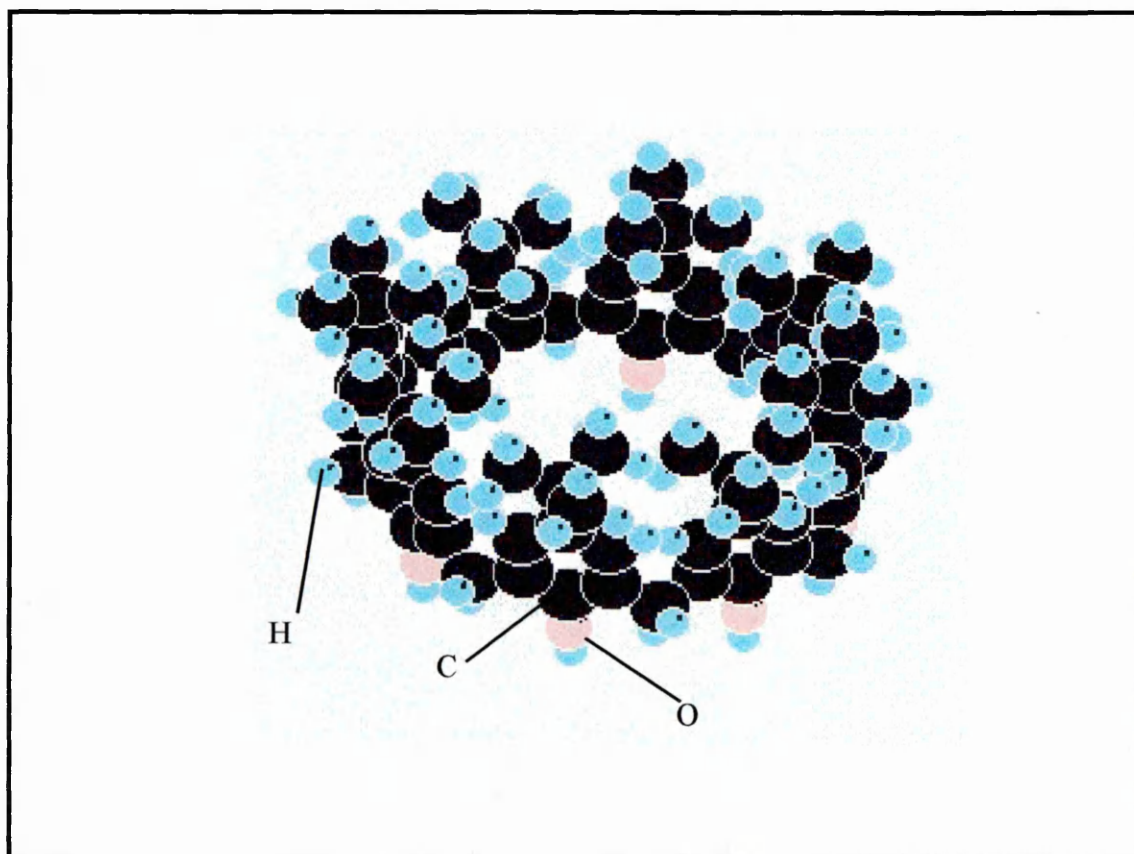


Figure 3.8. Space-filling model of calix[8]arene

### 3.2.5. Langmuir-Blodgett Films – Multilayers

Sequential deposition of monolayers onto a suitably solid substrate at a certain constant pressure forms the Langmuir-Blodgett films. The value of the critical pressure ( $\pi_c$ ) determines the pressure at which the substrate dipping should take place. The operational pressure value is usually chosen in the solid state region of the isotherm below a critical pressure. For fatty acids, the deposition generally proceeds at a surface pressure in the range of 20-40 mN/m and the temperature of 15-20 °C.

Two types of surfaces can be coated on by the LB technique; hydrophobic and hydrophilic. Deposition on a neutral surface is usually unsuccessful. Deposition onto a hydrophobic substrate begins on the downward motion of the substrate as shown in Figure 3.9. The surface of a substrate being coated with LB film changes from hydrophobic to hydrophilic with every layer. While transferring monolayers onto a hydrophilic surface proceeds in a similar manner, with the exception that the first layer starts on the upward motion of the substrate.

As shown, the hydrophobic tail groups are bound to the substrate surface with the remaining molecules normal to the substrate plane. Following the first deposition an upward motion of the substrate through the subphase forms the second monolayer. In the case of second monolayer, the hydrophilic head groups are attracted to the hydrophilic groups of the first monolayer. Subsequent monolayers are transferred in the same way until the desired film thickness is achieved. The resulting structure, which stacks in a head-to-head and tail-to-tail pattern, is known as Y-type structure of Langmuir-Blodgett films. Fatty acids and fatty acid salt monolayers normally deposit as Y-type films. However, some materials can be deposited on the up or down strokes only. These deposition modes are called X-type (monolayer transfer on the downstroke

only) and Z-type (transfer on the upstroke only). An alternate Langmuir trough enables deposition of two different types of material similar to the Y-type structure.

Usually, the deposition is quantified by a parameter called transfer ratio, which is defined as the ratio of the reduced area of subphase during the transfer of a single monolayer to the area of film deposited onto the substrate.

$$TR = \frac{A_1}{A_2} \quad (3.6)$$

where TR is the transfer ratio,  $A_1$  is area of monolayer removed from subphase and  $A_2$  is area of substrate immersed. The ratio is expressed as a percentage and ideally this should be close to 100 %. But in reality, this quantity differs from the ideal value due to several reasons like partial transfer or loss of molecules to the subphase and inaccurate determination of the trough and substrate area.

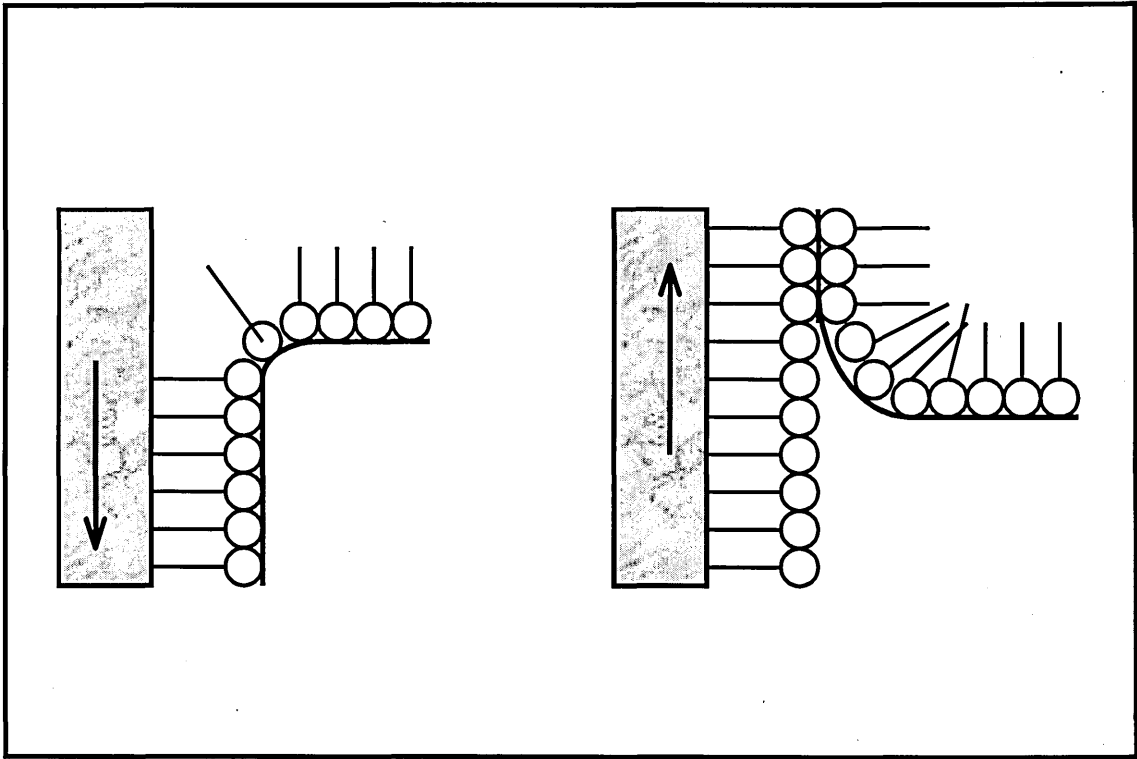


Figure 3.9. Langmuir-Blodgett films deposition onto a hydrophobic substrate

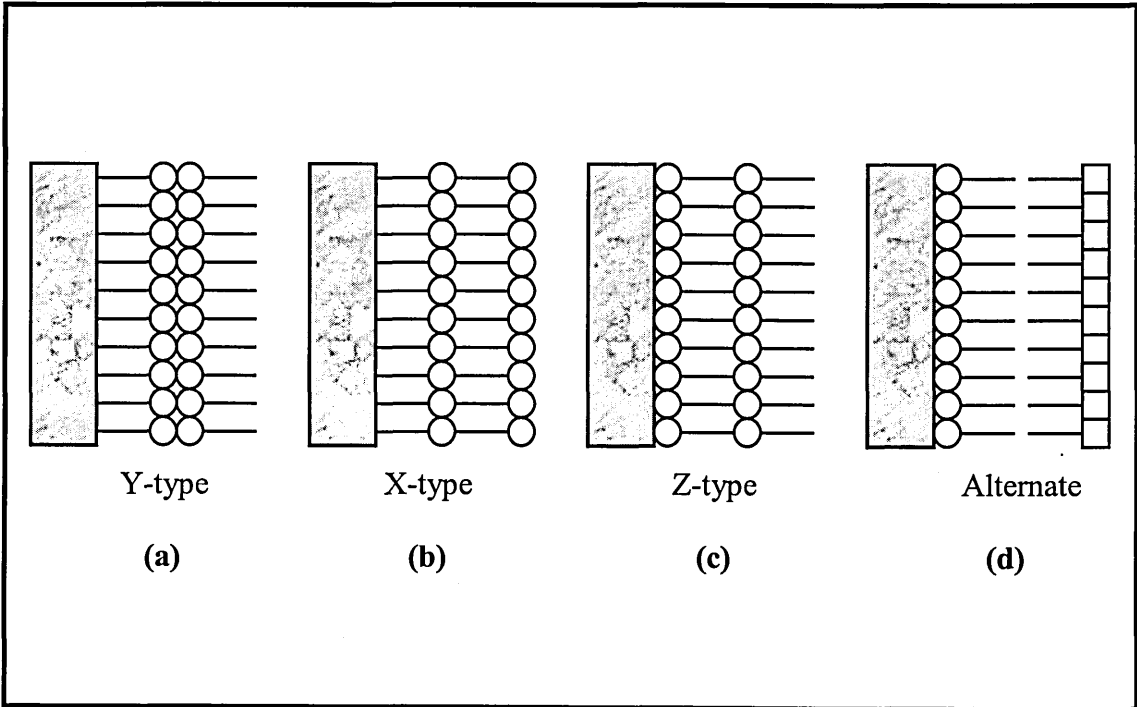


Figure 3.10. Schematic comparison of Langmuir-Blodgett film deposition type; (a) Y-type, (b) X-type, (c) Z-type and (d) alternate type depositions

### 3.2.6. Langmuir-Blodgett Trough

To study the formation of a monolayer at the air-water interface Langmuir developed a trough system, which allowed the interfacial surface tension to be measured for different confinement areas of the monolayer. Such a system is called Langmuir or Langmuir-Blodgett trough. The trough has undergone several modifications since the first one developed by Agnes Pockels. The principles of the Langmuir-Blodgett trough remain the same in the present days to those used by Langmuir, although current Langmuir troughs differ in their geometry and the methods of measurement of the surface tension of the layer. These days troughs are fully computerised with state-of-art-electronics involved in the design.

Figure 3.11 shows a schematic representation of the Nima Technology 611 Langmuir trough having two compartments and a linear dipping mechanism which was used throughout this research. The essential elements of the trough are (a) the bath, usually made of a highly hydrophobic material like polytetrafluoroethylene (PTFE, commercial name Teflon), (b) the mobile barriers (also made of PTFE) for controlling the area and hence pressure of the monolayer, (c) a dipper for dipping the substrate in the monolayer and (d) a Wilhelmy balance that measures the surface pressure. The latter contains a Wilhelmy plate, which is simply a strip of filter paper pulled down into the subphase by the surface tension of the water. The plate is suspended on a very sensitive electromagnetic microbalance by a thin wire. The pressure sensor actually measures the difference in the surface tension between clean water and that of floating monolayer on water. The movement of the substrate through the subphase is controlled by a motor driven micrometer. The devices can be manually controlled, or more commonly by a Computer.

The trough is enclosed in a transparent cabinet to eliminate the effect of constant airflow present in the clean room. Air flow over the Langmuir film causes ripples and hence disruption of the monolayer.

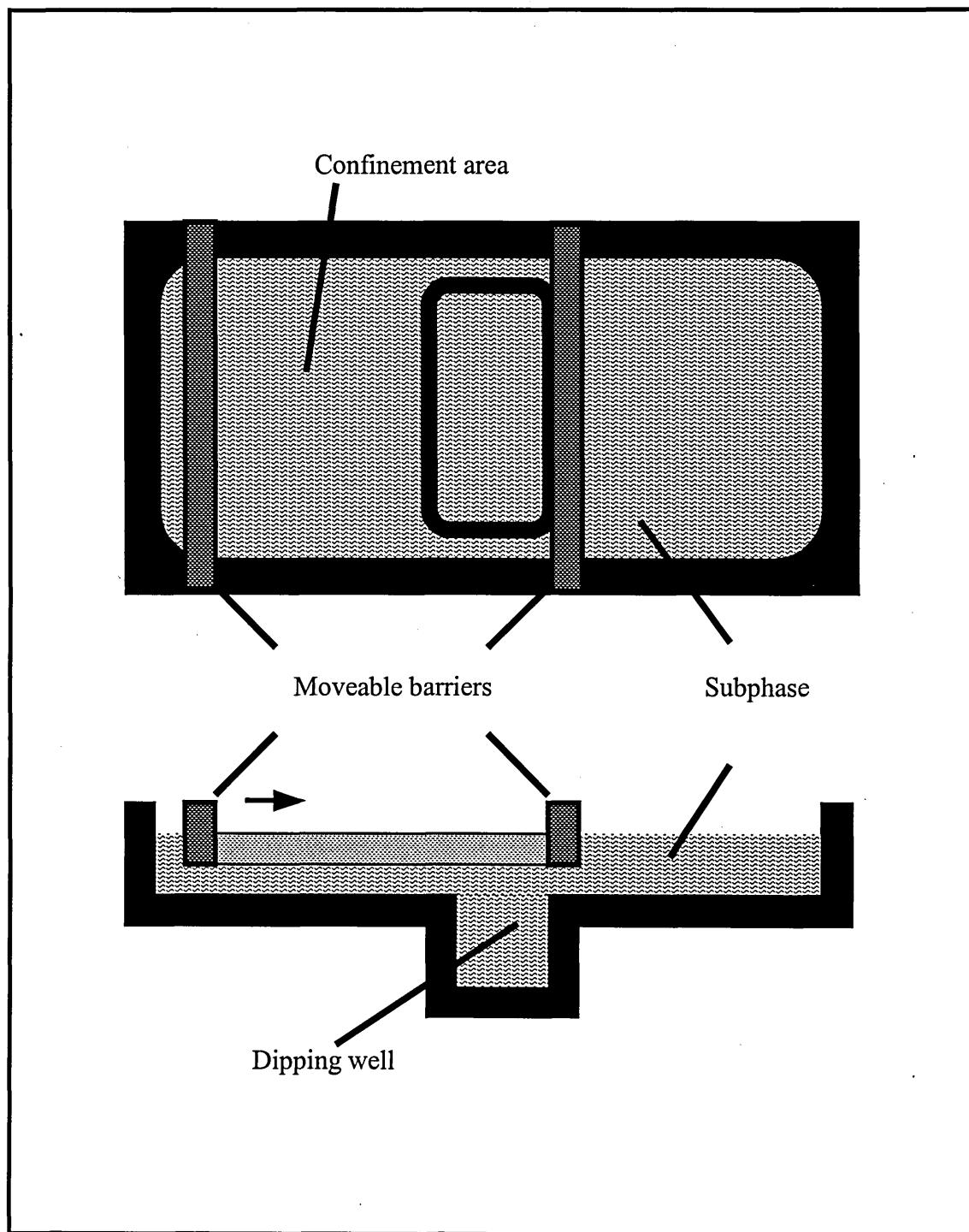
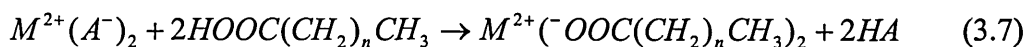


*Fig. 3.11. Schematic representation of the Langmuir trough used in this research*

### 3.3. Langmuir-Blodgett Film Deposition

The main requirement for successful Langmuir-Blodgett films is to reduce contaminants to a minimum. Another aspect of Langmuir-Blodgettry is that the substrate should be quite flat to avoid the possibility that the film could break at the interface.

The technique for the fabrication of Langmuir-Blodgett (LB) fatty acid metal salts films begins with spreading a solution of a long chain fatty acid,  $[\text{CH}_3(\text{CH}_2)_n\text{COOH}]$ , onto a subphase containing bivalent metal ions. A monolayer of fatty acid forms at the air-water interface and ion exchange between the protons of the fatty acid and the metal ions in solution occurs at certain pH and the metal ion concentrations [Elliot, 1998]. For a stearic acid monolayer spread onto a  $2.5 \times 10^{-4}$  M  $\text{CdCl}_2$  subphase, the exchange of fatty acid protons for  $\text{Cd}^{2+}$  ions occurs at approximately pH 5 [Linden et al, 1994]. The bivalent metal ion/fatty acid proton exchange can be represented by the following reaction:



The symmetric bilayer, with metal ions sandwiched between the polar head groups in the film, can be deposited onto vertically mounted substrates which are passed down and then up through the metal-surfactant monolayer at the air-water interface. Different metal ions, such as Cd, Hg and Pb can be incorporated into LB films using this technique. In this thesis the metal ion used was Cd from  $\text{CdCl}_2$  salt and the reaction of the formation the Cd-stearate monolayer is the same as Equation (3.7).



Figure 3.12 shows the formation of LB films of Cd-salt stearic acid.

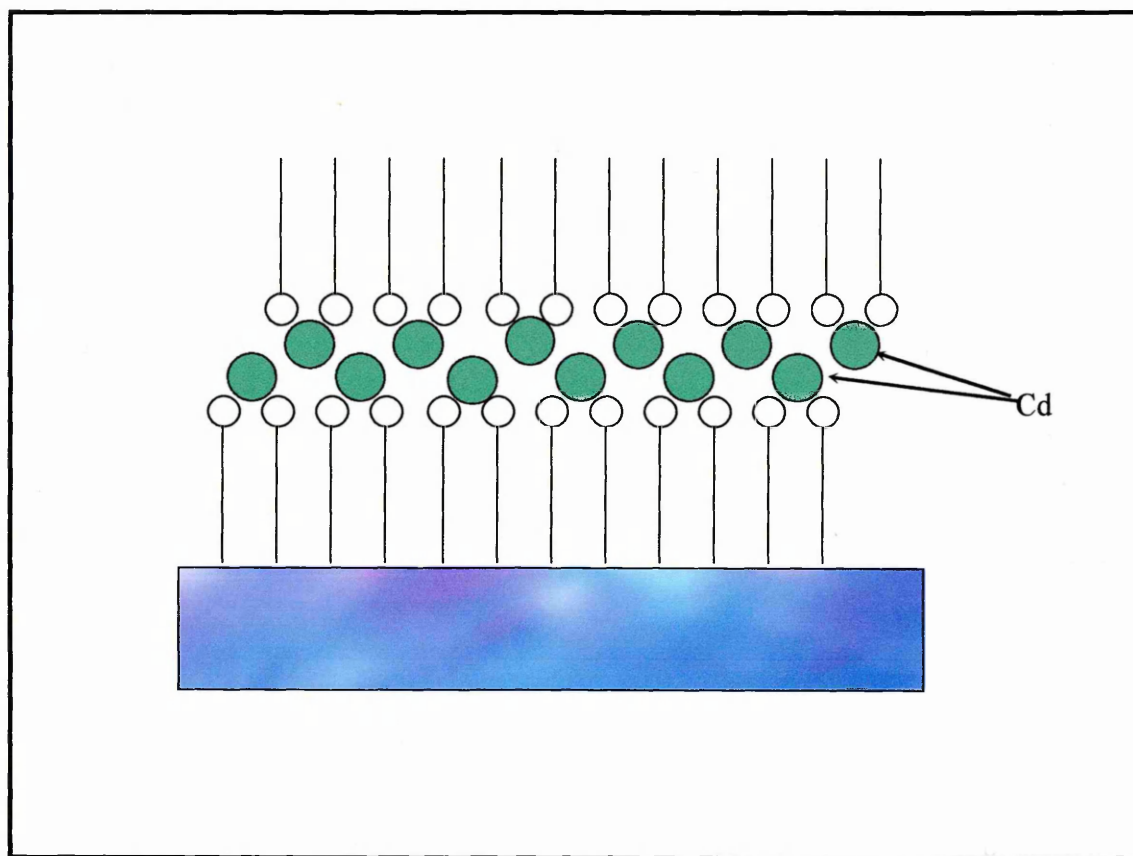


*Figure 3.12. Formation of LB films of Cd-salt stearic acid*

### 3.3.1. Preparation of Langmuir Monolayer

To perform successful deposition, a set of cleaning procedures of the Langmuir-Blodgett trough must be followed. The trough of 1.6 litre in volume is then filled with deionised water and with addition of 6 ml of 0.1 M cadmium chloride ( $\text{CdCl}_2$ ) solution. The resulting subphase containing a concentration of  $\text{CdCl}_2$  ( $5 \times 10^{-4}$  mol/l), is then checked for cleanliness by compression-decompression cycles. In the case of increasing surface pressure, which indicates contamination, the active area of the trough was cleaned with a water pump. The speed of the barrier is set to 200 cm/min. The Wilhelmy plate is used to measure the surface pressure of the subphase.

Both stearic acid and calixarene compounds were dissolved in chloroform to a concentration of 1 mg/ml. The solution of either stearic acid or calixarene was spread

onto the subphase using a 100  $\mu\text{l}$  syringe at room temperature ( $\text{pH} = 5.5$ ). Each drop of the solution was allowed time for the solvent to evaporate before the next was applied. The optimum amount of spreading solution was found by referring to the pressure area isotherms produced. For stearic acid solution the optimum quantity is about 80-100  $\mu\text{l}$ , while calixarene is about 100-120  $\mu\text{l}$ . In order to allow the evaporation of any residual solvent, a period of between 3 and 20 minutes was given prior to the compression.

An important test to examine the suitability of the material for Langmuir monolayer production and the effectiveness of the dipping procedure is the stability test. The monolayer is compressed to the target pressure and held at this point for about one hour. The surface pressure and the area of the monolayer are monitored as a function of time. If the changes in the area are small over this time, then the film is considered to be stable, and this demonstrates the suitability of the selected pressure for dipping. Pressures of 25  $\text{mN/m}$  and 28  $\text{mN/m}$  were selected for LB deposition of calixarene and stearic acid monolayers, respectively.

Figure 3.13 shows the  $\pi$ -A isotherm of stearic acid monolayer and demonstrates the area per molecule of the monolayer is about 21  $\text{\AA}^2$ . While the  $\pi$ -A isotherms of calix[8]arene derivatives are demonstrated in Figure 3.14. As can be seen, increasing the length of the substituting alkyl chain on the lower rim (from  $n=1$  to  $n=5$ ) leads to the shift of the isotherm to the larger area. This trend is believed to be due to the stabilisation of the molecule in its cone conformation.

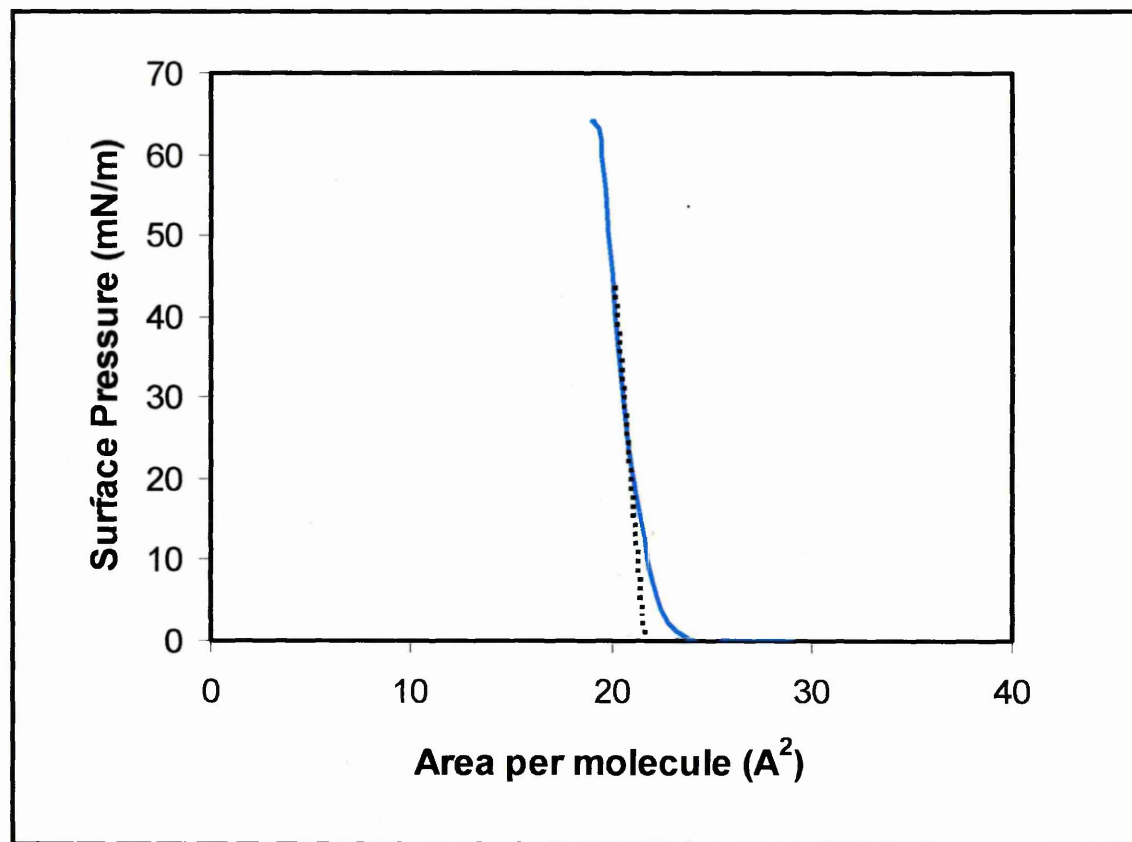


Figure 3.13. Area per molecule of stearic acid monolayer

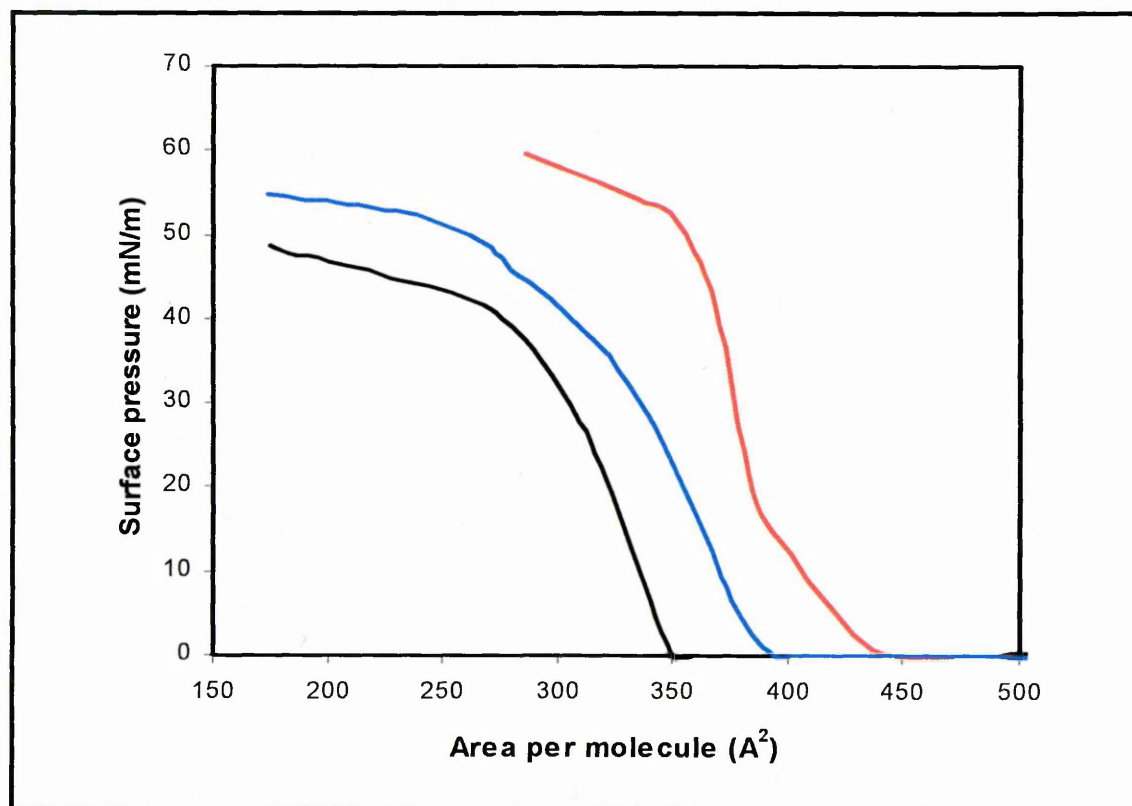


Figure 3.14.  $\Pi$ -A pressure isotherm of calix[8]arene carboxylic acids derivatives: (a) *tbC[8]A-1*, (b) *tbC[8]A-3* and (c) *tbC[8]A-5*

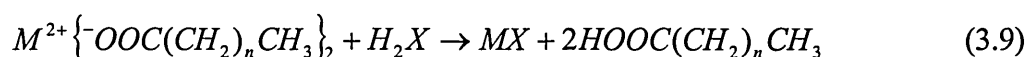
### 3.3.2. Formation of Langmuir-Blodgett Films

Deposition of all samples took place at room temperature and a subphase pH of 5.5. The monolayer is compressed to the target pressure of 25 mN/m or 28 mN/m for calixarenes and stearic acid, respectively before dipping commences. A suitable substrate was fixed in the holder and the top and bottom positions of the dipper were chosen to cover desired area. The speed of floating monolayer compression, film deposition and monolayer drying time are determined by experimentation for each material and substrate. The deposition is monitored by recording the pressure area isotherm and the transfer ratio. Deposition on a hydrophobic surface commences during the first down stroke of the substrate through the air-water interface. The meniscus at the water surface-substrate boundary dips below the water surface level and wets the substrate at an angle of about 120-130° when a substrate immerses into the aqueous subphase. Deposition on hydrophilic substrate does not take place during the first down stroke because of wetting of the substrate by the subphase. Deposition on the first up stroke onto a hydrophilic surface takes place in similar fashion as deposition on hydrophobic substrates. The direction of the meniscus now favours the end of the molecule attracted to the surface and deposition is encouraged.

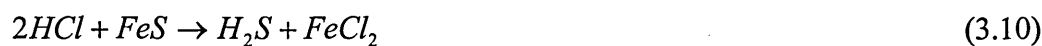
The deposition of the first layer is of a great importance as this predetermines the deposition of the subsequent layers. Subsequent depositions are more likely to be successful if the first monolayer is transferred in a homogenous and uniform manner. Once the first layer has been successfully deposited the deposition can continue by keeping similar bonding groups (hydrophilic or hydrophobic) adjacent. In this way the head-to-head and tail-to-tail structure of LB films is preserved. For subsequent layers, transferring onto existing film, the deposition should be homogeneous.

### 3.4. Formation of II-VI Semiconductor Nanoparticles within LB films

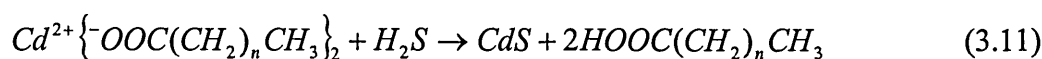
The concept of formation of II-VI semiconductor nanoclusters inside Langmuir-Blodgett (LB) films of fatty acid derives from the work of Barraud and co-workers [Barraud etc, 1986]. The II-VI semiconductor nanoparticles are formed by exposure of LB films containing metal ions to the dihydrogen chalcogenides  $H_2X$  ( $X=S, Se, Te$ ) gas at room temperature. The reaction of bivalent metal ion in LB films with dihydrogen chalcogenides  $H_2X$  can be depicted as below in Equation (3.9)



Cadmium Sulphide (CdS) was chosen for this work as one of the most studied among the II-VI compounds. To perform the reaction (3.9) the  $H_2S$  gas is generated by a reaction of ferrous sulphide (FeS) sticks with hydrochloric acid (HCl), which is firstly diluted in water:



$H_2S$  exposure of multilayer LB films is carried out in a sealed glass chamber at room temperature and at atmospheric pressure. The reaction of Cd ion in the LB films with  $H_2S$  can be depicted as below:



The initial idea is to create two dimensional semiconductor layers in LB films. These layers, however, showed unstable behaviour due to agregation. As a result, three-dimensional CdS clusters formed in LB film. The agregation most likely starts from small clusters of group of a few molecules of CdS, which formed nucleus of CdS particles. These molecules then interact with other molecules and form bigger CdS

clusters in order to reduce their surface tension or surface energy as shown in Figure 3.15. As a final result of the aggregation, there is formation of bigger CdS nanoparticles (a few nm in diameters) inside each bilayer of the LB films. When CdS nanoparticles formed in the LB films, the structure of the LB films may change (decreases layer-by-layer film order) as shown schematically in Figure 3.16. The important aspect of the formation of CdS nanoparticles in the LB films is that the particles formed in each bilayer of the film matrix create two-dimensional semiconductor layers.

Production of metal sulphide nanoclusters within LB films of fatty acid salts by their reduction with  $H_2S$  gas has been extended by using calixarene LB films as a matrix material. Formation mechanism of CdS nanoparticles in this film is similar to that in stearic acid Cd- salt LB film. However, it has been suggested that the presence of calixarenes restricts aggregation of CdS by capturing some of CdS molecules within molecular cavitant. Figure 3.17 shows the schematic structure of the formation of CdS nanoparticles inside calixarene Cd-salt LB films.

The formation of CdS clusters does not affect the layer-by-layer structure of calixarene LB films, as has been shown by both the low angle X-ray diffraction and ellipsometry. This fact can be explained either by the formation of very small three-dimensional CdS clusters comparable in size with the calixarene cavity, or by the formation of two-dimensional crystals within each calixarene bilayer.

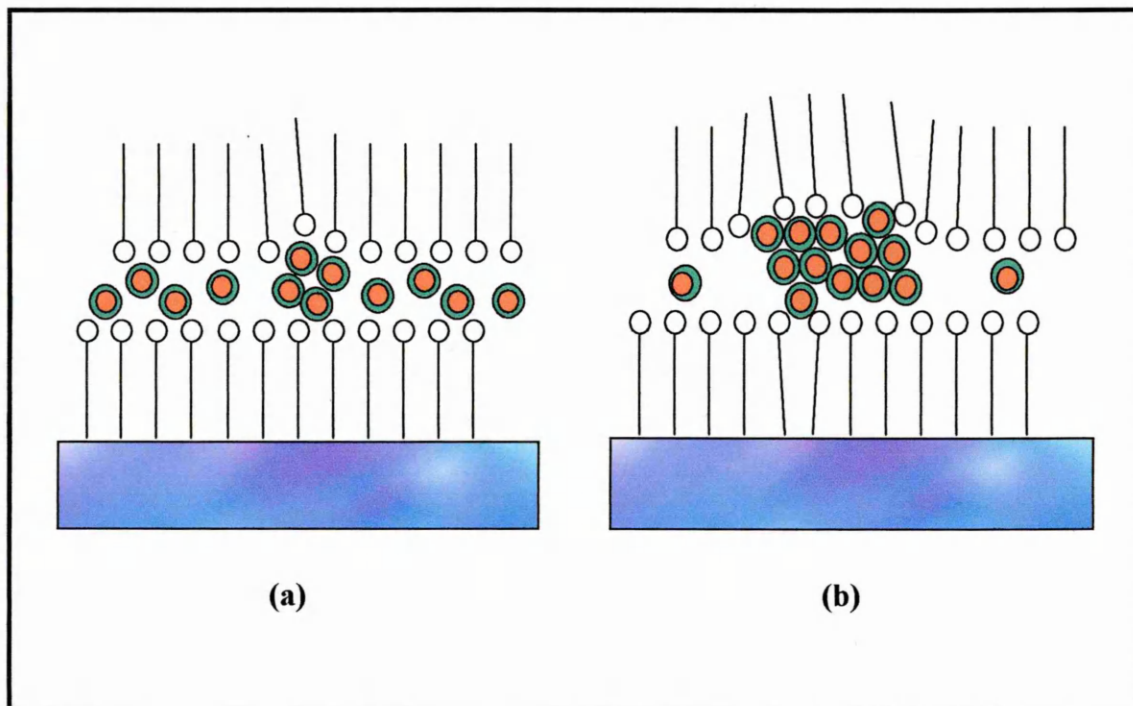


Figure 3.15. Aggregation of small clusters of CdS in LB films: (a) a group of a few molecules of CdS; (b) CdS molecules interact each other in order to reduce their surface energy

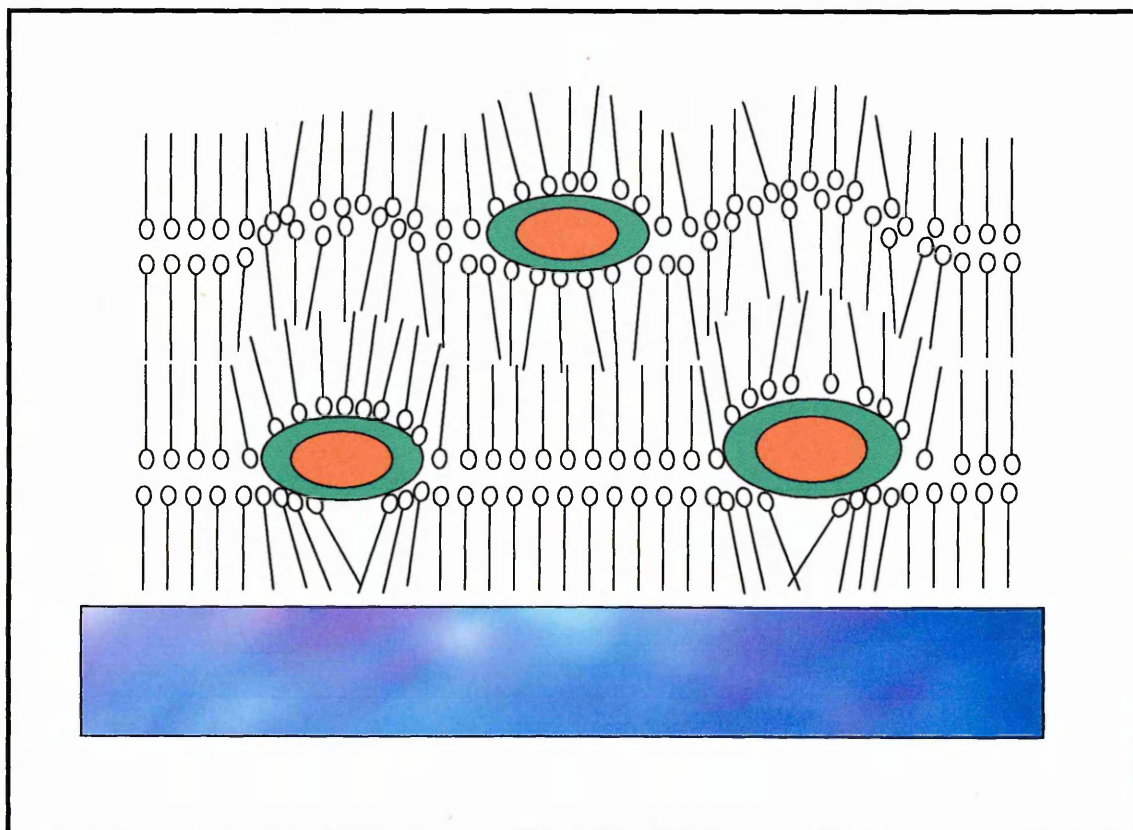
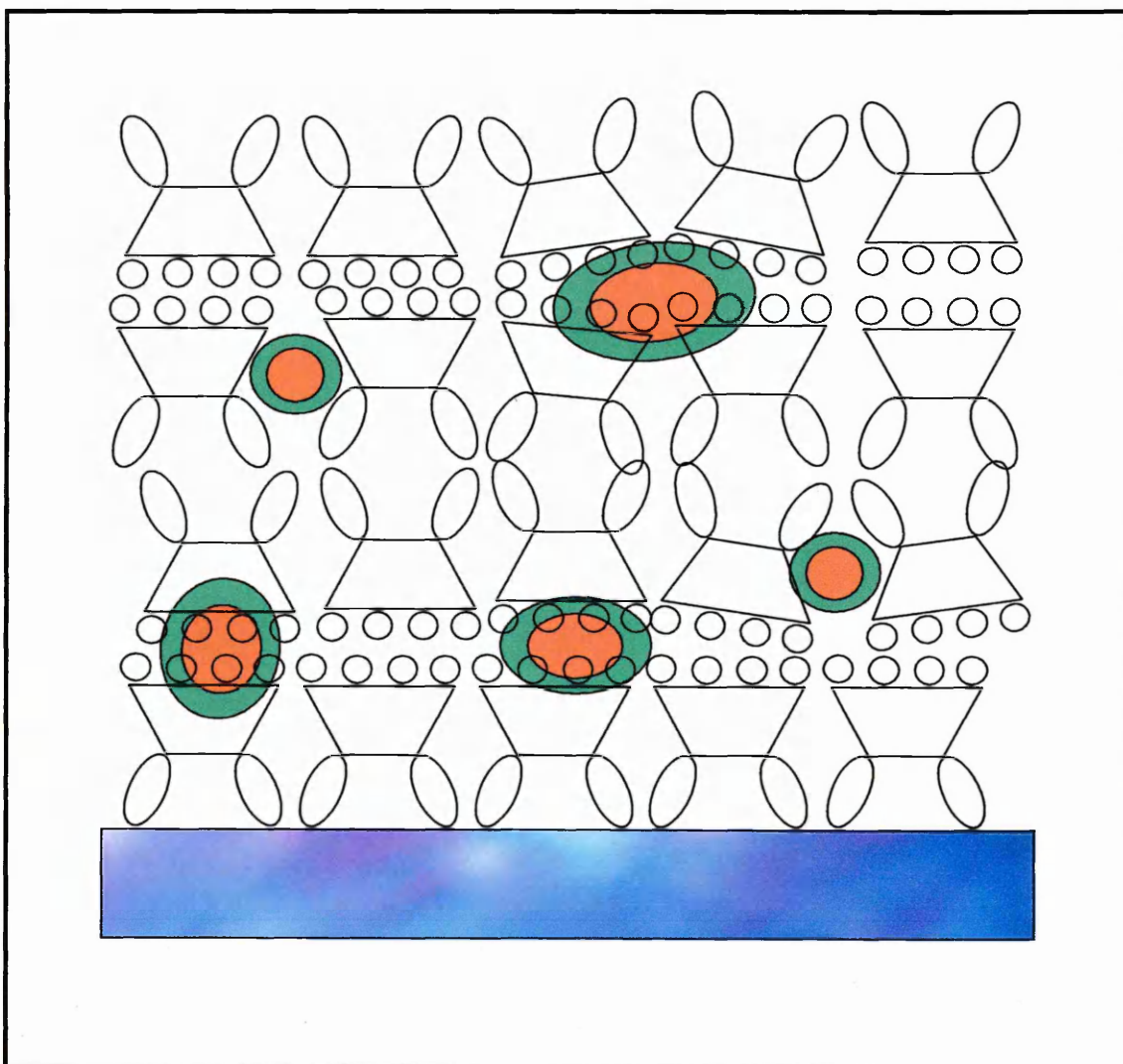


Figure 3.16. Formation of CdS nanoparticles inside each bilayer of the LB films of stearic acid. The structure of the films changes due to formation of the CdS particles.



*Figure 3.17. Formation of CdS nanoparticles inside LB films of Cd-salt calixarene. Much smaller CdS particles were formed within CA films due to CdS aggregation limited by calixarene cavities*

### 3.5. Summary

The LB films of stearic acids and calix[8]arene were successful deposited onto a variety of the solid substrates in different number of layers for different measurements. The surface pressures of 25 mN/m and 28 mN/m were selected for calix[8]arene and stearic acid LB films monolayer, respectively. The  $\pi$ -A isotherm of stearic acid monolayer demonstrates the area per molecule of the monolayer is about  $21 \text{ \AA}^2$ . While the  $\pi$ -A isotherms of calix[8]arene derivatives shows that increasing the length of the substituting alkyl chain on the lower rim (from  $n=1$  to  $n=5$ ) leads to a shift of the isotherm to higher area.

CdS nanoparticles were formed inside the LB films by exposing the films to dihydrogen sulphide ( $\text{H}_2\text{S}$ ) gas at room temperature. The  $\text{H}_2\text{S}$  gas is generated by a reaction of ferrous sulphide ( $\text{FeS}$ ) sticks with hydrochloride acid ( $\text{HCl}$ ). Production of metal sulfide nanoclusters within LB films of fatty acid salts by their reduction with  $\text{H}_2\text{S}$  gas has been extended by using calyx[8]arene LB films as a matrix material. Formation mechanism of CdS nanoparticles in these films is similar to those in Cd-salt stearic acid LB films.

# CHAPTER 4

## STUDY OF MORPHOLOGY OF CADMIUM SULPHIDE (CdS) NANOPARTICLES FORMED WITHIN LB FILMS

### 4.1. Introduction

This chapter presents a detailed study of morphology of cadmium sulphide (CdS) nanoparticles formed within Langmuir-Blodgett (LB) Films. One bilayer (2 layers) and four bilayers (8 layers) of stearic acid (SA) and calix[8]arene (CA) Cd-salt LB films were deposited on silicon wafer substrate. CdS nanoparticles were then formed inside the bilayers by exposure the LB films to H<sub>2</sub>S gas. Since electronic properties of semiconductor nanostructures depend very much on their shape and dimensions [Yoffe, 2001], the method of AFM was employed to study the morphology of LB films containing CdS nanoparticles. The results of the AFM study also help the interpretation of the observed features of absorption and luminescence spectra.

Section 4.2 of the present chapter describes a detail of AFM technique used in this research. AFM images of stearic acid (SA) and calix[8]arene (CA) Cd-salt LB films before and after H<sub>2</sub>S treatment and their analysis are presented in Section 4.3. Finally, Section 4.4 summarises current chapter.

## 4.2. Introduction to Atomic Force Microscopy (AFM) Technique

The Atomic Force Microscopy (AFM) has been used to solve processing and materials problems in a variety of technologies affecting the electronics, chemical, telecommunications, biological, automotive and energy industries. A wide range of materials has been investigated using this technique including semiconductors, polymers, thin and thick film coatings, synthetic and biological membranes, metals and composites. The AFM utilises a sharp nanometer size probe scanning the surface of a sample using a precise piezo-transducer. In the case of the AFM, the probe, which is a tip on the end of a cantilever, bends in response to the atomic force between the tip and the sample.

The first AFM was made by Gerd Binnig and Christoph Gerber in 1985. They used the cantilever made from a tiny diamond crystal glued onto one end of a gold foil strip to examine insulating surfaces. Lateral features as small as 300 Å were imaged. This first AFM used a scanning tunnelling microscope at the end of the cantilever to detect the bending of the lever. Nowadays most AFMs employ an optical lever technique.

The principles on how the AFM works are very simple. Figure 4.1 illustrates how the atomic force microscopy scans surfaces. A sharp tip typically made from Si or Si<sub>3</sub>N<sub>4</sub> scans the surface of a sample with feedback mechanisms that enable the piezo-electric scanners to maintain the tip at a constant force (to obtain height information), or at a constant height (to obtain force information) above the sample surface. The nanoscope AFM head employs an optical detection system. The movement of the tip (or the sample) is performed by a precise positioning device made from piezo-electric ceramics, most often in the form of a tube scanner. The scanner is capable of sub-

angstrom resolution in  $x$ -,  $y$ - and  $z$ -directions. The  $z$ -axis is conventionally perpendicular to the sample.

A diode laser beam is focused onto the back of the reflective upper surface of the cantilever. As the tip scans the surface of the sample, moving up and down following profile of the surface, the laser beam is deflected into a photo-detector. Both the size and position of the current created in the detector are linked via computer to a feedback circuit, which maintains the cantilever position at a defined location on the surface that is being analysed.

Meanwhile the cantilever is scanned backwards and forwards across the surface (raster scanner) to produce an image (or surface topography, using the simplest form of AFM) that reflects changes in the position of the cantilever tip. Other forms of imaging and measurements using AFM can be generated by analysing the different types of information produced in the feedback circuit and also by employing different mode of controlling the movement of the cantilever.

A variety of tip-surface interactions may be measured by atomic force microscopy (AFM), depending on the separation between the tip and the sample. Obviously, during contact with the sample the tip predominantly experiences repulsive Van der Waals forces. When lifted above the surface, however, long-range interaction, notably electric or magnetic forces, may dominate the interaction with the tip. The three main classes of operation are *contact mode*, *tapping mode* and *non-contact mode* [Bonnell, 2001].

**Contact mode** is the most common method of operation of the AFM. In this mode, the tip and sample remain in close contact as the scanning proceeds. The force on the tip is repulsive with a mean value of  $10^{-9}$  N. This force is set by pushing the cantilever

against the sample surface with a piezoelectric positioning element. Electrostatic and/or surface tension forces from the adsorbed gas layer pull the scanning tip toward the surface. It can damage samples and distort image data. Therefore, contact mode imaging is heavily influenced by frictional and adhesive forces compared to tapping or non-contact mode.

**Tapping mode** is the next most common mode and a key advance in AFM. This potent technique allows high resolution topographic imaging of sample surfaces that are likely to be damaged, loosely held to their substrate, or difficult to image by other AFM techniques. Tapping mode overcomes problems associated with friction, adhesion, electrostatic forces, and other difficulties that plague conventional AFM scanning methods. In this mode, the tip is placed in contact with the surface to provide high resolution and then the tip is lifted off the surface to avoid dragging the tip across the surface. The cantilever is oscillated at or near its resonant frequency (often hundreds of KHz) using a piezoelectric crystal when operated in ambient air. The piezo motion causes the cantilever to oscillate with a high amplitude (typically greater than 20 nm) when the tip is not in contact with the surface. The oscillating tip is then moved toward the surface until it begins to lightly touch or tap the surface. During scanning, the vertical oscillating tip alternately contacts the surface and lifts off, generally at a frequency of 50 kHz to 500 kHz. As the oscillating cantilever begins to intermittently contact the surface, the cantilever oscillation is necessarily reduced due to energy loss caused by the tip contacting the surface. The reduction in oscillation amplitude is used to identify and measure surface features. During tapping mode operation, the cantilever oscillation is maintained constant by a feedback loop. The oscillation amplitude of the tip is measured by the detector and input to the controller electronics.

**Non-contact mode** is another method that may be employed when imaging by AFM. The cantilever must be oscillated above the surface of the sample. This is a very difficult mode to operate in ambient condition with the AFM. In this mode, the tip hovers around 50-150 Å above the sample surface. Attractive Van der Waals forces acting between the tip and the sample are detected, and topographic images are constructed by scanning the tip above the surface.

The resolution of AFM method depends on the type of tip-sample interaction. The highest resolution can be achieved by using the contact AFM mode, which its photodetector can measure displacement of laser light as small as 10 Å. In this AFM mode, the speed of scanning is limited by the response time of the feedback circuit, but the total force exerted on the sample by the tip is well controlled. Contact mode is generally preferred for most applications. This constant-height mode is often used for taking atomic-scale images of atomically flat surfaces, where the cantilever deflections and thus variations in applied force are small. Even greater improvements in resolution have been attained with tapping mode, but contact mode imaging still is capable of highest resolution imaging. The non-contact mode generally provides low resolution and can also be hampered by the contaminant layer which can interfere with oscillation. Tapping mode AFM was developed as a method to achieved high resolution without inducing destructive frictional forces both in air and fluid. With this AFM mode, the very soft and fragile samples can be imaged successfully.

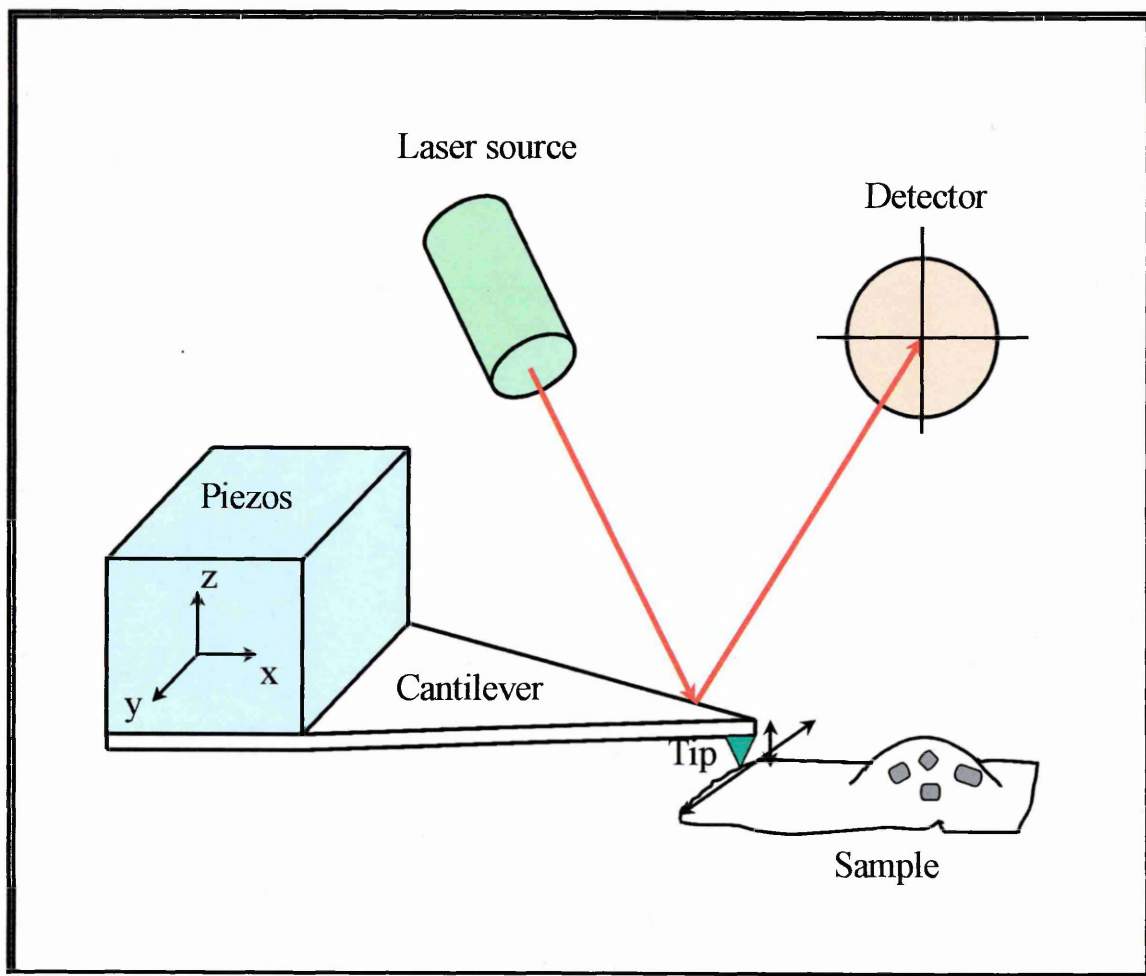


*Figure 4.1. Schematic illustration of the method of operation of an AFM*

### 4.3. Experimental Procedure

Two layers and eight layers of stearic acid (SA) and Cd-salt calix[8]arene (CA) Cd-salt LB films were deposited on silicon wafer substrates. The samples were then exposed to H<sub>2</sub>S gas in order to perform CdS nanoparticles inside the bilayers. Tapping mode of atomic force microscopy (AFM) measurements were performed on the samples using Nanoscope IIIa instruments (shown in Figure 4.2). The highly doped n-Si cantilever with the tip radius of 4 nm was used for tapping AFM imaging.



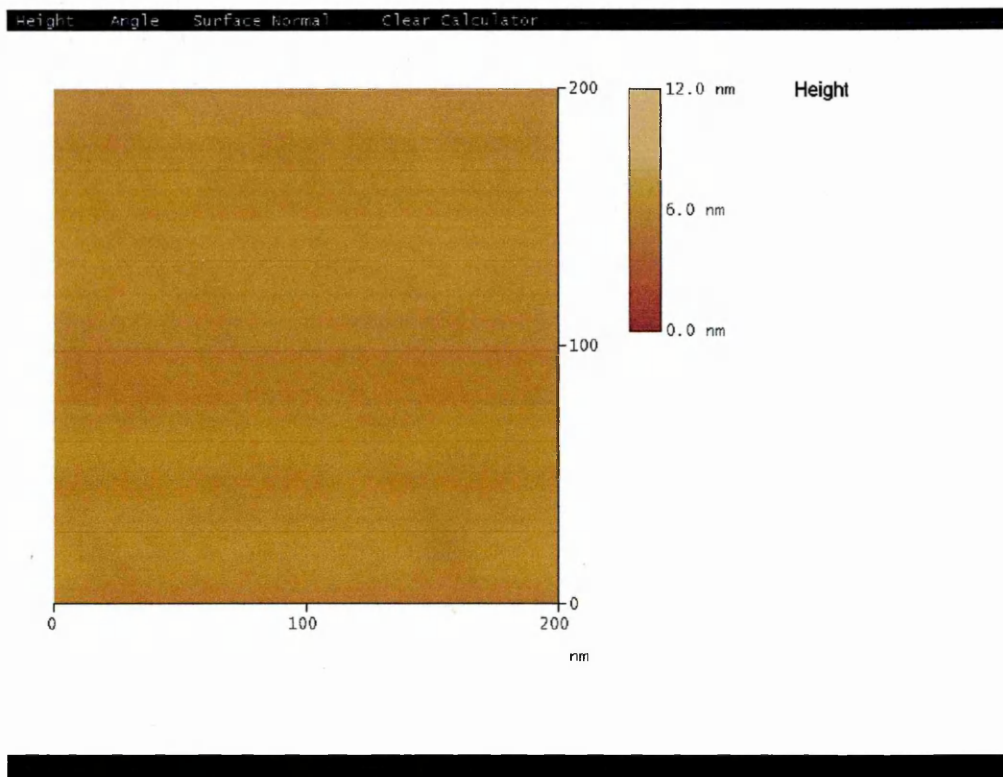
*Figure 4.2. Photograph of AFM instrument*

## 4.4. Results and Discussion

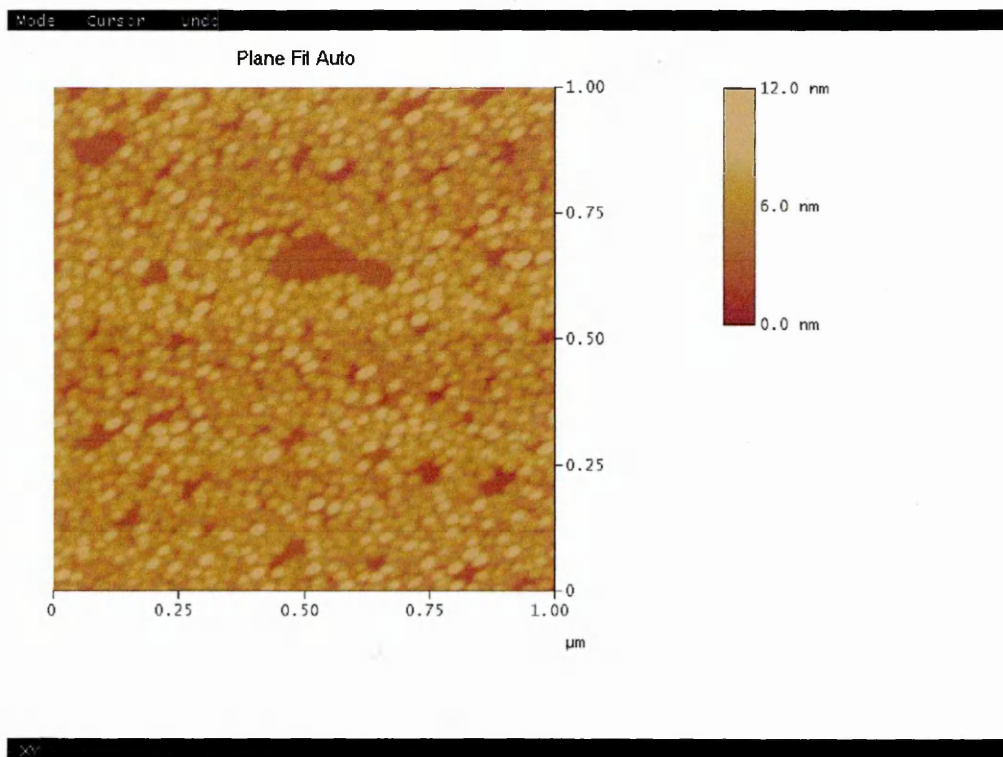
A typical AFM (tapping mode) image of the cadmium stearate bilayer before the treatment with  $H_2S$  gas is shown in Figure 4.3. The imaged area is 200 x 200 nm. Figure 4.4 (1.00 x 1.00  $\mu m$ ) shows an AFM image for the stearic acid (SA) Cd-salt LB bilayer after  $H_2S$  treatment, and an AFM image of 4 bilayers of SA LB films is shown in Figure 4.5. As can be seen from Figure 4.3, the sample of SA LB films before  $H_2S$  treatment did not show any features of particles or clusters. In contrast, the SA LB films after exposing to  $H_2S$  gas (Figure 4.4 and Figure 4.5) demonstrate clusters with the dimensions of tens of nanometer.

Figure 4.6 shows a three-dimensional AFM image of CdS nanoclusters formed in stearic acid Cd-salt LB films. Since  $z$ -axis is not in same scale as that of  $x$ - and  $y$ -axis, it is difficult to find out the structure and the size of the CdS nanoparticles.

In order to find out the structure and the size of the clusters, higher resolution tapping mode of AFM measurements were carried out. The higher resolution AFM images of the same samples are presented in Figure 4.7 (imaged area of 400 x 400 nm) and Figure 4.8 (imaged area of 200 x 200 nm).



*Figure 4.3. AFM image of SA LB films before H<sub>2</sub>S treatment*



*Figure 4.4. AFM image of CdS nanoparticles in SA LB films*

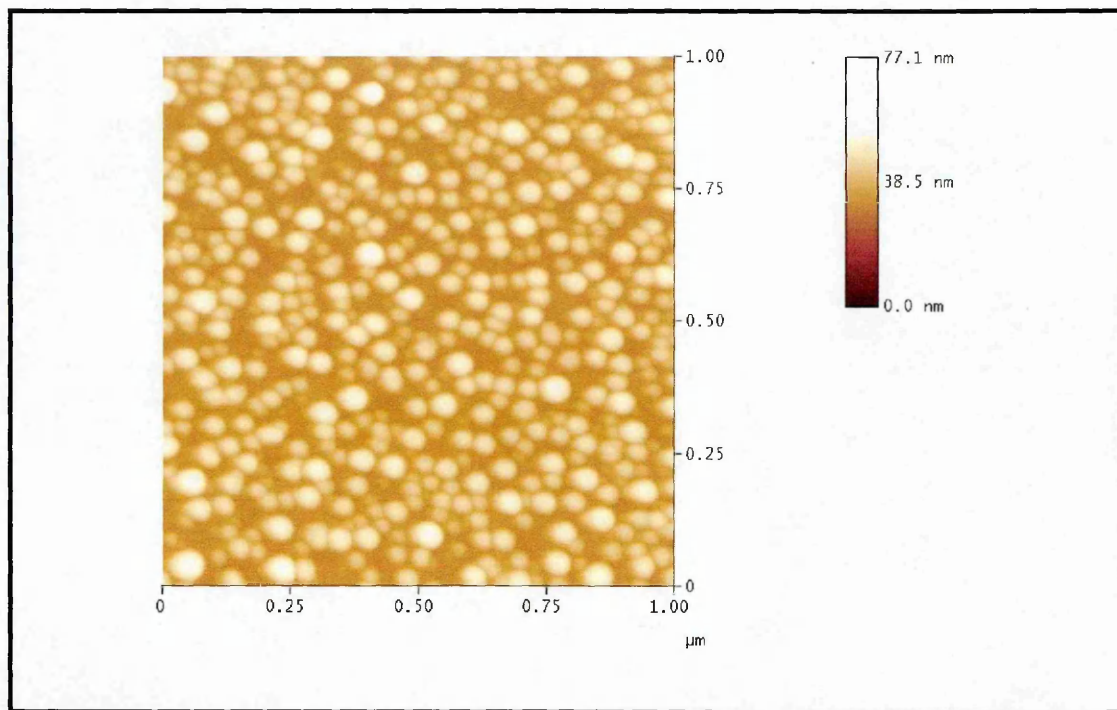


Figure 4.5. AFM image of Cd-salt SA LB films after  $H_2S$  treatment

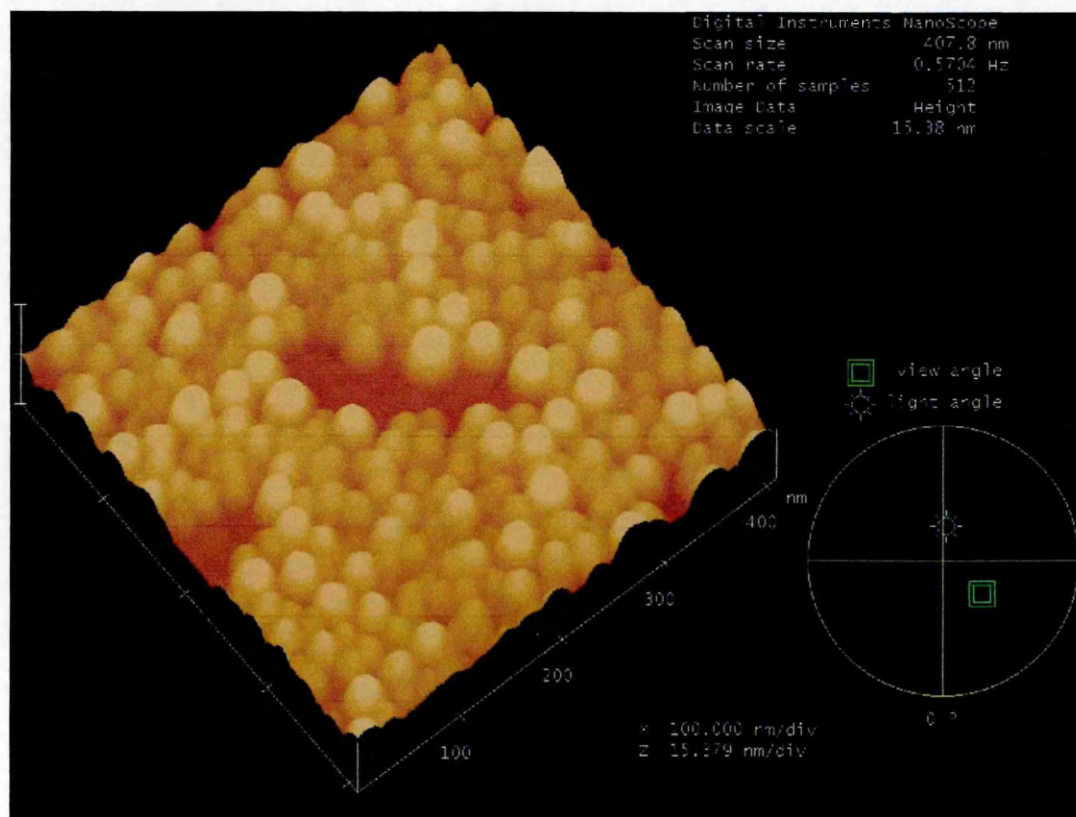


Figure 4.6. Three-dimensional AFM image of CdS nanoparticles in SA LB films

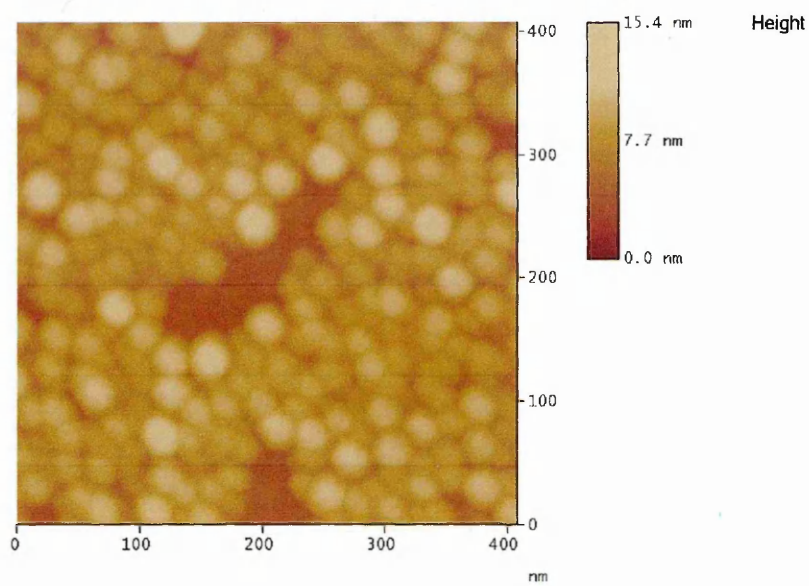


Figure 4.7. AFM image of CdS nanoparticles in SA LB films

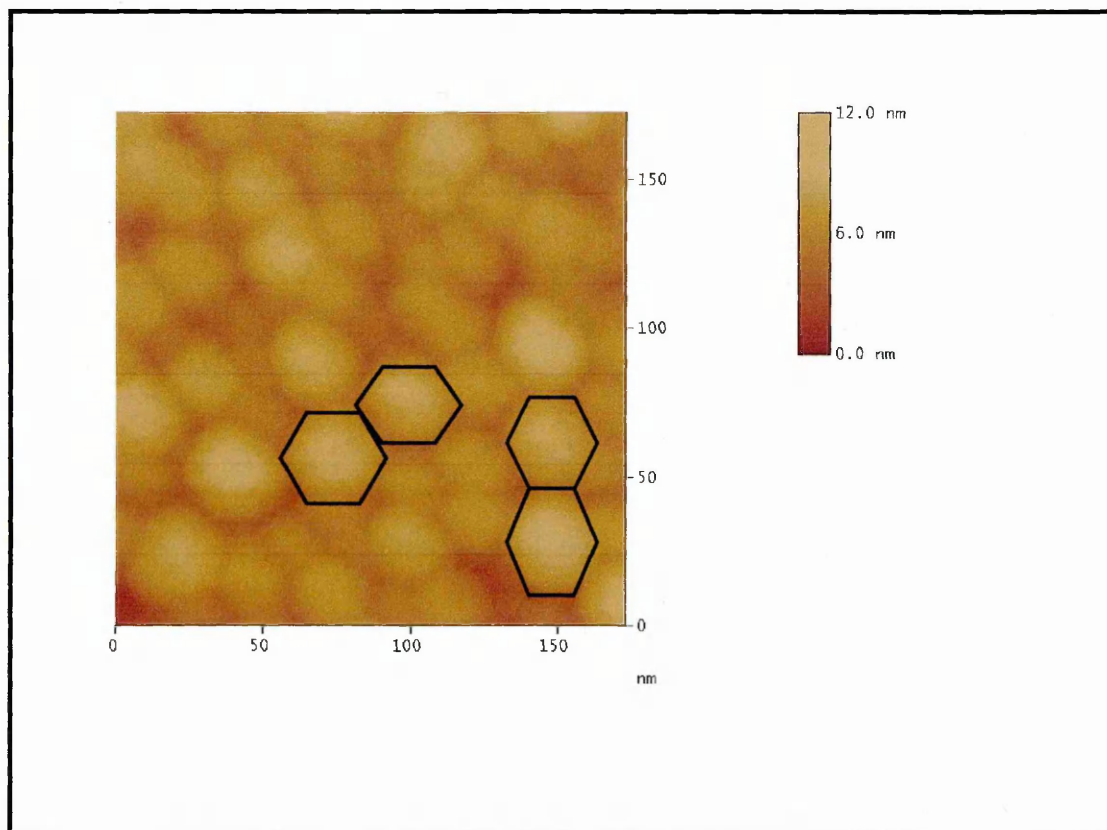


Figure 4.8. Small scale AFM image of CdS nanoparticles in SA LB films

As can be seen from figure 4.8, the CdS clusters are pseudo two-dimensional and have a shape of hexagonal platelets with the lateral dimensions of 20-30nm. Their thickness is predicted from optical study using UV-visible spectroscopy reported previously [Nabok et al, 1999] of about 2-3 nm. Similar optical study was also carried out in this thesis and will be described in details in the next chapter (Chapter 5). These clusters are faceted to an asymmetric hexagonal shape. Figure 4.9 presents a schematical hexagonal shape of the CdS nanoparticles formed in the stearic acid Cd-salt LB films.

CdS nanoclusters were also found in calix[8]arene (CA) Cd-salt LB bilayers as a result of H<sub>2</sub>S treatment. Figure 4.10 demonstrates an AFM image (1.00 x 1.00 μm) of CA LB films containing nanoclusters of CdS. A smaller scale with higher resolution AFM image of the same sample is presented in Figure 4.11.

The lateral dimensions of the CdS clusters in CA LB films were found to be about 10-15 nm. These dimensions are two times less than that of CdS nanoclusters formed in SA LB films. The vertical dimensions of the CdS nanoparticles of about 1-1.5 nm predicted from the previous results of Nabok et al [1999] were also smaller than that of SA film. Similar results were also obtained from the optical study, which will be given in details in Chapter 5.

An AFM image of calix[8]arene Cd-salt LB bilayers before H<sub>2</sub>S treatment does not show any features of the nanoclusters (see Figure 4.12). It is similar to that found previously in the AFM image of SA LB films before H<sub>2</sub>S treatment.

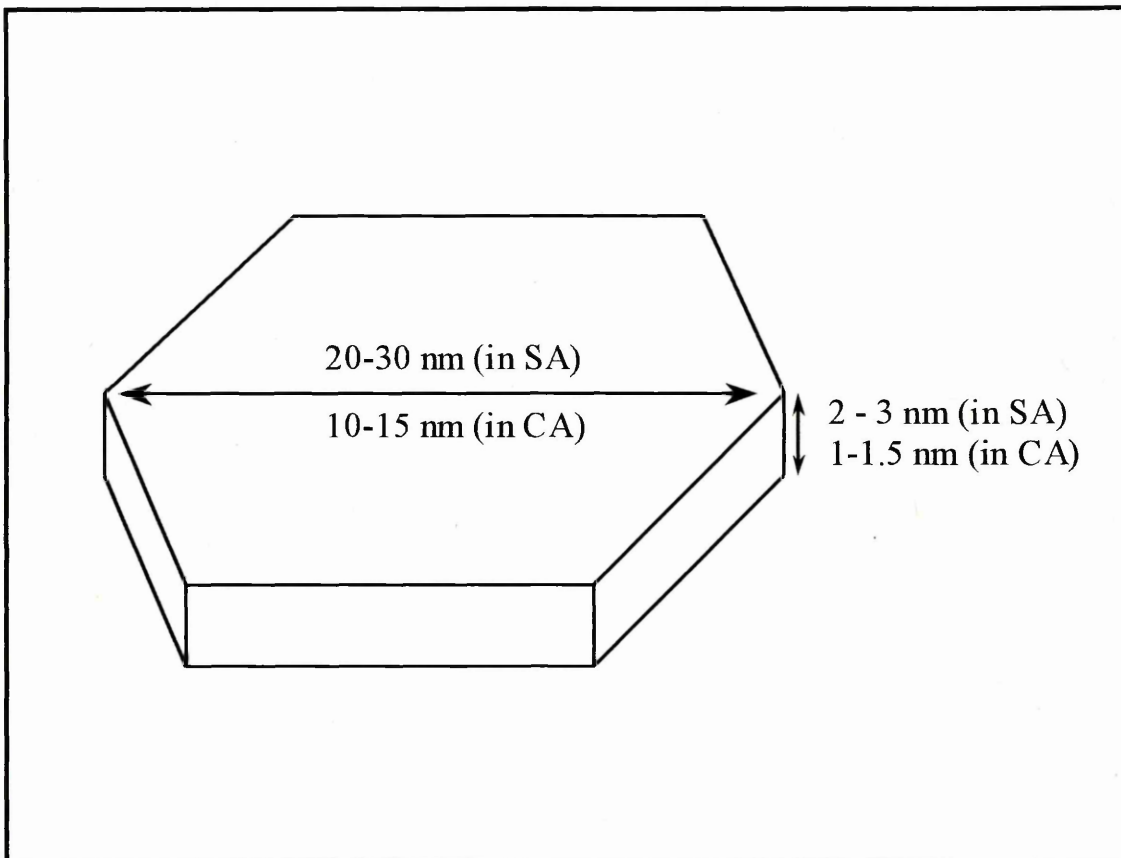


Figure 4.9. A schematical hexagonal shape of CdS nanoparticles in SA LB films

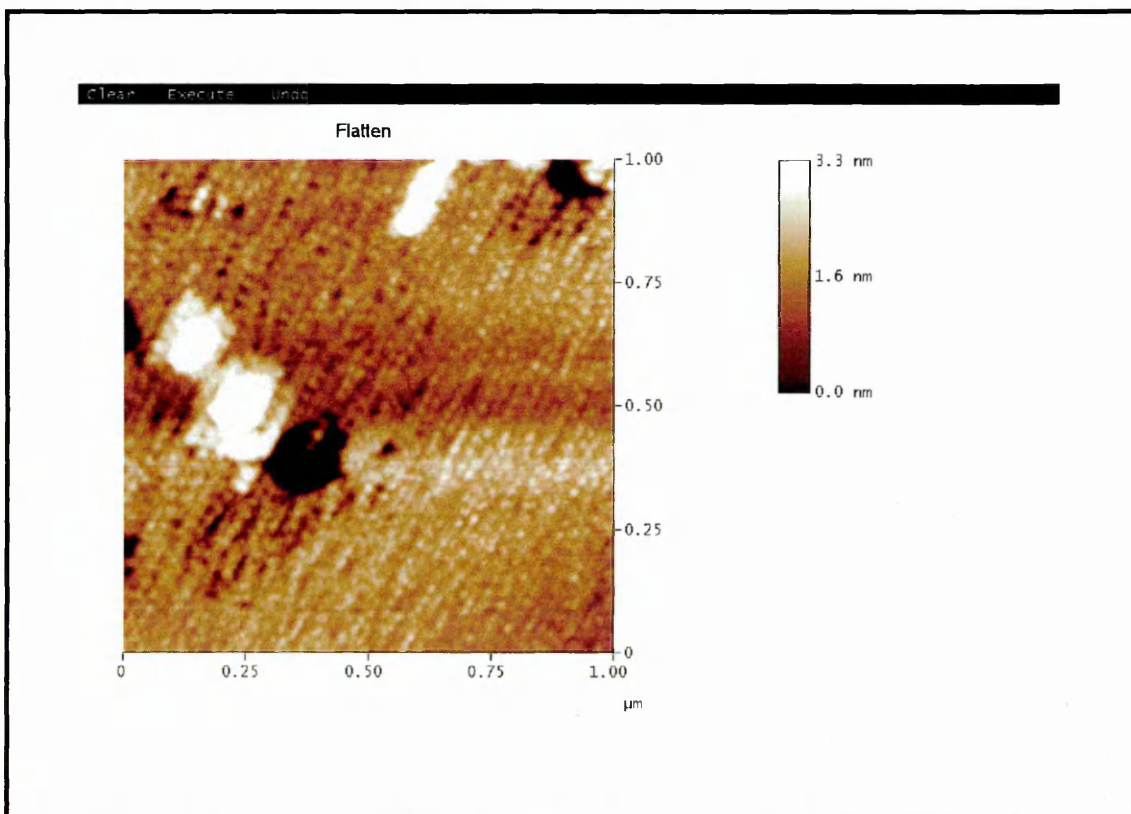


Figure 4.10. An AFM image ( $1.00 \times 1.00 \mu\text{m}$ ) of CA LB bilayers after  $\text{H}_2\text{S}$  treatment

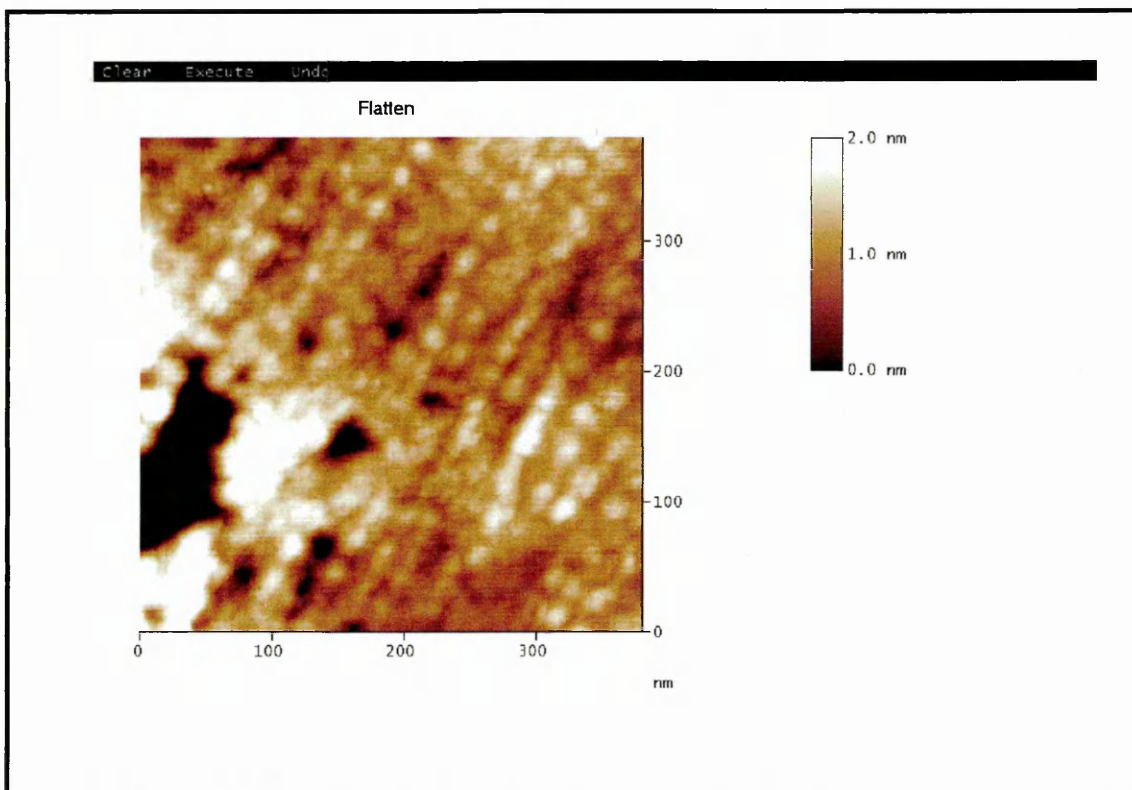


Figure 4.11. 400 x 400 nm scale of AFM image of CdS clusters in CA LB bilayers

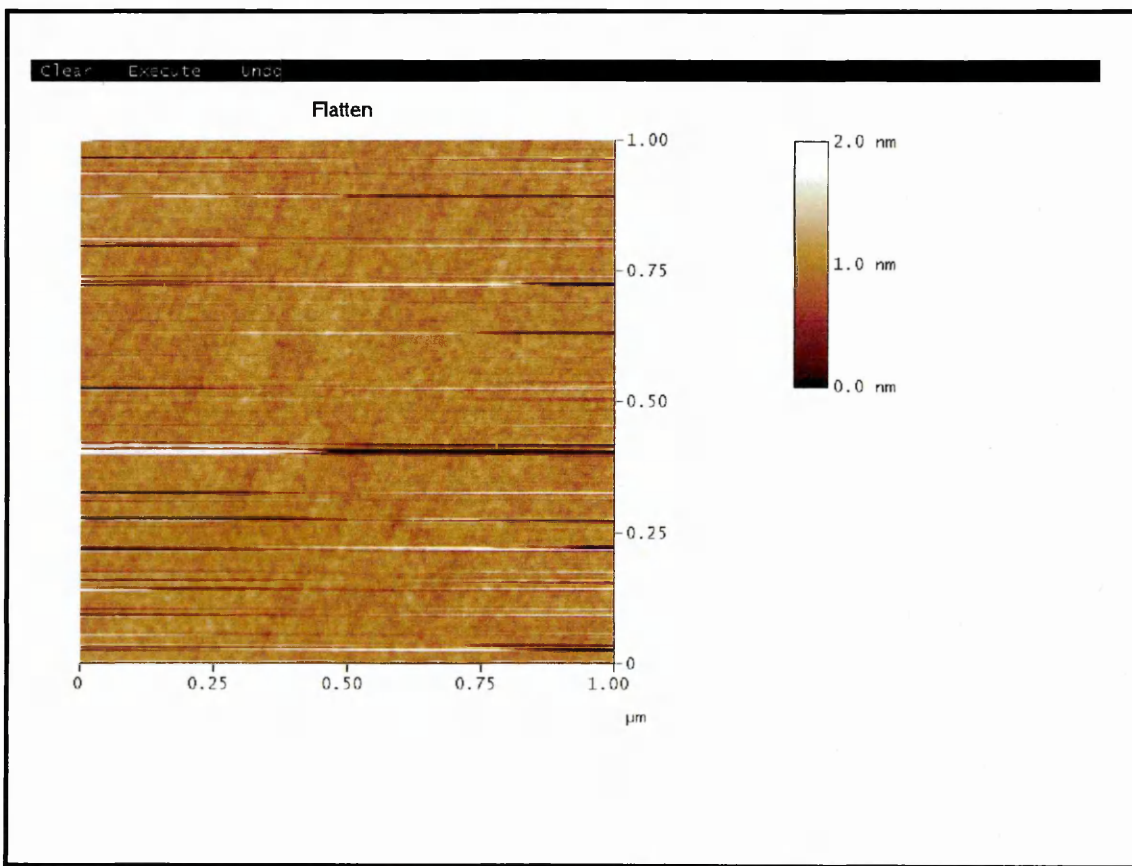


Figure 4.12. An AFM image (1.00 x 1.00 μm) of untreated CA LB bilayers

The current results of the AFM study (tapping mode) correspond well to previous AFM study of similar samples, which showed initially the regular structure of closely packed stearic acid molecules, which was distorted after exposure to H<sub>2</sub>S gas [Nabok et al, 1999]. Despite the large noise level in the previous AFM (contact mode) measurements on the samples containing CdS particles, the features of similar dimensions were reported. It should be emphasized that the size of 2 - 3 nm for CdS particles, obtained from UV-visible absorption spectroscopy measurements, is 10 times less than that from AFM study. The previous TEM study also showed particles with the size larger than 2 - 3 nm [Nabok et al, 2000]. This contradiction can be overcome now, and it is believed that CdS particles in stearic acid LB films are pseudo two-dimensional and have a shape of hexagonal platelets with the lateral dimensions of 20-30 nm and 2 - 3 nm in thickness. However, the real size of the CdS clusters could be smaller than that obtained from these AFM images. This is due to several reasons: the size of the AFM tip is about 4 nm in radius, which is bigger than the vertical dimension of the cluster, and the effect of the blanket of LB films that cover the CdS clusters. With the thickness of 5.03 nm and 3.54 nm reported previously [Nabok et al, 1998] for SA and CA LB bilayer, respectively, the LB films give a significant contribution to the size of the particles.

It looks like the size obtained from UV-visible spectra and photoluminescence measurements corresponds to the vertical dimensions of CdS nanoparticles. The thickness (vertical dimension) of the CdS nanoparticles will be investigated in more detail in Chapter 5. The hexagonal shape gives clear indication of wurtzite structure of CdS nanoparticles. Crystallographic lattice of the wurtzite CdS is schematically given in page 16 (Figure 2.5). This supports the suggestion of Ramakrishna [1993], Yoffe [1993] and Allais and Gandai [1992] that CdS lattice transform from cubic zinc-blende for bulk materials to wurtzite in nanoclusters.

## 4.5. Summary

The AFM measurements provide direct information on the existence of CdS nanoparticles in LB films and also allow the study of morphology of LB films at nanometer scale. AFM images of the cadmium stearate bilayer after the treatment with H<sub>2</sub>S gas demonstrate clusters with lateral dimensions in the range of 20 - 30 nm. These clusters are faceted to an asymmetric hexagonal shape. Similar but smaller CdS clusters of about 10 - 15 nm were found in calix[8]arene LB bilayers. The samples of both stearic acid and calix[8]arene Cd-salt LB films before H<sub>2</sub>S treatment did not show any features of these dimensions. It is believed that CdS nanoparticles in stearic acid LB films are pseudo two-dimensional and have a shape of hexagonal platelets with the lateral dimensions of 20 – 30 nm and 2 - 3 nm in thickness. Despite the AFM image of calixarene LB films containing CdS nanoparticles being not very clear, it is expected that the CdS nanoparticles in CA LB films are similar to those in SA LB films, pseudo two-dimensional hexagonal platelets. The lateral dimensions of the CdS particles in CA LB films are about 10 - 15 nm and 1 - 1.5 nm in thickness. The hexagonal shape found from the AFM images gives indication of wurtzite structure of CdS nanoparticles.

## **CHAPTER 5**

# **OPTICAL STUDY OF CADMIUM SULPHIDE (CdS) NANOPARTICLES FORMED WITHIN LANGMUIR-BLODGETT (LB) FILMS**

### **5.1. Introduction**

In this chapter, the optical study of cadmium sulphide (CdS) nanoparticles formed within Langmuir-Blodgett (LB) Films is given. The optical properties of the semiconductor nanostructures are very important and relate to their optoelectronic applications. Therefore, the knowledge of the information concerning the interaction of the light with the materials is essential. Useful optical properties can be gained from a variety of optical measurements, including UV-visible absorption and photoluminescence.

The observation of the blue spectral shift of the optical absorption edge for the nanoparticles in comparison with the respective bulk values is a typical experimental confirmation of nanoparticles presence. The particles' size can be evaluated from the position of the main absorption bands, however this requires subtraction of the experimental spectra measured on the same samples before and after exposure to H<sub>2</sub>S gas. This is particularly important for CA LB film matrix, which is a light-absorbing substance itself. However, the validity of the employed spectra analysis should be confirmed independently. Photoluminescence emission (PL) and photoluminescence

excitation (PLE) spectral measurements are undertaken in this work to provide direct information on the spectral changes due to CdS nanoparticles formation.

Ageing effect (transformation) of CdS nanoparticles formed in LB films is important to study, because the particles “grow” in the matrix materials. This effect cannot be explained simply in terms of quantum confinement. Transformations in the size of CdS nanoparticles are studied by applying UV-visible spectroscopy. In order to explain the observed behaviour, the Lifshitz-Slezov diffusion model is generalized for the two-dimensional (2D) case. A model for the formation and further transformations (ageing effect) of CdS nanoparticles in different LB films is also developed.

In Section 5.2, theoretical background of the techniques used to investigate the samples is described. Section 5.3 presents a review of previous study on this subject. Details of experimental techniques used in this chapter are given in Section 5.4. Section 5.5 presents results of the measurements together with their analysis and discussion. A summary of this present chapter is given in Section 5.6.

## 5.2. Theoretical Background

Many molecules absorb ultraviolet or visible light. The intensity of light passing an absorption material is reduced according to Beer's law:

$$I = I_0 e^{-\alpha d} \quad (5.1)$$

where  $I$  is the measured intensity after passing through the material,  $I_0$  is the initial intensity,  $\alpha$  is the absorption coefficient and  $d$  is the thickness of the material. If the light reflection ( $R$ ) is taken into account, Equation (5.1) would be rewritten:

$$\frac{I}{I_0} = (1 - R^2) e^{-\alpha d} \quad (5.2)$$

where  $R$  is the reflectance. At normal incidence of the light and transparent media,  $R$  usually does not exceed 1% and can be neglected. Absorption coefficient ( $\alpha$ ) can be obtained from the absorbance value,  $A$ :

$$\alpha = \frac{2.303A}{d} \quad [\text{cm}^{-1}] \quad (5.3)$$

and an extinction coefficient ( $k$ ), which is an imaginary part of the complex refractive index ( $N = n - ik$ ) can be obtained:

$$k = \frac{\alpha \lambda}{4\pi} \quad (5.4)$$

where  $\lambda$  is the wavelength of the light. Absorption coefficient  $\alpha$ , and thus  $k$ , has dispersion, i.e. depend on the wavelength of the light. The dispersion of optical parameters is the characteristic of the media, and in the case of thin organic films depends on molecular spectra. Molecular spectra consist of several spectral lines (bands) corresponding to electron transitions between the occupied and unoccupied

electron levels of molecules. Position, intensity and half-width of the band also depend on the structure of the molecular crystal. Therefore, UV-Visible spectra provide information about chemical contents and the structure of thin film.

A molecule in its ground state of electronic energy level can absorb a photon of light if the photon energy is equal to the difference between the two energy levels in the system. The molecule is then excited into a higher energy state so that

$$E_1 - E_0 = h\nu \quad (5.5)$$

where  $h$  is Plank's constant ( $6.626 \times 10^{-34}$  Js),  $\nu$  is the frequency of the radiation in Hz, and  $E_1$  and  $E_0$  are the excited and ground states of the molecule, respectively. The minimum photon energy required for absorption will be when  $E_0$  corresponds to the highest occupied molecular orbital and  $E_1$  to the lowest unoccupied molecular orbital.

Ultraviolet and visible (UV-Vis) absorption spectroscopy is the measurement of the attenuation of a beam of light after it passes through a sample or after reflection from a sample surface. The absorption measurements can be performed at a single wavelength or over an extended spectral range. Ultraviolet and visible lights are energetic enough to excite outer electrons to higher energy levels. The type of excitation depends on the wavelength of the light. Electrons are excited to higher orbitals by UV-Vis light, vibrations are excited by infrared light and microwaves excite rotations. In a molecule, the atoms can rotate and vibrate with respect to each other.

In case of the absorption process, a photon of certain energy excites an electron from a lower to higher energy state. By studying the changes in the transmitted radiation, one can discover the possible transitions of an electron, including band-to-band, excitons, subbands, between impurities, free carriers within a band, and also the resonances due to vibrational states of the lattice and of the impurities [Pankove, 1971].

The fundamental absorption referring band-to-band or exciton transition can be used to determine the energy gap of the semiconductor. However, the estimation of the energy gap from “absorption edge” is not a straightforward process, since the transitions are subject to certain selection rules. The absorption transitions take place between two direct valleys where all the momentum-conserving transitions are allowed (as described early in Chapter 2). Every initial state at  $E_i$  is associated with a final state at  $E_f$  such that

$$E_f = h\nu - |E_i| \quad (5.6)$$

In some materials, quantum selection rules forbid direct transitions without a change in momentum. Momentum is conserved via a phonon (a quantum of lattice vibration) interaction. Only phonons with the required momentum change are usable, although a broad spectrum of phonons is available.

The formation of excitons usually appears as narrow peaks in the absorption edge of direct-gap semiconductors, or as steps in the absorption edge of indirect-gap semiconductors. In direct-gap materials, the free exciton occurs when the photon energy is  $h\nu = E_g - E_x$  ( $E_x$  is the binding energy of the exciton). Excitons can also be created by higher-energy photons, since they can be created with some kinetic energy. In indirect-gap materials, phonon participation is needed to conserve momentum. Therefore, an increase in absorption coefficient is obtained at

$$h\nu = E_g - E_p - E_x, \text{ for the transition with phonon absorption}$$

$$h\nu = E_g + E_p - E_x, \text{ for the transition with phonon emission}$$

The transition between a neutral donor and the conduction band or between the valence band and the neutral acceptor (Figure 5.1a and b) can occur by the absorption of a low energy photon [Pankove, 1971]. In this case, the energy of the photon must be at

least equal to the ionization energy  $E_i$  of the impurity. The transition between the valence band and an ionized donor or between an ionized acceptor and the conduction band occurs at photon energies given by  $h\nu > E_g - E_i$  (Figure 5.1c and d).

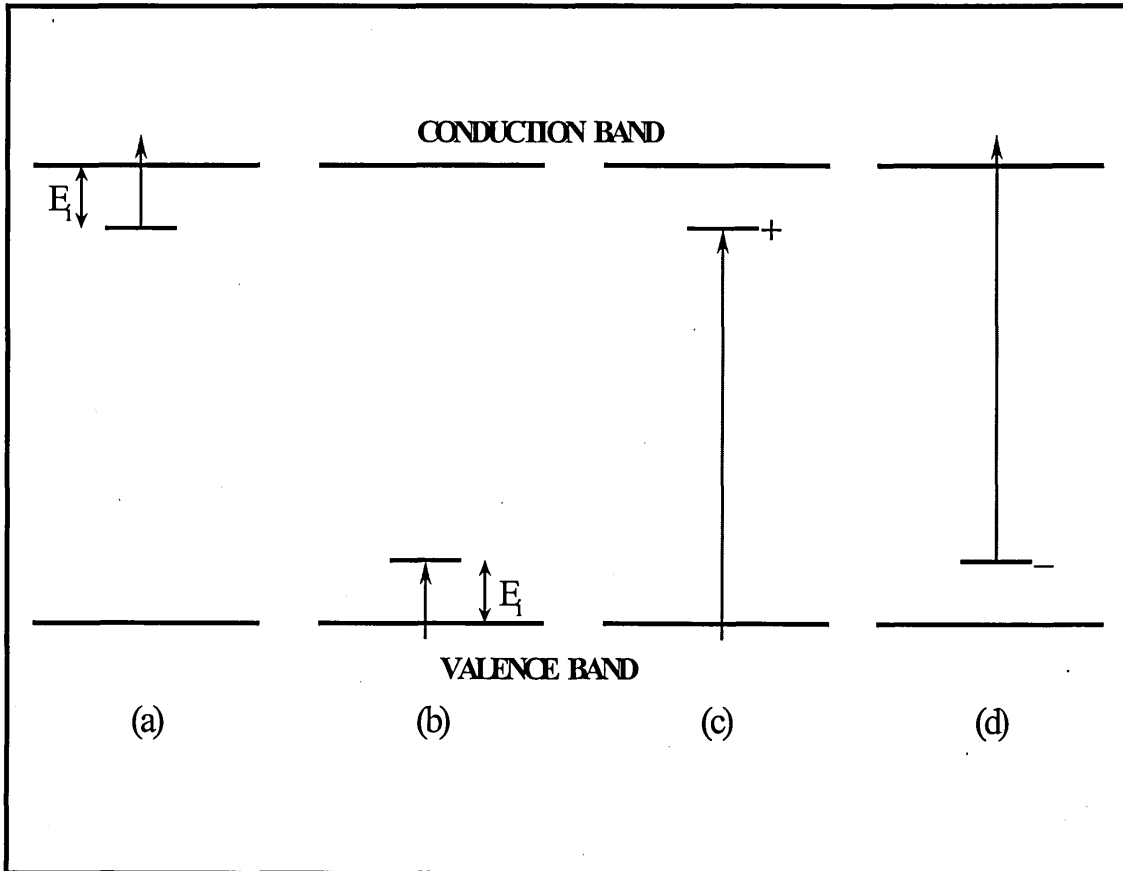


Figure 5.1. Absorption transitions between impurities and bands: (a) donor to conduction band; (b) valence band to acceptor; (c) valence band to donor; and (d) acceptor to conduction band [after Pankove, 1971].

Emission process is the inverse of the absorption. An electron occupying a higher energy state than that at equilibrium condition makes a transition to an empty lower-energy state and all or most of the energy difference between the two states can be emitted as electromagnetic radiation, which is usually described by the general term of luminescence. The rate of the radiation is determined by

$$R = n_u n_l P_{ul} \quad (5.7)$$

where  $n_u$  is the density of carriers in the upper state,  $n_l$  is the density of empty lower state carriers, and  $P_{ul}$  is the probability for 1 carrier/cm<sup>3</sup> in the upper state to make a radiation to 1 vacancy/cm<sup>3</sup> in the lower state. This expression is somewhat similar to that for the absorption process. However, emission is expressed as a rate of photon generation per unit volume, whereas absorption was described in terms of the mean free path for photon decay.

Most of the transitions that may occur in absorption mechanisms can also happen in the opposite direction and produce a characteristic emission. The important difference between the information, which can be obtained by absorption and by emission in a semiconductor, is the absorption process involving all the states in the semiconductors. This results in a broad spectrum whereas the emission process couples narrow band states, and thus produce a narrow spectrum.

Emission light (generally called luminescence) can be given off by the materials when carriers are excited into higher impurity levels from which they fall to their equilibrium states. These excited carriers are produced by different mechanisms: photon absorption (optical excitation), current introduction and high-energy electron bombardment. If carriers are excited by high-energy electron bombardment, the radiation resulting from the recombination of the excited carriers is called

cathodoluminescence. Excitation by electric current results in electroluminescence. When carriers are created by photon absorption, the mechanism is called photoluminescence. The latter method is used in this current work.

Photoluminescence method provides a non-destructive technique for the analysis of optical properties of semiconductors. This technique monitors an optical transition from an excited electronic state to a lower state, usually the ground state. Because of rapid relaxation ( $\sim 1$  ps) compared to the recombination lifetime ( $\sim 1$  ns), only transition from the lowest excited state can generally be detected if there is multiplicity of excited states.

When a semiconductor is excited with a light source emitting photons of energy greater than the band gap of material under investigation, the material absorbs the light, creating electron-hole pairs in the sample. These photoexcited carriers then relax to their band edges and excitons may form. Finally, recombination of the carriers now occurs via either radiative or non-radiative processes. It is the radiative recombination events that are recorded in a photoluminescence experiment with the emitted photons analysed by a suitable spectrometer and detector. The emitted photons' energy provides information about the band gap of the material. This energy can be modified by potential fluctuations of the band edges or the influence of impurities, both leading to a photon energy which is less than true band gap of the material [Dean, 1982].

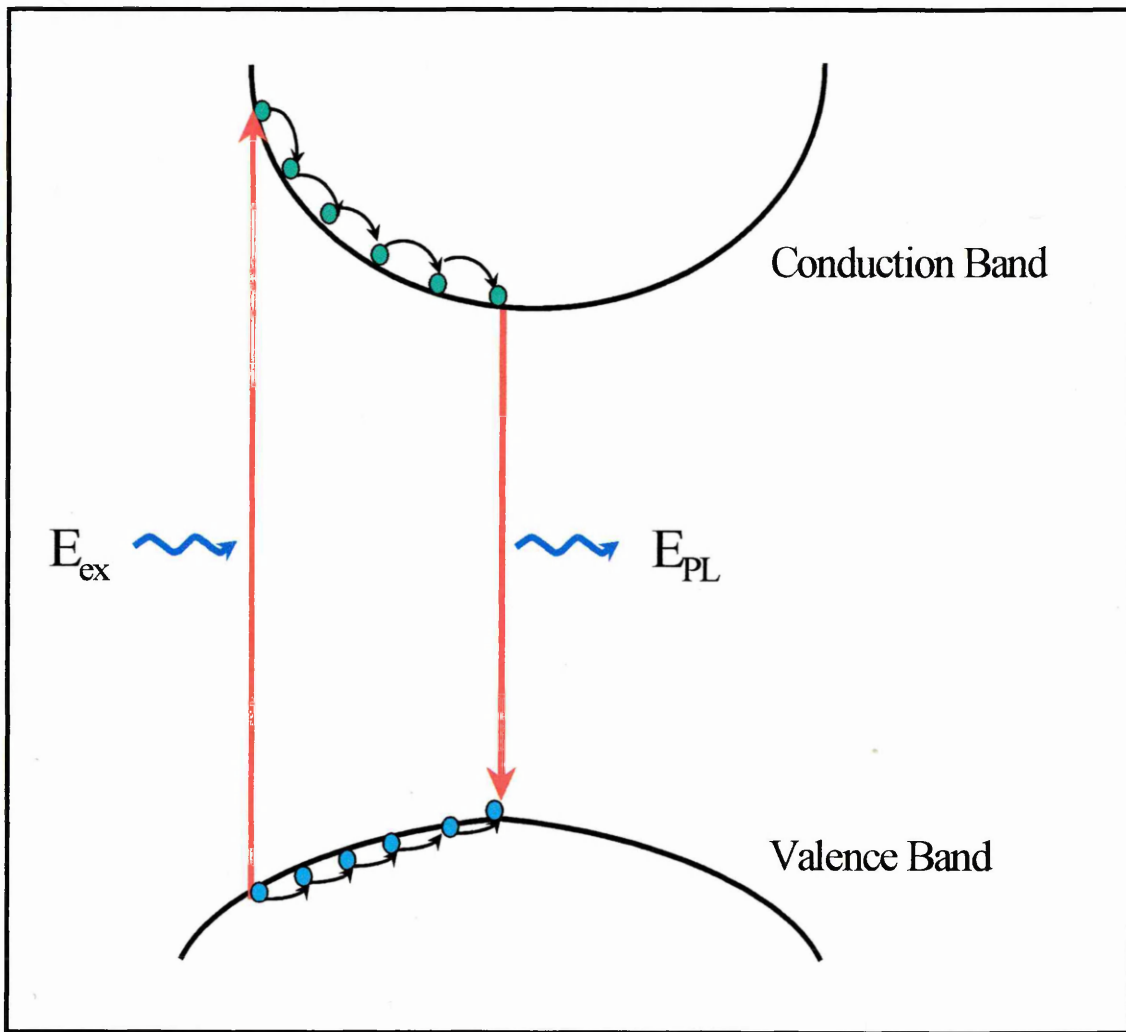


Figure 5.2. A Schematic diagram of the photoluminescence process in a semiconductor [after Dean, 1982]

There are several transitions, which occur at or near the band edges, including exciton recombination, band-to-band transitions, band-to-impurity level transitions and donor-acceptor transitions. A narrow spectral line is usually emitted from the recombination of excitons in a pure material. The energy of the emitted photon for a direct semiconductor, where momentum is conserved in a simple radiative transition (Figure 5.3a) is given by a simple expression:

$$h\nu = E_g - E_x \quad (5.8)$$

where  $E_g$  is the energy gap of the material and  $E_x$  is the exciton energy. In an indirect-gap semiconductor, where momentum conservation requires that a phonon be emitted to complete the transition (see Figure 5.3b), the energy of the emitted photon is [Aven and Prener, 1967]

$$h\nu = E_g - E_x - mE_p \quad (5.9)$$

where  $E_p$  is the energy of the phonon involved and  $m$  is the number of optical phonons emitted per transition.

A direct transition can also occur with emission of one or more optical phonons (Figure 5.4), although the transition with phonon emission is less probable than the direct recombination. The resulting phonon has a greater chance of escape because it occurs at a lower photon energy than the direct recombination.

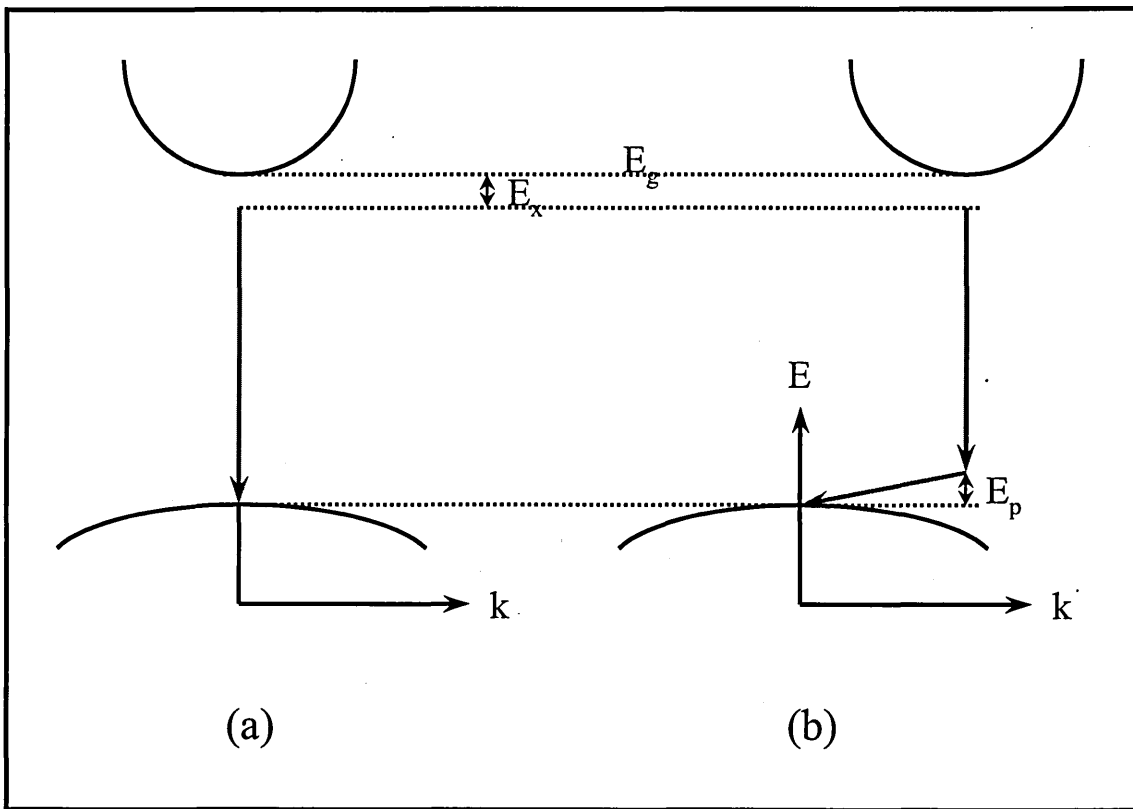


Figure 5.3. Exciton recombination: (a) direct, (b) indirect

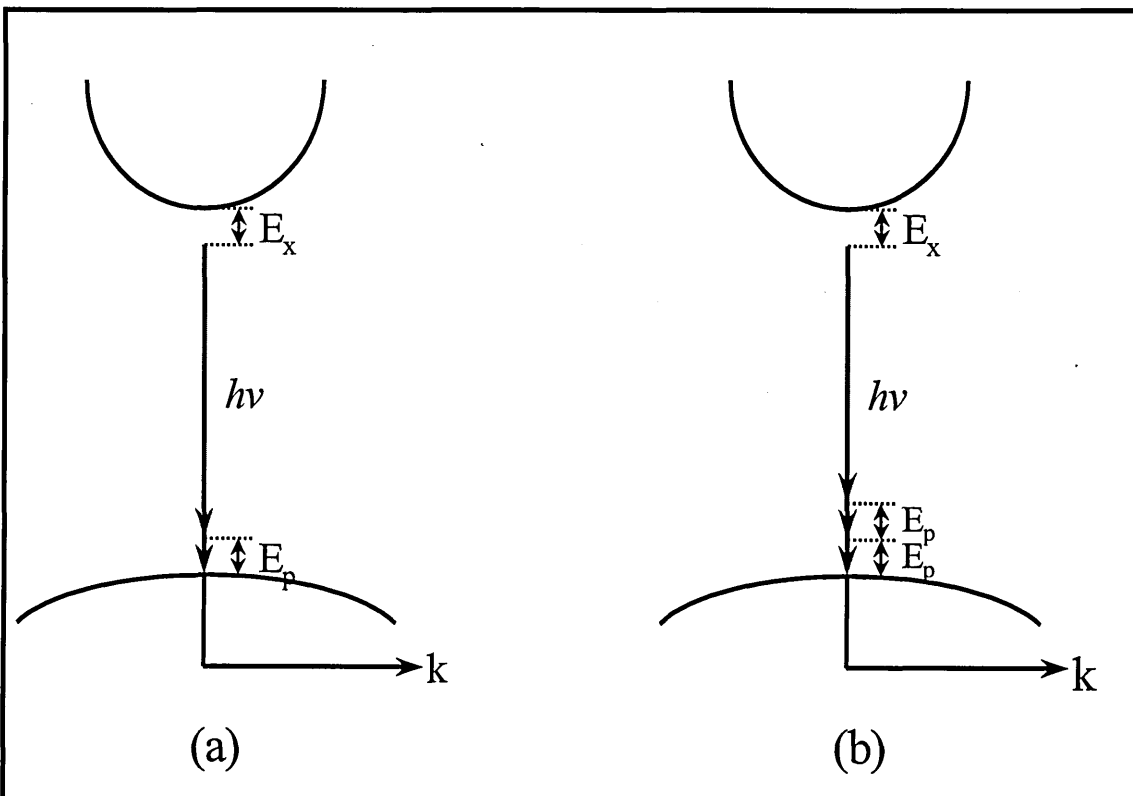


Figure 5.4. Direct exciton recombination with (a) one optical phonon emission, (b) two optical phonon emission [after Pankove, 1971]

Because free excitons are able to move through the crystal, they may be produced in one part of a crystal and can be detected in another region of the semiconductor. Excitons may have a short lifetime (e.g.  $10^{-8}$  s in CdS), at the end of which they become a photon. The photon, having a short distance propagation through the crystal, can generate another exciton. This resonant interaction can transport energy. The migration of excitons can be detected by the light emitted when the exciton recombines radiatively. When free excitons are formed, they can thermalize along the parabolic portion of the dispersion curve toward the knee of the curve, emitting acoustical phonons. They can also emit optical phonons, in such case the exciton transforms into a photon (below the knee of the curve) and can either propagate through the crystal or be emitted. Hence luminescence is obtained when it is scattered by an optical phonon.

In general, a fraction of the excited excitons remain as free carriers occupying band states. At a temperature such that  $kT > E_x$ , local fields tend to break up the exciton into free carriers. The free excitons may then recombine radiatively in a band-to-band transition (Figure 5.5). As the excitation rate and the temperature increase, states deeper in band become filled, permitting emission at higher photon energies. Therefore, free carriers recombination is characterised by a temperature-dependent high-energy, while the low-energy edge is abruptly cut off at  $h\nu = E_g$ .

Deep transitions (band-to-impurity level transitions) represent either the transition of an electron from the conduction band to an acceptor state or a transition from a donor state to the valence band (Figure 5.6a). These transitions emit a photon  $h\nu = E_g - E_i$  for direct transitions. In most direct-gap semiconductors, the electron effective mass is smaller than the hole effective mass. Therefore, the donor ionisation energy  $E_D$

is lower than the acceptor ionisation energy  $E_A$ . Hence the deep transitions can be distinguished as

- (1) Conduction band-to-acceptor transition producing an emission peak at  $h\nu = E_g - E_A$
- (2) Donor-to-valence band transition, which produces an emission peak at the higher photon energy  $h\nu = E_g - E_D$

Figure 5.6b illustrates donor-to-acceptor transitions. When donor and acceptor impurities are present in a semiconductor, coulomb interaction between donor and acceptor modifies the binding energies. The energy separating the donor-acceptor pair states is given by [Pankove, 1971]

$$h\nu = E_g - E_A - E_D + \frac{q^2}{\epsilon r} \quad (5.10)$$

where  $r$  is the donor-acceptor separation. For distant pairs the coulomb interaction term is very small and the lowest possible photon energy is obtained. In the case of the distance separating the impurities greater than the effective Bohr radius, the transition is assisted by a tunneling process.

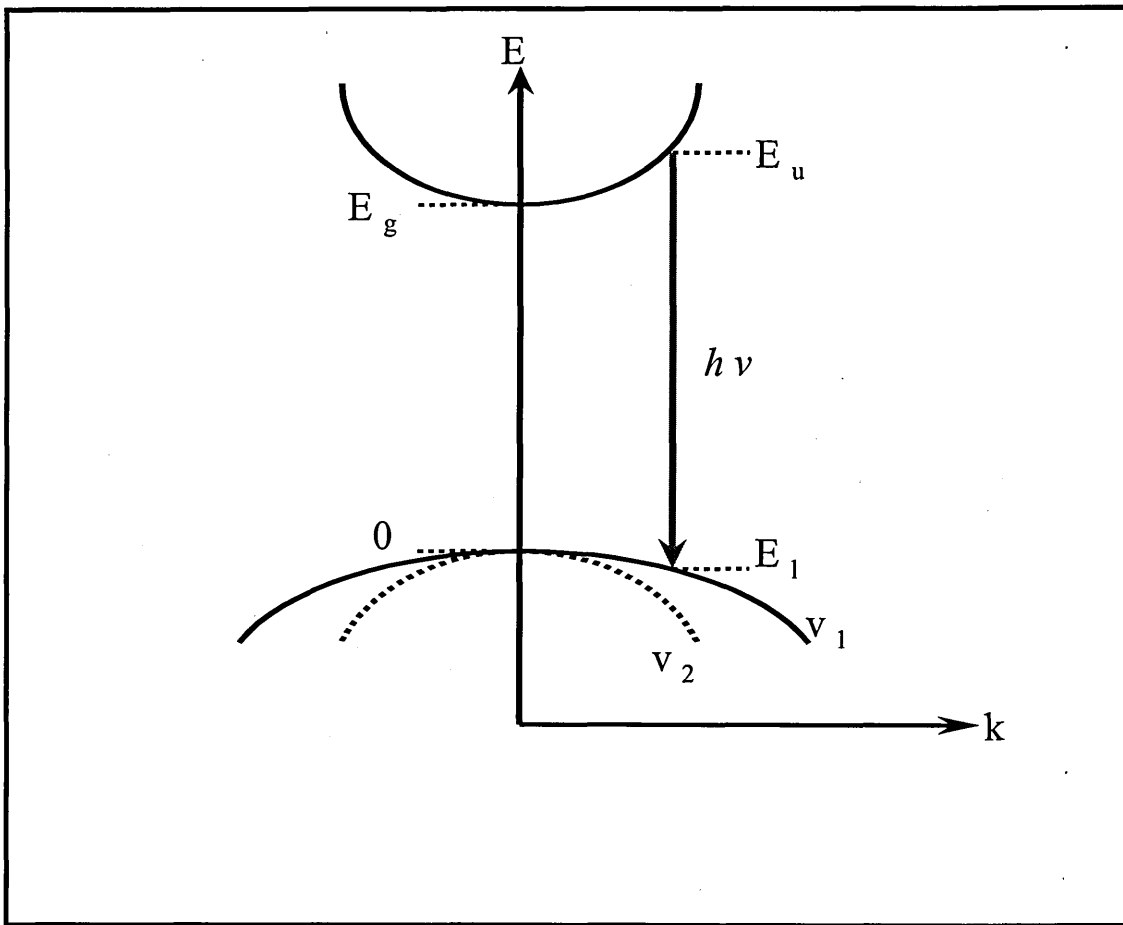


Figure 5.5. Direct band-to-band radiative transition [after Pankove, 1971]

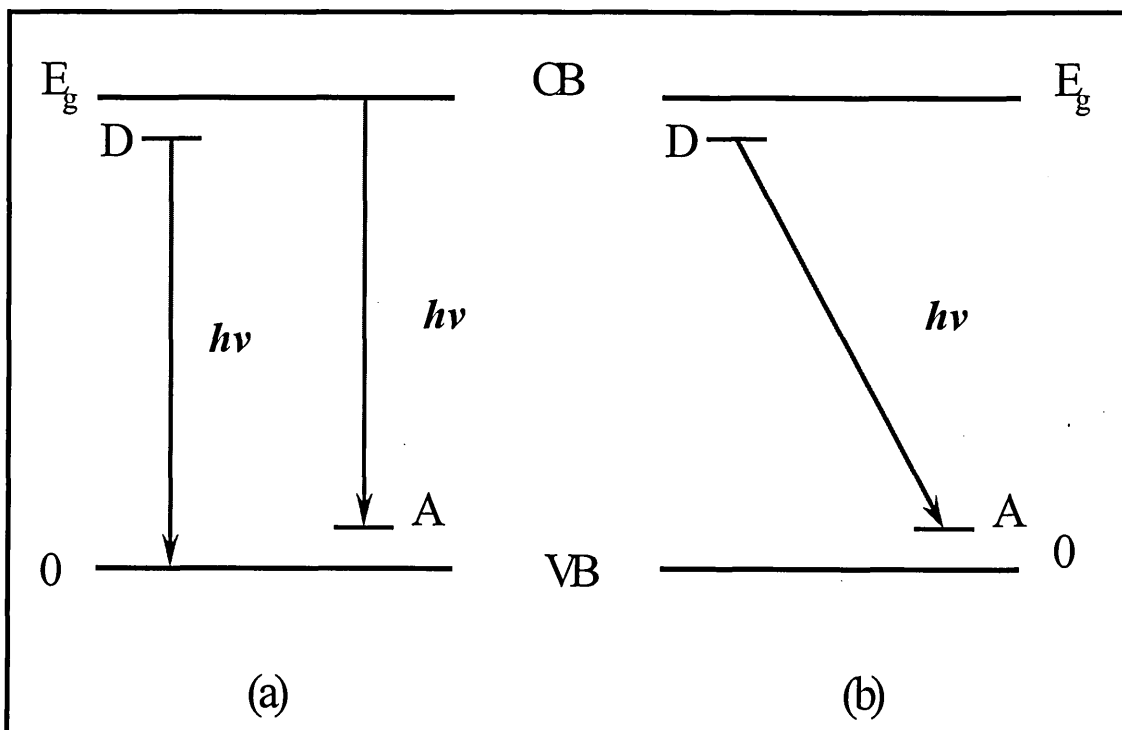


Figure 5.6. Deep transitions: (a) band-to-impurity transitions and (b) donor-to-acceptor transition

### 5.3. Review of Previous Work on Optical Study of II-VI Semiconductor Quantum Structures

The optical transitions appropriate to wurtzite CdS was shown in Figure 2.8 (Chapter 2) represented on the simple energy level diagram corresponding to the band extrema at  $\Gamma$  ( $k=0$ ) [Ray, 1969]. There will be variations for the other II-VI semiconductors owing mainly to different spin-orbit splitting energies. Mikhailov et al [1990] gave the variation of the  $n = 1, 2$  exciton A, series with thickness  $L_z$  for CdSe platelets. A similar linear dependence of the transition energies with  $1/L_z^2$  was found for both ground exciton states ( $n = 1$ ) and first excited exciton state ( $n = 2$ ). This gives shifting the energy gap as  $\Delta E_g \propto 1/L_z^2$ . They believe that the Coulomb term  $E_b$  between electron and holes is not the variable because the thicknesses of the CdSe crystal are large,  $L_x > a_B$  ( $0.25 - 0.1 \mu\text{m}$ ).

For two-dimensional (2D) semiconductors, such as quantum wells, the 2D confinement of an exciton leads to a decrease in the exciton Bohr radius, and an increase in exciton binding energy [Yoffe, 1993]. D'Andrea and Del Sole [1990] who consider films with  $L_z > 2.5 a_B$  argued for the presence of a thin transition layer near the surfaces, which are roughly equal to the exciton radius. Reasonably reliable results for CdS with  $L_z \geq 2.5 a_B$ , with  $a_B \approx 3.2 \text{nm}$ , are obtained using the theory involving a complex derivation applying variational exciton wavefunctions for the two lowest states of excitons in thin slabs. For  $L_z \geq 16 a_B$ , the exciton energies are given by [Yoffe, 1993]

$$E_n = -E_b + \frac{n^2 \hbar^2 \pi^2}{2M(L_z - 2d)^2} \quad (5.11)$$

where  $M = m_e^* + m_h^*$  (the exciton centre of mass). This expression can be used with reasonable accuracy down to thickness  $L_z \approx 20 \text{nm}$ , giving  $E_2 - E_1$ , for  $n_2$  and  $n_1$  exciton

levels, as 6 meV. This is in good agreement with calculation results using the other approaches, which give a value of 5 meV [Yoffe, 1993].

Babaev et al [1983, 1984] and Pokatilov et al [1990] studied thin single-crystal films of CdTe with cubic structure. This compound is a direct bandgap semiconductor with band gap energy ( $E_g$ ) in the region of 1.6 eV,  $E_b \approx 10$  meV and  $a_B \approx 70$  Å. The blue shift of excitonic features due to size quantization was obtained as the film thickness was decreased to 10 nm.

For the film thickness below 10 nm ( $L_z \approx a_B$ ), the energy bands are no longer concerned and size-quantized discrete subbands (levels) replace them. The energy shift of optical features as a function of film thickness  $L_z$  is now given by [Yoffe, 1993]

$$E_n - E_b = -\Delta E_n = \frac{\pi^2 \hbar^2}{2\mu L_z^2} n^2, \quad n = 1, 2, 3 \quad (5.12)$$

In case of  $L_z < a_B$ , it is important to consider the field produced by the charges in the surrounding medium having dielectric constant  $\epsilon_1$  if  $\epsilon_2 > \epsilon_1$ . The Coulomb interaction between electron and hole, and the binding energy for the ground state of exciton can be larger than  $E_b(n=1) = \frac{\mu e^4}{2\epsilon_2^2 \hbar^2}$ , and the exciton radius can also be different [Shinada and Sugano, 1966]. Keldysh [1979], Andryushin and Silin [1980] and Hanamura et al [1988] estimated the values for the effective radius  $a$  and the binding energy  $E_n$  for hydrogenic-type states of excitons as a function of film thickness.

Allais and Gandai [1992] studied the cluster shape by using transmission electron microscopy (TEM). They reported that, the II-VI semiconductor clusters having wurtzite structures, the shape is close to spherical or have a structure close to hexagonal

wurtzite for sizes of order of 10 nm or less. For clusters having sizes above 10 nm, the shape adopts a prismatic habit, and the clusters tend to grow longer in the c direction.

The behaviour of the cluster systems of CdSe with  $R \approx 1.6$  nm and  $R < a_B$  was studied by Borrelli et al [1987]. The absorption feature is due to electron-hole pairs created by optical transitions between quantum-confined subband states. Little dissociation to free electrons and holes was found as the temperature was increased. There was also obtained a very little temperature dependence of the features, in contrast with the situation for excitons.

### **5.3.1. Dark Excitons in II-VI Semiconductor Quantum Dots (QDs)**

The dark exciton was first reported by Smotkin [1988]. Later Efros et al [1991] also obtained this dark exciton when studying prolate shape quantum dots having a hexagonal wurtzite structure. The dark excitons form following excitation to high energy fine structure states that rapidly thermalize to the lowest excited or exciton e-h ground state as shown in Figure 5.7. This type of exciton is optically passive, dark. The evidence of this dark exciton state can be found in photoluminescence (PL) spectra. The other facts supporting this type of exciton come from the manner in which the dark exciton varies with the application of a magnetic field [Nirmal et al, 1996].

The dark exciton state is usually an optical forbidden transition [Yoffe, 2001]. These electron transitions having angular momentum projection of  $F = \pm 2$ . One of the ways for the wurtzite II-VI quantum dots to allow the parity forbidden transition to take place, is by the formation of an internal electric field in the QDs. In good small platelets of such materials, the top and bottom faces of the platelets consist of ions having

opposite charges, i.e  $\text{Cd}^{2+}$  and  $\text{S}^{2-}$ . This charge separation results in the existence of an internal electric field, whose value depends on the thickness of the platelet. This phenomenon was obtained experimentally by Chadderton et al [1964]. These electric fields are also thought to be present in small spherical QDs, due to the presence of facets on the surface. These aspects have also been studied by Colvin and Alivisatos [1992]. They obtained evidence for the presence of a dipole moment for the first excited state of the CdSe QDs. The formation of "dark excitons" leads to a larger Stokes shift in the range of 100 meV [Yoffe, 2001].

### **5.3.2. Optical Properties of CdS Particles in LB Films**

UV-visible absorption spectra have been used by Nabok et al [1997] to confirm the presence of much smaller CdS nanoparticles inside the LB films of calixarene compared to those formed in Cd-salts stearate LB films and other fatty acid LB films. The levels of size quantisation were clearly resolved on the absorption spectra even at room temperature. The absorption edge of calixarene LB films was about 3.3 eV, while a lower absorption edge value of about 2.7 eV was found for the Cd-salts stearate films. The size of the CdS particles in LB films of calixarene and stearic acid was estimated from the position of absorption bands to be  $1.5 \pm 0.3$  nm and 3.3 nm, respectively. However, The size of CdS particles formed in CA LB films estimated from the position of the absorption edge was about 1.8 nm. It was shown that the particle size did not depend on the number of LB layers or on the dimensions of the calixarene but increased with increasing pH of the subphase [Nabok, 1997].

In order to derive the size of the CdS nanoparticles formed in the LB films of Cd-salts calixarene and stearic acid, Nabok et al [1998] performed further analysis of UV-visible absorption spectra. The absorption spectra of CdS formed in the calixarene

LB films represented three clearly resolved absorption bands near the absorption edge. It was suggested that these bands are related to electron transitions between levels of size-quantization. However, Ekimov et al [1985] reported that such quantum behaviour was usually observed only at low temperature. To derive the size distribution of CdS nanoparticles in LB films of calixarene, the experimental absorption spectra were decomposed into three Gaussian bands. The size distribution of CdS clusters in CA LB films can be described well by a simple Gaussian error function. The size of the CdS clusters and their dispersion were found to be  $1.43 \pm 0.28$  nm and  $1.47 \pm 0.28$  nm, respectively for calix[4]arene and calix[8]arene LB films. The presence of very small CdS particles in Cd-salts calixarene LB films did not affect their layer-by-layer film order. This fact was confirmed by small angle X-ray diffraction and ellipsometry measurements performed on the samples. While, formation of larger CdS particles in Cd-salts stearate LB films nearly destroyed their periodicity. Much smaller CdS clusters formed in CA LB films as compared to those in fatty acid LB films were believed to be as a result of restriction of 2D aggregation of CdS within bilayers of the LB films caused by some CdS molecules being captured in calixarene cavities.

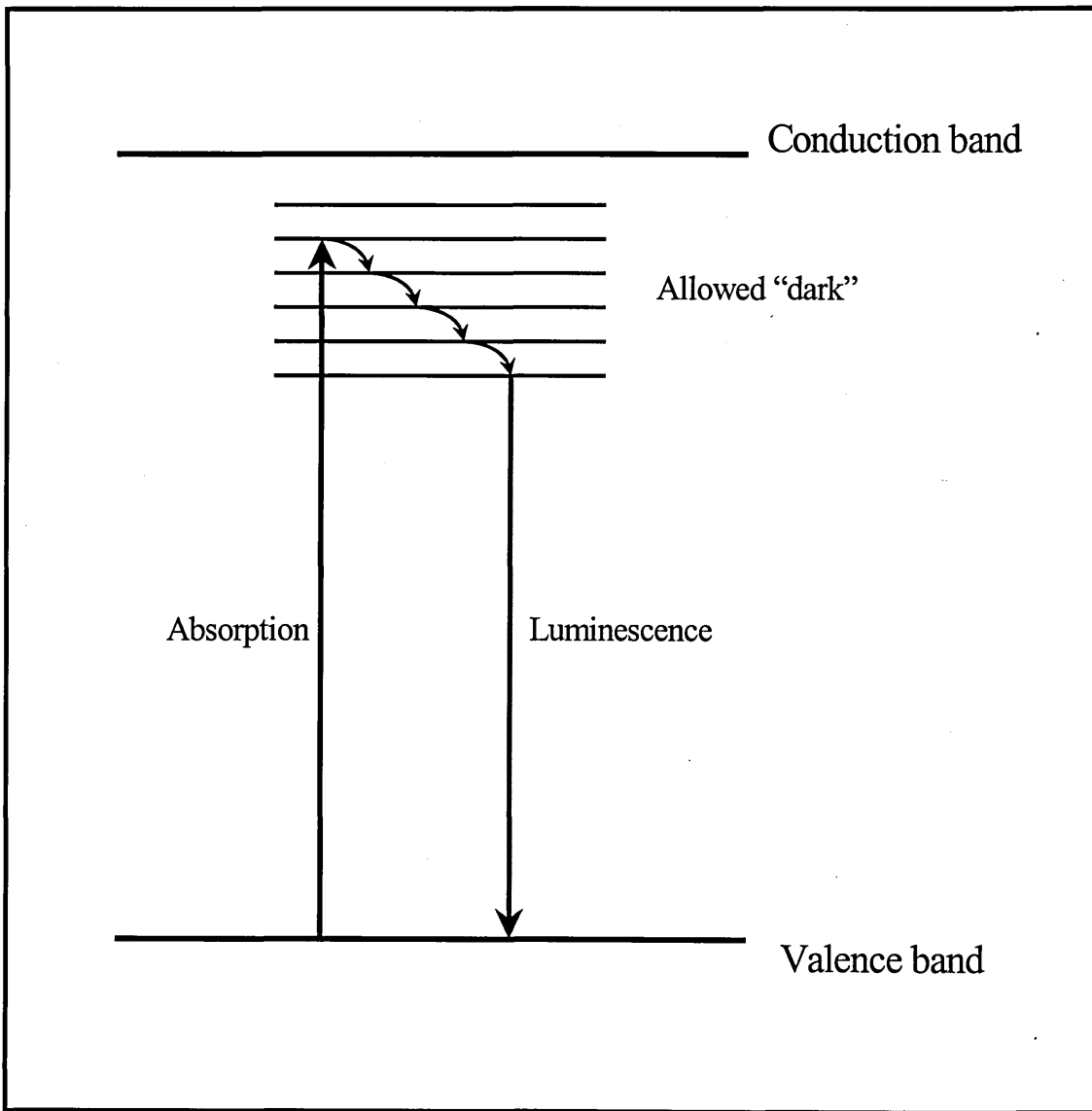


Figure 5.7. Schematic illustration of dark exciton in semiconductor [after Yoffe, 2001]

### 5.3.3. Photoluminescence of CdS Nanoparticles

Luminescence studies provide results, which at times tend to be difficult to interpret in a simple straightforward manner. Ekimov et al [1990] for instance, reported that, for  $R \gg a_B$ , luminescence lines originate from both free and bound exciton annihilation, with the luminescence intensity decreasing as  $R$  decreases from several thousand angstroms to a few tens of angstroms. However, as  $R$  is reduced below several hundred angstroms, the luminescence spectra become mixed with transitions involving excitons bound to impurities and lattice defects including neutral donors and acceptors. When  $R$  is reduced still further to the condition  $R < a_B$  (for example for CdSe with  $R \approx 1.6$  nm), then the atoms lie at or near the surface.

Different types of photoluminescence bands were also obtained for CdS nanoparticles when the electrons decay by radiative pathway. The first one is superradiant luminescence due to the band gap emission with a typical lifetime of a few picoseconds, which is rarely observed [Misawa et al, 1991; Wu et al, 2002]. The second one is near bandgap emission with a lifetime from several picoseconds to several nanoseconds [O'Neil et al, 1990; Matsumoto et al, 1994]. The third is deep trap state emission, which has a lifetime from picoseconds to microseconds [Kuczynski et al, 1984; Misawa et al, 1991; Wu et al, 2002].

The study of photoluminescence of CdS nanocrystals prepared by the sol-gel method was carried out by Zhao et al [1996]. The photoluminescence spectra at 30 K exhibit two emission bands: a strong one at about 2.5 eV and a weak broad band in the range of 1.7 to 2.0 eV. The first energy band (2.5 eV) is referred to as band-edge luminescence. Temperature dependence of photoluminescence measurements concluded that the band is related to a recombination luminescence of shallow traps or surface

defects, localised excitons and intrinsic excitons. The low energy band is possibly related to surface states.

The photoluminescence measurements performed by Chevreau et al [1996] on CdS nanoparticles sequestered in spin-coated polymer films shows a single peak luminescence at 540 nm (2.30 eV), which red shifted with respect to the first absorption peak which occurred at about 370 nm (3.35 eV). They also claimed that the CdS particles prepared by this simple method have not aggregated.

Nanda and Sahu [1999] investigated the effect of ageing on the photoluminescence of CdS nanocrystals prepared using a chemical route. The band gap of the 12 nm sized CdS sample is 3.14 eV. Two bands of 1.74 and 2.185 eV are obtained in the energy range 1.55 – 2.48 eV at room temperature. Their intensity was found to increase with ageing. As the energy of these two bands is less than the band gap energy, the transition involves donors, acceptors and surface traps. In the case of nanocrystals, there is a good wave-function overlap between the host and impurity even at room temperature, and donor-acceptor transition is expected. Tanaka et al [2000] studied photoluminescence properties of CdS nanocrystals in polymer having an average diameter of about 2 nm. The photoluminescence spectrum of the samples consists of two bands with peaks at 1.92 and 2.42 eV for a  $\text{Mn}^{2+}$  doped sample, while an undoped sample only contains a single peak at 2.42 eV. These peak energies are red shifted from their excitonic peak energy of about 3.5 eV, observed in the absorption spectrum. It is believed that the green luminescence band (2.42 eV) is attributed to the transition involving the deep trap states (or localized states) of the CdS nanocrystals, while the band peaked at 1.92 eV is ascribed to the Mn-related transition.

## 5.4. Details of the Experimental Technique

10 to 30 layers of Langmuir-Blodgett (LB) films of Cd-salts stearic acid (SA) and calix[8]arene (CA), respectively, were deposited by the LB technique. The LB films were transferred at a constant surface pressure of 25-28 mN/m onto quartz substrates. Cadmium sulphide (CdS) nanoparticles were formed within LB films by exposure the samples to H<sub>2</sub>S gas for a few hours.

UV-Visible absorption spectroscopy measurements were performed using UV4-UNICAM Spectrometer with Vision Software. The light source absorption was measured over the UV-Visible light range (190-900 nm). The UV-Vis spectrometer works on the principle of comparing the absorbance of a reference slide to that of the sample in two separate light beams. LB films samples were deposited on quartz slides using the LB technique. The absorption is recognised as a decrease in light intensity of the sample beam compared with a reference light beam.

Firstly, reference bare slides were used in both beams to obtain an instrument baseline for the whole wavelength range. It compensates for any intensity variation between the two beams (reference and sample). The sample was then located in the place of one of the reference slides (sample light beam). The schematic diagram of the absorption measurement set-up is shown in Figure 5.8. The computer-controlled instrumentation then compares the light absorbed by the reference slide and the sample over the wavelength range. Taking the baseline into account, a plot of absorbance versus wavelength can be obtained. The light was scanned through a wavelength range of 190-900 nm. The same measurements were carried out for the LB films before and after H<sub>2</sub>S treatment. The absorption spectra of CdS nanoparticles were obtained by subtraction of the two measured spectra, before and after the exposure of H<sub>2</sub>S gas.

In order to perform UV-visible absorption measurements at high temperatures, the samples were heated in a carbolite furnace. The UV-visible absorption measurement was then performed on the heated samples every 15 and 20 minutes. Experimental data of different samples of stearic acid and calixarene LB films before and after H<sub>2</sub>S treatment over a wide range of temperatures were analysed in order to extract more information about the ageing effect at the elevated temperatures.

The photoluminescence emission (PL) and excitation (PLE) of the samples were performed using the equipment shown in Figure 5.9. Both photoluminescence emission and excitation measurements were performed using a SPEX FluoroLog FL3-22 spectrofluorimeter (SPEC industries Inc.). Both kinds of measurements were carried out at room temperature. The excitation light was provided from a Xenon light source, being controlled by neutral density filters. The PL was dispersed with UV blazed grating with 1200 l/mm giving a spectral resolution  $\pm 1$  nm/mm slit width. Detection of the light in this system was done by CCD. For all experiments, the spectrometer and data acquisition were computer controlled.

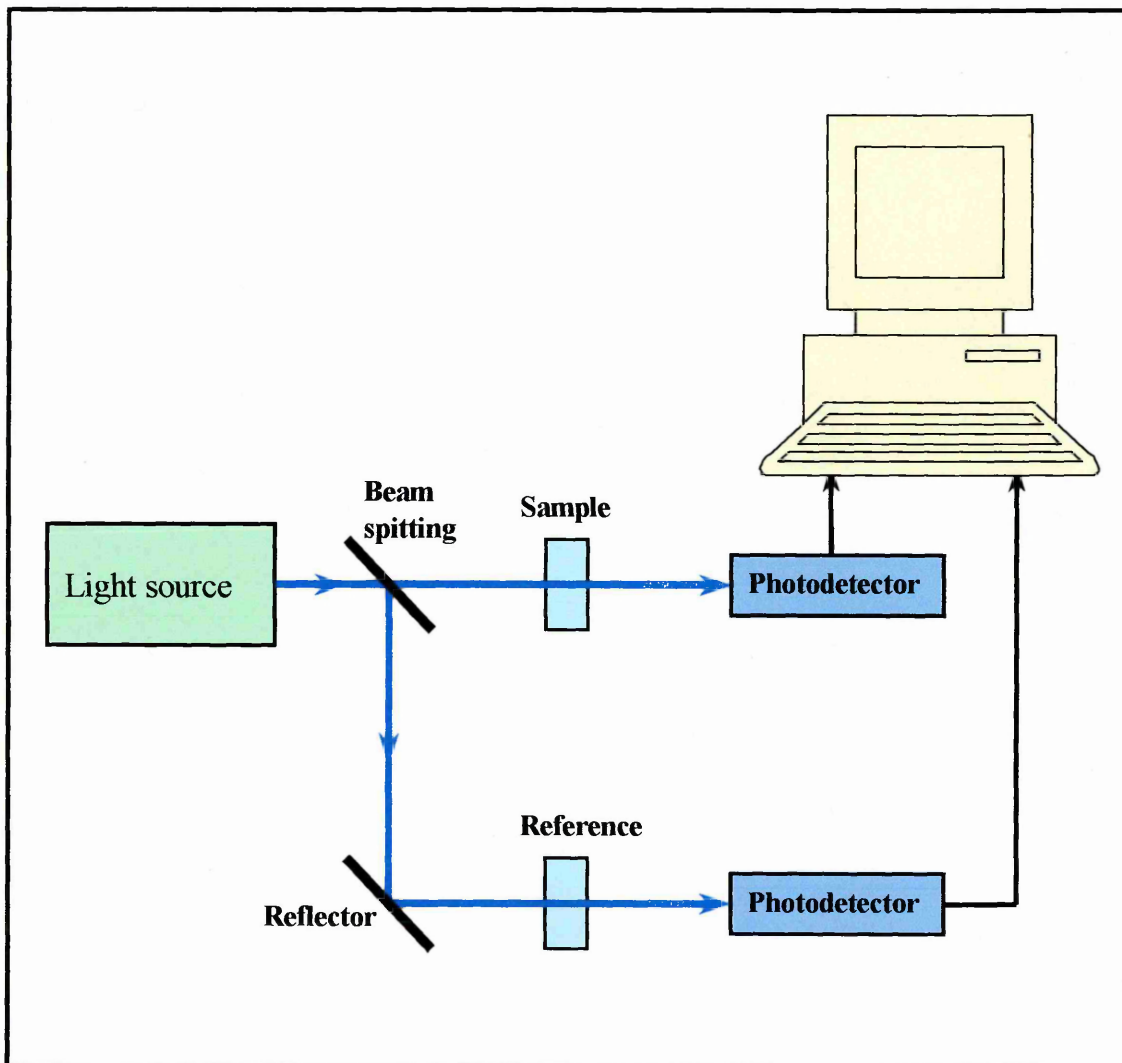


*Figure 5.8. A Schematic diagram for absorption measurement set-up*



## 5.5. Results and Discussion

### 5.5.1. Analysis of the Absorption Spectra

Typical UV-visible absorption spectra of 10-30 layers of LB films of stearic acid (SA) (before and after the exposure of H<sub>2</sub>S gas) are shown in Figure 5.10. As can be seen, the absorption spectra before H<sub>2</sub>S treatment have very low intensity of absorbance. This shows that the LB films of stearic acids are transparent materials. However, a small intensity recorded in the range wavelength of 200 – 250 nm is believed to represent the absorption of the light by the quartz slide substrate. In contrast, the absorption spectra of the same samples measured after H<sub>2</sub>S treatment present significant absorbance, starting from around 450 nm and increases consistently as wavelength decreases. This absorbance increases dramatically from at about 250 nm to 200 nm for all samples studied. The increase of intensity of the samples after the exposure H<sub>2</sub>S gas (as compared to that of LB films before H<sub>2</sub>S treatment) is believed due to the formation of absorbance materials inside the LB films. It can also be seen that the intensity of absorbance increases as the number of LB films (thickness of LB films) increase. In order to evaluate more details of this absorption behaviour, the two absorption spectra of the same samples were subtracted. Figure 5.11 shows the subtracted absorption spectra of 10-30 layers LB films of stearic acid. An enlarged part of the absorption spectra near the absorption edge is presented in Figure 5.12. It is believed, however that the main spectral features presented in Figure 5.11 and Figure 5.12 are characteristics of CdS particles, since they were reproducible for the samples having different number of LB layers (10-30 layers).

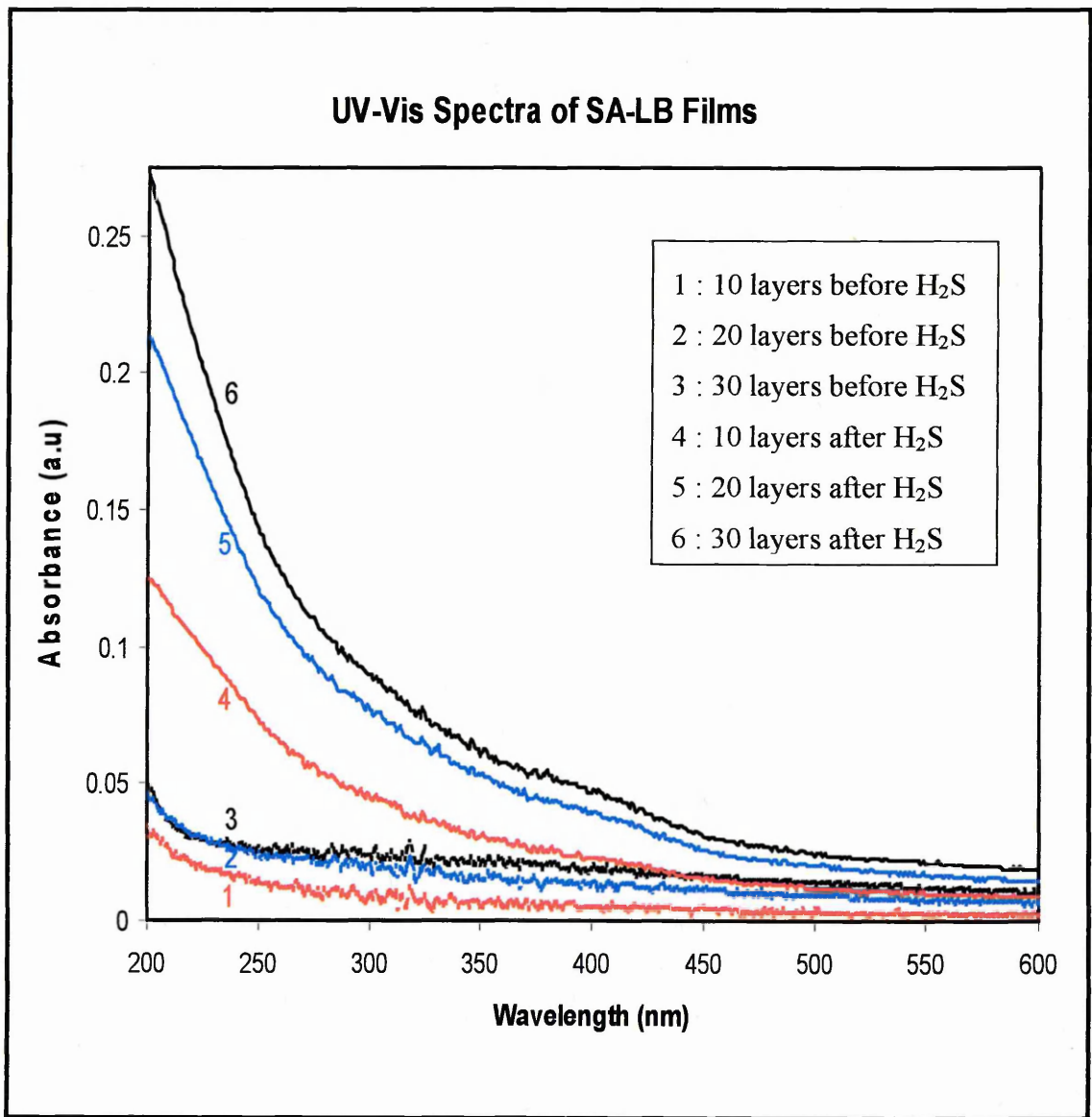


Figure 5.10. Absorption spectra of SA-LB Films, before and after the exposure of H<sub>2</sub>S gas (before and after H<sub>2</sub>S treatment)

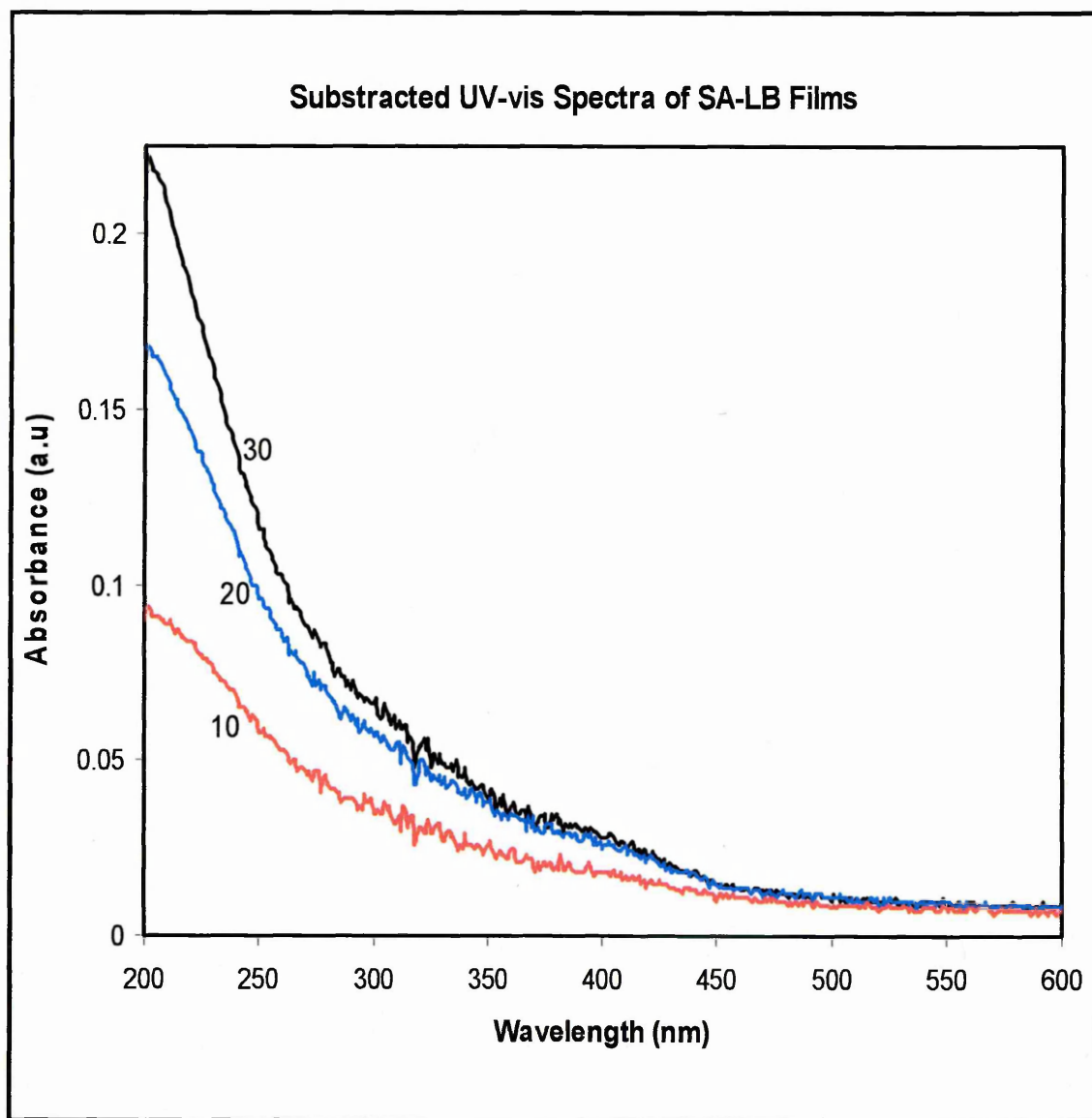


Figure 5.11. Subtracted absorption spectra (before and after  $H_2S$  gas treatment) of CdS nanoparticles formed in SA-LB Films. The number of LB layers is shown near respective curves

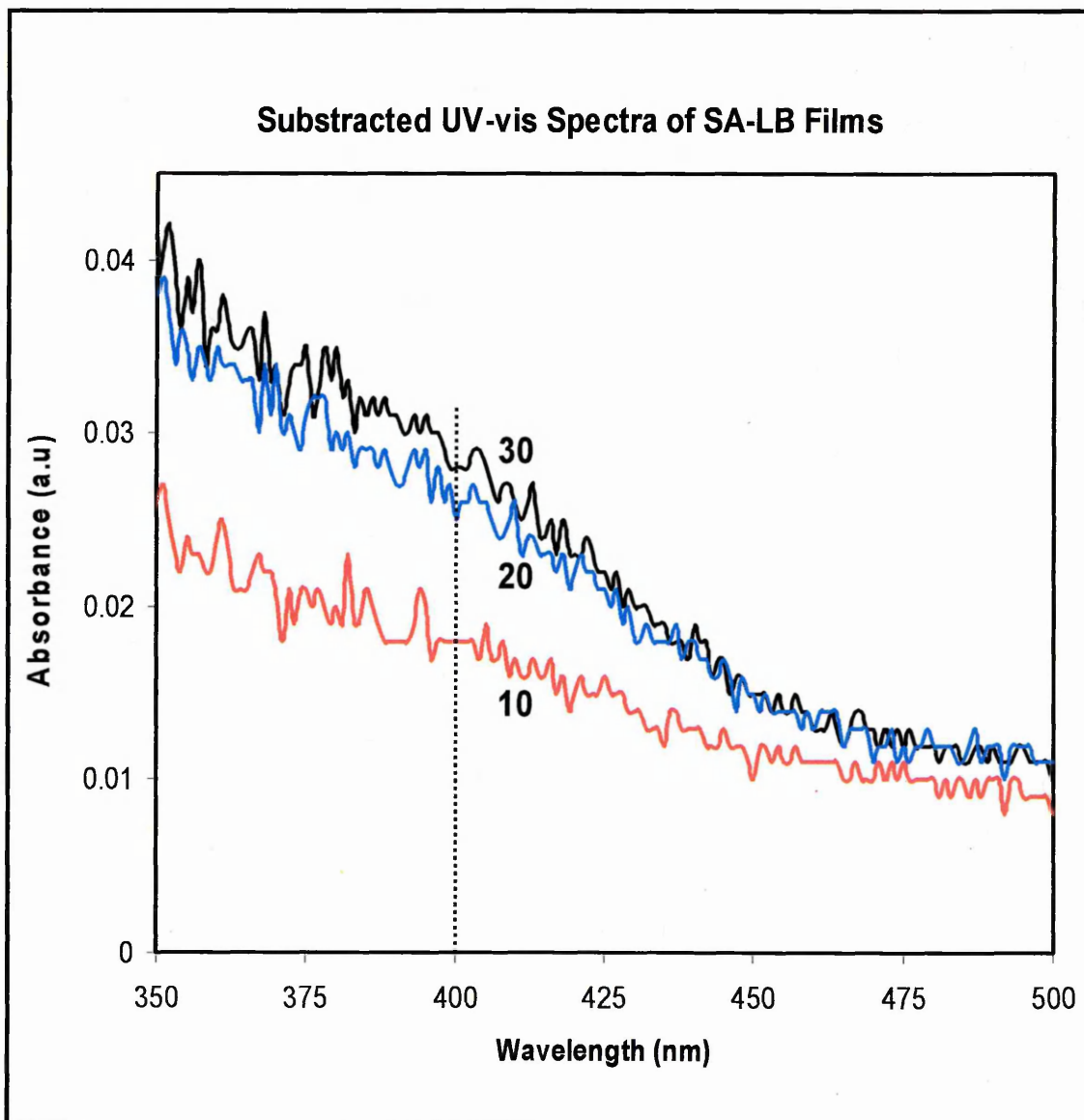


Figure 5.12. Absorption spectra of CdS nanoparticles in SA-LB Films near the absorption edge. The number of LB layers is shown near respective curves

The absorption spectra of CdS in SA LB films, shown in Figure 5.11 and Figure 5.12, represent gradually increasing absorbance starting from the absorption edge of about 450 nm. These absorption spectra are clearly blue shifted with respect to bulk CdS material (about 590 nm). The main absorption band is estimated to be at about 400 nm. This band is relatively broad, probably due to the size distribution of CdS clusters [Nabok et al, 2002].

Typical UV-visible absorption spectra of 10-30 layers of LB films of calixarene (CA) for both measured on the same samples before and after the exposure of H<sub>2</sub>S gas are presented in Figure 5.13. Unlike the absorption spectra of SA LB films, the spectra obtained from the CA LB films before H<sub>2</sub>S treatment shows a significant increasing absorbance starting from the absorption threshold at around 380 nm. This fact shows that calixarene is a light-absorbing substance. The intensity of absorbance is comparable to the number of LB layers. The exposure of the samples to H<sub>2</sub>S gas results in an increasing the absorbance for all samples of different number of layers. Figure 5.14 shows the subtracted spectra of two measured spectra before and after H<sub>2</sub>S treatment of CA LB films. These subtracted spectra are believed to be the characteristics of CdS particles, since they were reproducible for all the samples under investigation, which have different number of layers (10-30 layers).

As can be seen in Figure 5.14, the absorbance increases gradually starting from the absorption edge at about 380 nm. These absorption spectra are much blue shifted (as compared to those of CdS in SA LB films) with respect to bulk CdS material. Two absorption bands at about 310 nm and 240 nm were also obtained. These bands are believed to be related to the two characteristic sizes of CdS clusters, which are relatively broadened.

### UV-Vis Spectra of CA-LB Films

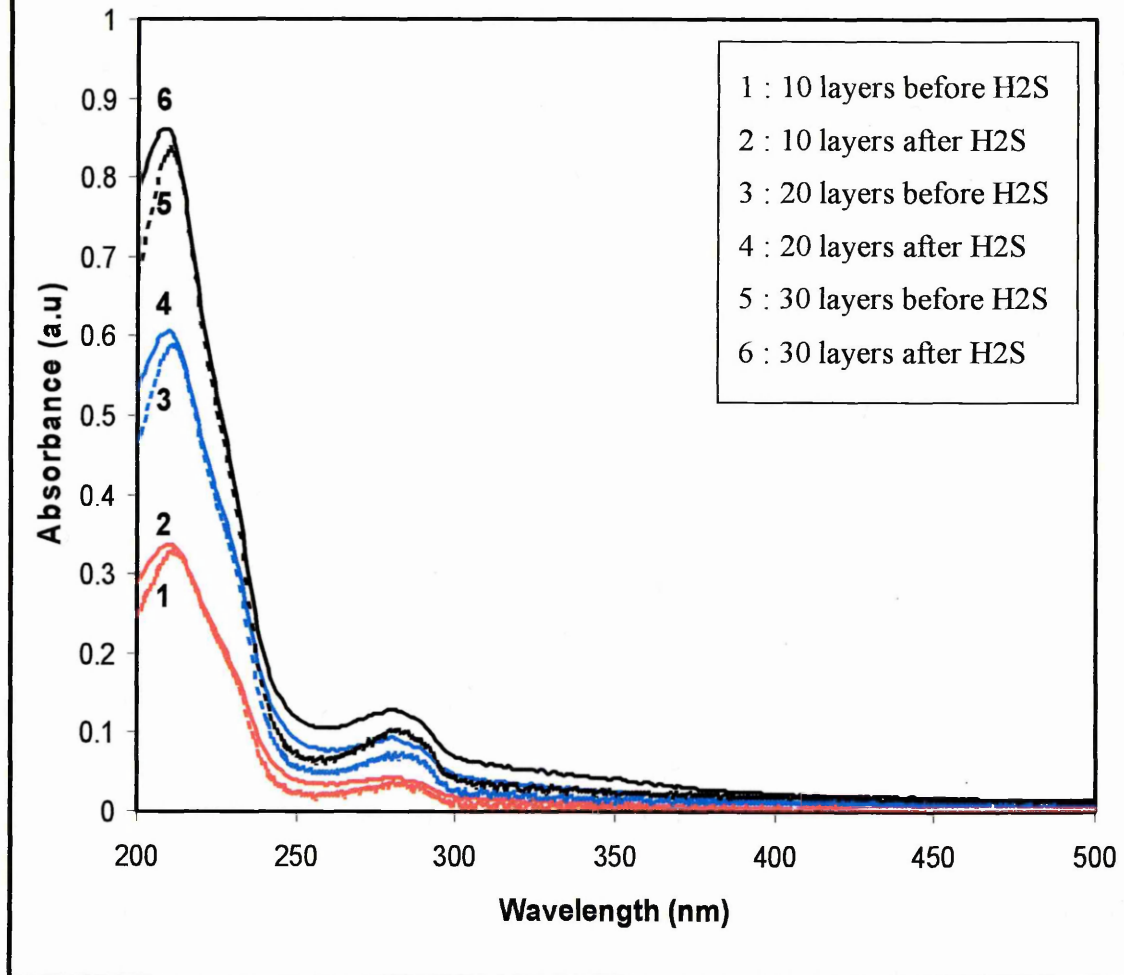


Figure 5.13. Absorption spectra of CA-LB Films (before and after the exposure of H<sub>2</sub>S gas)

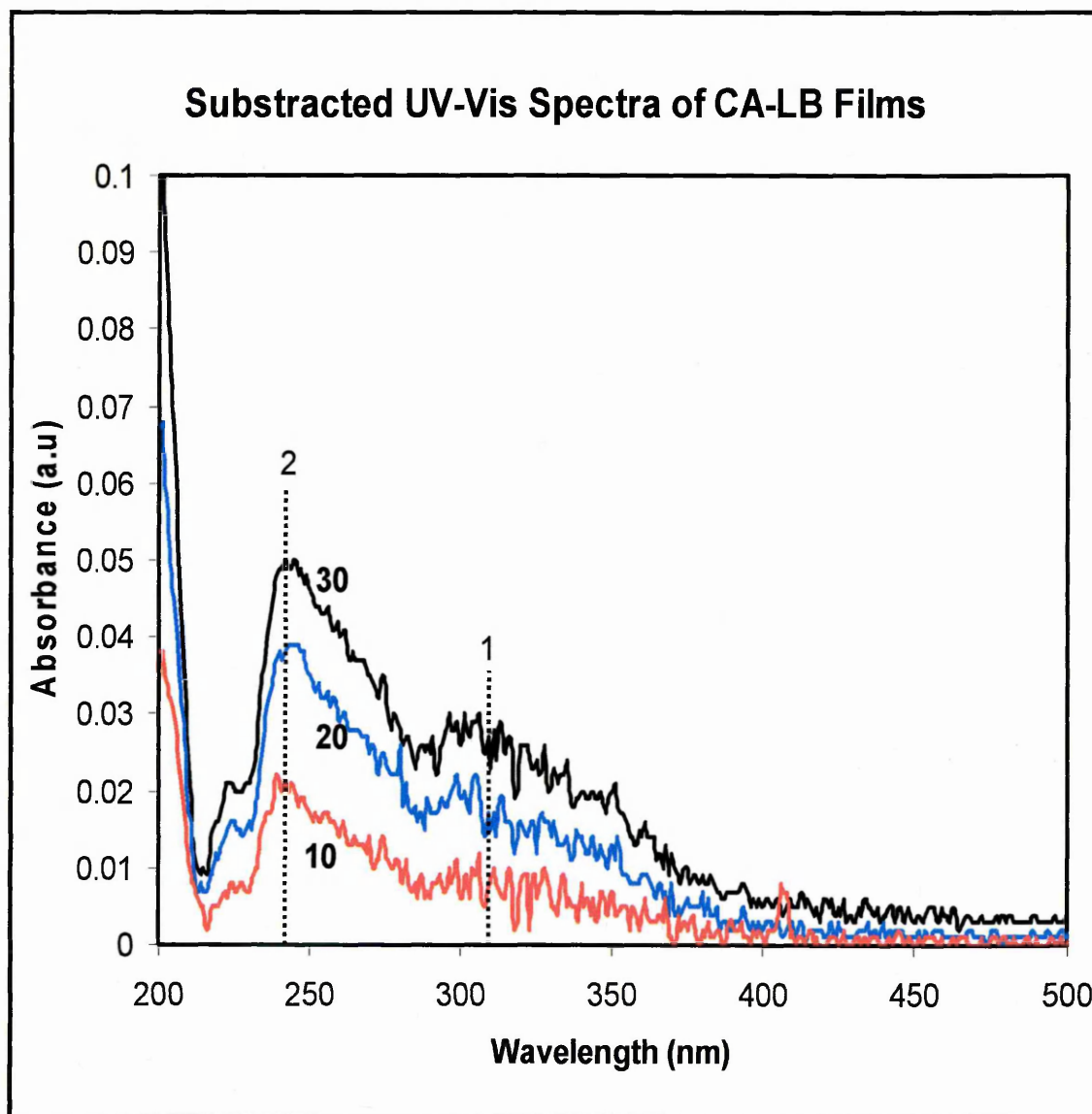


Figure 5.14. Substracted absorption spectra (before and after  $H_2S$  gas treatment) of CdS nanoparticles formed in CA-LB Films. The number of LB layers is shown near respective curves

The observation of the blue spectral shift of the optical absorption edge for the nanoparticles in comparison with the respective bulk values is a typical experimental confirmation of nanoparticles' presence. The particles' size can be evaluated from the position of the main absorption bands. However this requires subtraction of the experimental spectra measured on the same samples before and after exposure to H<sub>2</sub>S gas. This is particularly important for CA LB film matrix, which is a light-absorbing substance itself. A fine spectral structure, which was observed in CdS/CA films, could be interpreted either in terms of electron transitions between levels of size quantisation or, more likely, by size dispersion of CdS nanoparticles. However, the validity of the employed spectra analysis should be confirmed independently. Photoluminescence emission (PL) and photo-luminescence excitation (PLE) spectral measurements are undertaken in this work to provide direct information on the spectral changes due to CdS nanoparticles formation.

Photoluminescence measurements were undertaken to gather conclusive information regarding the formation of CdS nanoparticles. Typical photoluminescence excitation (PLE) spectra of the LB films containing CdS nanoparticles are presented in Figure 5.15 and Figure 5.16, respectively, for both LB films of stearic acid and calixarene. These spectra closely resemble the respective absorption spectra taken by UV-visible absorption spectroscopy (Figure 5.12 and 5.14) as well as the spectral data reported earlier [Nabok et al, 1997; 1998; 1999]. The LB films of stearic acid have the first absorption peak at 390 nm (Figure 5.15), while two absorption peaks occur at 280 nm and 341 nm for the LB films of calixarene (Figure 5.16).

The observed changes in the absorption edge of both samples are due to the quantum confinement. Two absorption peaks obtained for CdS nanoparticles in the LB films of calixarene have been suggested as a representation of: (i) electron transitions

between levels of size quantisation [Ekimov et al, 1985; Nabok et al, 1997; Nabok et al, 1998], and (ii) size distribution of CdS clusters [Salata et al, 1996; Nanda and Sahu, 1999; Nabok et al, 2002]. In case of electron transitions between levels of size quantisation, the lines should be very symmetric and identical. In fact, neither the experimental data obtained from the UV-visible absorption spectra nor the photoluminescence measurements support the requirement. In addition to that, this approach does not explain the different in the broadening of the absorption peaks. Ekimov et al [1985] have also noted that the bands corresponding to electron transitions between levels of size quantisation are usually observed in chalcogenide glasses only at low temperature.

It is concluded, however, that the observed spectra correspond to the main electron transitions and represent the size distribution of CdS clusters. This approach can explain the different absorption spectra of SA LB films from those of CA LB films. The different of absorption spectra of SA and CA LB films shows that the size distribution of CdS particles in such type LB films is different.

The size of CdS nanoparticles can be evaluated from the blue shift of the absorption bands with respect to the band gap value of bulk CdS. This is the consequence of quantum confinement effect. In the case of pseudo-two dimensional (2D) CdS clusters, the size quantisation occurs in both lateral and normal directions, and changes in the ground state energy for the cluster having platelet shape can be written as [Yoffe, 2001]:

$$\Delta E = \frac{\hbar^2 \pi^2}{2\mu(L_{x,y})^2} + \frac{\hbar^2 \pi^2}{2\mu(L_z)^2}, \quad (5.13)$$

where  $\mu = \frac{\mu_e \mu_h}{\mu_e + \mu_h}$  is the reduced mass of excitons,  $L_{x,y}$  and  $L_z$  are the dimensions

of the CdS cluster in lateral and normal directions, respectively.

This formula was derived for semiconductor clusters smaller than the exciton Bohr radius ( $r_B$ ) and having simple parabolic bands. Since  $a_B = 3.2 \text{ nm}$  in quasi-2D CdS structures [Yoffe, 2001], Equation (5.13) is definitely valid for  $L_z \approx 2 - 3 \text{ nm}$  and still acceptable for  $L_{x,y} \approx 20 - 30 \text{ nm}$  (see Chapter 2). For the platelet-type CdS clusters having  $L_{x,y} \approx 10L_z$ , the first term is negligibly small compared to the second one. Therefore, quantisation in the Z-direction is dominant.

Calculations of the cluster thickness  $L_z$  using Equation (5.13) yield the value of  $1.42 \pm 0.1 \text{ nm}$  and  $1.08 \pm 0.04 \text{ nm}$  for CdS clusters in the CA LB films from the first and second peaks, on the experimental spectra in Figure 5.14 (obtained from UV-visible spectra). The band at 400 nm in the spectrum of CdS clusters in the SA LB films yields a value of  $1.9 \pm 0.1 \text{ nm}$ . The values of  $\mu = 0.125 m_0$  where  $m_0$  is the rest mass of electrons and  $E_g = 2.425 \text{ eV}$  [Ray, 1969] were used for this calculation. The photoluminescence data yield the value of 2 nm for CdS clusters in SA matrix and two values of 1.2 nm and 1.6 nm for CA LB films. The obtained values of the nanoparticles size from the photoluminescence are very similar to those found from the analysis of the UV-visible absorption spectra.

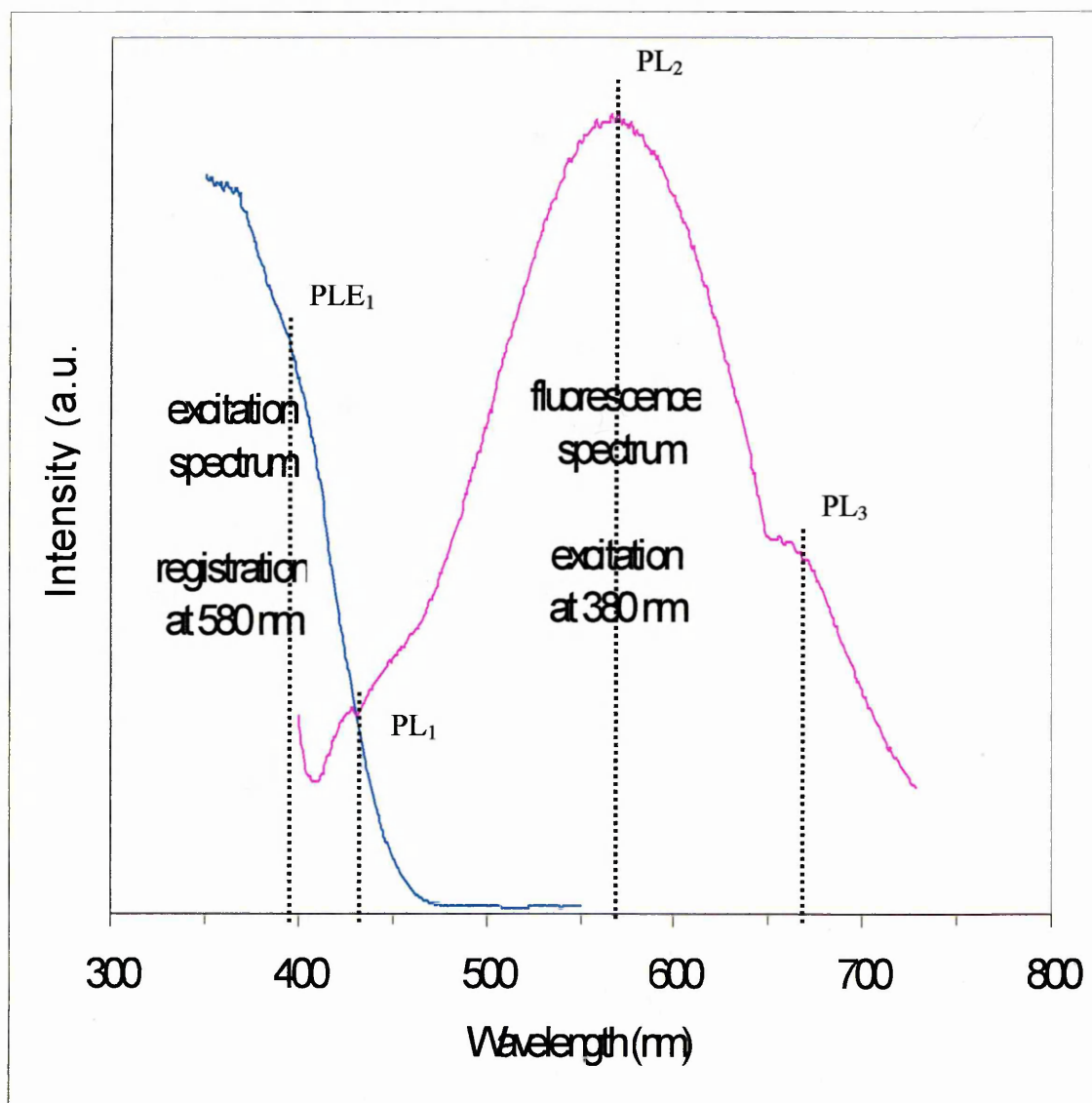


Figure 5.15. Photoluminescence emission (PL) and excitation (PLE) spectra of LB films of stearic acid containing CdS nanoparticles

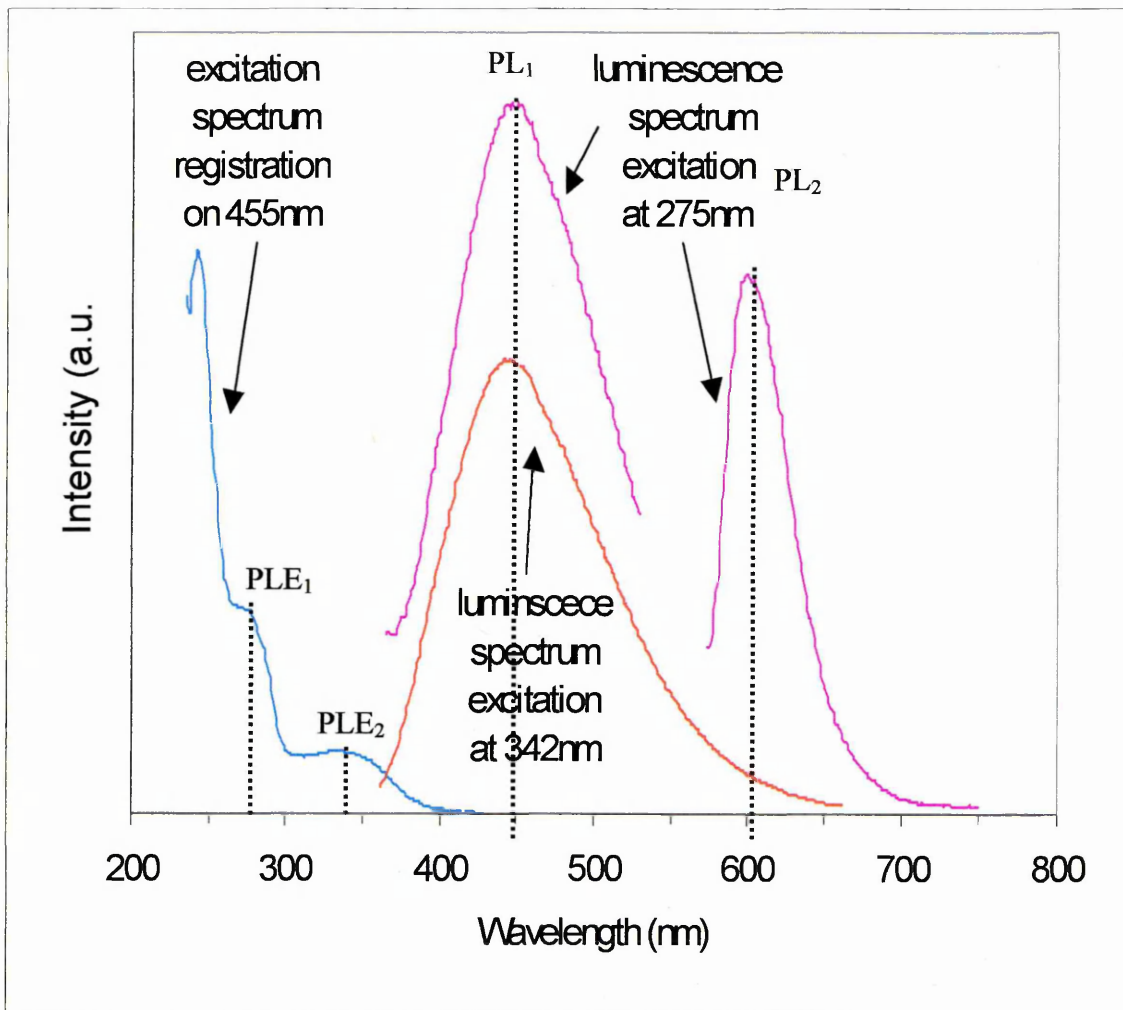


Figure 5.16. Photoluminescence emission (PL) and excitation (PLE) spectra of CdS nanoparticles within the LB films of calixarene

## 5.5.2. Photoluminescence

Photoluminescence (PL) spectra of Cd-salts LB films exhibit broad emission bands at about 570 nm (2.18 eV), labelled PL<sub>2</sub>, as shown in Figure 5.15, sandwiched between two smaller bands at 430 nm (2.88 eV) (PL<sub>1</sub>) and 660 nm (1.88 eV) (PL<sub>3</sub>) appearing as shoulders. Photoluminescence spectra of Cd-salts calixarene LB films show two luminescent peaks at 455 nm (2.82 eV), labelled PL<sub>1</sub> and 610 nm (2.03 eV), namely PL<sub>2</sub> (Figure 5.16). These photoluminescence spectra clearly confirm the presence of CdS particles inside the LB films of stearic acid and calixarene. Values of the emission energy together with corresponding absorption energies are summarized in Table 5.1. It should be noted from Figure 5.16 that only one luminescent band appeared at 2.82 eV when the excitation at 3.63 eV was used while a high-energy excitation at 4.51 eV yielded both luminescent bands.

The observed shift of the luminescence bands with respect to the corresponding absorption bands is relatively large. Most likely, only the first luminescence band at 2.88 eV with the Stokes shift of 0.22 eV represents the real resonance luminescence from the excited levels of CdS. The other two bands may be associated with impurities. Similarly, in CA LB films, the first band at 2.82 eV with the energy shift of 0.81 eV is taken to be due to resonance and related to band edge of emission, while the second band at 2.03 eV is most likely due to the energy transfer to the impurity level. Since the energy of the band is less than the band gap energy, the transition may involve donors, acceptors and surface traps. In the case of nanocrystals, there is a good wave-function overlap between the host and impurity even at room temperature, and donor-acceptor transition is expected.

There are also possibilities that the bands are related to transition of shallow traps or deep trap bands. Chestony et al [1986] gave the energy band diagram of a nanoparticle and the bulk counterpart (Figure 5.17). It can be noted that the shallow traps move along with the intrinsic band as the crystalline size decreases. However, the shift of the deep traps lying close to the middle of the forbidden gap, is negligible. Thus, the transition involving the deep traps should not change in the energy with decreasing or increasing crystalline sizes.

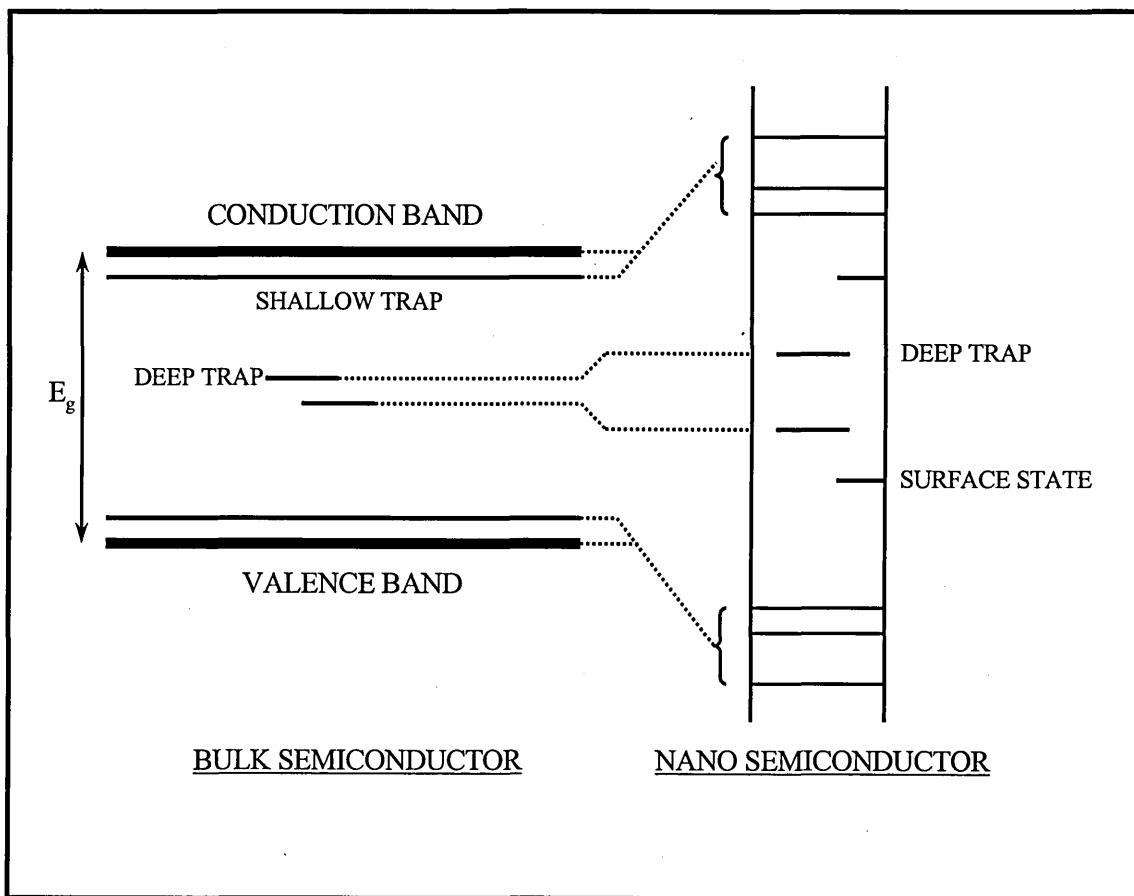


Figure 5.17. Energy level diagram of bulk and nano semiconductors

Values of the Stokes shift are found to be 0.22 eV and 0.81eV for CdS nanoparticles in SA and CA LB films, respectively. This very large Stokes shift of the luminescence of CdS nanoparticles is the strength of the experimental results, as typical values of the resonance Stokes shift are in the range of 10 meV [Yoffe, 2001]. The formation of "dark excitons" was recently reported [Smotkin et al, 1988] and the process is shown schematically in Figure 5.7. These electron transitions having angular momentum projection of  $F = \pm 2$ , which are usually forbidden, can occur under special conditions, when II-VI semiconductor particles of prolate shape have non-compensated ( $\text{Cd}^+ - \text{S}^-$ ) dipole moments on their surface. The formation of "dark excitons" leads to a larger Stokes shift in the range of 100meV [Yoffe, 2001]. The observed large Stokes shift in the present studies can be explained by assuming a platelet shape of CdS nanoparticles in LB films. The energy shift for CdS clusters in CA LB films is larger than that in SA LB films. This difference may be accounted for the fact that the effect of surface dipole moments is more pronounced in smaller CdS clusters in CA than those of SA LB films.

*Table 5.1 Characteristic energies for the luminescence of CdS nanoparticles in LB films*

Material	Absorption energy (eV)	Emission energy (eV)	Stokes shift (eV)
SA	3.10 (PLE <sub>1</sub> )	2.88 (PL <sub>1</sub> )	0.22
		2.18 (PL <sub>2</sub> )	
		1.88 (PL <sub>3</sub> )	
CA	3.63 (PLE <sub>2</sub> )	2.82 (PL <sub>1</sub> )	0.81
	4.42 (PLE <sub>1</sub> )	2.03 (PL <sub>2</sub> )	

### 5.5.3 Evolution of CdS particles within 2D LB Layers

Transformations in the size of CdS nanoparticles were studied by UV-visible absorption spectroscopy. In order to explain the observed behaviour, the Lifshitz-Slezov diffusion model was generalised for the two-dimensional case, and the resulting time-dependent equations were simulated. Moreover, apart from the shift of the absorption band edge, the UV-visible absorption spectra of these films show two well-resolved peaks at room temperature [Nabok *et al*, 1998; Nabok *et al*, 1999]. This effect cannot be explained simply in terms of quantum confinement.

Direct observation of the evolution of CdS nanoparticles with TEM is questionable, since increases in both the number and size of the CdS clusters caused by the high-energy electron beam was found recently [Nabok *et al*, 2000]. The main goal of this work was to investigate and to develop a model for the formation and further transformations (ageing effect) of CdS nanoparticles in different LB films. The model for the formation of CdS/CdSe nanoclusters in halcogenide glass by Lifshitz and Slezov [1959] is generalised here for the case of two-dimensional diffusion within the LB layers. A mechanism of two-dimensional aggregation is believed to be common and thus applicable to other system, such as semiconductor quantum dots in layered systems produced by MBE.

The transformations of the absorption spectra caused by ageing were recorded and presented in Figure 5.18 and Figure 5.19 as time dependencies of the CdS nanoparticles size. A monotonic increase in size with the tendency of saturation was observed in all cases, although the changes in size are much more pronounced for SA films compared to those in CA films.

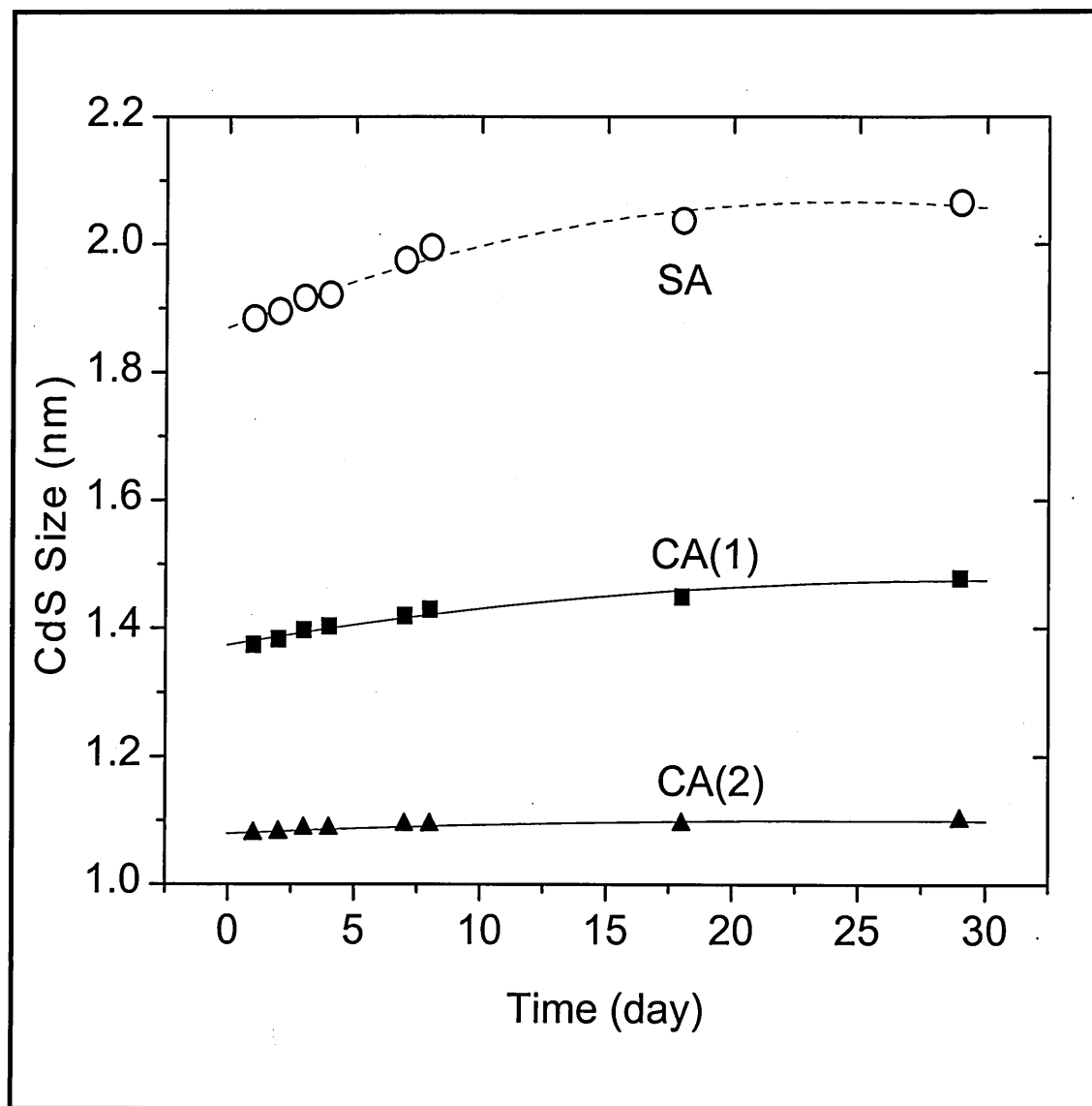


Figure 5.18. Room temperature time dependencies of the size of CdS nanoparticles in LB films of stearic acid (SA) and calix[8]arene (CA1 and CA2), obtained from the first and the second peaks, respectively.

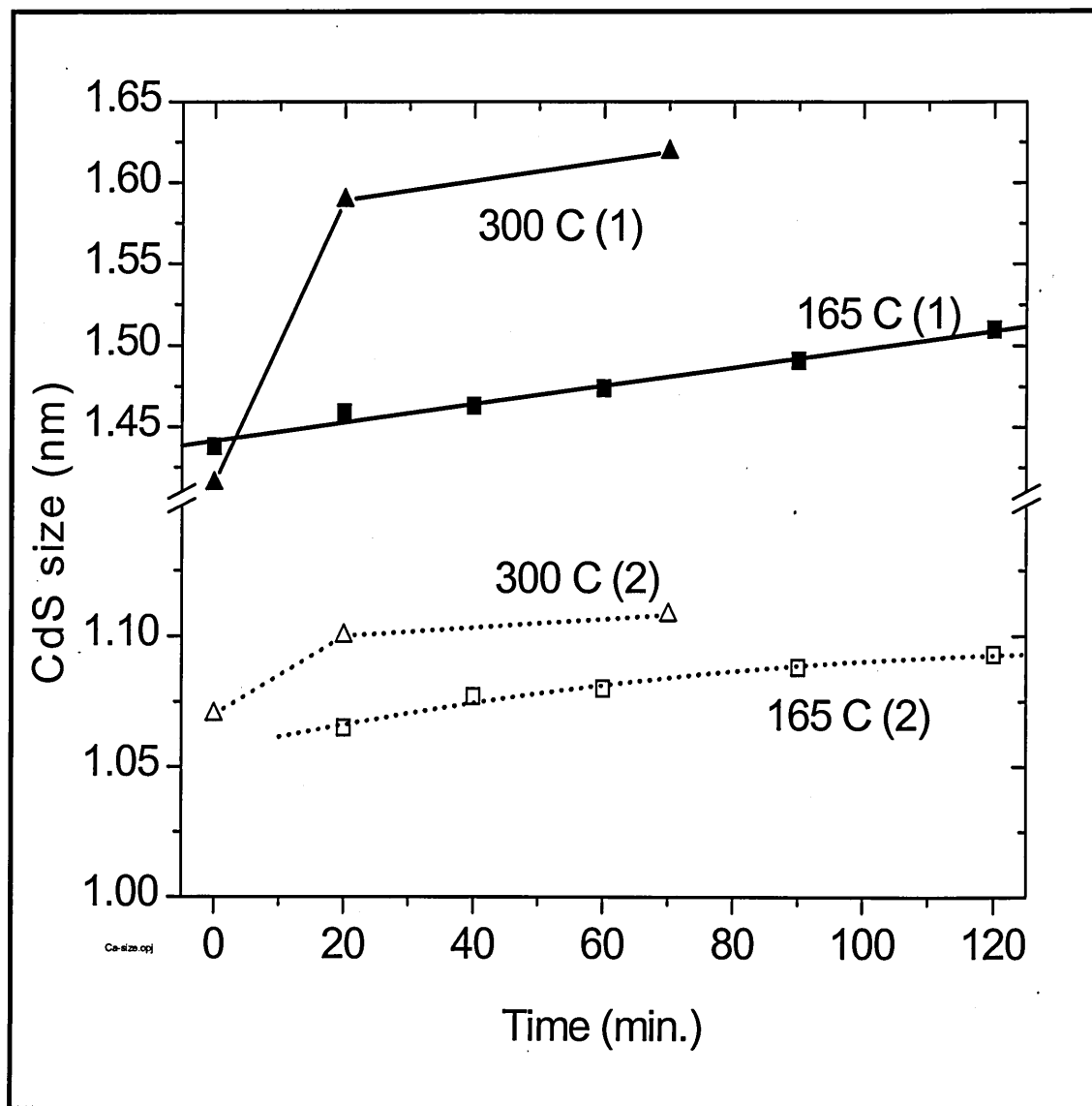


Figure 5.19. Time dependencies of the size of CdS nanoparticles in LB films of calix[8]arene (CA1 and CA2) at elevated temperatures

### 5.5.3.1. Two-dimensional (2D) Diffusion Model

The absorption spectral features obtained by UV-visible and the changes in size of CdS clusters (Figure 5.18 and 5.19) can be explained by the model of two-dimensional diffusion. Assuming that initial nucleation has happened, and CdS grains develops further due to a slow, quasi-stationary diffusion, the distribution of CdS molecules in the LB film obeys Laplace's equation:

$$\nabla^2 C(x, y) = 0 \quad (5.14)$$

where  $C(x, y)$  is the two-dimensional concentration of CdS. Unlike the 3D situation, where the solution of Laplace's equation decays at infinity as  $1/r$ , in the two-dimensional case it grows logarithmically with the distance from a single grain. Therefore, the quasi-stationary average concentration is determined self-consistently by the size distribution of the grains. The radial distribution of CdS concentration near the grain is given by:

$$C(r) = \frac{(C_{oa} - C_{av}) \ln(r/d_0)}{\ln(a/d_0)} + C_{av} \quad (5.15)$$

where  $C_{oa}$  is the equilibrium concentration near the grain of the radius  $a$ ,  $C_{av}$  is the average concentration in the film and  $d_0$  is a parameter of the system of the grains which is determined self-consistently. According to  $C_{oa} = C_{o\infty} (1 + 2\sigma v/kTa)$  [Lifshitz and Slezov, 1959], where  $\sigma$  is the surface tension coefficient and  $v$  is the molar volume of solid CdS, the parameter  $C_{o\infty}$  is the equilibrium concentration of CdS molecules near the grain of an infinite size. The whole distribution of CdS concentration in the film is given by:

$$C(x, y) = C_{av} + \sum_i \frac{(C_{o\infty}(1 + 2\sigma v / kTa_i) - C_{av}) \ln(r_i / d_o)}{\ln(a_i / d_o)} \quad (5.16)$$

where  $r_i = \sqrt{(x - x_i)^2 + (y - y_i)^2} < d_o$  is the distance from the  $i$ -th grain, parameter  $d_o$  is approximately three time less than the intergrain distance. To derive the time-dependent equation for the variation of the grain size  $a_i$ , it is assumed that the grains remain spherical during coalescence. The total diffusion flux near the grain is then

$$I(a_i) = -2\pi r D \frac{\partial C(r)}{\partial r} \quad (5.17)$$

where  $D$  is the two-dimensional diffusion coefficient. As a result, a time dependent equation for  $a_i$  can be defined as

$$\frac{da_i}{dt} = D v \frac{C_{av} - C_{o\infty}(1 + 2\sigma v / kTa_i)}{2a_i^2 \ln(a_i / d_o)} \quad (5.18)$$

Note that the parameter  $C_{av}$  is also time dependent, to ensure the CdS conservation.

Similarly to the Lifshitz-Slezov model, the critical radius is defined as

$$a^* = \frac{2\sigma v C_{o\infty}}{kT(C_{av} - C_{o\infty})} \quad (5.19)$$

Equation (5.18) shows that large grains with  $a_i > a^*$  grow slowly, whereas small grains ( $a_i < a^*$ ) disappear within finite time of  $\tau \sim a^3 / DC_{av}v$  for  $C_{av} \sim C_{o\infty}$  or  $\tau \sim a^4 kT / DC_{o\infty} \sigma v^2$ .

Numerical simulation of the Equation (5.18) is shown in Figure 5.20. The initial condition was set for particles distributed randomly with sizes less than 1 nm and initial  $C_{av}$  corresponds to  $a^* = 0.5$  nm. The evolution of the distribution function  $f(a)$  at large

times for the two-dimensional case is similar to the Lifshitz – Slezov model (Lifshitz and Slezov, 1959). It also has a peak at  $a = a^*$ , and is not very sensitive to the initial distribution. However, the shape is flatter at small  $a$ , and drops more rapidly at large  $a$  than in the three-dimensional case. The average concentration in the two-dimensional case decreases slower and the critical radius  $a^*(t) \sim a_0^* t^{1/4}$ .

According to the above model, CdS molecules in the SA films, initially evenly distributed within each LB bilayer, aggregate and form "large" particles with an average size of 1.9 nm and smaller particles with their size distributed over a wide range down to single molecules. The distribution function is shown in Figure 5.21 as black bars. In the case of the CA films, the minimum size of the particles is restricted at the level of about 1.1 nm, which corresponds well to the size of CA cavity. It can be assumed that some of CdS molecules were captured inside CA "baskets". To model this phenomenon the coefficient  $D$  that controls CdS diffusion from small particles was reduced. For the SA films, the aggregation, described by Equation (5.18), remains longer until  $a_i$  becomes very small, explaining why the typical size of large grains in the SA is greater than in the CA films. The aggregation of CdS continues with time since large particles grow by absorbing the small ones. The observed saturation of the particle size is caused by the limited amount of CdS in the film.

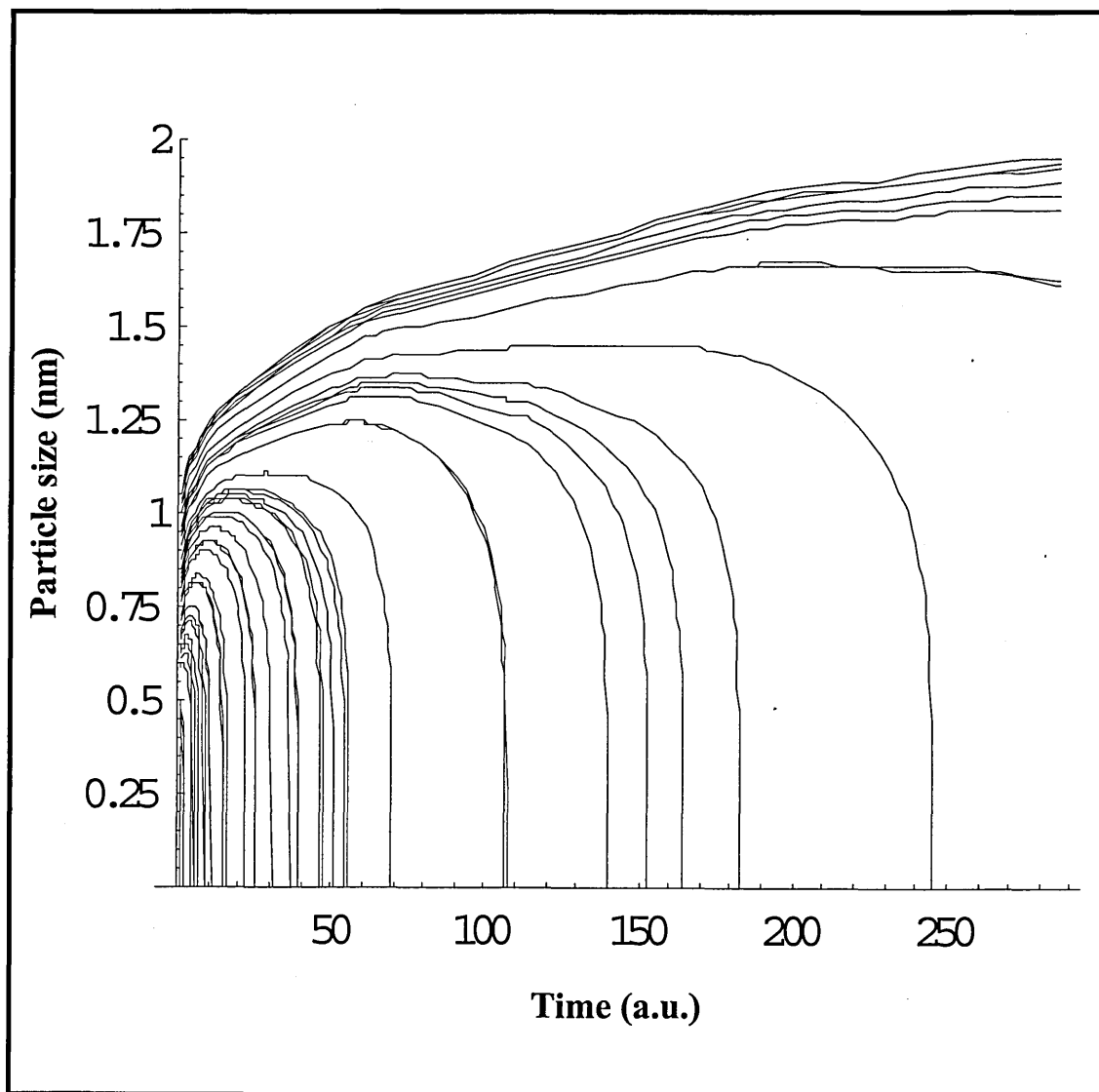


*Figure 5.20. Numerical simulation of the Equation (5.18) for CdS grains*

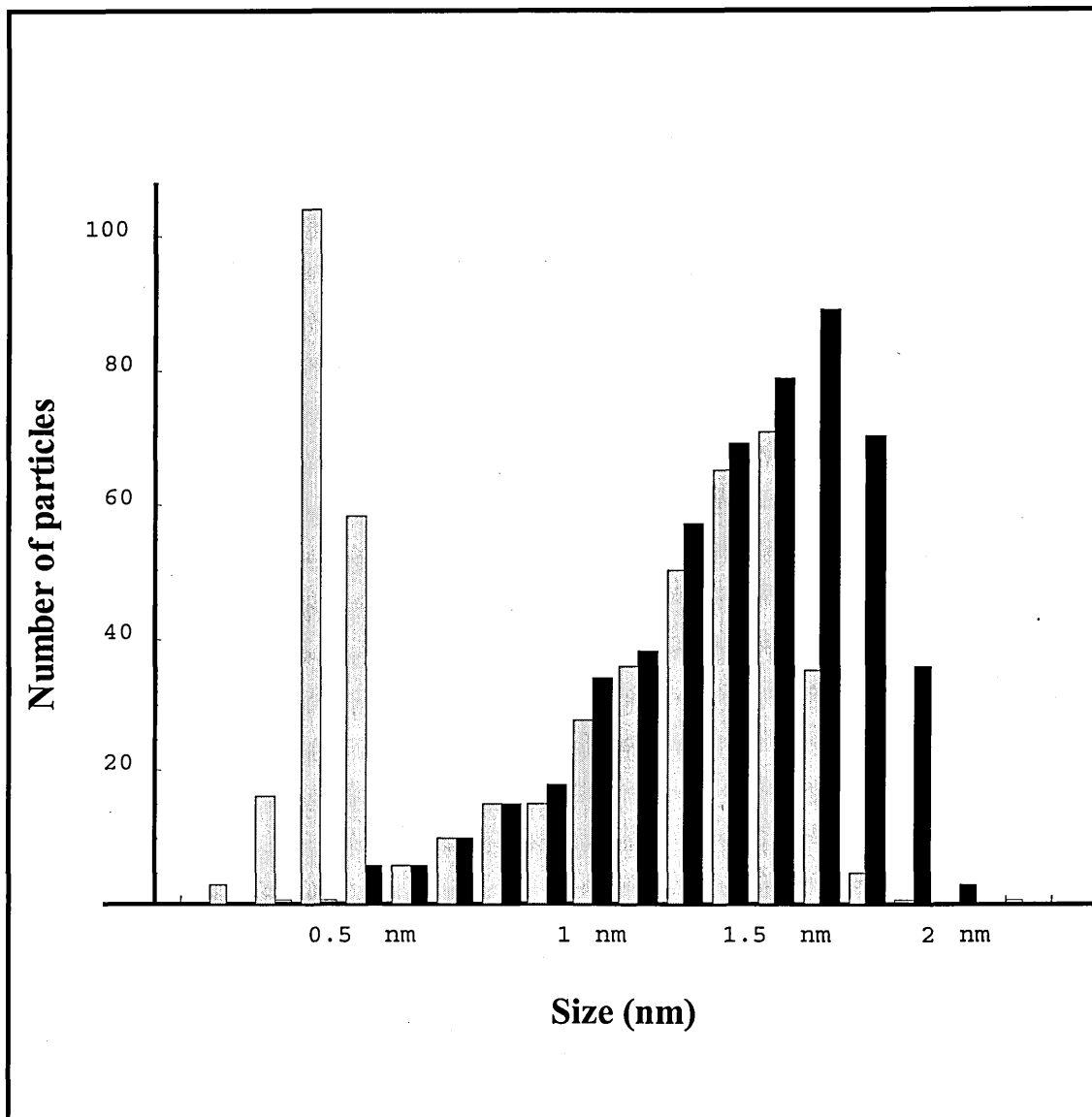


Figure 5.21. Distribution function of the CdS particles: black bars relate to the SA film, grey bars relate to the CA film.

## 5.6. Summary

The main result of UV-visible absorption measurement is the confirmation of CdS nanoparticles formation in the LB films during exposure H<sub>2</sub>S gas. The absorption spectra of CdS nanoparticles within both kinds of LB films show the blue shift in respect to that in bulk CdS. Much more blue-shifted absorption spectra have been obtained from calixarene LB films (as compared to those of stearic acid LB films). This optical method can also be applied to evaluate the size of CdS nanoparticles using the procedure of subtraction of two absorption spectra of the same sample measured (before and after the sample was exposed to H<sub>2</sub>S gas). The size of the CdS nanoclusters have been found to be much smaller in calix[8]arene LB films (compared to those formed in fatty acid LB films).

Photoluminescence spectra of the LB films, containing CdS nanoparticles, provide direct information about the formation of CdS particles and particles size distribution. Photoluminescence excitation (PLE) spectra resemble very much respective UV-visible absorption spectroscopy. PLE measurements confirmed directly the blue spectral shift in respect to bulk CdS caused by CdS nanoparticles formation inside the LB films, a fact previously observed with UV-vis absorption spectroscopy. A large Stokes shift of photo-luminescence emission (PL) can be related to the formation of “dark excitons” in the platelet-type CdS nanoclusters.

However, in order to find out the origin of photoluminescence bands of the photoluminescence spectra, it is important that temperature dependent photoluminescence and lifetime of luminescence peaks measurements be carried out, since each recombination centre has different temperature behaviour and emission lifetime.

The aggregation of CdS molecules in the LB layers, and thus the size of the nanoclusters formed, can be controlled by using organic cavitand compounds instead of fatty acids. In particular, much smaller CdS nanoparticles (as compared to those formed in fatty acid LB films) have been formed in calixarene LB films. Transformations in the size of CdS nanoparticles were studied by UV-visible absorption spectroscopy.

Two-dimensional aggregation of CdS nanoparticles in the LB films is a well – known phenomenon. It requires complex mathematical tools for analyzing their formation. An elegant two-dimensional diffusion model was proposed and the model provides a qualitative description of principal features of the two-dimensional aggregation of CdS in the LB films. Resulting size distribution of CdS nanoparticles can also be adequately predicted.

# CHAPTER 6

## SURFACE PLASMON RESONANCE (SPR) AND ELLIPSOMETRY STUDIES OF LB FILMS CONTAINING CdS NANOPARTICLES

### 6.1. Introduction

This chapter provides a combined surface plasmon resonance (SPR) and ellipsometry study of Langmuir-Blodgett (LB) Films containing cadmium sulphide (CdS) nanoparticles. CdS nanoparticles formed inside LB films of stearic acid (SA) and calix[8]arene (CA) by exposing the LB films to H<sub>2</sub>S gas.

Among optical sensing techniques, surface plasmon resonance (SPR) is one of the most sensitive methods. This inherent property makes SPR well suited for non-destructive studies of surfaces, interfaces and very thin layers. The SPR technique can be used to determine the optical constants of a material and uniformity of deposition across a LB film. However, single SPR measurements do not offer simultaneous evaluation of optical parameters, i.e. thickness ( $d$ ), refractive index ( $n$ ) and extinction coefficient ( $k$ ) of LB films. The problem was tackled here by undertaking an independent measurement of ellipsometry, another unique optical reflectance method, in conjunction with SPR studies. The ellipsometry technique can yield accurately

information about layers. This method is able to probe a range of optical properties, including the layer thickness, refractive index and extinction coefficient.

Although several optical experiments have been done to study the growth of the particles, the mechanism of the formation of CdS nanoparticles inside LB films is still not well known. In order to aid the understanding about it, the process of the formation of CdS nanoclusters in LB films was studied in situ by using SPR technique. The changes of the optical parameters of LB films were monitored during the exposure of samples to H<sub>2</sub>S gas.

In this chapter, detail principles of the experimental methods of both SPR and ellipsometry are described in Section 6.2, while the descriptions of experimental techniques are given in Section 6.3. Section 6.4 presents the results of the measurements along with the discussion, and then briefly summarised in Section 6.5.

## 6.2. Principles of the Experimental Methods

### 6.2.1. Surface Plasmon Resonance (SPR)

The surface sensitivity of surface plasmon resonance has led to its exploitation in numerous applications. Initial application of SPR involved the investigation of optical properties of thin metal films. It has grown into a versatile technique used in variety of applications, including refractive index measurements, thin film characterisation and biosensing. This optical detection technique investigates the effect organic films have on the surface plasmon resonance properties of a thin metal film.

The surface plasmons are usually excited by coupling the transverse-magnetic (TM) polarized energy contained in an evanescent field to the plasmon mode on a metal film. The number of coupling, and thus the intensity of the plasmon, is directly affected by the refractive indices of materials on both sides of the metal film. If the sample is put on one side of the film, changes in the refractive index of the sample can be monitored by measuring changes in the evanescent field to surface plasmon coupling efficiency. Surface plasmons represent the quanta of the oscillations of surface charges that are produced by application of an external electric field to a conducting medium. The dispersion relation for nonradiative plasmons is given in the following expression for a plasmon wavevector [Gordon and Swalen, 1977]:

$$k_{sp} = \frac{2\pi}{\lambda} \sqrt{\frac{\epsilon_m \epsilon_d}{\epsilon_m + \epsilon_d}} \quad (6.1)$$

where  $k_{sp}$  is the wavevector of surface plasmon along the x-direction,  $\lambda$  is the wavelength of the excitation light,  $\epsilon_m$  and  $\epsilon_d$  are the real part of the dielectric constant of the metal and the medium outside the metal, respectively.

If the excitation light is incident to the surface with an angle of  $\theta$ , then wavevector of the light incident on the surface is given by

$$k_x = \frac{2\pi}{\lambda} n_p \sin \theta \quad (6.2)$$

where  $n_p$  is the refractive index of the prism. It must be noted that the dielectric constant is the square root of the refractive index. Figure 6.1 shows a graphical representation of wavevector matching.

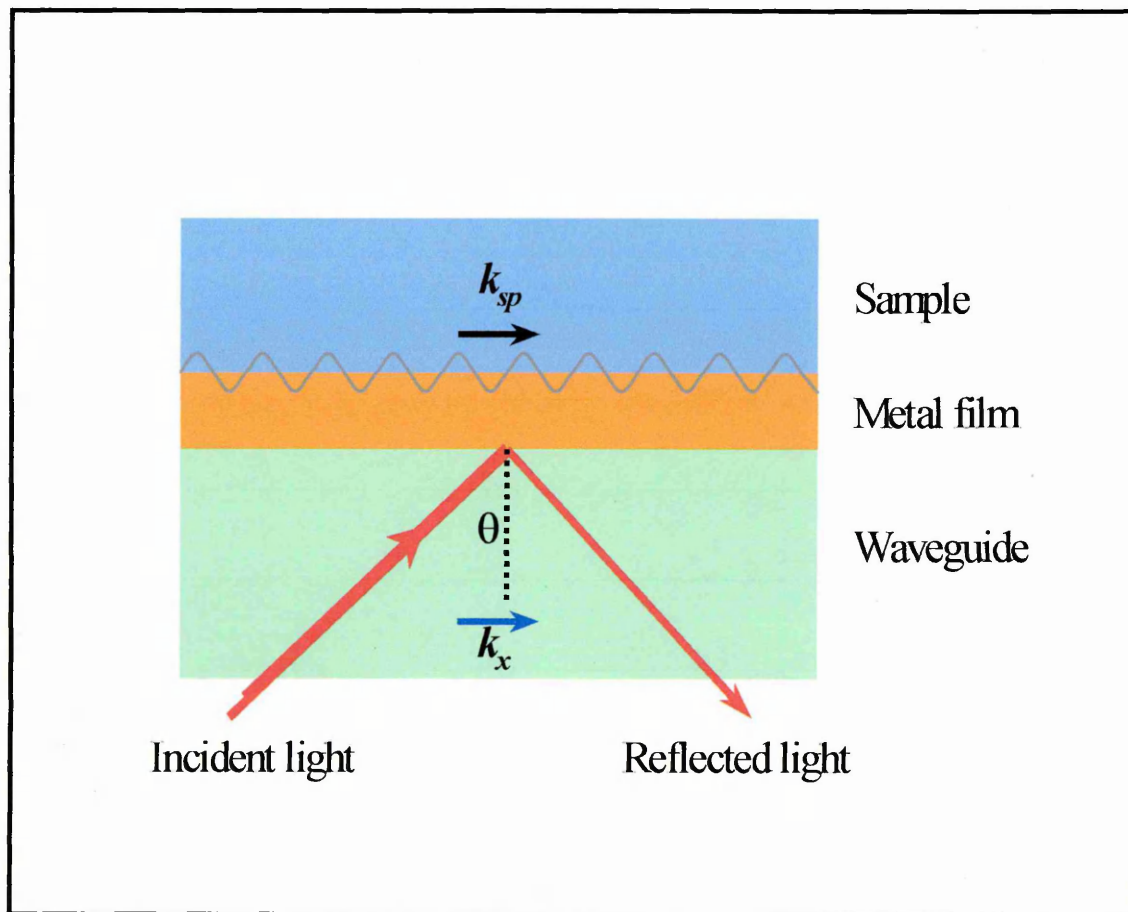


Figure 6.1. Graphical representation of wavevector matching [after De Bruijn, 1991]

It is important to remark that only p-polarized light can be coupled into the plasmon mode; because this particular polarization has the electric field vector oscillating in a plane of incidence, which is normal to the plane of the metal film. This is sometimes referred to as the transverse magnetic (TM) polarization in reference to its magnetic field vector orientation.

Two kinds of prism configuration can be used to perform SPR: Otto and Kretschmann arrangements. Both arrangements use a prism in the experimental set-up, with Kretschmann using prism/metal/air (PMA) and Otto using prism/air/metal (PAM). In PAM configuration an evanescent field is present in the air gap under the total internal reflection conditions. If the metal layer is close enough, the evanescent field can generate surface plasmons. In case of PMA the evanescent field penetrates the metal film directly, making such configuration sensitive to film thickness. This fact makes the Kretschmann configuration to be more appropriate for the purposes of this experiment.

The Kretschmann prism arrangement is essentially a structure where a glass substrate coated with a thin film of metal is brought into a direct optical contact with one side of prism, which has a high refractive index, 1.4 – 1.7. A ray of light propagates into the prism and couples into a surface plasmon (SP) that can exist in a metal film.

Using the Kretschmann prism arrangement, it is possible to couple light into surface plasmons (SP). Surface plasmon resonance may occur when the component of the light wavevector matches the wavevector of the surface plasmon. Varying the frequency of the light or varying the angle of incidence can achieve SPR. The reflected intensity of the light drops dramatically at the point resonance occurs. The position of the SPR is extremely sensitive to the refractive index of the sample. Hence, SPR is an excellent technique for measuring refractive index, as well as thickness of thin film.

The SP can be described as an oscillation of electrons on the surface of a solid, typically a conductor, however SP waves have been generated on the surface of semiconductors as well. Thin conductive film (usually gold) is commonly used to support the SP. The surface chemistry of gold and its resistance to oxidation make it the prime choice for SPR experiments although many other materials, such as Ag and Cu can support SP waves. The main criterion for a material to support SP waves is that it has a negative real dielectric component. The thin film used for support of the SP will be surrounded on both sides by a dielectric material. The SP can exist at the metal-dielectric interface within which it is possible to have components of an external electric field,  $E$ , present in both media.

This electric field will have a distribution throughout the interface, which will begin or end at charges contained on each of the interface constituents. The SP mode, which has an electric field that decays into the surroundings, is trapped within the interface. This surface mode will be bound to a charge density wave of electrons that oscillate on the metal film, and by changes in optical properties of the surroundings this surface mode will be greatly influenced. Figure 6.2 shows the mechanism by which an external electric field is coupled to the SP mode. This technique is known as the Kretschmann prism arrangement.

SPR curves are registered experimentally by scanning the angle of incidence and measuring the reflected light intensity. Altering the angle of incidence changes the component of the wavevector parallel to the prism base. Surface plasmons are excited when this component matches the real part of the surface plasmon wavevector (at  $\theta_0$ ). This process may be detected by a pronounced reduction in the intensity of the reflectivity as shown in Figure 6.3.

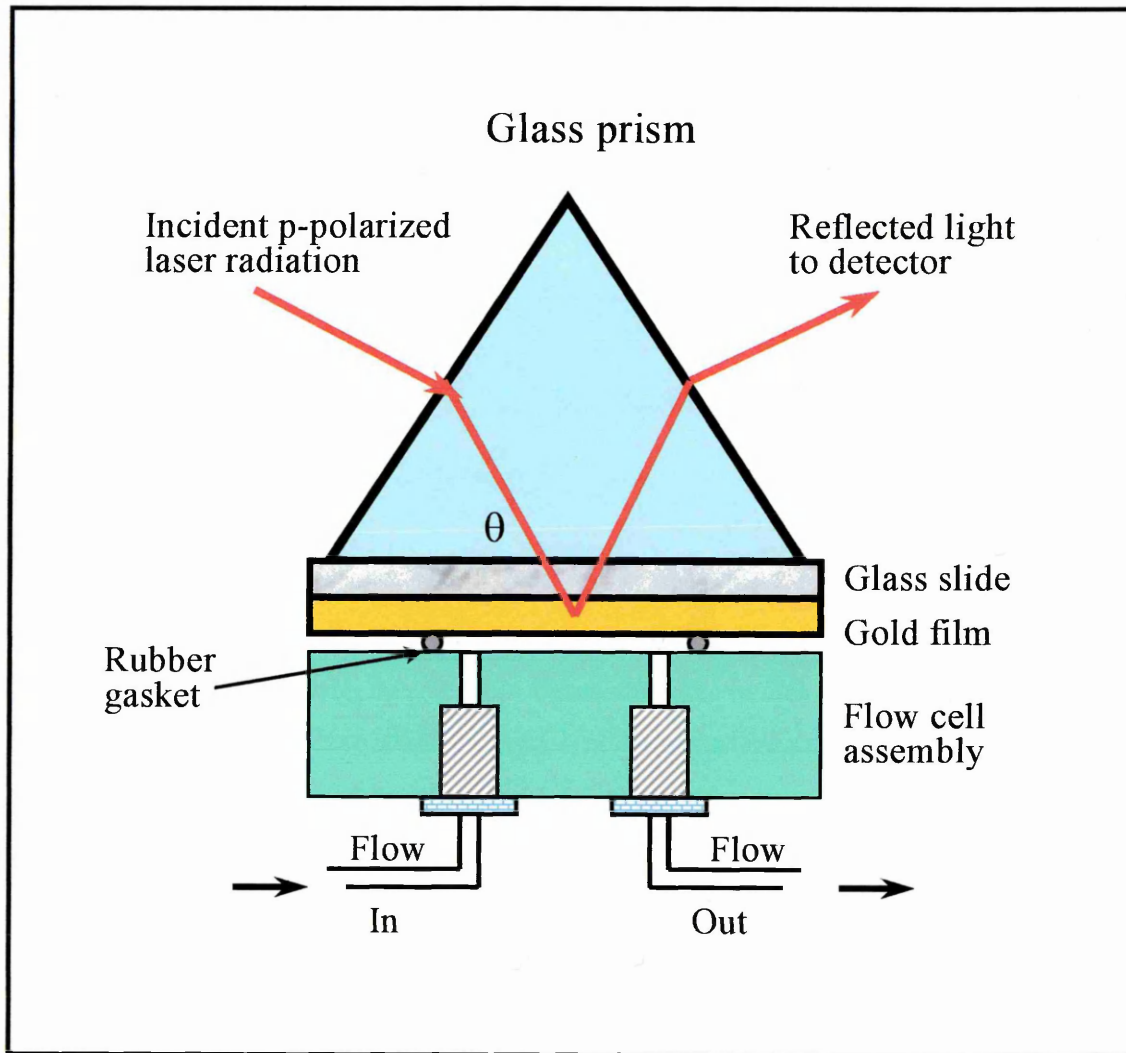
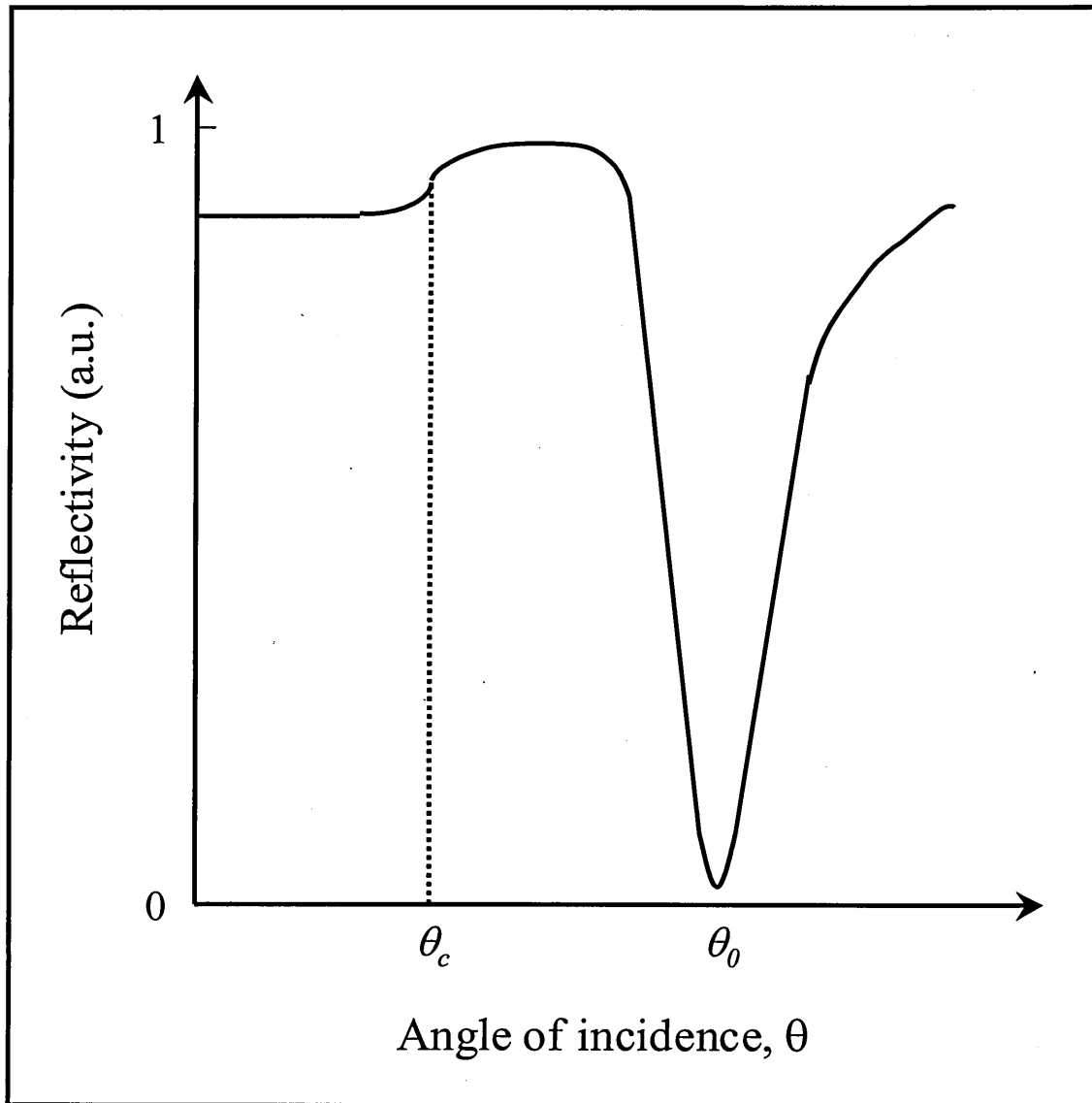


Figure 6.2. Kretschmann's prism arrangement [after De Bruijn, 1991]



*Figure 6.3. Typical SPR curve of metal film, showing critical angle ( $\theta_c$ ) and angle of incidence minimum ( $\theta_0$ )*

The position of the SPR minimum and the half-width of the SPR curve depend on the optical parameters (thickness, refractive index, and extinction coefficient) of metal film. The optical coupling is considered to be complete if the reflected intensity disappears at the resonance angle. The presence of a thin dielectric film on the metal surface causes shift the surface plasmon dispersion curve to higher momentum. Consequently, the SPR curve will move to higher angle and possibly broadening of the SPR curve. Figure 6.4 shows the experimental SPR curves for calix-4-resorcinarene monolayers deposited onto gold film [Hassan et al, 1999]. The optical constants (refractive index and film thickness) for the organic film can be obtained from the curves by using a least-squares fit to the exact Fresnel equations. However, it is impossible to determine optical constants ( $d$  and  $n$ ) simultaneously without performing another measurements such as SPR in another different medium or ellipsometry measurement [Hassan et al, 1999].

SPR technique can also be used for sensing. In such type of application, changes in the optical parameters of an active layer in response to external ambients are monitored. The first work on this subject was performed by the Lincöping group who studied gas sensing and biosensing application of SPR [Liedberg et al, 1983; Nylander et al, 1983]. An angle of incidence close to the plasmon resonance angle was chosen, and changes in the resonance angle and in reflected intensity were found. LB films of calix-4-resorcinarene have also been used as the gas sensing layer in detectors based on SPR [Hassan et al, 2001]. A fixed angle of incidence of  $\theta^* = 46^\circ$  was chosen for the kinetic measurements during the flow of ethylbenzene vapour into the gas cell (in situ measurement). Figure 6.5 presents the effect of ethylbenzene vapour in shifting of the coupling angle for the SPR curve of the unexposed LB film.

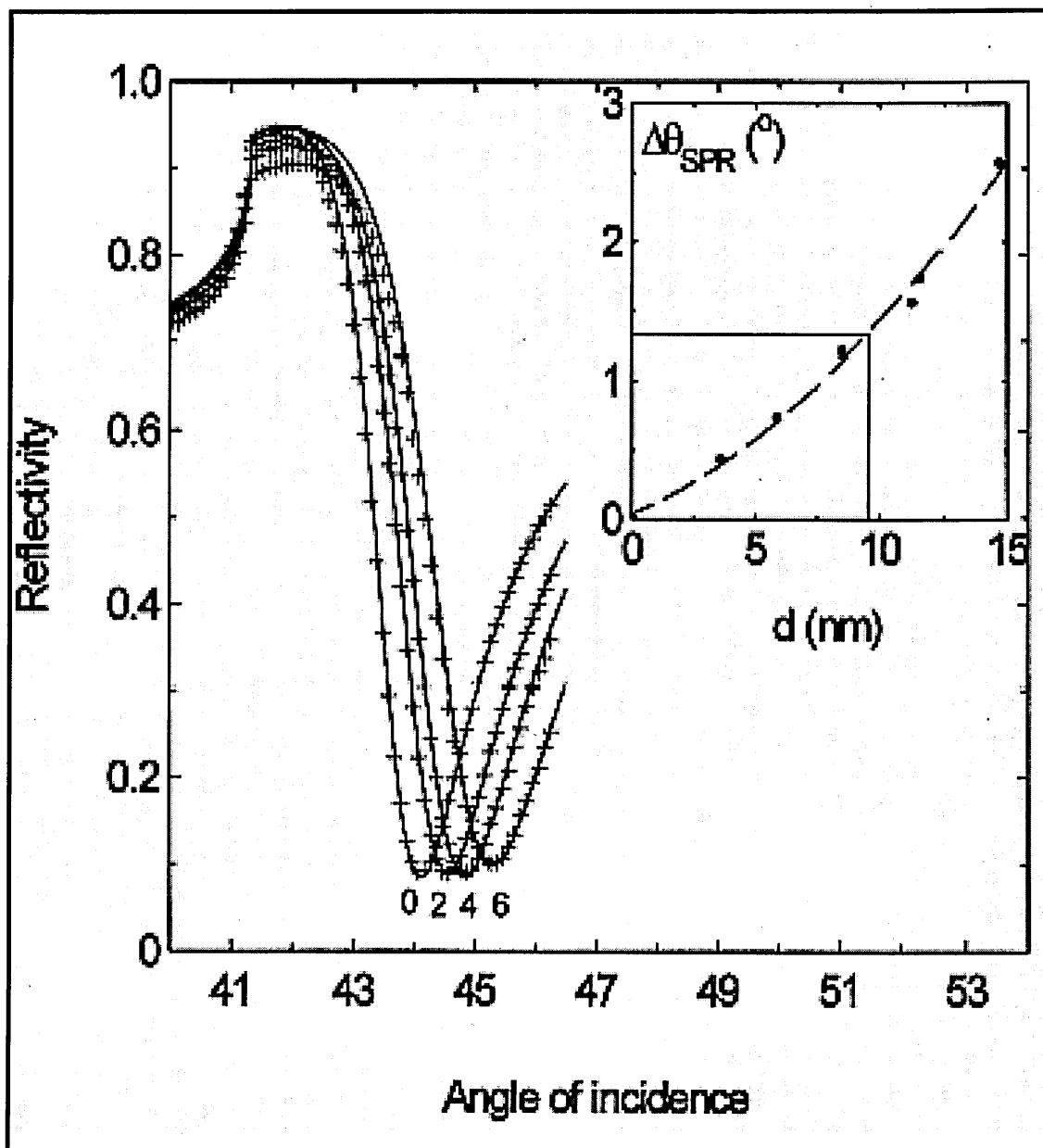


Figure 6.4. Experimental SPR curves for gold film, and those of LB films of calix-4-resorcinarene coated on it. The number of monolayers is indicated on the corresponding curve. The inset presents the dependence of resonance shift ( $\Delta\theta_{SPR}$ ) on the thickness of the LB films [after Hassan et al, 1999].

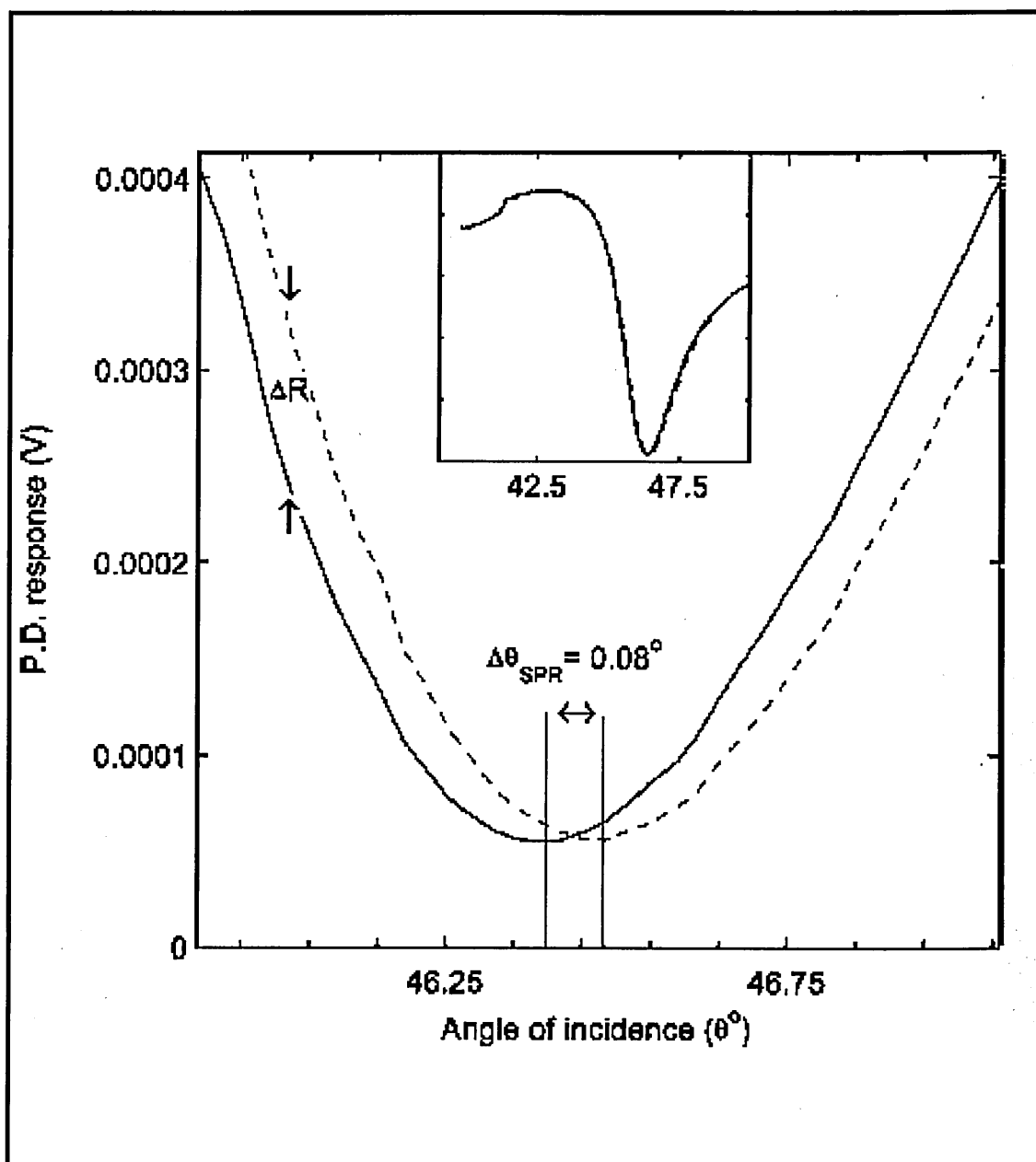


Figure 6.5. SPR curves of LB film of calix-4-resorcinarene before (solid line) and during (broken line) exposure to ethylbenzene vapour. The inset shows the full measured SPR curve [after Hassan et al, 2001].

## 6.2.2. Ellipsometry

Ellipsometry is non-destructive optical technique for investigation of thin organic films, which based on measurements of the ellipticity of polarized light due to its reflection from the surface under investigation. The name “ellipsometry” stems from the fact that the most general state of polarization is elliptic. This technique is a sensitive optical reflectance technique that is extensively used for the determination of the optical constants of thin films (refractive index, thickness, extinction coefficient). The technique can probe a range of properties including the layer thickness, refractive index, extinction coefficient, morphology, or chemical composition. Today, the method has many standard applications. It is mainly used in semiconductor research and fabrication. However, ellipsometry is also becoming more interesting to researchers in other disciplines such as biology and medicine.

The reflectivity from a surface differs in both amplitude and phase for s- and p-polarized incident radiation. A comparison of these reflectivities is ellipsometry [Swalen, 1986]. The presence of a surface film alters the ratio of the electric vectors vibrating in the plane of incidence and perpendicular to it. The theory of ellipsometry relates the parameters  $\psi$  and  $\Delta$  to the optical thickness of the layer and the optical constants of the surface (isotropic non-absorbing film).

$$\Psi = \Psi(n,d) \quad (6.3)$$

$$\Delta = \Delta(n,d) \quad (6.4)$$

The reflection behaviour can be fully described by two Fresnel coefficients, if there is no mixing between the polarizations. The change of the state of polarization upon reflection can be expressed in terms of the ratio of the two complex reflection

coefficients  $r_p$  and  $r_s$  for light polarized parallel and perpendicular to the plane of incidence [Azzam and Bashara, 1977]

$$\rho = \frac{r_p}{r_s} = \tan \psi e^{i\Delta} \quad (6.5)$$

It is common to measure indirectly the ratio of these quantities by finding  $\psi$  and  $\Delta$ . The exact mathematical dependence of  $n$  and  $d$  on  $\psi$  and  $\Delta$  is given by Fresnel's formulas. The numerical solution of Equation (6.5) for transparent dielectric film is given graphically in the Figure 6.6. The distance along the curve for each refractive index ( $n$ ) represents film thickness ( $d$ ).

The angle  $\psi$  is the ratio of the amplitudes of the s- and p- components of the elliptically polarized light,

$$\Psi = \tan \left( \frac{A_s}{A_p} \right) \quad (6.6)$$

and  $\Delta$  is the phase difference between the s- and p- components,

$$\Delta = \varphi_s - \varphi_p \quad (6.7)$$

Experimentally, by setting compensator at  $\pm 45^\circ$  and adjusting the orientation of the polarizer (angle called P) and analyser (angle called A) the intensity of the light reaching the photodetector is zero. Using at least two different measured values of each of A and P, the values of  $\psi$  and  $\Delta$  can be determined as follows:

$$\Delta = P_1 + P_2 \quad (6.8)$$

$$\Psi = [(180 - A_2) + A_1] / 2 \quad (6.9)$$

Theoretical values of  $\Psi_{th}$  and  $\Delta_{th}$  can be obtained from the solution of a forward ellipsometric problem:

$$\tan \Psi e^{i\Delta} = 1 \quad (6.10)$$

In order to determine the complex refractive index of the substrate ( $n_1 - ik_1$ ), where  $n_1$  is the refractive index and  $k_1$  is the extinction coefficient, a reverse ellipsometry problem is designed. The Nelder-Mead algorithm is employed for minimization of the error function,

$$E = \sqrt{(\Psi_{exp} - \Psi_{th})^2 + (\Delta_{exp} - \Delta_{th})^2} \quad (6.11)$$

where  $\Psi_{exp}$  and  $\Delta_{exp}$  are experimental values. The analysis of ellipsometric data allows the evaluation of optical parameters of the substrate and those of multilayer film by using Equation (6.8) - (6.11).

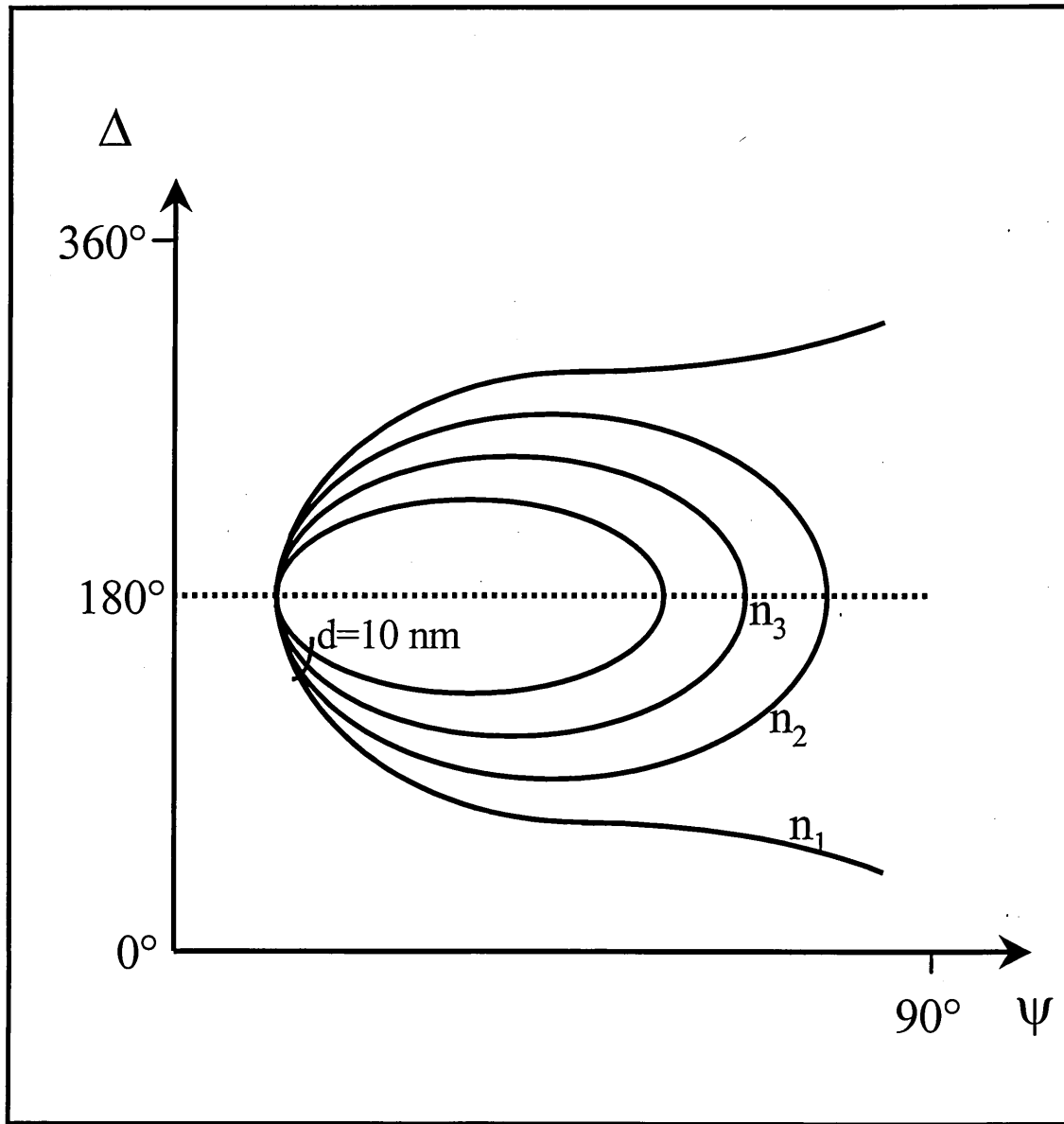


Figure 6.6. Numerical solution of the equation (6.5) for transparent dielectric film

In this present work, the formation of CdS nanoparticles formed inside LB films was monitored *in-situ* changes by the SPR technique during exposure to H<sub>2</sub>S gas. The complex refractive index (n) and thickness (d) of the LB films (before and after H<sub>2</sub>S treatment) are also determined. Because the change in reflectivity starts to deviate at large absorption (thick film: more than 10 nm), the SPR fitting procedure can precisely determine the optical parameters especially for thinner films [Swalen, 1986]. On the other hand, the thinner films only give much smaller angular shifts and the computational procedure (fitting procedure) does not converge well. As a result, only one parameter could be determined accurately. In order to tackle this problem, both SPR and ellipsometry measurements needed to be performed. The value of the refractive index of the LB films, which is obtained from ellipsometric measurements, is used as a starting value. On the other hand, ellipsometry has the disadvantage of not being suitable for determining the optical parameters of thinner films (lower 10 nm). As can be seen from Figure 6.6, all curves are very close and accuracy of evaluation of n and d is poor. The ellipsometric fitting procedure does not converge well in this range. As a result, it is difficult to get the accurate value with high resolution of the optical parameters in thinner LB films. This is why thicker films (20-60 layers) are prepared on which to perform the ellipsometry measurement.

### 6.3. Experimental Details

Langmuir-Blodgett (LB) films of Cd-salts stearic acid (SA) and calix[8]arene (CA) were deposited by the LB technique. Two to eight layers thick of LB films were transferred at a constant surface pressure of 25-28 mN/m onto gold (Au) coated glass slides for SPR measurements. 20 to 60 layers of SA and CA LB films were deposited onto a silicon wafer for ellipsometry. A 50 nm thick gold (Au) coating was formed on the surface of microscopic glass slides by thermal evaporation technique. A procedure of the thermal evaporation for deposition Au thin film on glass slides will be described in Chapter 7. Cadmium Sulphide (CdS) nanoparticles were formed within the LB films during exposure of the samples to H<sub>2</sub>S gas.

Surface Plasmon Resonance (SPR) measurements were performed using an in-house made Kretschmann type experimental set-up as shown in Figure 6.7. Two types of SPR measurements were carried out on the samples of 2-8 layers thick:

- (i) Registration of the whole SPR curve over the angle range of 39-51°; and
- (ii) Monitoring of the reflected light intensity at a fixed angle of incidence chosen on the left linear side of the curve close to a minimum.

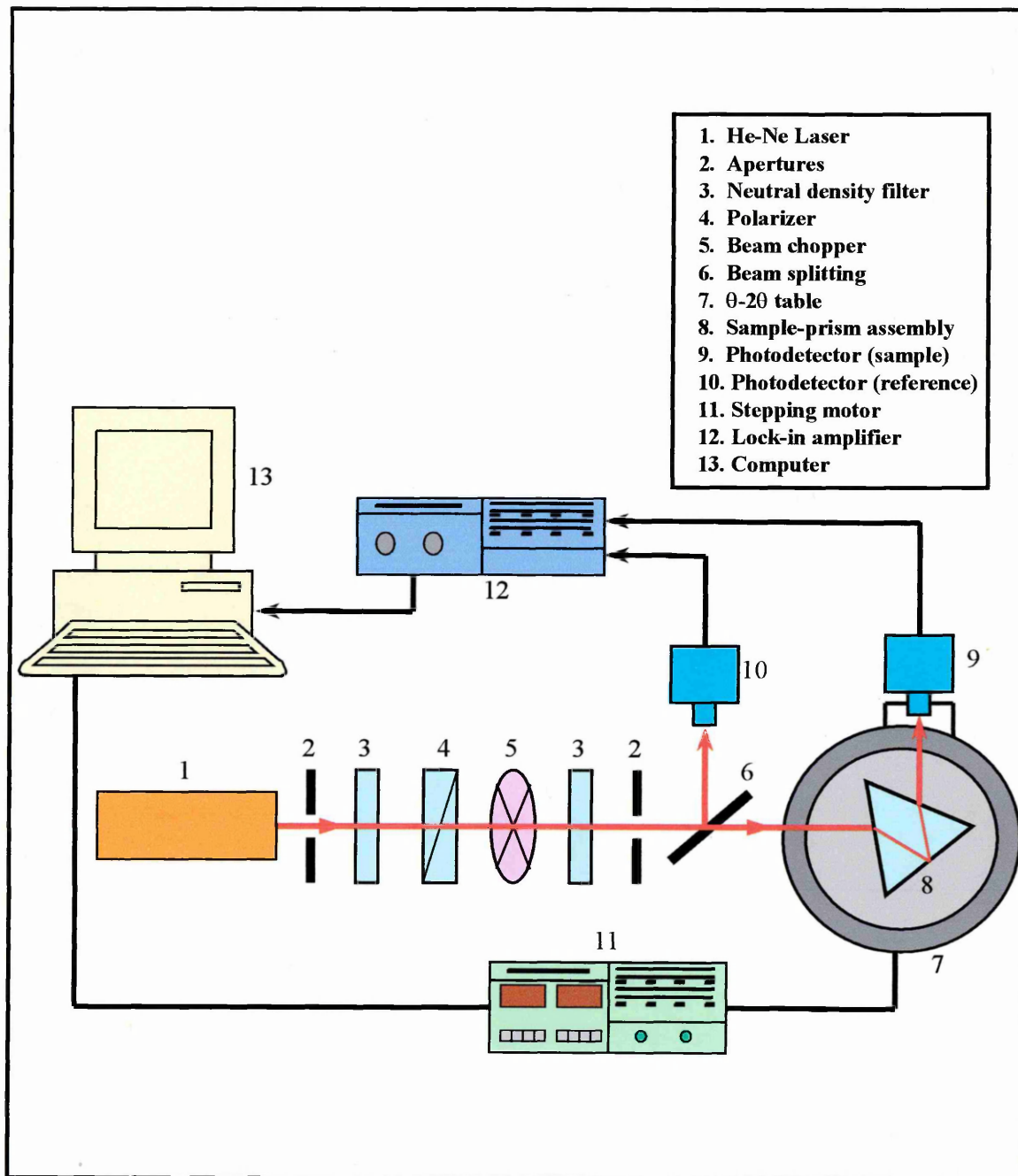
The latter was used to monitor *in-situ* the formation of CdS nanoparticles within LB films.

The glass side (sample) is coupled to a prism by using index matching fluid and a beam of p-polarized He-Ne laser light at 633 nm is directed into the prism. The beam was passed through an optical chopper before being focused onto the prism. The reflected light from the sample is detected by a photodiode with the entire prism arrangement mounted on a rotating table. This allows measurement of the reflectivity across a range of angles, beginning below the critical angle and scanning past the angle

at which surface plasmons are produced. The signal from the sample was then fed into the lock-in amplifier, which used a signal from the beam splitting as a reference. With this set-up all the background current and noise, which is not at the same frequency as the chopper, is eliminated. The whole set-up is microprocessor controlled.

The optical parameters of the LB film, i.e. thickness ( $d$ ), refractive index ( $n$ ) and extinction coefficient ( $k$ ) were evaluated by fitting the experimental SPR curves to Fresnel's theory using a least-square technique [Nabok *et al*, 1997].

Ellipsometry measurements were performed on the same compounds samples of thicker LB films of 20-60 layers using zero-type "Nanotechnology" instrument. Figure 6.8 shows the experimental set-up for ellipsometry measurement. The values of thickness ( $d$ ), refractive index ( $n$ ), and extinction coefficient ( $k$ ) were evaluated from the experimental parameters of  $\Psi$  and  $\Delta$  by solving the reverse ellipsometric problem using least-square algorithm [Bruijn *et al*, 1991].



- 1. He-Ne Laser
- 2. Apertures
- 3. Neutral density filter
- 4. Polarizer
- 5. Beam chopper
- 6. Beam splitting
- 7.  $\theta$ -20 table
- 8. Sample-prism assembly
- 9. Photodetector (sample)
- 10. Photodetector (reference)
- 11. Stepping motor
- 12. Lock-in amplifier
- 13. Computer

Figure 6.7. An in-house made Kretschmann type experimental set-up used to obtain SPR

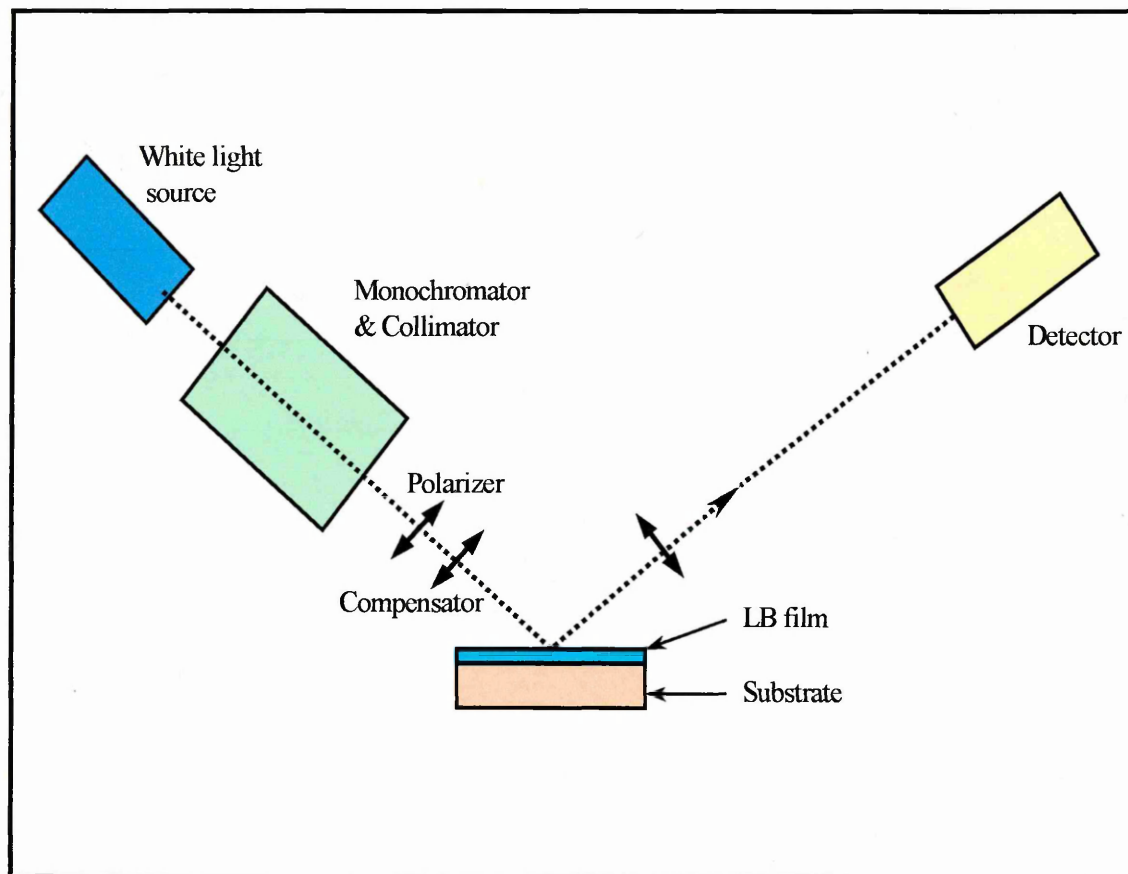


*Figure 6.8. Experimental arrangement for an ellipsometry measurement*

## 6.4. Experimental Results and Discussion

The first SPR measurement was carried out for the gold (Au) thin film coated on the glass slide showing the surface plasmon resonance angle,  $\theta_{sp}$ . The same procedure was followed by the measurement for the sample of LB film deposited on Au. The curves for both samples show an increase in reflectivity until total internal reflection is achieved. This reflectivity remains constant until the angle  $\theta_{sp}$ , at which the reflectivity decreases dramatically in relation to resonance of the surface plasmons. The position and shape of this minimum are dependent upon the thickness and extinction of the materials.

The measured SPR curves of gold thin film and overlayers of Cd-salt calix[8]arene (CA) and Cd-salt stearic acid (SA) LB films of different thickness (2-6 layers thick) are shown in Figure 6.9 and 6.10, respectively, as a dependence of reflected light intensity on the internal angle incidence.

The curves clearly show a consistent shift in the resonance toward higher angles with increasing number of LB layers with respect to the SPR curve of a bare gold. This is believed due to the presence of the calixarene or stearic acid films on the gold, while broadening of the SPR curve is probably caused by the film surface, which is rougher than that of the bare gold. The calix[8]arene and stearic acid LB films have a different refractive index, extinction coefficient and thickness to the gold. This is why they produce the change in the resonance angle of the curve. As can be seen from both Figure 6.9 and 6.10, the bare gold films exhibit resonance at an angle of around 44°. At this angle the reflectivity disappears indicating the complete optical coupling.

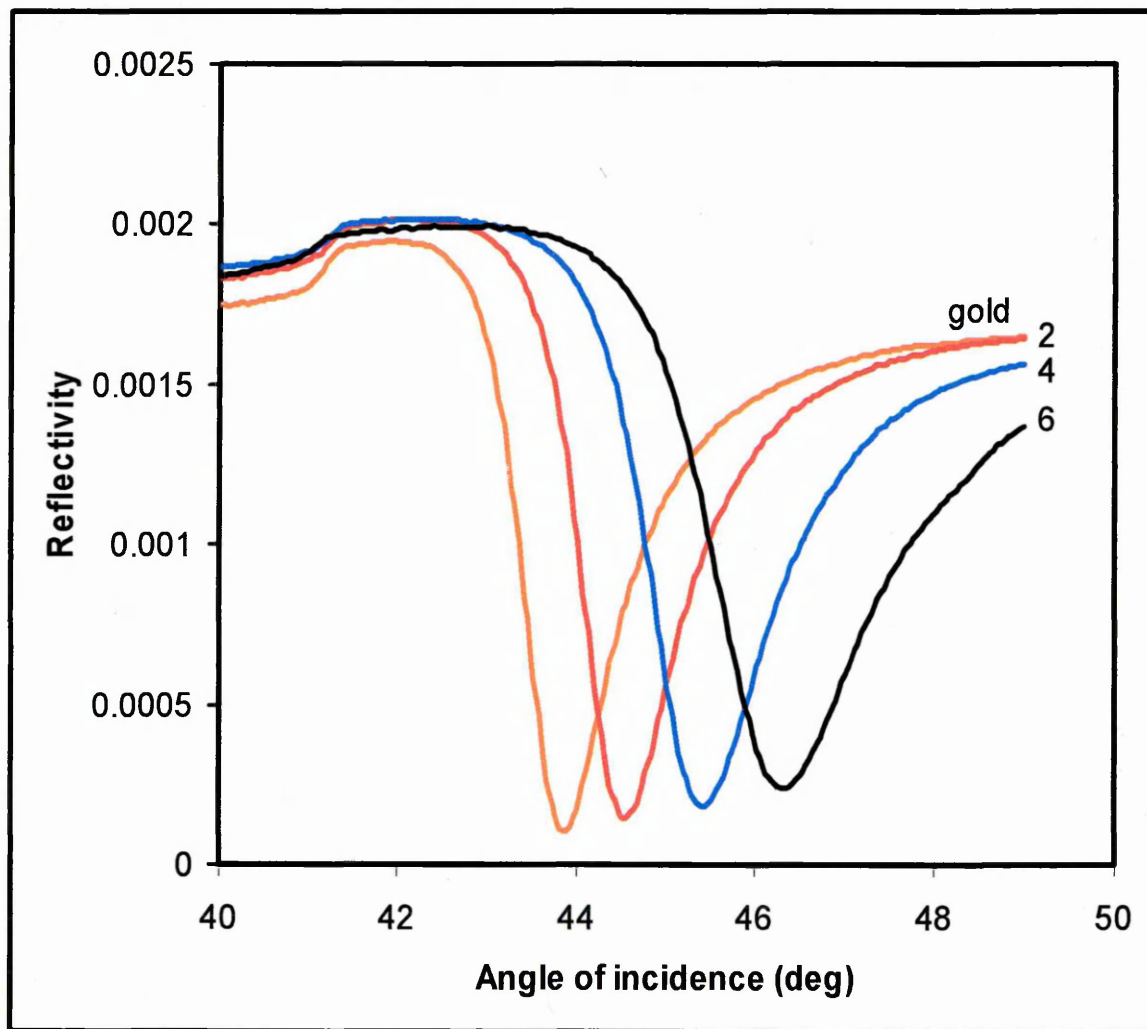


Figure 6.9. Experimental SPR curves obtained for bare gold film and overlayers of stearic acid LB films deposited on gold. The number of monolayers is indicated on the corresponding curves

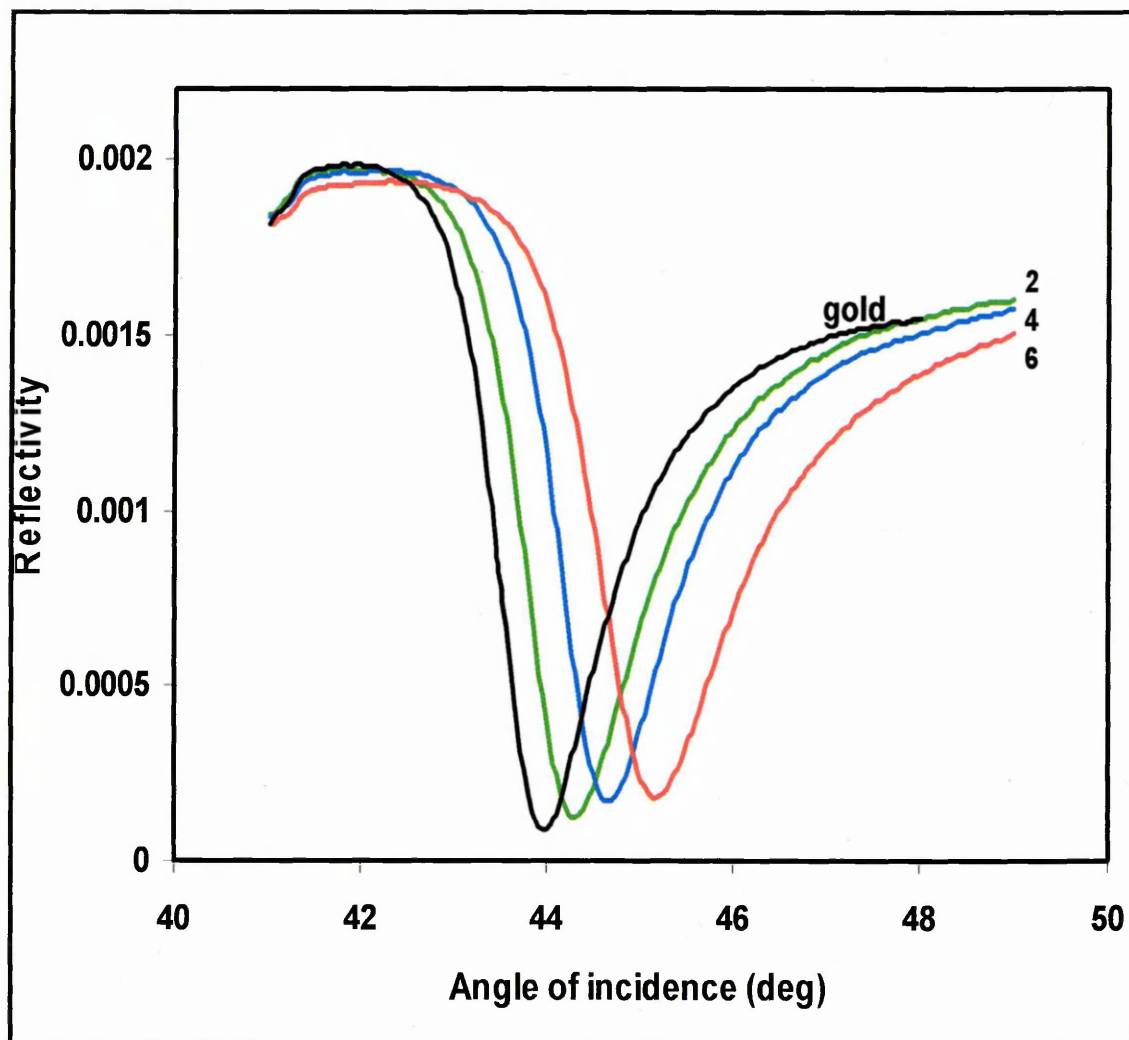


Figure 6.10. Experimental SPR curves of gold films and over layers of calix[8]arene LB films deposited on bare gold. The number of monolayer is indicated on the corresponding curves

Figure 6.11 and 6.12 show the dependence of the resonance shift ( $\Delta\theta_{\text{SPR}}$ ) on the thickness of the LB films (number of LB layers), respectively for SA LB films and CA LB films. The values of the resonance shift versus the number of layers for both LB films are shown in Figure 6.13. It suggests the increasing of the resonance shift of the LB overlayers with respect to the curve of bare gold is proportional to the number of layers of both LB films. Figure 6.13 shows that the value of the resonance shift of SA LB films is bigger than that of CA films. The average values of the resonance shift are about  $0.175^\circ$  and  $0.317^\circ$  for each layer of CA and SA LB films, respectively. These may indicate that the thickness and/or refractive index of SA LB films are bigger than those of CA LB films.

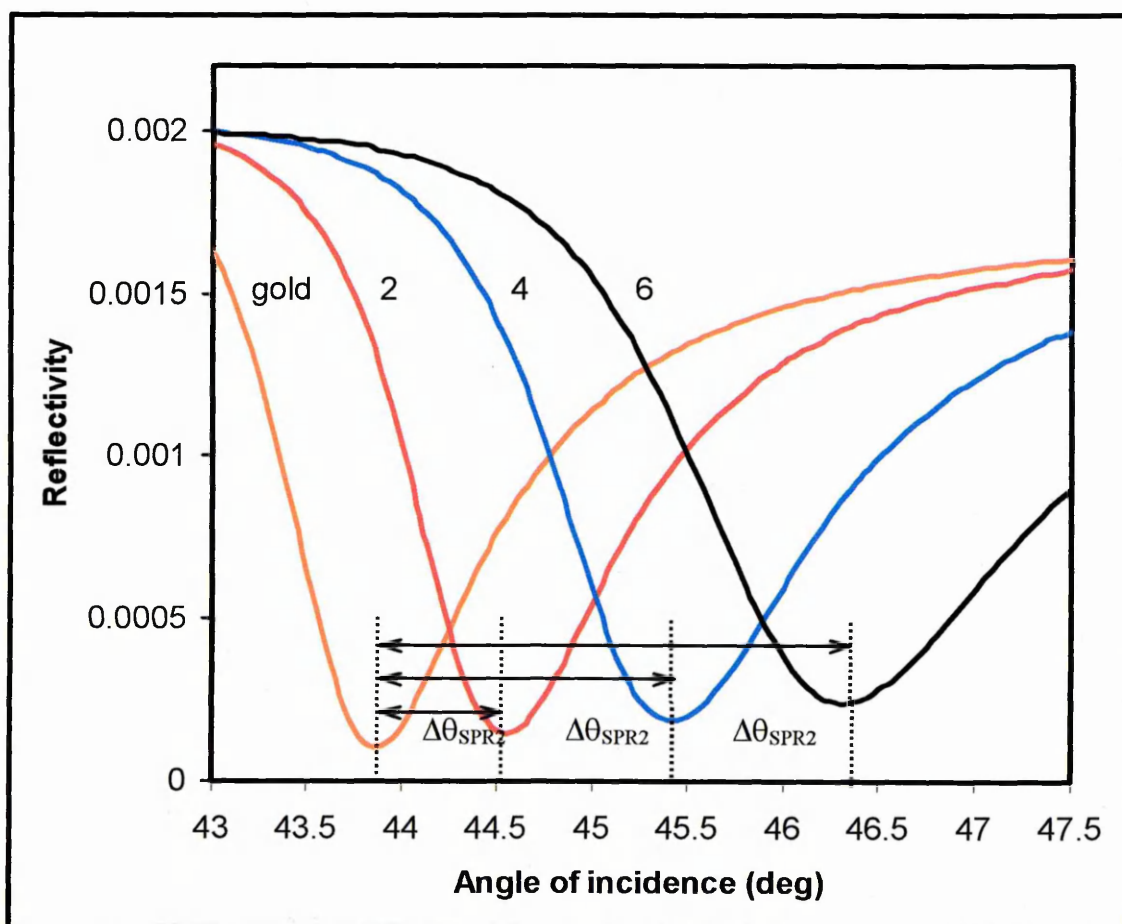


Figure 6.11. Resonance shift of SA LB overlayers with respect to Au SPR curve

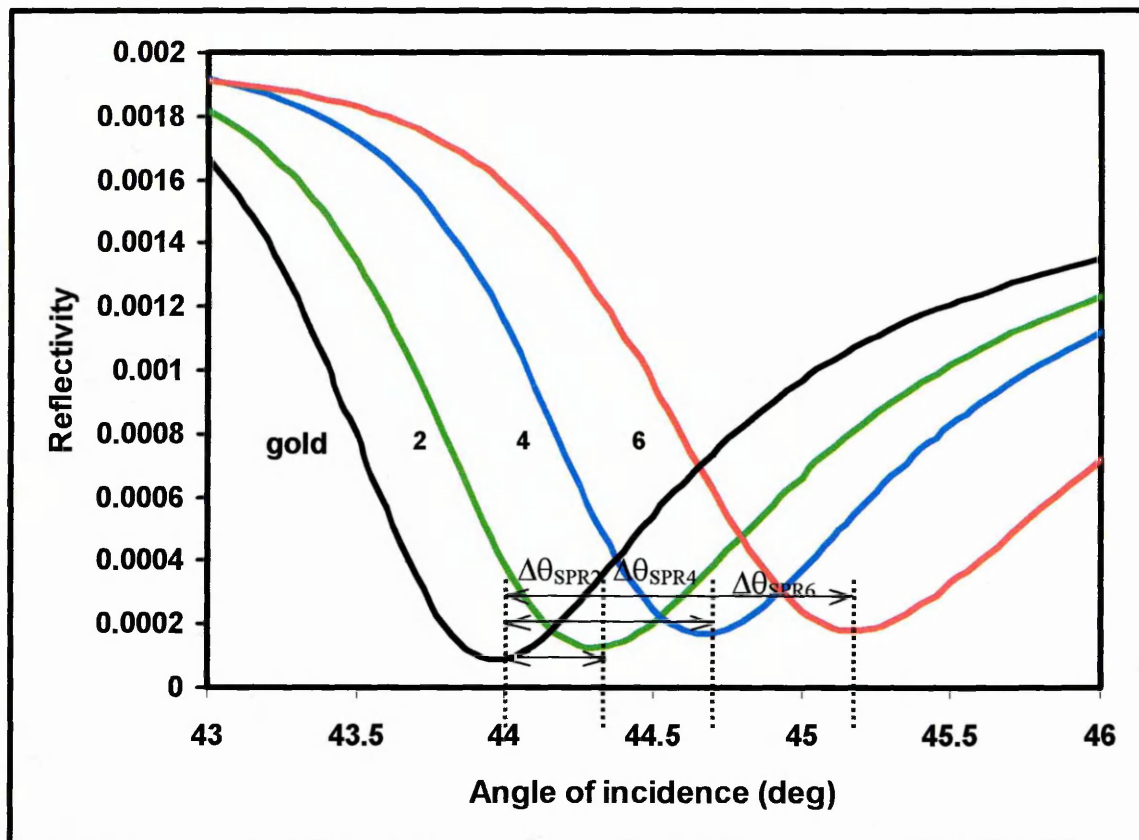


Figure 6.12. Resonance shift of CA LB overlays with respect to Au SPR curve

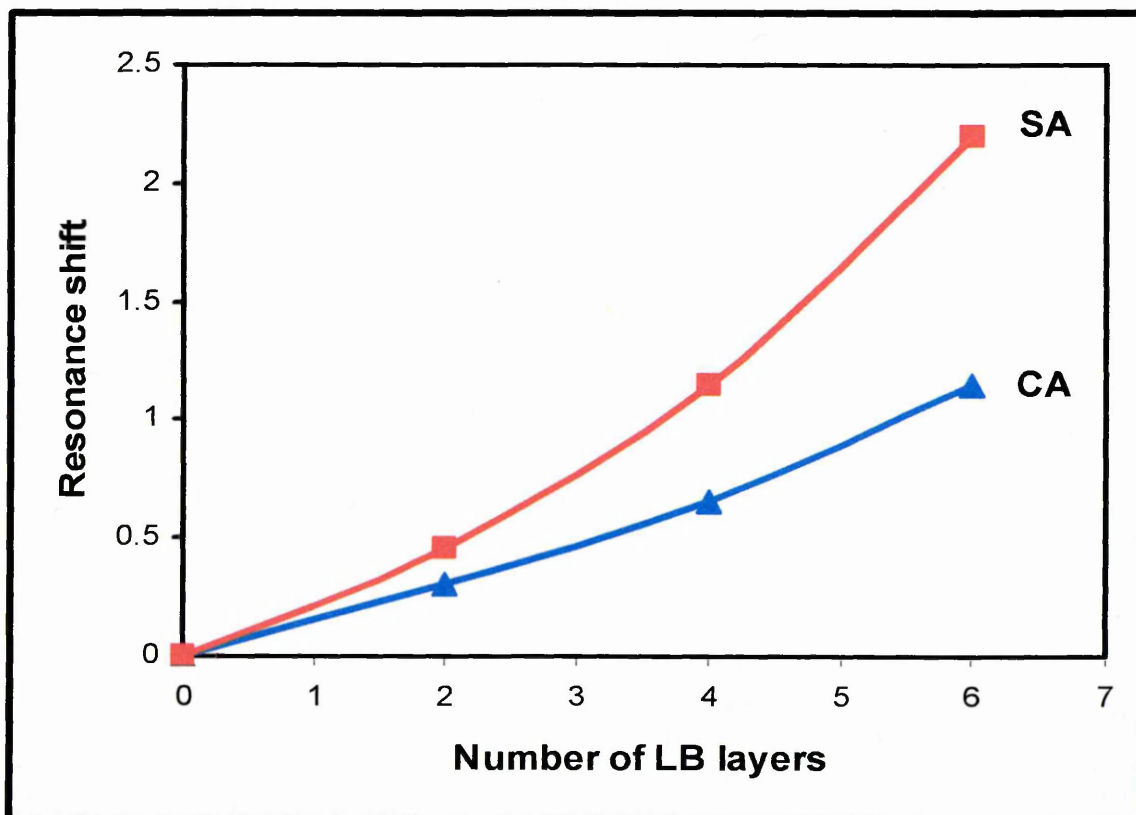


Figure 6.13. Dependence of the resonance shift ( $\Delta\theta_{SPR}$ ) on the thickness of the LB films (number of the LB layers)

The resonance shift ( $\Delta\theta_{SPR}$ ) of the SPR curve with respect to the bare metal films (including gold and silver) can be written as [Hassan et al, 2001]

$$\Delta\theta_{SPR} = \frac{2\pi / \lambda (|\varepsilon_m| \varepsilon_a)^{3/2} d_2 (\varepsilon - \varepsilon_a)}{n_p \cos \theta (|\varepsilon_m| - \varepsilon_a)^2 \varepsilon} \quad (6.12)$$

where  $\varepsilon_m$ ,  $\varepsilon$ , and  $\varepsilon_a$ , are dielectric permittivities of the metal film, dielectric overlayer, and the air (surrounding media), respectively;  $d_2$  is the dielectric film thickness;  $n_p = 1.515$  is the refractive index of the glass prism; and the angle  $\theta$  corresponds to resonance conditions in the bare gold film. The appearance of film parameters  $\varepsilon$  and  $d$  in the Equation (6.12) indicates that a simultaneous evaluation of both thickness and refractive index is not possible for transparent films. In order to tackle this problem, a method has been employed and the complement ellipsometry measurement has also been applied. In addition to that, the fact that both samples have a very small broadening and an increase in the reflectivity minimum value of the SPR curves as shown in Figure 6.11 and 6.12 indicates the LB films are very close to non-absorbing films behaviour. The ideal non-absorbing film has no broadening and an increase in the reflectivity minimum value of the SPR curve on the internal angle incidence dependence [Hassan et al, 1999]. In order to evaluate the optical parameters, i.e., film thickness ( $d$ ), refractive index ( $n$ ) and extinction coefficient ( $k$ ), of gold film and overlayers of SA and CA LB films, the SPR data have been fitted to Fresnel's reflection formula. The value of  $k$  was assumed as  $k = 0$  for both LB films, since the LB films are transparent at the wavelength  $\lambda = 633$  nm.

In present work, ellipsometry measurements of the samples were performed in order to find out the value of refractive index and the thickness of the LB films. The refractive index value was then used as an initial value for the fitting procedure. The

thickness of film found from this measurement was also introduced into the fitting programme.

Ellipsometry data ( $P_1$ ,  $P_2$ ,  $A_1$  and  $A_2$ ) for both LB films of SA and CA before  $H_2S$  treatment obtained from the measurements using the set-up shown in Figure 6.8 are presented in Table 6.1. The values of  $\Delta$  and  $\psi$  are calculated using Equation (6.8) and (6.9), respectively.

The following routine for data analysis was applied: (i) values of the extinction coefficient at 633 nm were estimated from UV-visible absorption spectra measurements; (ii) ellipsometry of relatively thick films of 20-60 layers was carried out, and previously obtained values of  $k$  were used as a fixed parameters for ellipsometry data fitting; (iii) SPR data fitting was carried out using the values of  $n$  obtained from ellipsometry as a fixed parameter. The extinction coefficient ( $k$ ) of the LB films was found from the results of UV-visible absorption spectroscopy by using Equation (5.3) and (5.4). The calculations yield the value of 0.0045 and 0.0223 for SA and CA LB films, respectively. The value of  $\lambda=633$  nm (infra red light source) and its absorbance were used for this calculation.

Table 6.1. Ellipsometry data for both SA and CA LB films before H<sub>2</sub>S treatment

P <sub>1</sub> (°)	P <sub>2</sub> (°)	A <sub>1</sub> (°)	A <sub>2</sub> (°)	Δ (°)	Ψ (°)
<u>Bare Si</u>					
40.5	130.4	10	171.2	170.9	10.55
<u>20 layers of SA</u>					
171.2	268.1	22.2	151.2	85.3	26.65
176.5	268.6	22.4	150.9	85.1	26.90
<u>30 layers of SA</u>					
172.7	264.0	26.9	145.4	76.7	31.9
173.2	264.3	26.7	146.2	77.5	31.4
<u>40 layers of SA</u>					
169.7	258.8	36.0	134.9	68.5	41.7
170.2	261.0	35.8	134.8	71.2	41.65
<u>50 layers of SA</u>					
159.5	248.9	54.6	111.3	48.4	62.8
154.4	247.1	69.8	107.5	41.5	72.3
<u>40 layers of CA</u>					
179.3	268.7	20.8	152.4	88.0	25.35
179.3	268.3	20.9	152.9	87.6	25.15
<u>50 layers of CA</u>					
175.4	264.8	24.8	147.9	80.2	29.6
174.9	264.4	24.8	147.9	79.3	29.6
<u>60 layers of CA</u>					
172.3	261.2	30.8	141.7	73.5	35.7
172.4	261.2	30.8	141.6	73.6	35.75

The derived film thickness of both LB films, which were found from SPR data fitting are plotted as a function of the number of LB layers and are shown in Figure 6.14. The derived film thickness approximates well by a linear function, and the slope yields an average thickness of a monolayer of  $2.44 \pm 0.034$  nm and of  $1.33 \pm 0.058$  nm for SA and CA LB films, respectively. Figure 6.15 shows the film thickness obtained from ellipsometry measurement as a function of the number of layer dependence. The average values of film thickness obtained from ellipsometry is  $2.42 \pm 0.090$  nm and  $1.37 \pm 0.007$  nm for SA LB and CA LB monolayers, respectively. These values are in good agreement with the results obtained by other workers: Pan *et al* [1997] of 2.50 nm, Nabok *et al.*, [1998] of 2.501 nm; and Nabok *et al.*, [1998] of 1.235 nm (by XRD), Nabok *et al.* [2000] of 1.5 nm (by ellipsometry) for SA and CA LB monolayer, respectively.

Figure 6.16 presents the variation of the refractive index with the number of the LB films, which was obtained from ellipsometry measurements. The refractive index tends to increase as the number of films increases. The mean values of refractive index and film thickness together with extinction coefficient of SA and CA LB films are presented in Table 6.2.

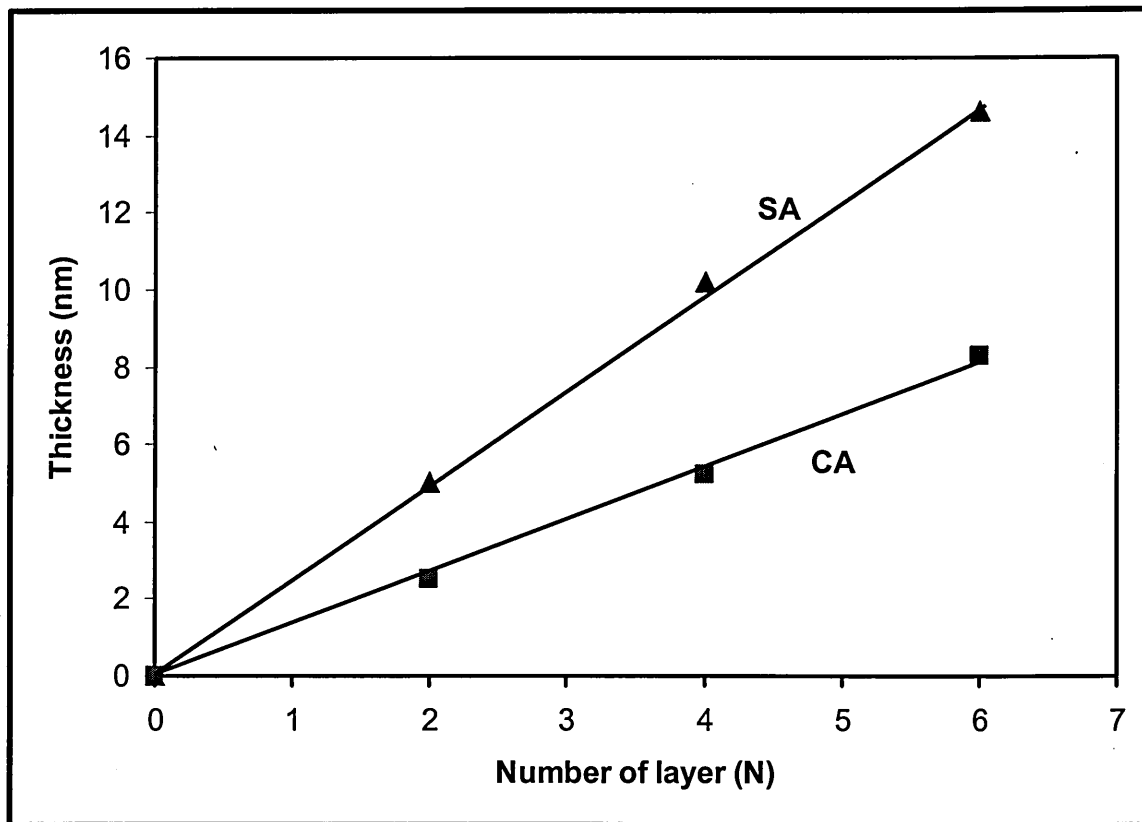


Figure 6.14. Increase in film thickness with the number of LB films acquired from SPR

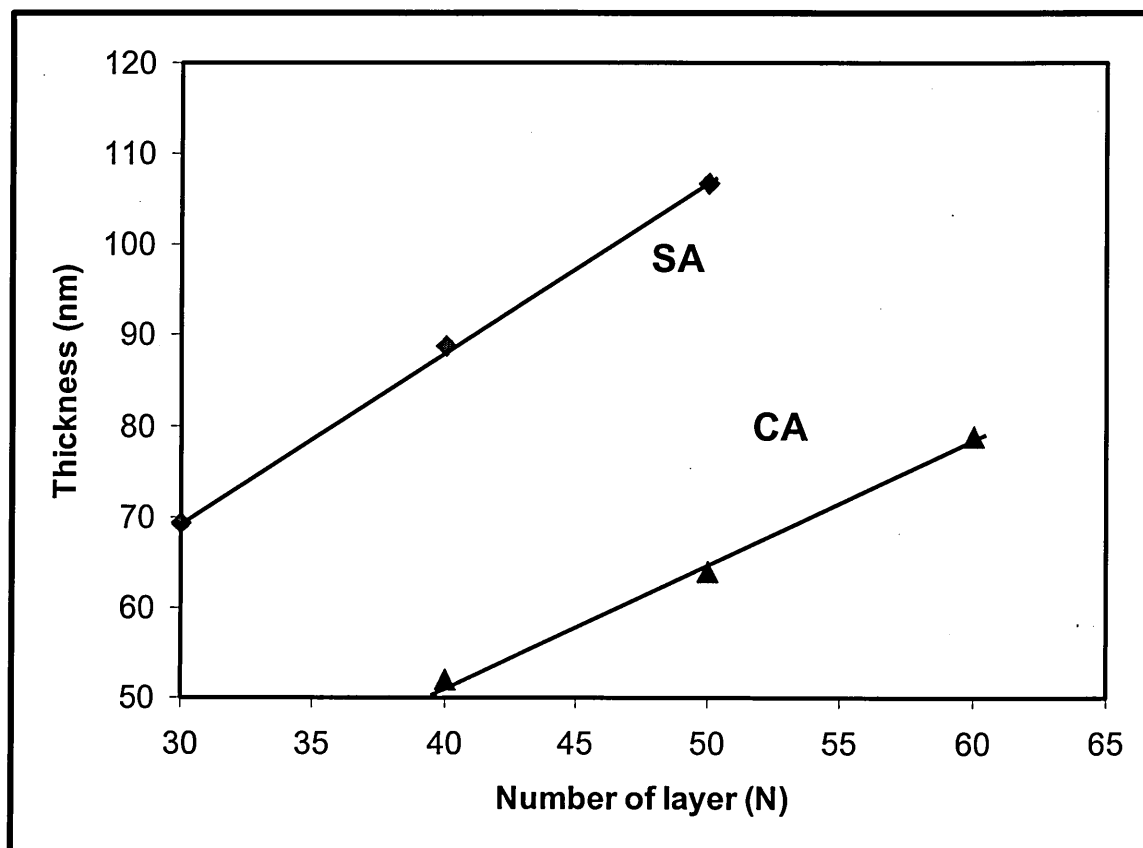
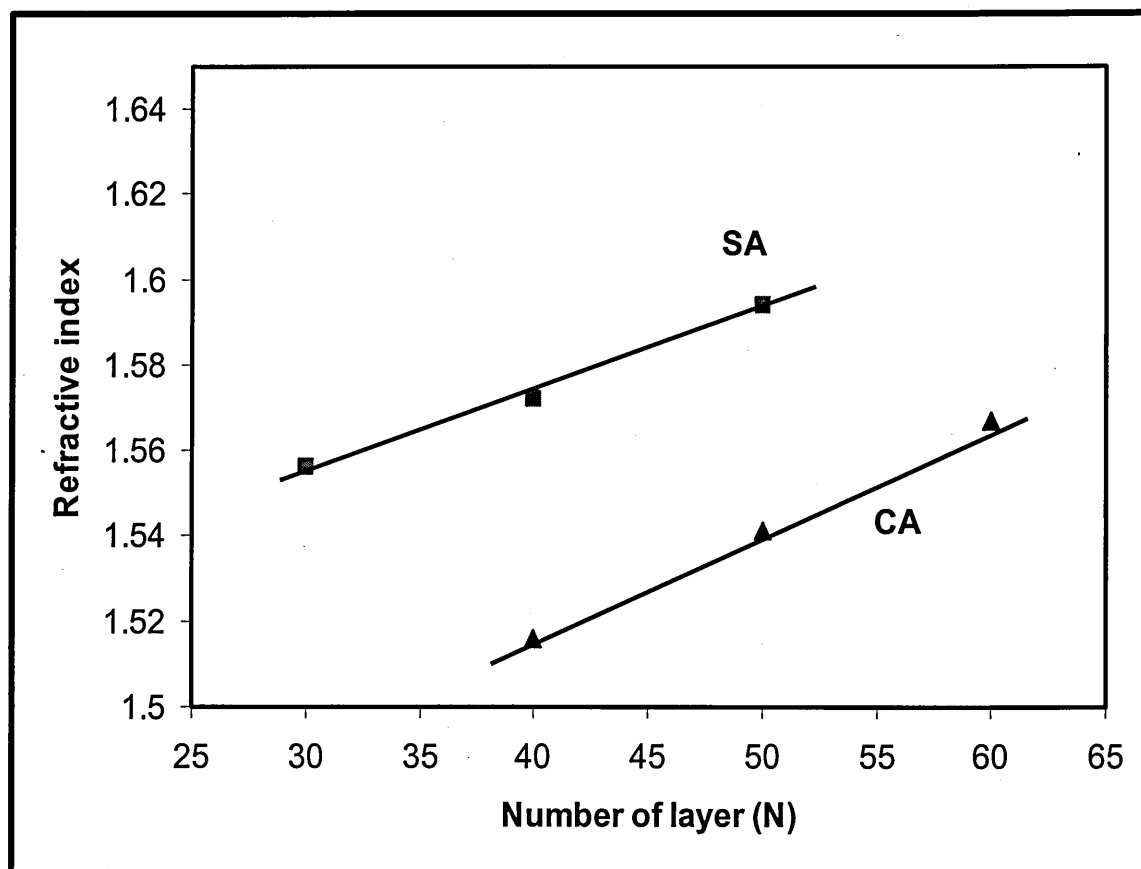


Figure 6.15. Dependence of thickness on the number of layer obtained from ellipsometry



6.16. Variation of refractive index with the number of LB films obtained from ellipsometry measurements

Table 6.2. Optical parameters of LB films obtained from UV-visible absorption, ellipsometry and SPR measurements. Thickness per monolayer is given in nm

Compound	UV-visible	Ellipsometry		SPR	
	$k$ (at 633nm)	$n$	$d(\text{nm})$	$k$	$d(\text{nm})$
SA	0.0045	$1.563 \pm 0.019$	$2.42 \pm 0.090$	$0.0299 \pm 0.0060$	$2.44 \pm 0.034$
CA	0.0223	$1.514 \pm 0.008$	$1.37 \pm 0.007$	$0.0186 \pm 0.0055$	$1.33 \pm 0.058$

For the first time, the formation of CdS clusters in LB films was monitored with SPR measurements. Typical results of the SPR measurements during the exposure to H<sub>2</sub>S gas are shown in Figure 6.17 and Figure 6.18 for SA LB films and CA LB films, respectively. As can be seen, the SPR results demonstrate both the resonance shift and broadening curves. These behaviours are believed due to the formation of light absorbing CdS clusters inside the LB films. Table 6.3 presents the value of the minimum angle of resonance and its resonance shift of 2-6 layers of SA and CA LB films. The changes of the resonance shift after the exposure of H<sub>2</sub>S gas is given in the form of [Hassan et al 2001]

$$\Delta\theta_{SPR} = \frac{2\pi / \lambda (\epsilon_m | \epsilon_a)^{3/2}}{n_p \cos \theta (\epsilon_m | \epsilon_a)^2} \frac{d_2 (\epsilon_b - \epsilon_a)}{\epsilon_b} \quad (6.13)$$

where  $\epsilon_b$  is the dielectric constant of the LB films after the exposure of H<sub>2</sub>S gas. The values of  $\epsilon$  and  $\epsilon_b$  are given by the least squares solution of Equation (6.12) and (6.13).

The kinetics measurements on both samples were carried out at a fixed angle of incidence of  $\theta^* = 46^\circ$  and  $45.2^\circ$  (for SA and CA LB films, respectively) during the flow of H<sub>2</sub>S gas into the gas cell. The reflected light intensity as a function of exposure time for SA and CA LB films are shown in Figure 6.19 and 6.20, respectively. These results show that the formation of CdS clusters happened very fast with response to time in the region of a few minutes only and almost reaches the saturation in 30 minutes. This agrees with the results reported previously [Tattabi et al, 2000].

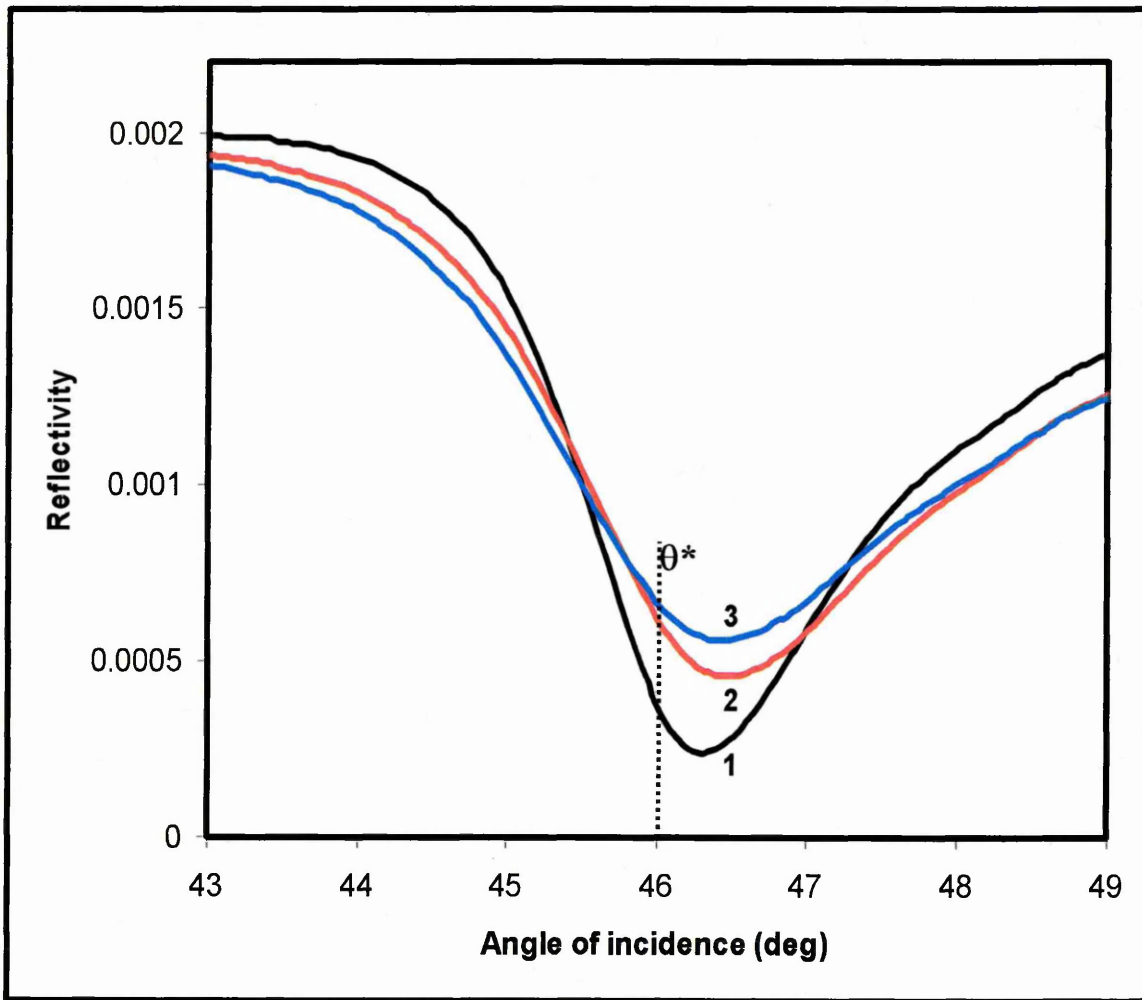


Figure 6.17. Changes in SPR curves of SA LB films (6 layers) due to formation of CdS nanoparticles: (1) initial curve, (2) after 18 minutes exposure to H<sub>2</sub>S, (3) after 36 minutes exposure to H<sub>2</sub>S

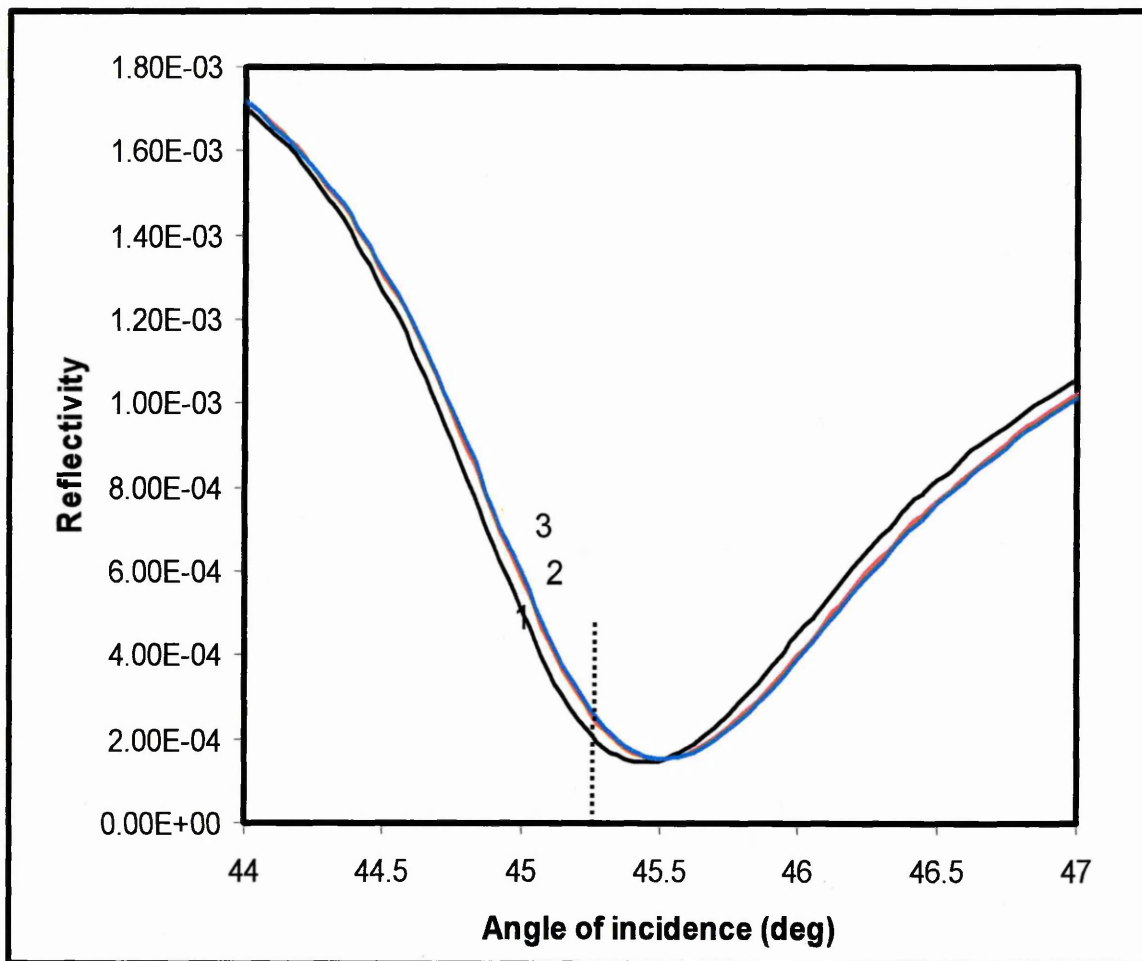


Figure 6.18. Changes in SPR curves of CA LB films (6 layers) due to formation of CdS nanoparticles: (1) initial curve, (2) after 18 minutes exposure to H<sub>2</sub>S, (3) after 36 minutes exposure to H<sub>2</sub>S

Table 6.3. The value of minimum angle of resonance and the minimum intensity of SPR curve of SA and CA LB films

Changes of SPR curve	Stearic Acid (SA)			Calixarene (CA)		
	2 layers	4 layers	6 layers	2 layers	4 layers	6 layers
<u>Minimum angle</u>						
Before H <sub>2</sub> S	44.55	45.40	46.30	44.30	44.65	45.15
After 18 minutes	44.65	45.50	46.50	44.35	44.75	45.25
After 36 minutes	44.65	45.50	46.50	44.35	44.75	45.25
<u>Minimum intensity</u>						
Before H <sub>2</sub> S	0.00015	0.00018	0.00024	0.00012	0.00017	0.00018
After 18 minutes	0.00017	0.00033	0.00046	0.00013	0.00019	0.00019
After 36 minutes	0.00018	0.00042	0.00056	0.00013	0.00020	0.00019

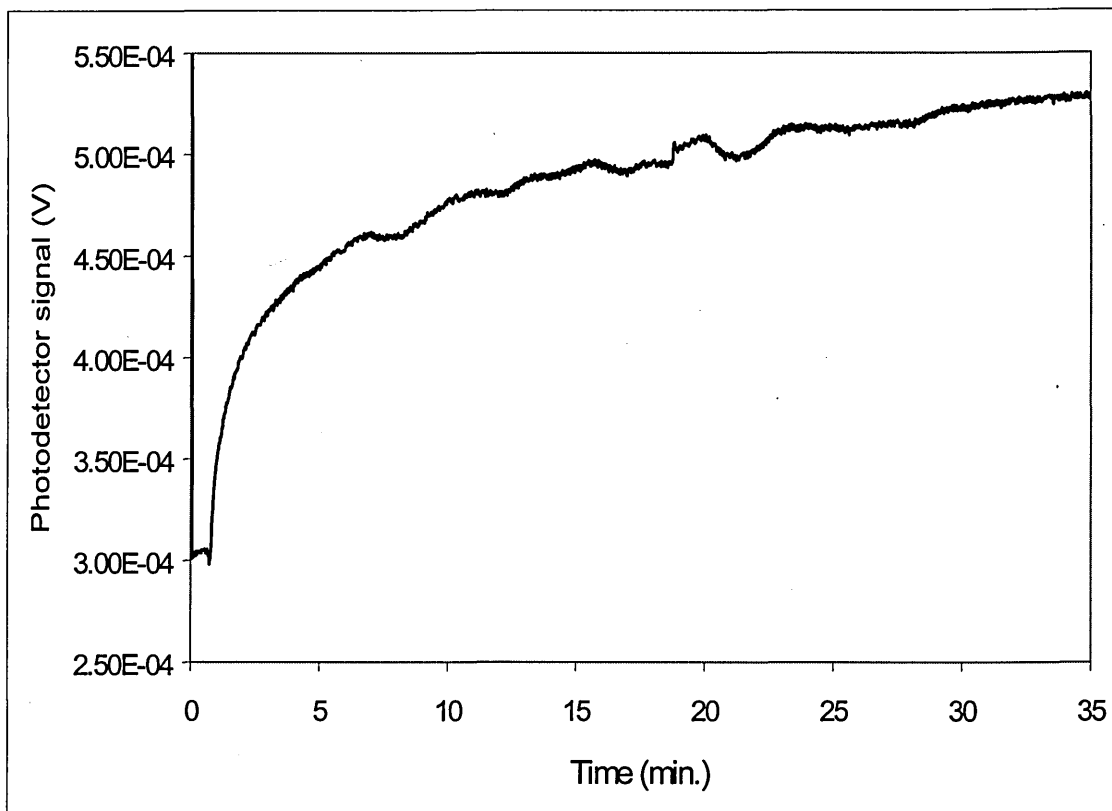


Figure 6.19. Kinetics of CdS nanoparticles formation in SA LB films (6 layers) measured at a fixed angle of incidence ( $\theta^*=46^\circ$ )

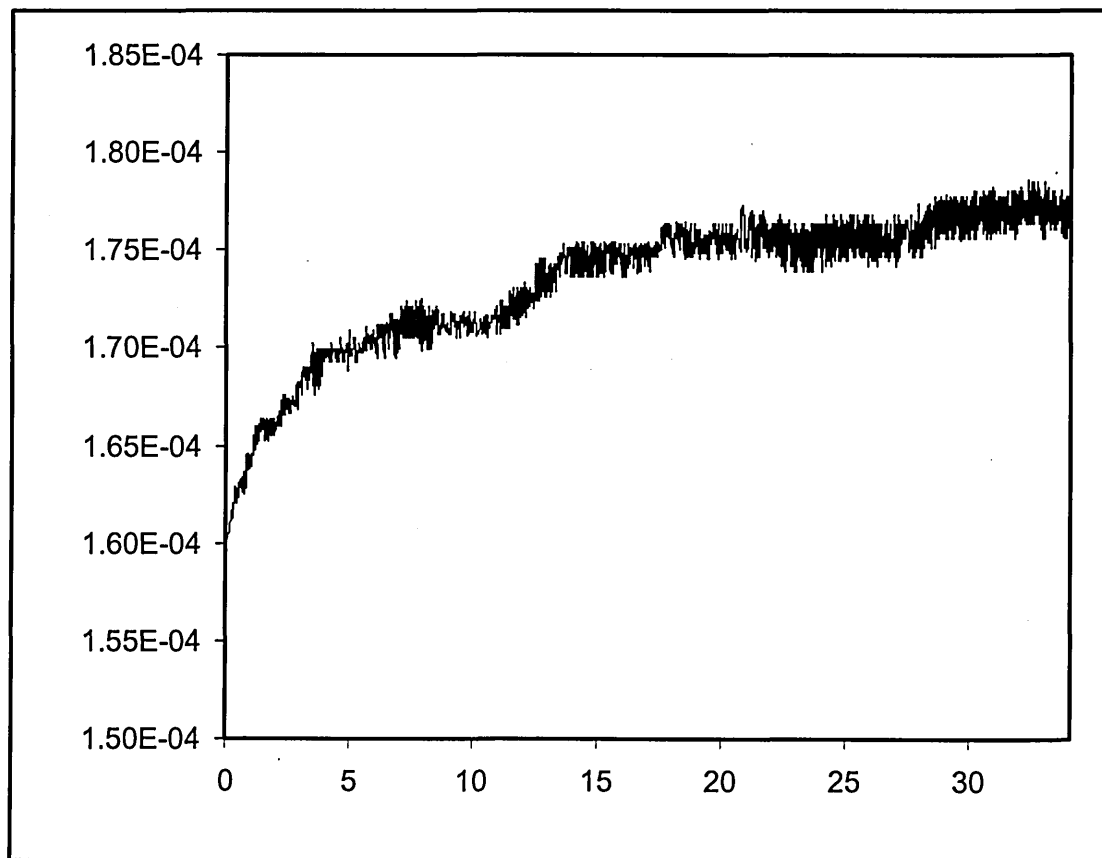


Figure 6.20. Kinetics of CdS nanoparticles formation in CA LB films (6 layers) measured at a fixed angle of incidence ( $\theta^*=45.2^\circ$ )

Following H<sub>2</sub>S gas treatment, the samples were then measured using ellipsometry technique. Ellipsometry data obtained are presented in Table 6.4. Calculations of the optical parameters ( $k$ ,  $n$ ,  $d$ ) of the LB films after H<sub>2</sub>S treatment were carried out using the same procedure of those before the exposure of H<sub>2</sub>S gas. The results of the calculations are presented in Table 6.5. The results, presented in the Table 6.5, indicate that all three optical parameters  $d$ ,  $n$  and  $k$  of the LB films increase after exposure of LB films to H<sub>2</sub>S gas. The increase of LB film thickness may be attributed to the film swelling caused by the formation of CdS nanoparticles inside the LB films. Increases in both  $k$  and  $n$  are also indicate the formation of the light absorbing material having the refractive index higher than that of the film matrix.

The effective value of refractive index ( $n^*$ ) for LB film containing CdS nanoparticles can be estimated using a simple linear superposition of values of  $n_1$  and  $n_2$  for the film matrix and CdS inclusion, respectively:

$$n^* = n_1(1 - v_2) + n_2v_2 \quad (6.14)$$

where  $v_2$  is the volume fraction of CdS in the films. The value on  $n^* = 1.71$  was found, taking  $n_2 = 2.3$  for the bulk CdS [Stroud, 1998] and estimating  $v_2 = 0.2$ . The latter comes from the ratio of the concentration of Cd atoms in cadmium stearate LB films of  $10^{27} \text{m}^{-3}$  and that in the “zinc blend” cubic crystal of CdS of  $5 \times 10^{27} \text{m}^{-3}$  [Stroud, 1998]. Similar calculations for CA LB films, having a concentration of Cd atoms of  $8 \times 10^{26} \text{m}^{-3}$  [Nabok et al, 1997], yield  $n^* = 1.61$ . The estimated values of  $n^*$  are in a reasonable agreement but slightly higher than experimental values shown in Table 6.5. This can be explained by deviation of both the refractive index and concentration of Cd atoms in CdS nanoclusters as compared to respective values for bulk CdS.

Table 6.4. Ellipsometry data for both SA and CA LB films after H<sub>2</sub>S treatment

P <sub>1</sub> (°)	P <sub>2</sub> (°)	A <sub>1</sub> (°)	A <sub>2</sub> (°)	Δ (°)	Ψ (°)
<u>Bare Si</u>					
39.8	130.4	10.3	171.4	170.2	10.55
<u>20 layers of SA</u>					
174.5	263.2	22.5	149.3	77.7	27.70
174.3	264.5	22.4	149.8	78.8	27.40
<u>30 layers of SA</u>					
173.0	260.7	28.3	145.0	73.7	32.75
173.2	260.6	28.5	145.5	73.8	32.60
<u>40 layers of SA</u>					
161.7	252.3	47.1	125.8	54.0	51.75
168.5	257.0	40.6	130.8	65.5	46.00
<u>50 layers of SA</u>					
129.6	221.4	61.5	121.4	351.0	61.15
128.7	217.9	59.1	126.0	346.6	57.65
<u>40 layers of CA</u>					
178.2	267.1	21.8	151.9	85.3	26.05
177.6	267.1	21.5	152.0	84.7	25.85
<u>50 layers of CA</u>					
174.6	263.4	25.8	147.1	78.0	30.45
175.0	263.4	26.1	147.3	78.4	30.50
<u>60 layers of CA</u>					
172.2	260.5	31.7	140.9	72.7	36.50
172.3	260.6	31.8	141.1	72.9	36.45

Table 6.5. Optical parameters of LB films obtained from the absorbance, ellipsometry and SPR measurements. Thickness is given in nm perlayer

Compound		Absorbance	Ellipsometry		SPR	
		$k$ (at 633nm)	$n$	$d(nm)$	$k$	$d(nm)$
SA	initial	0.0045	1.563±0.019	2.42±0.090	0.0299±0.0060	2.44±0.034
	after H <sub>2</sub> S	0.0358	1.616±0.026	2.54±0.092	0.0768±0.0183	2.56±0.045
CA	initial	0.0223	1.514±0.008	1.37±0.007	0.0186±0.0055	1.33±0.058
	after H <sub>2</sub> S	0.0268	1.535±0.006	1.39±0.005	0.0325±0.0066	1.42±0.056

## 6.5. Summary

Cadmium sulphide (CdS) nanoparticles formed within Langmuir-Blodgett (LB) films of stearic acid (SA) and calix[8]arene (CA) were investigated using combined surface plasmon resonance (SPR) and ellipsometry measurements. Undertaking complex measurements of ellipsometry and SPR tackled the difficult problem of simultaneous evaluation of optical parameters, i.e. thickness ( $d$ ), refractive index ( $n$ ) and extinction coefficient ( $k$ ) of the LB films. The SPR measurements performed before the exposure of H<sub>2</sub>S gas give an average thickness of  $2.44 \pm 0.034$  nm and  $1.33 \pm 0.058$  nm per-monolayer for SA and CA LB films, respectively. These values are in good agreement with the result obtained from ellipsometry measurements, which gives the average values of  $2.42 \pm 0.090$  nm and  $1.37 \pm 0.007$  nm for SA LB films and CA LB films, respectively. Meanwhile, the refractive index has been found to increase as the number of films increases with the value of refractive index of SA LB films slightly higher than that of CA LB films.

For the first time, the formation of CdS nanoparticles inside LB films was monitored *in-situ* with SPR. These measurement results demonstrate both the resonance shift and broadening of SPR curves due to the formation of light absorbing CdS clusters. The fitting results of these combination measurements indicate that both thickness and refractive index of the LB films increase due to the formation of CdS nanoparticles inside. Smaller changes in the LB films of CA can be caused by smaller size of CdS nanoparticles compared to that of SA LB films.

# CHAPTER 7

## THE STUDY OF ELECTRICAL PROPERTIES OF CdS NANOPARTICLES IN LB FILMS

### 7.1. Introduction

This chapter presents a detailed study of electrical properties of CdS nanoparticles formed in Langmuir-Blodgett films. The electrical properties are obviously important when considering the materials for nanoelectronic applications. Since the knowledge of the electrical properties of LB films with embedded CdS nanoparticles is still very limited, it is very important here to study this subject. The main goal of the present study is to find the effect of the presence of semiconducting CdS nanoparticles formed in the insulating LB film matrix on their electrical properties. A series of DC and AC electrical measurements were carried out for both planar (interdigitated electrodes) and sandwich (metal/organic/metal) structures over a wide range of frequencies and temperatures.

This chapter also provides theoretical background and review of previous studies (Section 7.2). Section 7.3 gives details of experimental technique and their results and discussion are presented in Section 7.4. This chapter summary is presented in Section 7.5.

## 7.2. Theoretical Background and Review of Previous Studies

In order to respond to applied electric field, organic materials with completely saturated chemical bonds, such as polyethylene, possess few charge carriers. These compounds having conductivity of about  $10^{-18} \Omega^{-1}\text{m}^{-1}$  and carrier mobility less than  $10^{10} \text{m}^2\text{V}^{-1}\text{s}^{-1}$  at room temperature are highly insulating. The displacement of fixed charges and the formation of dipoles are the most essential effect in such dielectric materials. The movement of electrons in the conduction band and holes in the valence band produces the electrical conduction. Only few carriers are available at low temperatures, and as the temperature is increased, the conductivity increases as a result of the generation of electrons and holes by thermal energy. The electrical conductivity variation with temperature may be approximated as exponential if the carrier mobility changes little with temperature [Okamoto and Brenner, 1964].

Two different configurations, parallel (in the film plane) and perpendicular (normal to the plane) to the substrate surface, are usually used for the electrical studies of LB films as shown in Figure 7.1. The conductivity of sandwich structures is usually dominated by highly insulating hydrocarbon chains. Some defects such as pin-holes also contributes to the conductivity of the materials measured in this configuration.

The electrical measurements of LB films usually require the films to be in direct contact with two solid electrodes [Petty, 1996]. Figure 7.2 shows typical configurations for both in-plane and through-plane measurements. The sandwich structure shown in Figure 7.2(a) is fabricated by first thermally evaporating a metal onto a part of the substrate. The LB film is deposited over.

Top electrodes are then coated by evaporating another metal layer through the mask. The conductivity is evaluated from the relationship

$$\sigma = \frac{Id}{VA} \quad (7.1)$$

where  $d$  is the film thickness, and  $A$  is the area of the electrodes overlap.

The interdigitated electrodes (Figure 7.2(b)) are made by depositing two metal electrodes onto an insulating substrate and the LB film coated on top. The in-plane conductivity can be calculated by using

$$\sigma = \frac{Ix}{Vld} \quad (7.2)$$

where  $x$  is the distance between fingers,  $l$  is the length of their overlap, and  $d$  is the film thickness.

DC conduction and AC conduction are independent quantities (for most part). At low frequency, both quantities can contribute to a total conductance. The total conductivity as a function of frequency may then be expressed in the form

$$\sigma(\omega) = \sigma_{dc} + \sigma_{ac}(\omega) \quad (7.3)$$

where  $\sigma_{dc}$  is the DC conductivity and  $\sigma_{ac}(\omega)$  is the AC component.

In order to measure the AC conductivity of a sample, a voltage at an appropriate frequency is applied and then measures both the in-phase and 90° out-of-phase components of current. The out-of-phase component of current is proportional to the real part of the sample's relative permittivity,  $\epsilon'$ , which provides a measurement of capacitance.

The in-phase conductivity is related to the imaginary part  $\varepsilon_r''$  by

$$\sigma_{ac}(\omega) = \omega \varepsilon_0 \varepsilon_r''(\omega) \quad (7.4)$$

where  $\varepsilon_0$  is the permittivity of free space ( $8.854 \times 10^{-12}$  F/m). However, many inorganic and organic samples exhibit a simple-law relationship in the form of

$$\sigma_{ac}(\omega) \sim \omega^n \quad (7.5)$$

where  $n < 1$ . This agrees with the “Universal” model for the response of dielectric materials [Jonscher, 1983]. The nature of the equivalent circuits of electrode/LB film/electrode structures can be explored by measuring the complex impedance of the network over a wide frequency range [Jonscher, 1983].

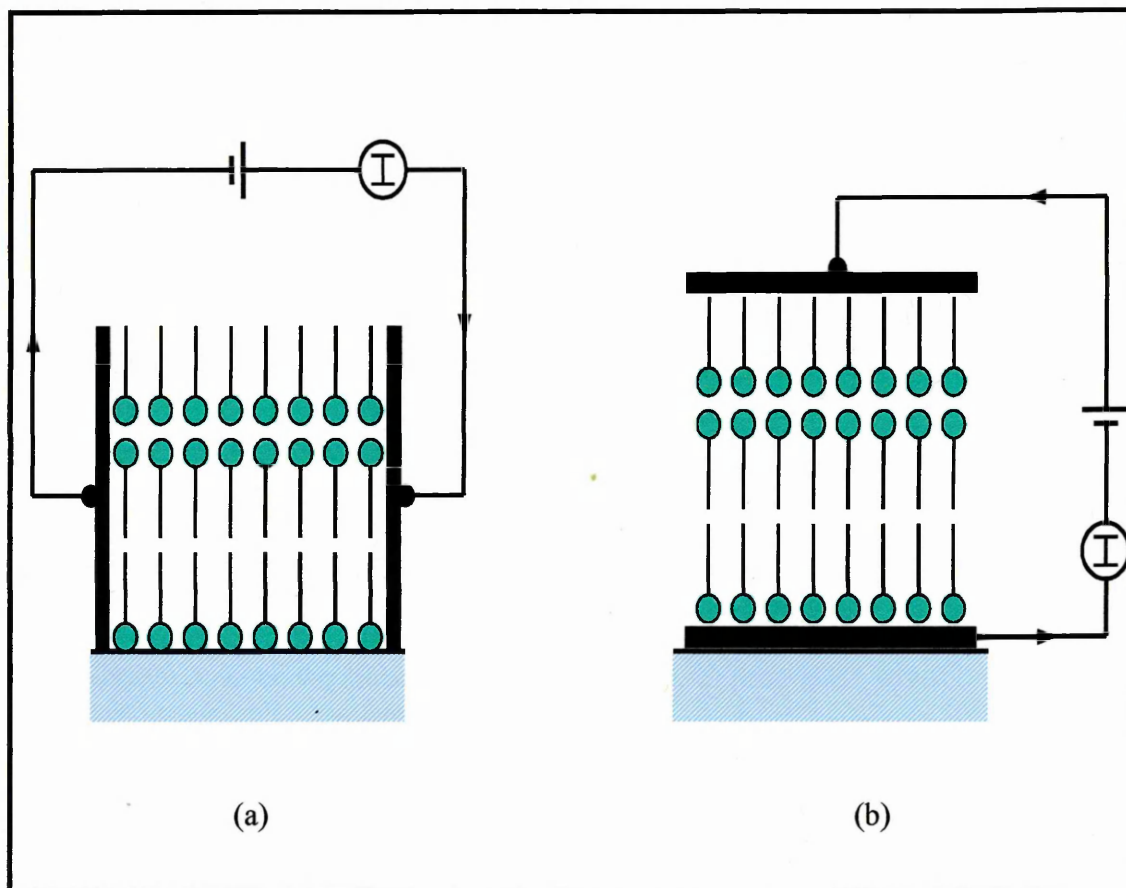


Figure 7.1. Two configurations often used for measuring electrical conductivity in LB films structures: (a) in-plane; (b) normal to the plane [after Petty, 1996]

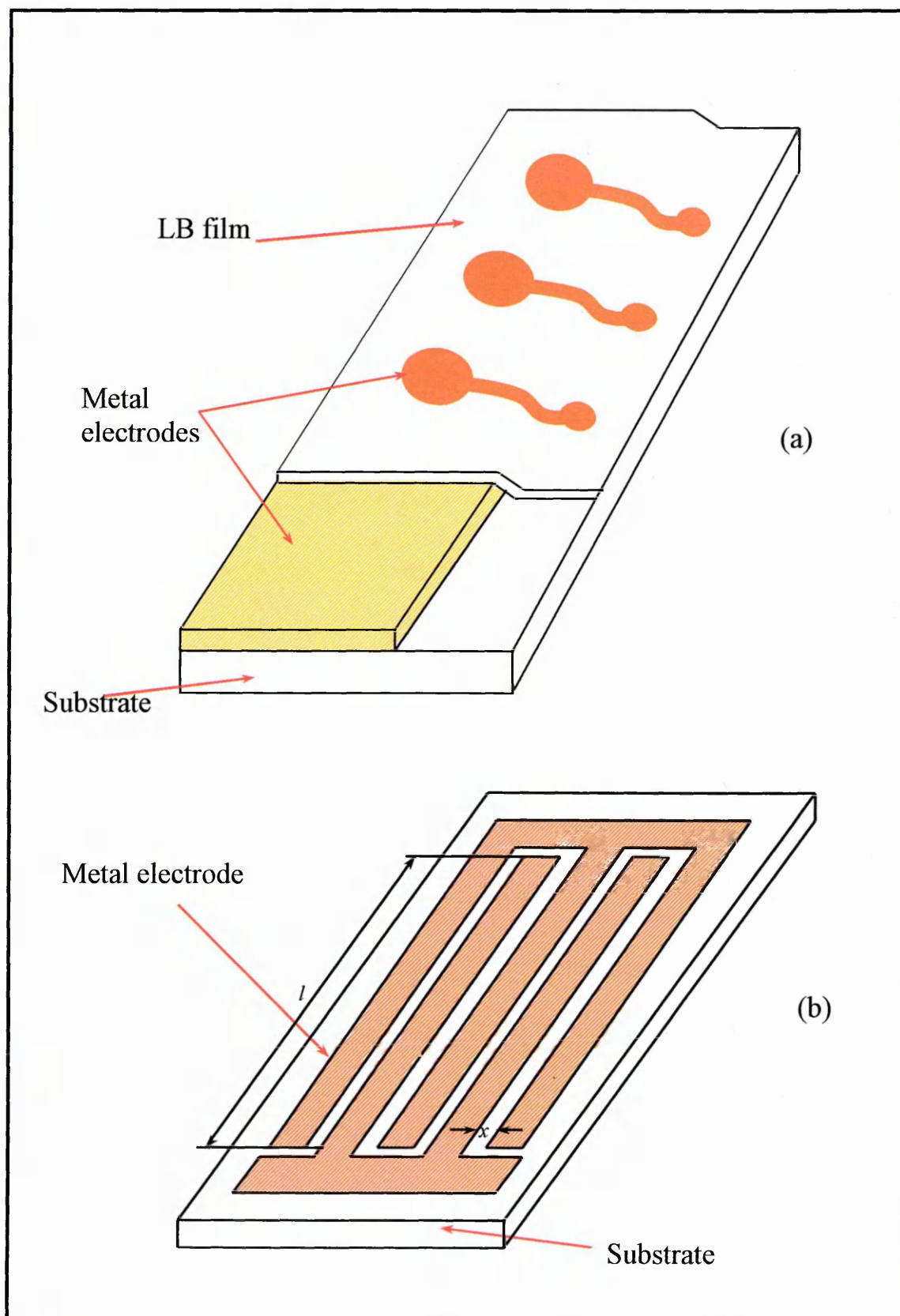
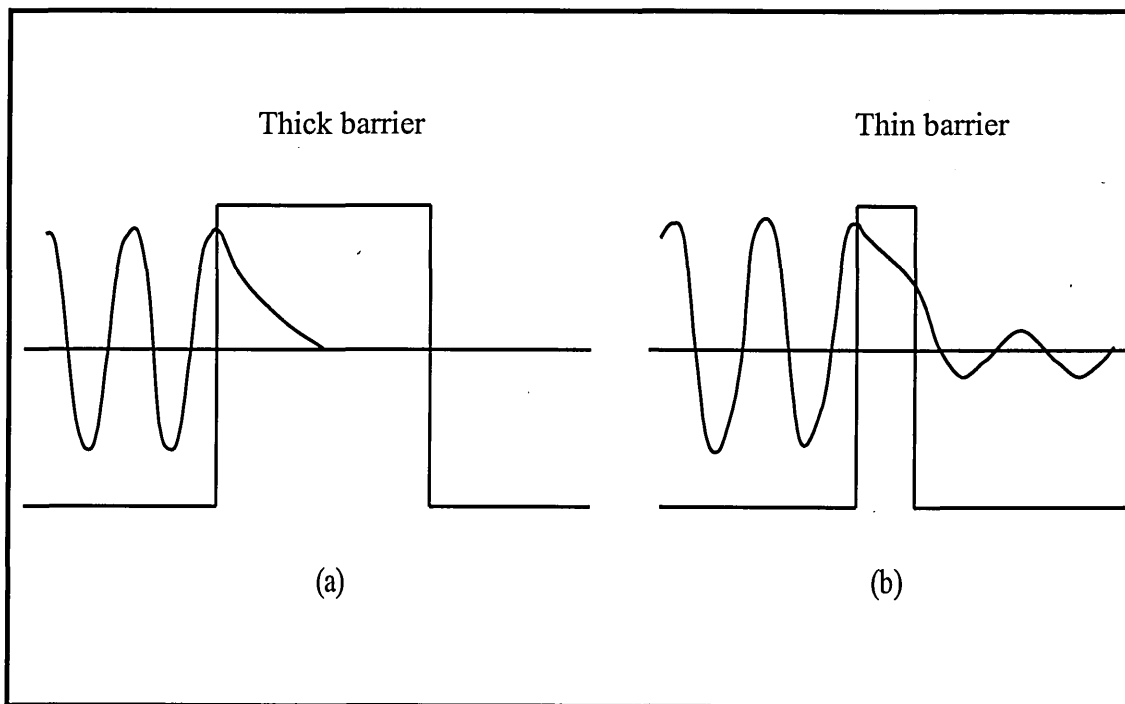


Figure 7.2. Electrode arrangements for electrical measurements of (a) normal to the plane and (b) in-plane conductivities

According to classical physics, when the energy of an electron is less than the potential barrier in metal/insulator/metal (MIM) structure the electron will reflect at the interface, since the electron cannot penetrate through the barrier. In contrast, quantum mechanics opposes this view. The wave nature of the electron allows the penetration through the forbidden region of the barrier, since the electron wavefunction decays exponentially with depth of penetration from the electrode-insulator interface. The wavefunction is equal to zero at the opposite interface for thick barriers (macroscopic thickness) as shown in Figure 7.3(a). This means a zero probability of finding an electron on the other side of a barrier. In the case of very thin barriers (less than 5 nm), the wavefunction has a nonzero value; therefore there is a finite probability that the electron can get through the barrier (Figure 7.3(b)). This phenomenon is referred as a quantum mechanical tunnelling (or tunnelling).



*Figure 7.3. Quantum mechanical tunnelling in: (a) thick barrier; (b) thin barrier [after Petty, 1996]*

Three different types of barrier as shown in Figure (7.4) can be considered in studying electron tunnelling. The transparent coefficient of an independent shape  $\Phi(x)$  barrier is given by

$$T = T_0 \exp\left(-\frac{4\pi}{\hbar} \int_{x_1}^{x_2} 2m[\Phi(x) - E]^{1/2} dx\right) \quad (7.6)$$

where  $T_0$  is the coefficient close to 1,  $m$  is the electron mass, and  $E$  is the electron energy. In the case of a rectangular barrier (Figure 7.4(a)), the transparent coefficient derived from Equation (7.6) is

$$T = T_0 \exp\left(-\frac{4\pi}{\hbar} [2m(\Phi_0 - E)]^{1/2}\right) \quad (7.7)$$

where  $\Phi_0$  is the barrier height. When an external bias is applied this rectangular barrier transforms to trapezoidal (Figure 7.4(b)), and the transparent coefficient of such barrier has become

$$T = T_0 \exp\left(-\frac{8\pi W \sqrt{m}}{3\hbar} \frac{[\Phi_0^{3/2} - (\Phi_0 - eV_0)^{3/2}]}{eV}\right) \quad (7.8)$$

where  $W$  is the barrier thickness. At a large applied bias, such barrier transforms to triangular barrier (Figure 7.4 (c)), with reduced thickness  $W^*$

$$T = T_0 \exp\left(\left[-\frac{8\pi W^* \sqrt{2m}}{\hbar}\right] \left[\frac{\Phi_0^{3/2}}{eV}\right]\right) \quad (7.9)$$

where  $W^* = W \frac{\Phi_0}{eV}$

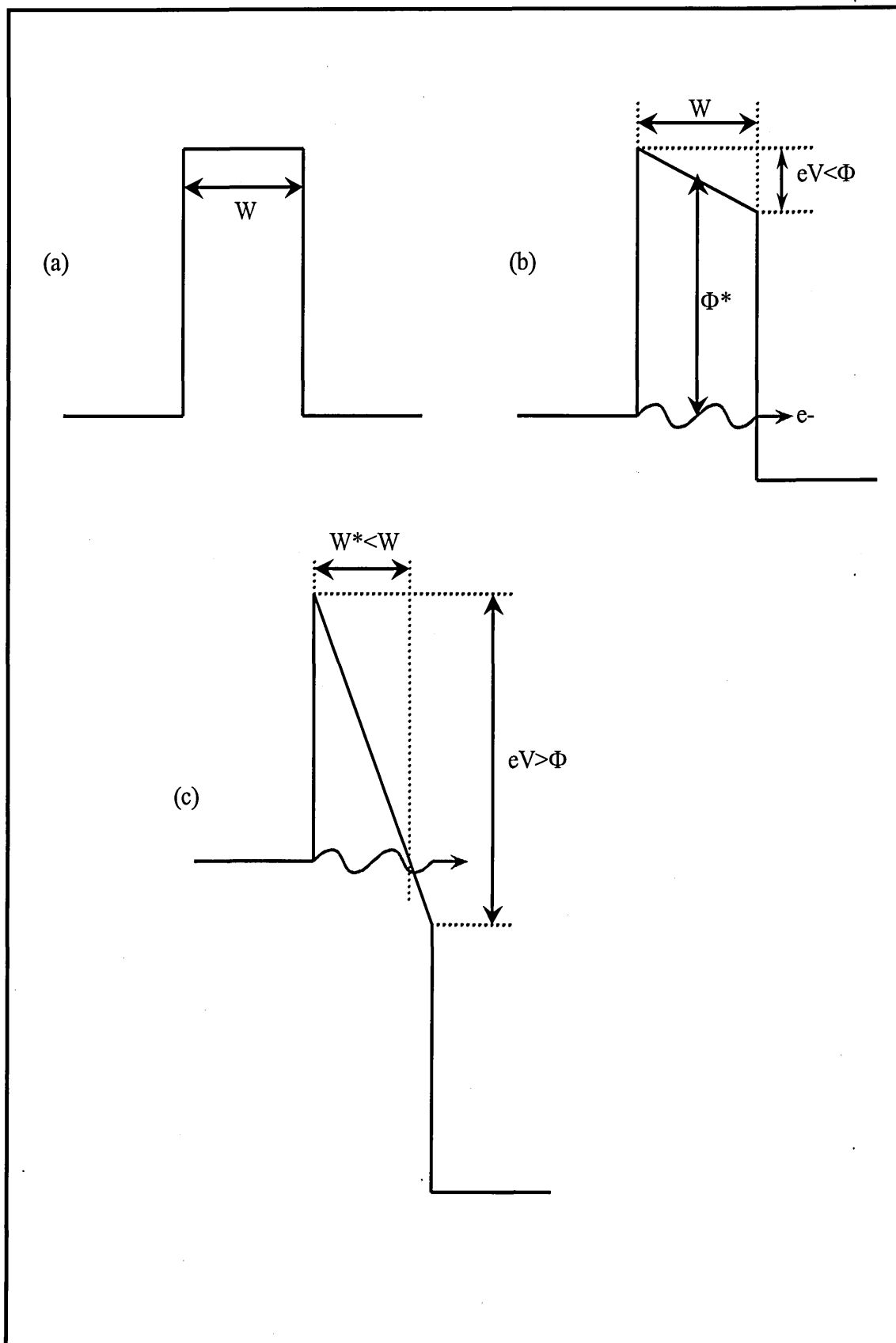


Figure 7.4. Models of electron tunnelling in different barriers: (a) rectangular barrier; (b) trapezoidal barrier; (c) triangular barrier

Since having a well-defined thickness in the tunnelling range of 2-3 nm, LB films are excellent materials for studying quantum mechanical tunnelling. In 1967, Kuhn and his co-workers for the first time proved experimentally that

$$I \approx \exp(-\alpha d) \quad (7.10)$$

where  $I$  is the current,  $\alpha$  is the tunnelling factor and  $d$  is the film thickness. They measured tunnelling current in the system Al/LB monolayer/Al by using fatty acids of different hydrocarbon chain length  $n$  from  $C_{14}$  to  $C_{24}$ . Such system chosen was unique because of an extra insulating layer of  $Al_2O_3$  (see Figure 7.5). The results of their experiments confirmed that the conductivity  $\sigma$  of this system is found to decrease exponentially with increasing  $n$ . The linear relationship between the thickness  $d$  and  $n$  is given by

$$\sigma = \sigma_0 \exp[-2\alpha d(n)] \quad (7.11)$$

This relationship is derived from the theory of electron tunneling through an insulating barrier of thickness  $d$ . The parameters  $\sigma_0$  and  $\alpha$ , the pre-exponential factor and the wavefunction damping constant in Equation (7.11) are given by

$$\alpha = \frac{2\pi}{h} \sqrt{2m\Phi} \quad (7.12)$$

$$\sigma_0 = \frac{e^2 \alpha}{2\pi h} \quad (7.13)$$

where  $e$ ,  $h$ ,  $m$  and  $\Phi$  are the unit charge, Planck's constant, the electron mass and the effective barrier height, respectively. Polymeropoulos [1977] measured the value of  $\alpha$  and found to be about  $0.8 \text{ \AA}^{-1}$  for Al/ $C_n$ /Au and Al/ $C_n$ /Al junction and about  $0.5 \text{ \AA}^{-1}$  for Al/ $C_n$ /Mg junction ( $C_n$  is the fatty acid with the hydrocarbon chain length,  $n$ ).

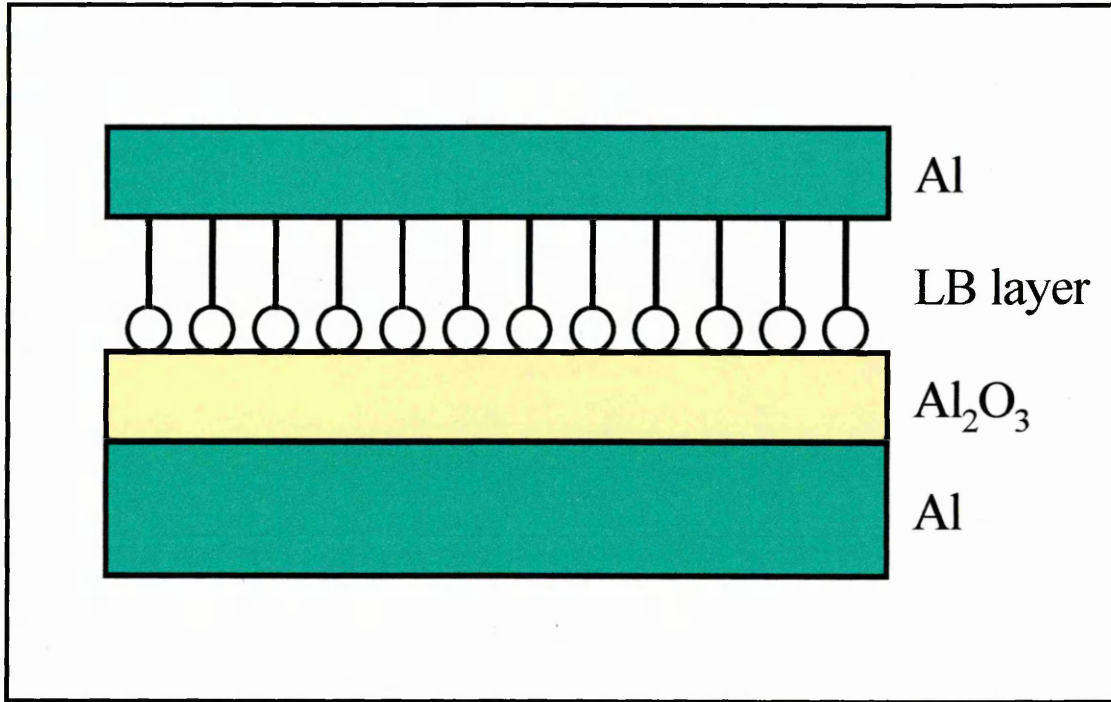


Figure 7.5. Al/LB monolayer/Al system was applied by Mann and Kuhn [1971] to measure the electrical transport through LB film

Sugi et al [1979] studied electrical properties of the multilayer junctions Al/MC<sub>n</sub>/Al (where *M* is the number of monolayers). The relationship between  $\sigma$  and *n* is similar to that in Equation (7.11) with identifiable  $\alpha$  and a temperature-dependent  $\sigma_0$  varies as

$$\log \sigma_0 \sim T^{-1/2} \quad (7.14)$$

Sugi [1985] suggested that a combination of two mechanisms of electron tunnelling through the barrier formed by hydrocarbon chains and thermally assisted hopping in the plain of head groups model is expected to happen in the multilayer LB films (see Figure 7.6). The traversing rate  $\lambda$  is given by

$$\lambda = \lambda_0 (2\alpha d)^{\frac{3}{2}} \exp \left[ -(2\alpha d) - \left( \frac{4\alpha}{\pi N_i d k T} \right)^{\frac{1}{2}} \right] \quad (7.15)$$

where  $d$  is the thickness of LB monolayer. The interface state density  $N_i \approx 10^{15} \text{ cm}^{-2} \text{ eV}^{-1}$  and the frequency factor  $\lambda_0 \approx 10^{13} \text{ s}^{-1}$  are evaluated by comparison with experimental data.

The work of Mann and Kuhn stimulated similar investigation by other groups. During 1970s, electrical data of certain validity began to be reported for LB films, offering scope for applications in electronics. For example, Roberts et al [1978] reported a field-effect transistor (FET) with a LB insulating layer using InP. They together with Sugi *et al* [1977] also reported that  $\text{Cd}^{2+}$  salt films are highly insulating dielectric media. For each  $C_n$ , the dielectric constant is insensitive to both temperature and frequency.

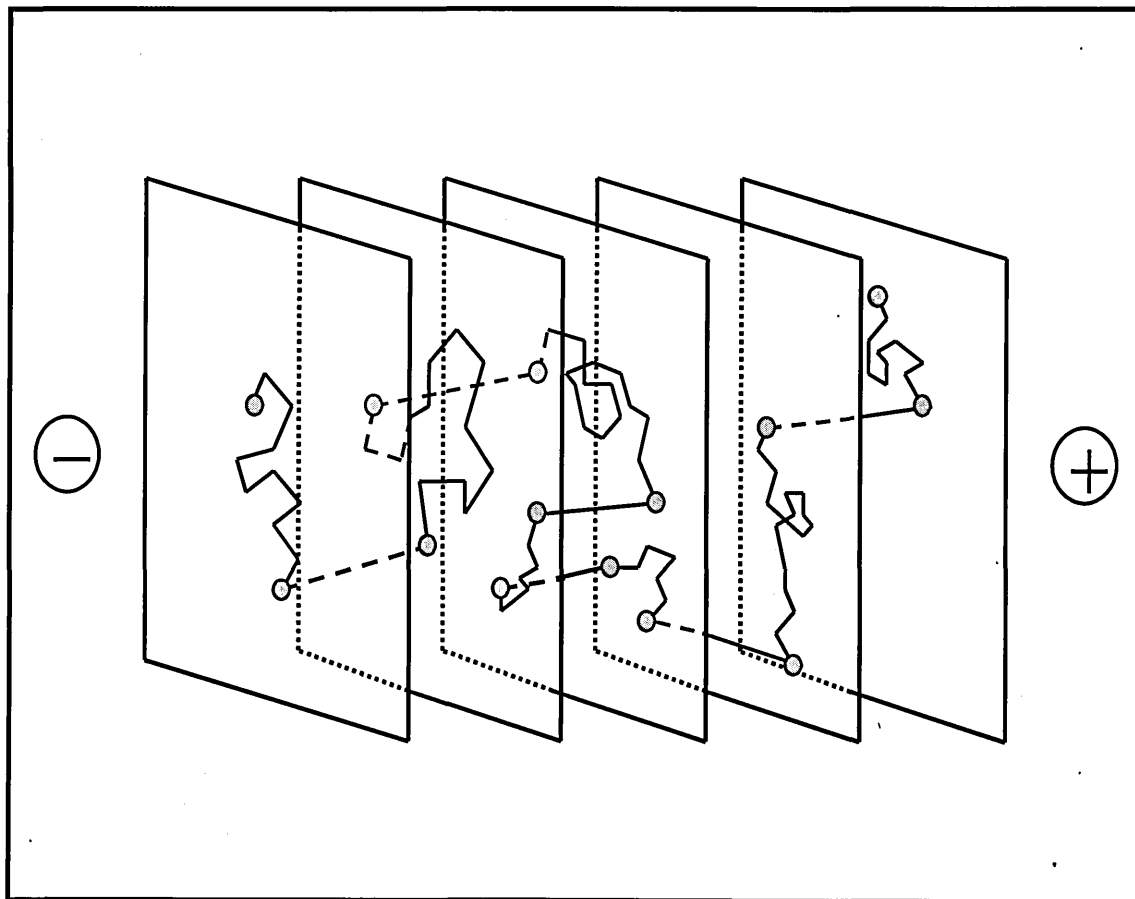


Figure 7.6. Hopping process in the multilayer system described by Sugi [1985]. An electron moves about the system, sometimes along the interface, sometimes traversing the hydrocarbon barrier, to drift stochastically towards the positive electrodes [after Sugi, 1985]

The relative permittivity of LB films of fatty acids and fatty acid salts were measured by several groups. It was found to be in the range 2.0 to 3.0. Sugi [1985] reported the value in the range of 2.67 and 2.77 at room temperature and between 2.74 and 2.82 at 77 K (for Cd stearate film). The relative permittivity of Cd palmitate films is in the range of 2.86 to 3.08 at room temperature and 2.91 to 2.93 at 77 K, while for Cd arachidate films the value is in the range of 2.44 to 2.47 at room temperature and 2.48 to 2.53 at 77K. Petty [1990] found the value of 2.7 and 2.5 for Cd octadecanoate and Cd eicosanoate, respectively.

The electrical measurement of LB films containing CdS nanoparticles is still very limited, although several experimental studies have attempted to study the electrical properties of CdS nanoparticles prepared by different methods. For examples, Gupta *et al* [1995] carried out the electrical characterisation of nanostructured CdS films deposited by the high-pressure magnetron sputtering technique at the temperatures ranging from 80 to 350 K. The electron conduction process was found to be dominated by variable range hopping within the Coulomb gap, quantum mechanical tunneling and thermionic emission as the temperature increased.

Abdulkhadar and Thomas [1998] performed the measurements of DC conductivity of nanoparticles of CdS produced by freshly prepared aqueous solutions of the chemical method. They reported that DC conductivity of CdS nanoparticles is almost independent of temperature over the range of about 300 K to about 500 K. The numerical value of DC conductivity was found about  $1.2 \times 10^{-7}$  S/cm and the conductivity increased, attaining a value of about  $3.7 \times 10^{-7}$  S/cm at 523 K. The DC conductivity of CdS nanoparticles has been found to be much larger than that of single crystal.

Later experiment [Liang et al, 2001] reported the electroluminescence properties of nanoparticle powder of CdS synthesized by modification of Pietro's method using Cadmium acetate dihydrate [ $\text{Cd}(\text{CH}_3\text{COO})_2 \cdot 2\text{H}_2\text{O}$ ] and deposited on silicon substrates (both n- and p-type) by spin coating technique. Electroluminescence from the light emitting active layer was achieved by quantum tunnelling of carriers into the nanoparticles. I-V characteristics of this device (for both types of substrates) have rectifying I-V curves, but with opposite polarities. This rectifying effect corresponds to metal-insulator-semiconductor tunneling effect. To be specific, the thin potential barrier of organic coating and low substrate doping level result in Schottky-diode-like behaviour.

### 7.3. Details of Experimental Technique

Electrical measurements on LB films are stringent test of film quality and possibly the most difficult of all the available characterisation tools. In this electrical study, a series of electrical tests, such as DC and AC measurements, were carried out for both planar (LB films deposited on the interdigitated electrodes) and sandwich – MIM (metal electrode-Aluminium / organic film / metal electrode-Aluminium) structures over a wide range of frequencies and temperatures. In order to measure the electrical characteristics, both sandwich and planar structures were produced. Metal electrodes of the sandwich structures were deposited using a thermal evaporation technique. A detailed procedure of the thermal evaporation will be described in the following section (Section 7.4.1).

The sandwich samples were fabricated by first thermally evaporating a thin metal (aluminium) film onto a part of a glass substrate (for bottom electrode). Y-type LB films of both stearic acid (SA) and calix[8]arene (CA) of different odd number of layers from 31 to 61 were then coated on this system at a surface pressure of about 25-28 mN/m. Finally, the top contacts were deposited by evaporating another metal (aluminium) layer through a specially designed contact mask (see Figure 7.10 and 7.11) to provide the “lollipop” shaped electrodes. The deposition of this Aluminium electrode top contact was carried out very carefully in order to avoid damaging the organic film. A slow evaporation rate of less than 0.1 nm/s was chosen, and the samples were cooled down by interrupting the evaporation after every 5 nm of Al deposited.

Planar structure samples consisted of interdigitated electrodes. Such structures formed by photolithography contain platinum fingers separated by 60  $\mu\text{m}$  gap. Electrodes' overlap was 3.5 mm. LB films (30 – 90 layers) of either stearic acid or

calixarene were deposited onto the substrate containing the electrodes. The conductivity value can therefore be calculated as

$$\sigma = \frac{I}{V} \frac{x}{l(N-1)d} \quad (7.16)$$

where  $x$  is the distance between fingers,  $d$  is the thickness,  $l$  is the total length of the overlap and  $N= 16$  is the number of fingers. A typical number of CdS nanoclusters exist between one pair of electrodes with 60  $\mu\text{m}$  spacing between the electrodes were calculated and were found to be about 750 clusters and 33 clusters for SA and CA LB films, respectively. These calculations also gave the estimation of concentration of CdS molecules of  $4.76 \times 10^{14}$  and  $2.5 \times 10^{13}$  per  $\text{cm}^2$  for SA and CA LB films, respectively. A wurtzite structure of bulk CdS has the nearest neighbour separation of 0.25 nm [Nabok et al., 1998]. So, a hexagonal platelet CdS particle with a lateral dimension of about 20 nm and a thickness of around 2 nm for SA LB films contains 32500 molecules of CdS. While a hexagonal platelet CdS particle in CA LB films with a lateral dimension of about 10 nm and a thickness of 1 nm contains around 8125 CdS molecules. The concentrations of CdS clusters within bilayer of SA and CA LB films are estimated to be  $1.54 \times 10^{10} \text{ cm}^{-2}$  and  $3.08 \times 10^9 \text{ cm}^{-2}$ , respectively.

To provide the electrical connection between the measuring equipment and the samples, thin copper wires were attached to the sample electrodes using a silver conducting paste. The diagram of the sample structures used for identification of the electrical properties of CdS nanoparticles formed in LB films is shown in Figure 7.7 and Figure 7.8 for sandwich structure of Al/LB films/Al and planar structure, respectively.

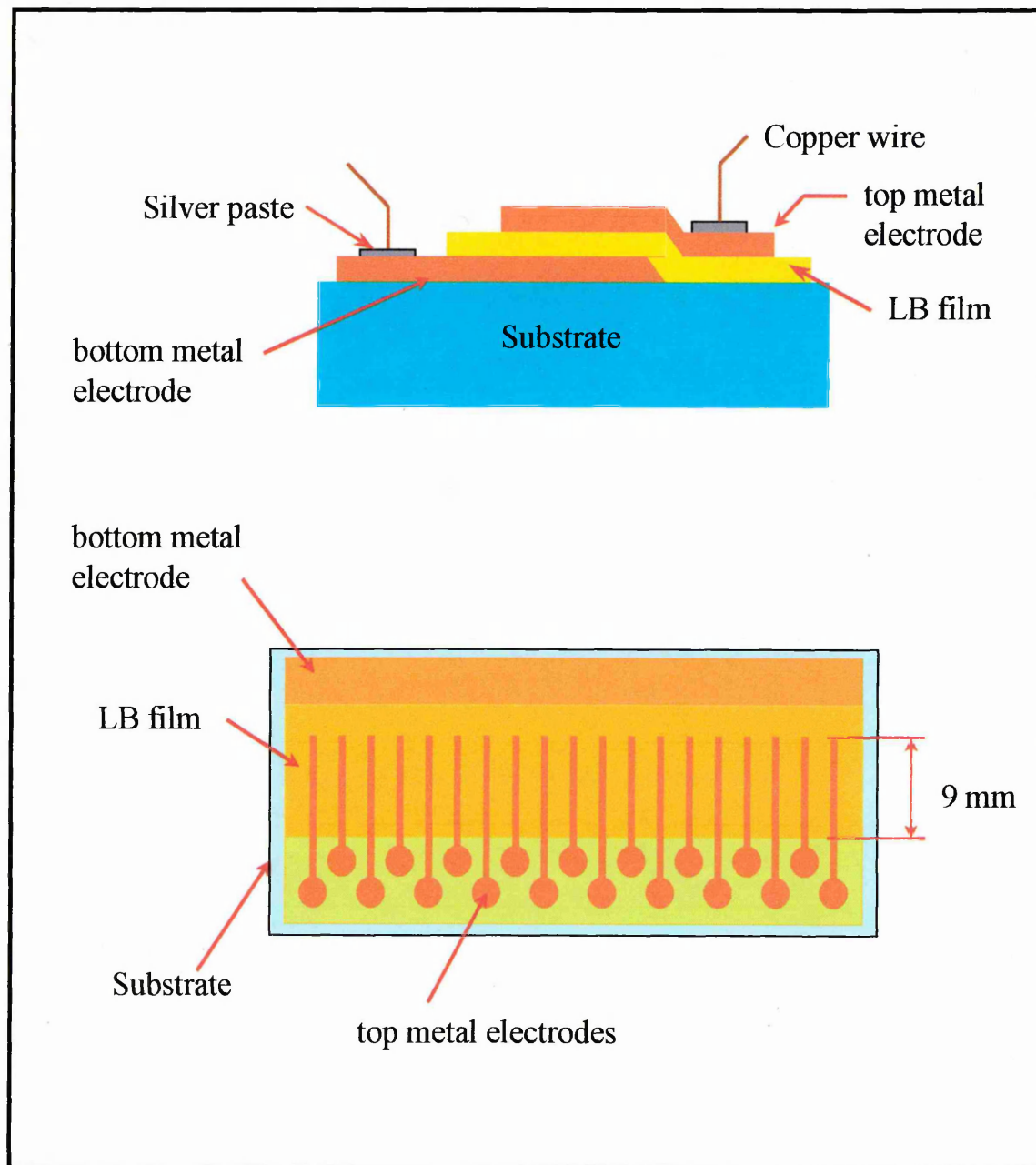


Figure 7.7. Sandwich structure of Al/LB film/Al samples used in this experiment

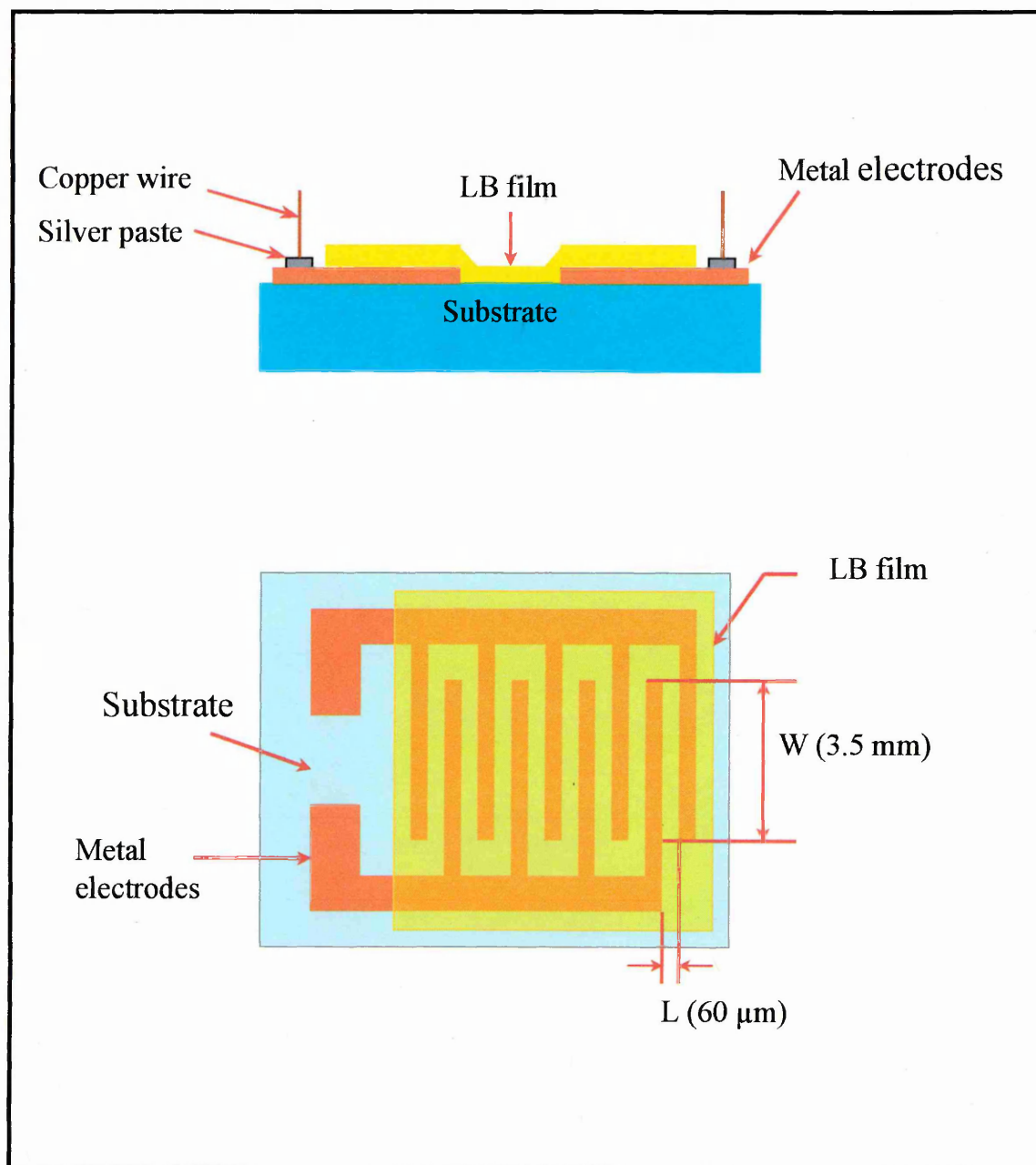


Figure 7.8. Planar structure samples using interdigitated electrodes

## 7.3.1. The Evaporation System

### 7.3.1.1. Evaporation Principles and Techniques

An Edwards Bir-Vac coating unit was used for the deposition of the aluminium bottom contact and for the subsequent deposition of metal on the top of the LB film. This coating unit consists of a vacuum system and coating chamber (Figure 7.9). The vacuum system, that is commonly used, is a combination of a rotary mechanical pump and an oil diffusion pump working together to produce an ultimate vacuum of about  $10^{-5}$ - $10^{-6}$  Torr. The rotary pump is used to create a pre-vacuum of  $10^{-3}$  Torr, roughing the coating chamber and backing the diffusion pump. When such vacuum is attained, the diffusion pump can be switched on to draw the vacuum down via the high vacuum valve. The diffusion pump usually produces the vacuum down to around  $10^{-6}$  Torr.

A quartz crystal film thickness monitor is incorporated into the coating system in order to control the rate of evaporation and the thickness of the evaporated metal. The thickness of the metal deposited on the substrate can be calculated from the frequency reduction of the quartz crystal microbalance (QCM). A mechanical shutter is used to block the sample substrate from the heating source at the early stage of evaporation in order to avoid sample contamination by any low boiling impurities. In order to supply the required current for heating the filament, an external current supply is connected to the coating system.

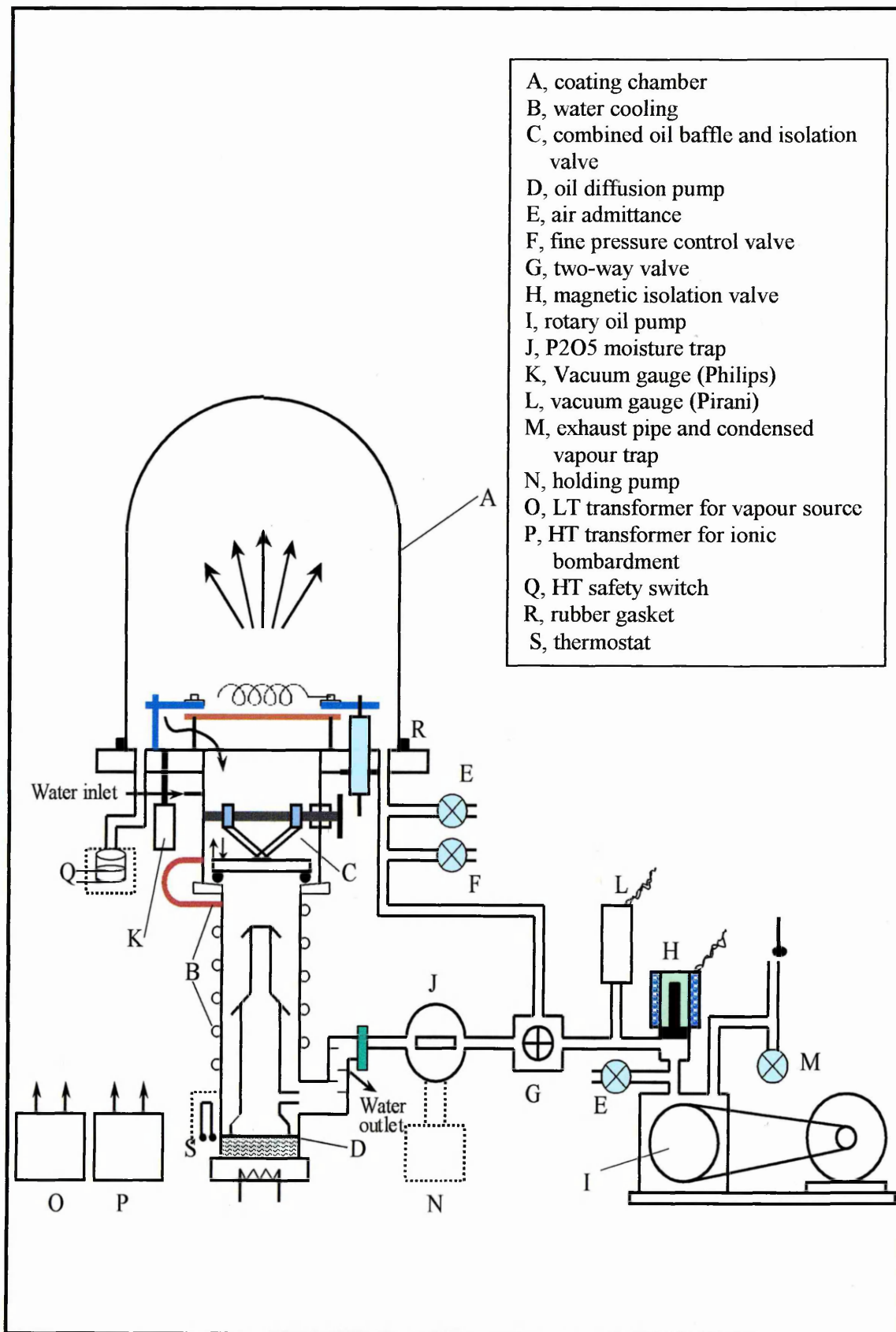
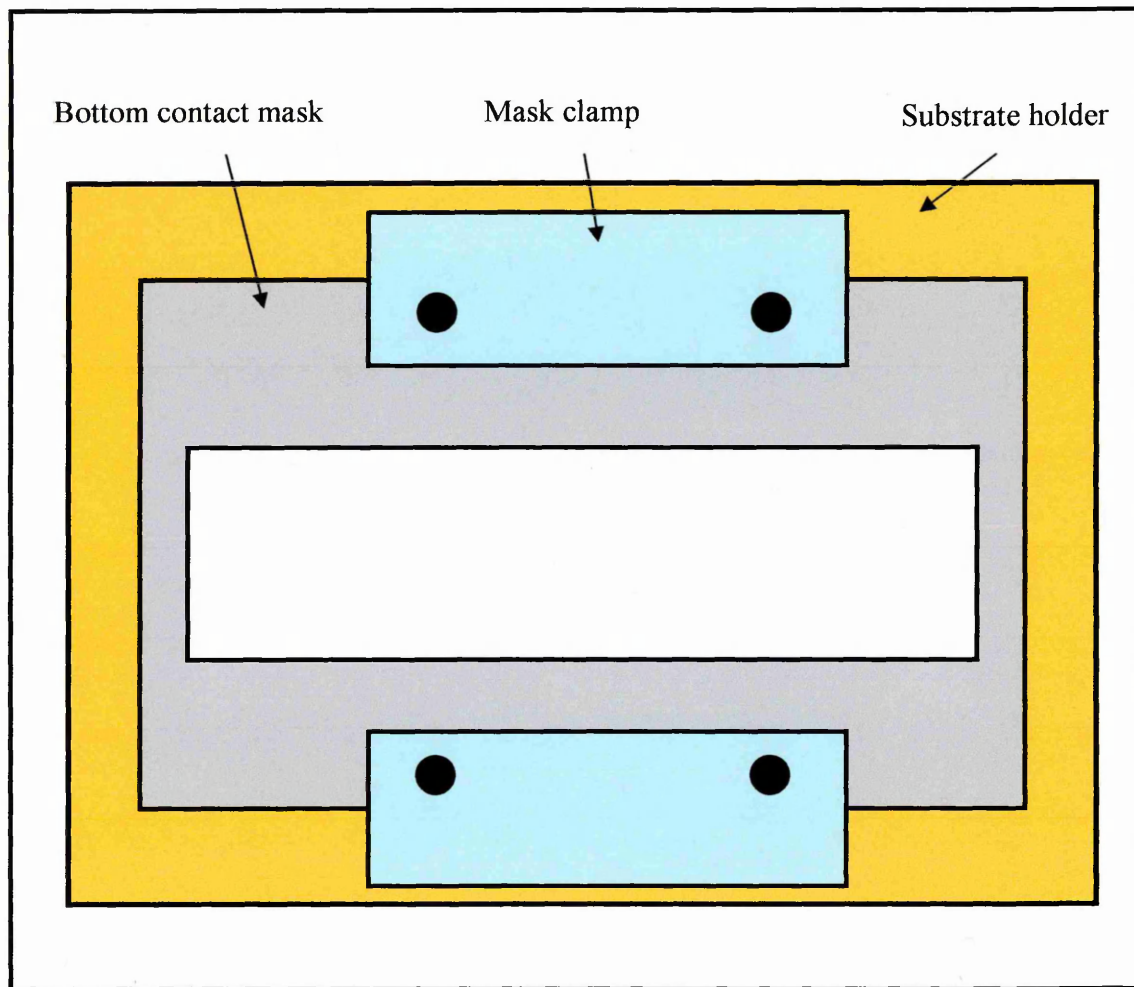


Figure 7.9. Schematic diagram of the coating system of thermal evaporation

### 7.3.1.2. Evaporation Procedure for Deposition Electrodes

The thermal evaporation system described above was used to deposit metal electrode onto the LB film surface (top electrode) and onto part of a glass slide (bottom electrode). A masking system was used for each contact to determine the electrode configuration and dimensions in order to give an accurate device action area. Aluminium (Al) was evaporated onto part of the glass slide through a specially design mask as shown in Figure 7.10, while a mask shown in Figure 7.11 was used to evaporate Al onto the LB films. The masks were made from a thin metal plate (stainless steel) with holes of different shapes and sizes. The samples were placed inside the vacuum chamber adjacent to the quartz crystal monitor and pumping sequence was then initiated. The filament is heated and metal evaporates from the element and condenses on the samples.

As the LB film is very thin, there is a high probability that molten metal can damage (burn) the film. In order to avoid LB film damage, the evaporation process took place at a very low rate. The deposition of this Al top contact was carried out by a slow evaporation rate of less than 0.1 nm/s, and the samples were cooled down by interrupting the evaporation after every 5 nm of Al deposited. The shutter was closed when the evaporated electrode reaches the required thickness (about 35 nm) to prevent further deposition on the electrode. Directly afterwards, switching off the external current source terminated the evaporation process. The samples were then cooled down for at least 15 minutes, before extraction from the vacuum chamber in order to prevent oxidation of Al layers.



*Figure 7.10. Specially design mask using to evaporate aluminium thin film on the glass slide for a bottom electrode*

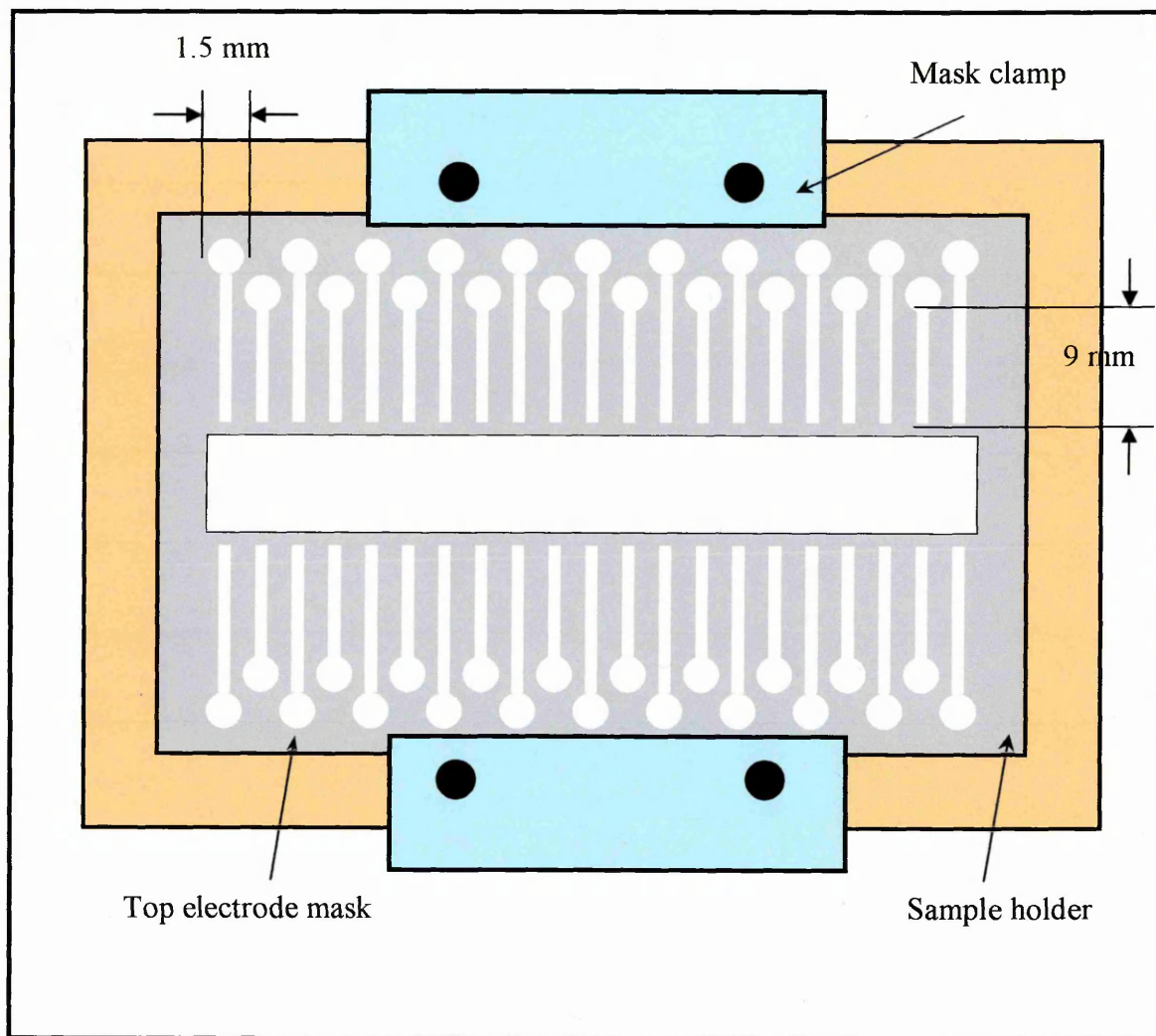


*Figure 7.11. Specially design mask used to evaporate aluminium thin films for the top contact of the sandwich structures*

### 7.3.2. Electrical Measurements

Electrical measurements were carried out on the same samples of stearic acid and calixarene LB films before and after exposure to H<sub>2</sub>S gas. DC (I-V characteristics) and AC measurements were performed for the temperature range between 80 and 300 K (room temperature). A Farnell SW1B IEEE switching unit provided connection to the measuring equipment and an IBM-PC. A National Instrument IEEE GPIB interface card was installed in the IBM-PC to control all the measuring equipment with the exception of the temperature controller.

I-V characteristics were carried out in the DC bias range of -3 V to 3 V with a 0.05 V step. The AC conductance, capacitance and dielectric constant of the samples were measured at semi-logarithmic preset steps in the frequency range of 20 Hz – 1 MHz using a computer controlled measurement set-up. In order to measure electrical characteristics at various temperatures, the samples were mounted in the Oxford Instruments liquid nitrogen cryostat (Figure 7.12). The cryostat was connected to a temperature controller, which was driven by the IBM-PC computer through its serial communication port. The cryostat system was also used to keep the sample in a clean and dry environment to prevent the effect of humidity during electrical tests.

To perform the DC current-voltage (I-V) characteristics, a voltage was applied across the LB-films-based sandwich structure (Al/LB/Al) and the current passing through the structure was measured. A Keithley 6517A digital electrometer with built-in voltage source was deployed to record the current as a function of the applied DC voltage. This electrometer is able to measure currents in the range of 1 pA ( $10^{-12}$  A) to 1 mA ( $10^{-3}$  A). Between the recordings of data, a time delay (5 seconds) was applied in order to give the current enough time to stabilise and reduce the effect of polarisation of

the sample. A schematic diagram of the electrical measurement system is shown in Figure 7.13.

Experimental data of different samples (different number of layers) of stearic acid and calixarene LB films before and after H<sub>2</sub>S treatment over a wide range of temperatures were analysed in order to extract more information about the carrier transport mechanisms and the dielectric properties.

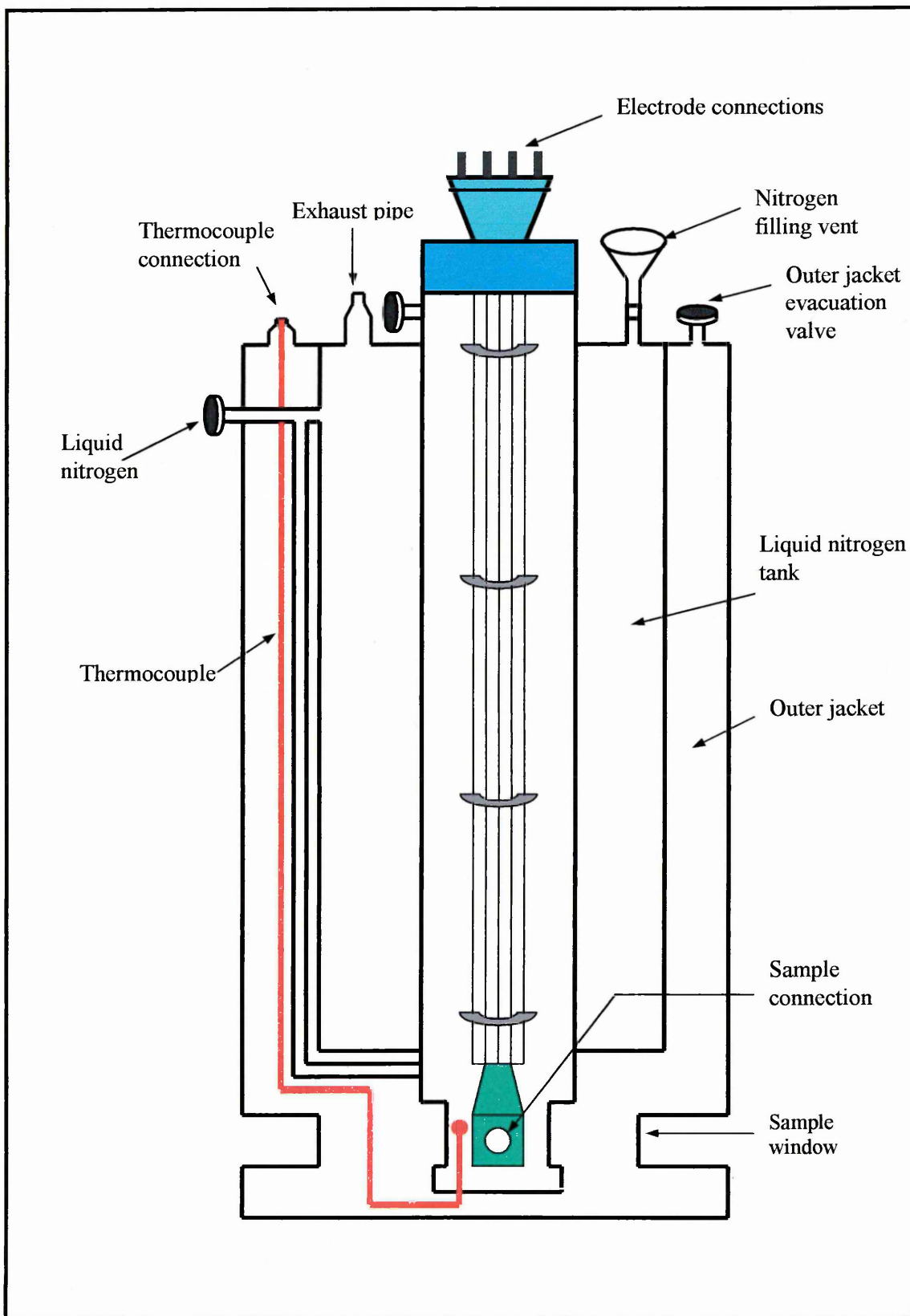


Figure 7.12. Liquid nitrogen cryostat used for electrical measurements at different temperatures.

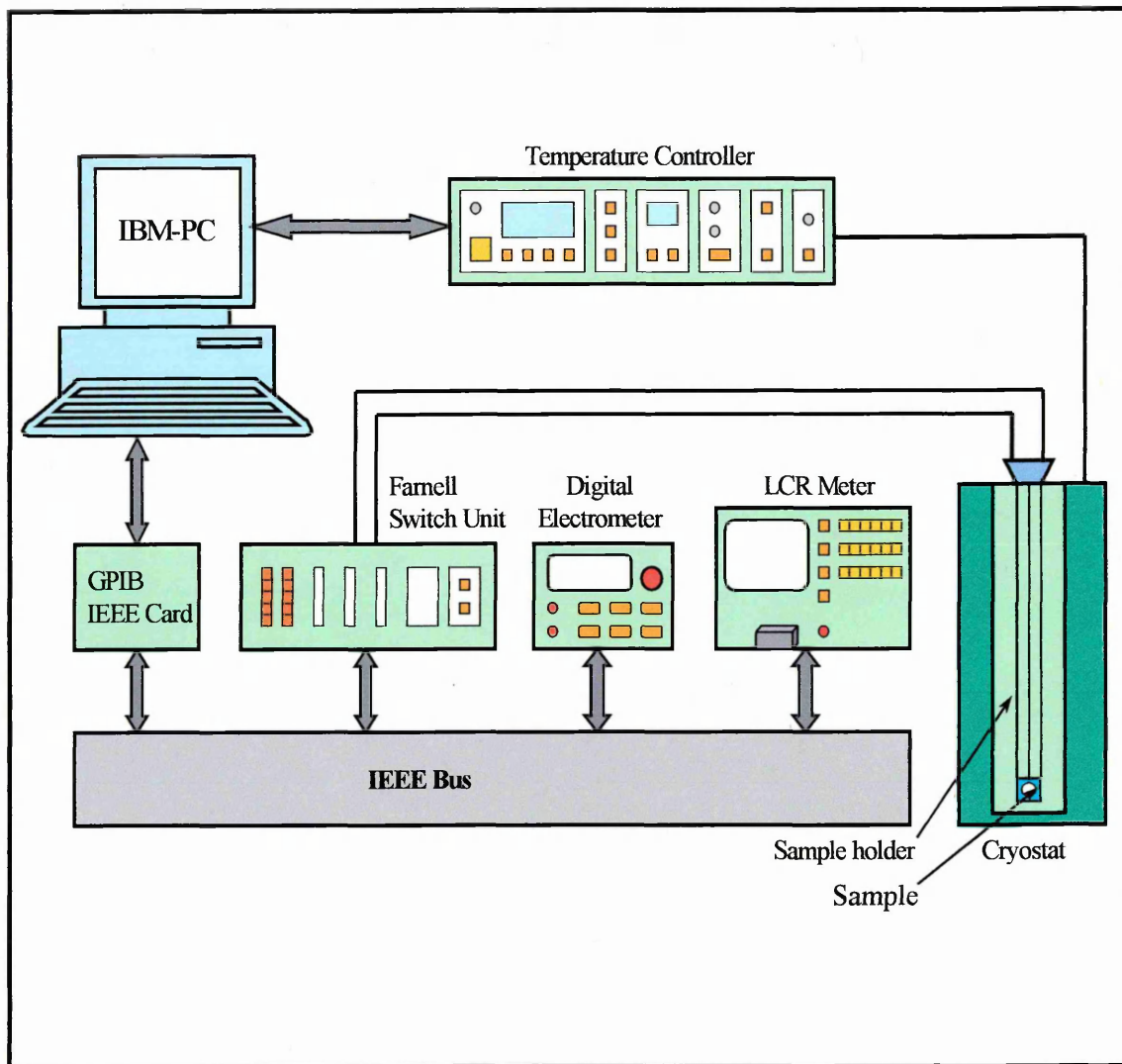


Figure 7.13. Schematic diagram of the electrical measurement system

## 7.4. Results and Discussion

### 7.4.1. DC I-V Characteristics

Typical room temperature forward bias current-voltage (I-V) characteristics of the sandwich structures of metal/insulator /metal (MIM) of Aluminium (Al) / SA LB film / Aluminium (Al) for both before and after H<sub>2</sub>S treatment samples are shown in Figure 7.14. The number of layers of SA LB films used in such structure is 33 layers with the thickness of each layer of about 2.43 nm and 2.55 nm, respectively for before and after H<sub>2</sub>S treatment of samples. This thickness value is taken from the average thickness obtained from SPR and ellipsometry measurements (Chapter 6). Figure 7.15 presents the I-V characteristics of Aluminium / CA LB film / Aluminium for both treated and untreated samples. 37 layers of CA LB films are applied in such structure with the average thickness of around 1.35 nm and 1.405 nm per layer, respectively for untreated and treated samples. As can be seen, the I-V characteristics of both films demonstrate exponential behaviour in all samples investigated. Such I-V characteristics are found to be reproducible for different number of LB layers. Several mechanisms are considered for the explanation of these experimental results, including Schottky, Poole-Frenkel and tunnelling. Sugi [1985] concluded an electron tunnelling mechanism for multilayered LB films of MIM (Al/fatty acid LB films/Al). The latter suggestion is believed to describe the current results due to three major experimental facts considered (will describe in the following section): temperature dependent behaviour, thickness dependence and the effect of CdS particles formation in the LB films. In contrast, neither Schottky nor Poole-Frenkel mechanism can explain the three above facts properly.

Exposure H<sub>2</sub>S gas to the LB films at room temperature results in decreasing significantly the values of current and thus conductivity for both SA and CA LB films. It is believed that such decreasing conductivity is caused by a reduction of the ordered structure of the LB films. This is due to formation of CdS nanoparticles in the LB films. In consistence with this, the effect of larger CdS nanoparticles formed in the SA LB films (Chapter 5) on their conductivity is much more pronounced as compared to smaller CdS particles formed in the CA LB films. It also found that the treatment of H<sub>2</sub>S gas to the LB film samples does not change the conductivity mechanism process, as the similar exponential behaviour appears on both treated LB films.

Logarithmic scale (plotted in log I versus V coordinates) shown in Figure 7.16 and Figure 7.17 for SA LB films and CA LB films respectively gives better analysis of the conduction mechanism. Flat line in logarithmic scale, which can be seen in both types LB films, proves tunnelling behaviour through the multilayered LB films. The current value is found from Figure 7.16 to be in the range of 10<sup>-6</sup> to 10<sup>-4</sup> A for the 33 layers of untreated SA LB films. This value is almost four orders of magnitude more than that of the 37 layers of untreated CA LB films, which obtained to be in the range of 10<sup>-10</sup> to 10<sup>-9</sup> A (obtained from Figure 7.17). Different number of SA and CA LB layers (51, 51 and 75 layers) also produced the current values in the same order of magnitude. So the film thickness do not affect the current values (conductivity). The reduction of current values is clearly observed in both films (Figure 7.16 and 7.17) as a result of H<sub>2</sub>S gas treatment to the LB films. The current values of treated SA LB film are found to be in the range of 10<sup>-8</sup> – 10<sup>-5</sup> A, which are around two orders of magnitude lower than that of untreated LB films. Similar significant reduction (about two orders of magnitude) of the current values are also found in the treated CA LB films (in the range of 10<sup>-12</sup> – 10<sup>-10</sup> A).

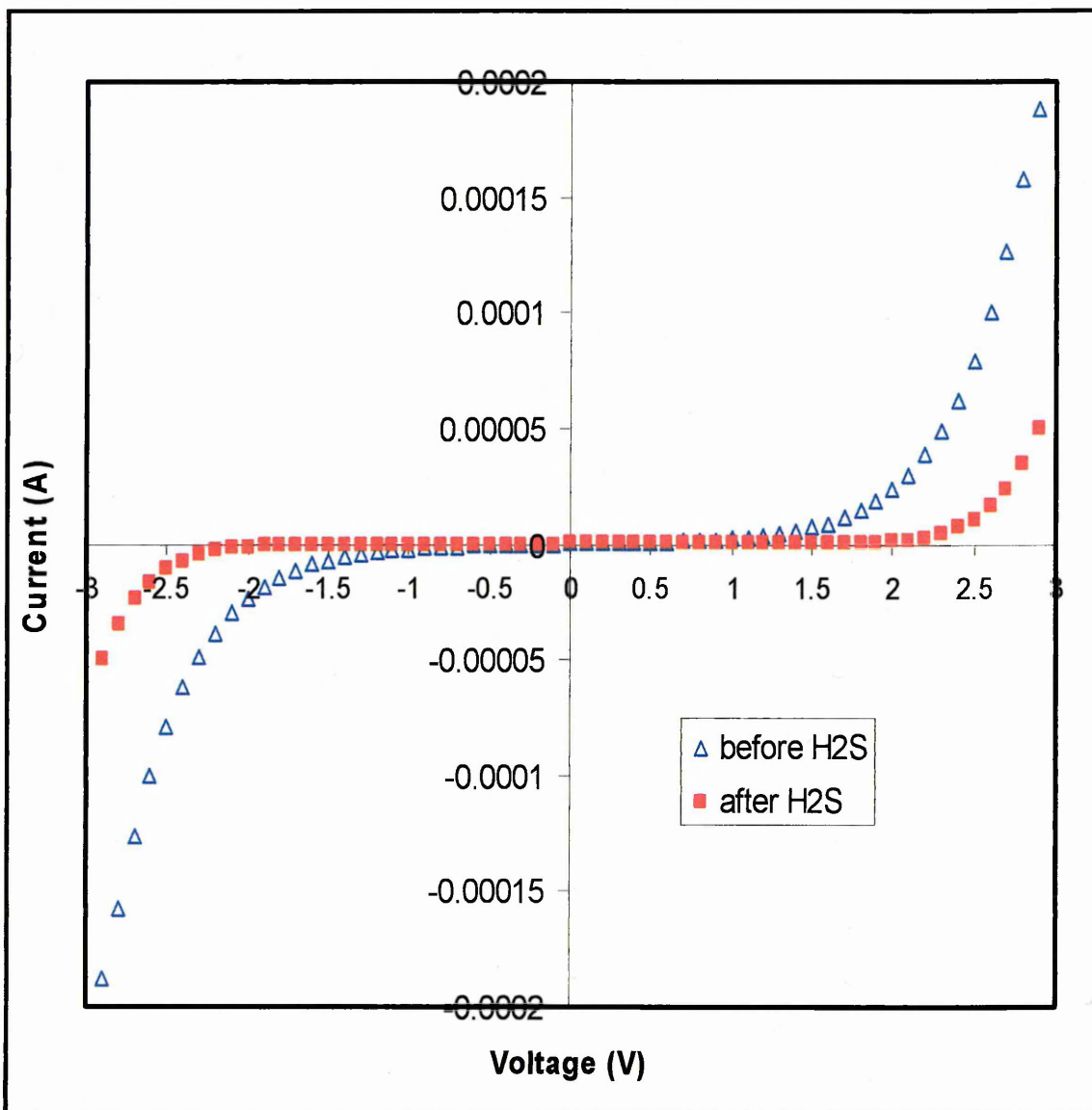


Figure 7.14. *I-V* characteristics of 33 layers of SA LB films for both treated and untreated samples

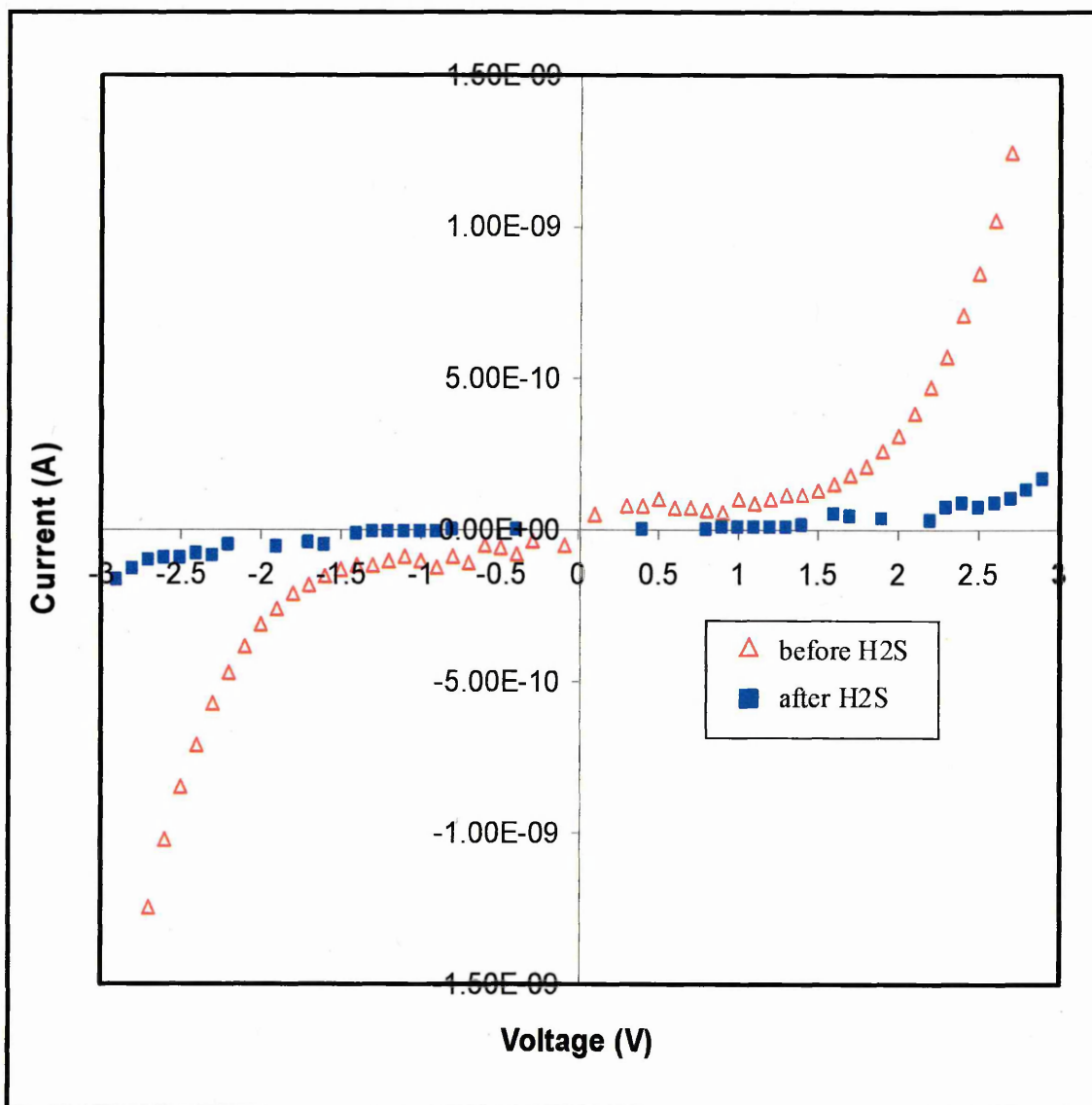


Figure 7.15. I-V characteristics of 37 layers of CA LB films

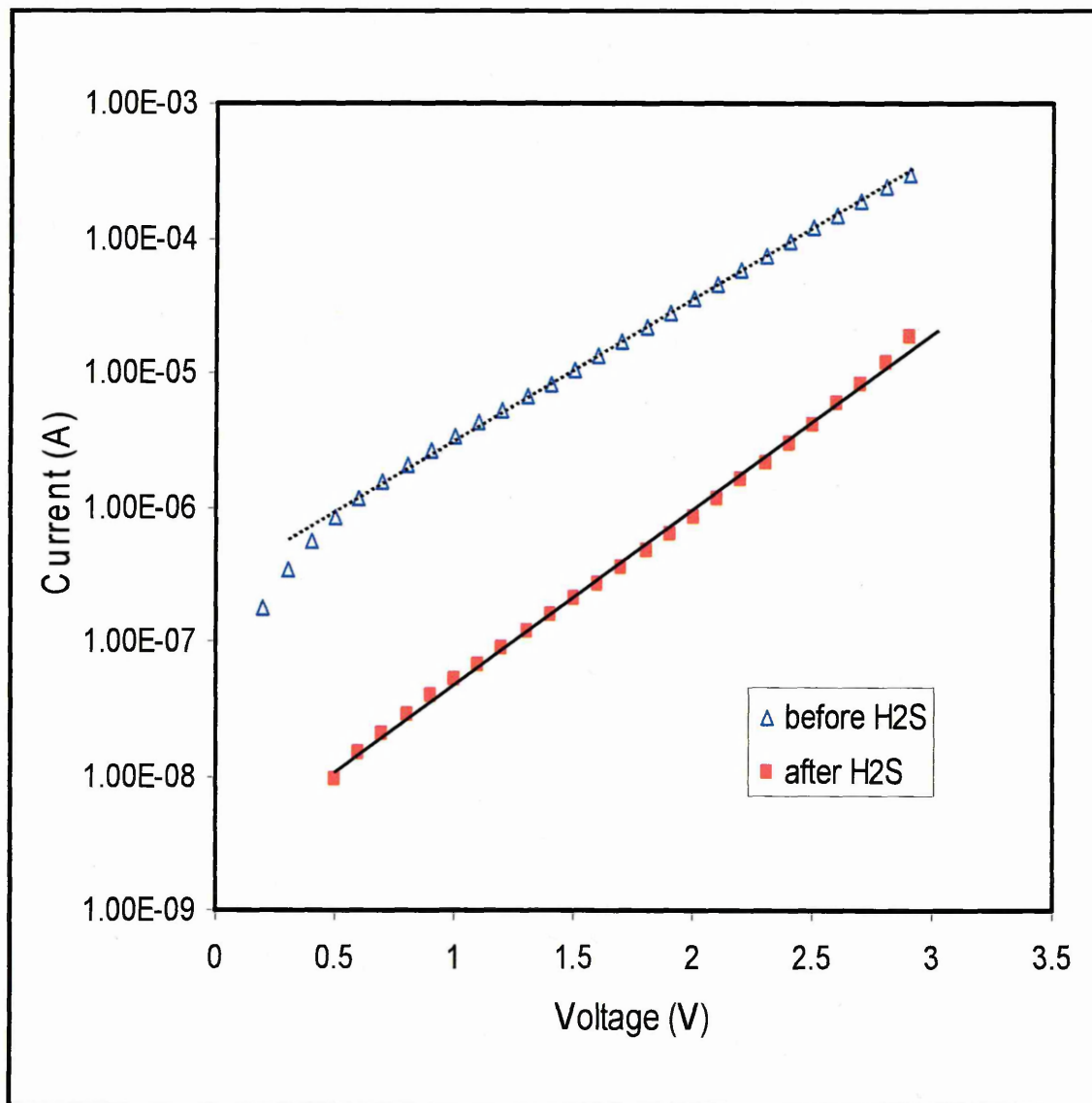


Figure 7.16 Semi-logarithmic scale of I-V characteristics of 33 layers of SA LB films for both treated and untreated samples

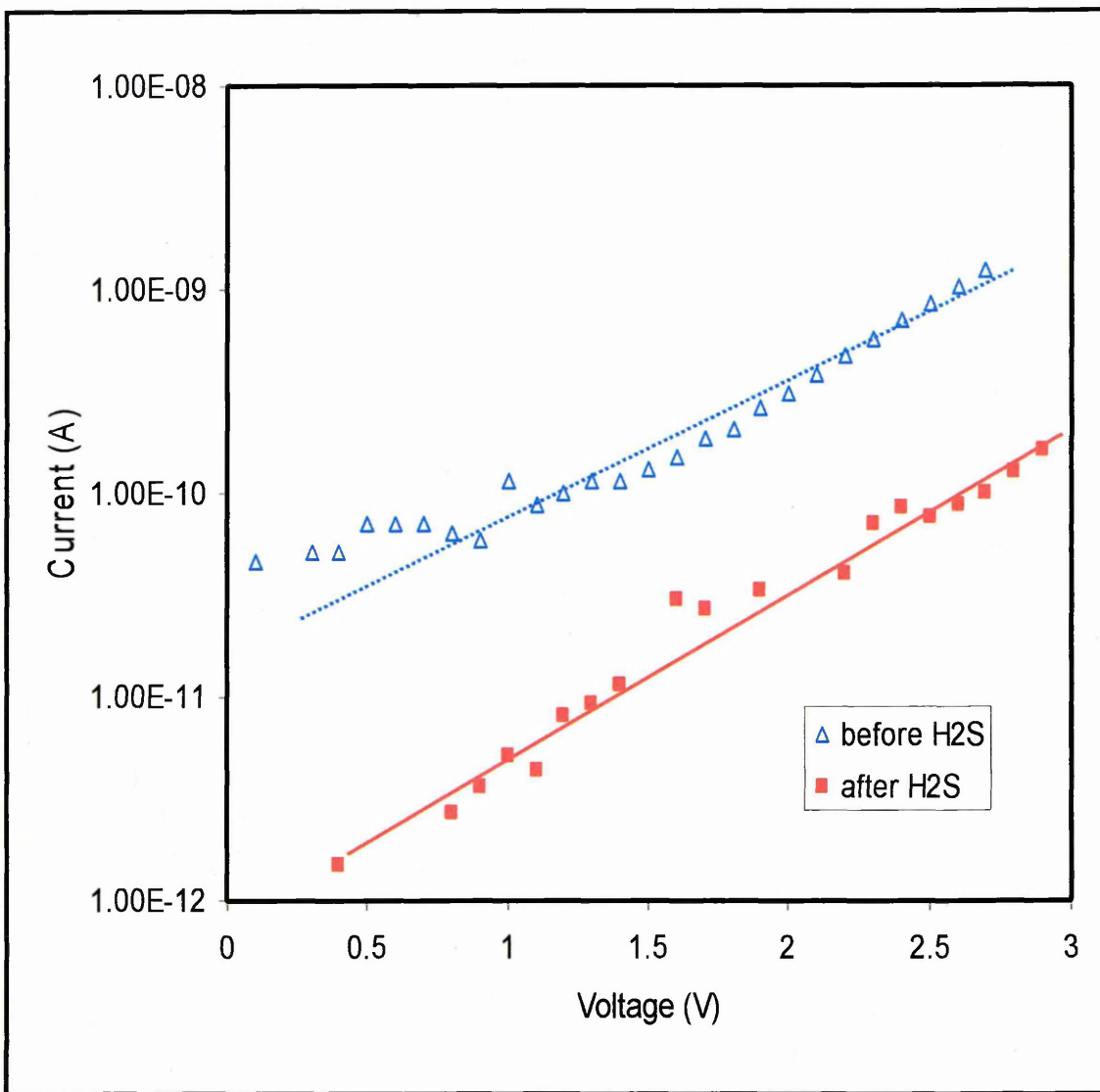


Figure 7.17 Semi-logarithmic scale of I-V characteristics of 37 layers of CA LB films for both treated and untreated samples

Further investigations of DC electrical behaviour of the LB films containing CdS nanoparticles were carried out by performing I-V characteristic measurements at a variety of temperatures (80-340K). The temperature dependence of tunnelling current is derived from the Equation (7.15) (see page 195):

$$\ln I \sim \left( \frac{4\alpha}{\pi N_d kT} \right)^{1/2} \quad (7.17)$$

The dependencies of  $\ln I$  versus  $T^{-1/2}$  at low (0.5 V) and high (2.5 V) applied bias for SA LB films (both before and after H<sub>2</sub>S treatment) are given in Figure 7.18. Figure 7.19 presents the temperature dependence of current for CA LB films.

Two linear regions, A and B, can be seen in both types of LB films. The flat lines, B (very small slope) obtained in the low temperature range (80-293 °K) demonstrate weak temperature dependence of conductivity. Such behaviour indicates that the conduction mechanism in such LB films at low temperatures is dominated by the electron tunnelling. For higher temperatures in the range of 293-340 °K, the observed linear dependence with higher slope is believed to correspond to the combination previously reported by Sugi [1985].

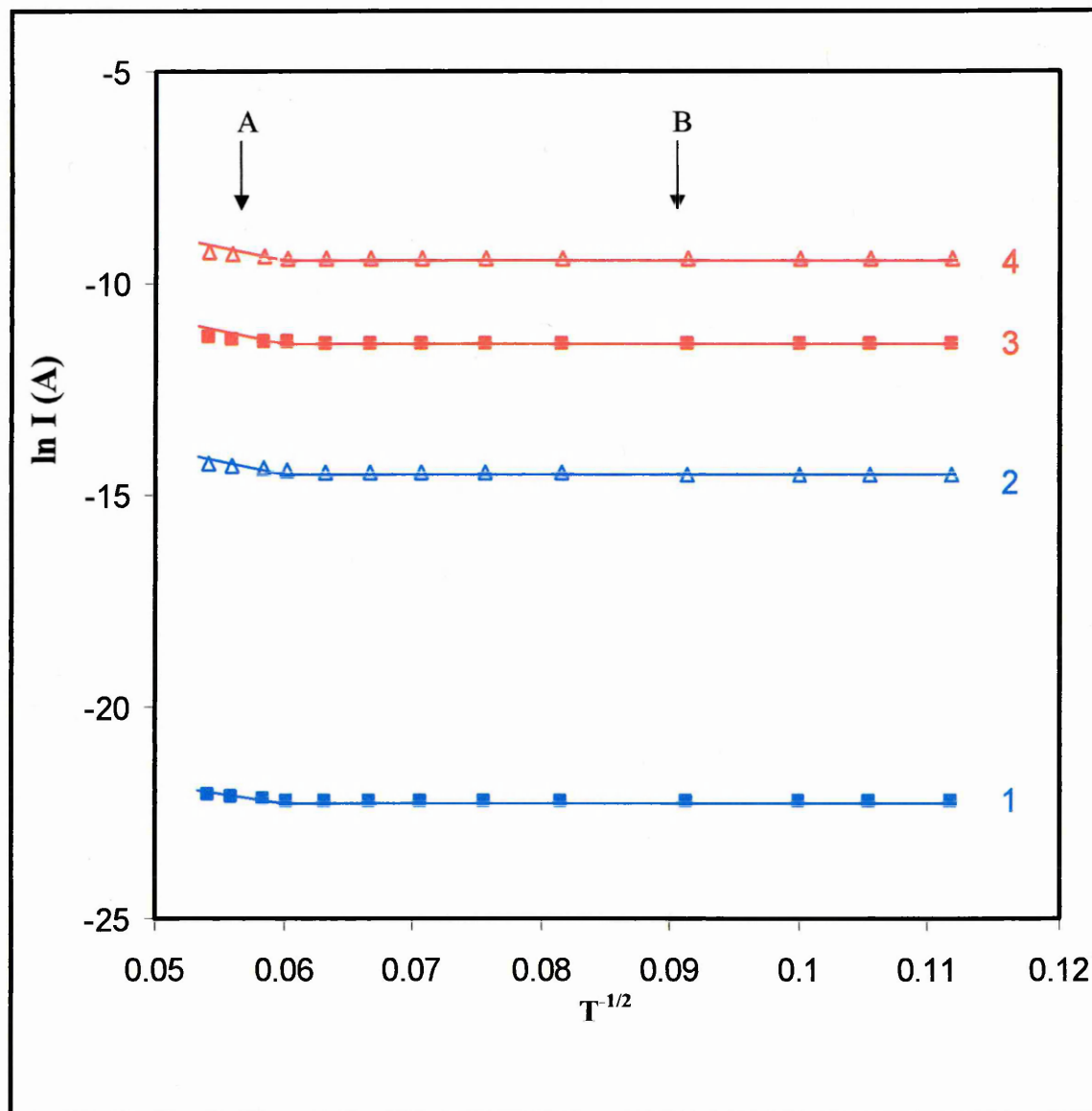


Figure 7.18. Temperature dependence of conductivity of SA LB films: (1) after H<sub>2</sub>S at 0.5 V, (2) before H<sub>2</sub>S at 0.5 V, (3) after H<sub>2</sub>S at 2.5 V, (4) before H<sub>2</sub>S at 2.5 V.

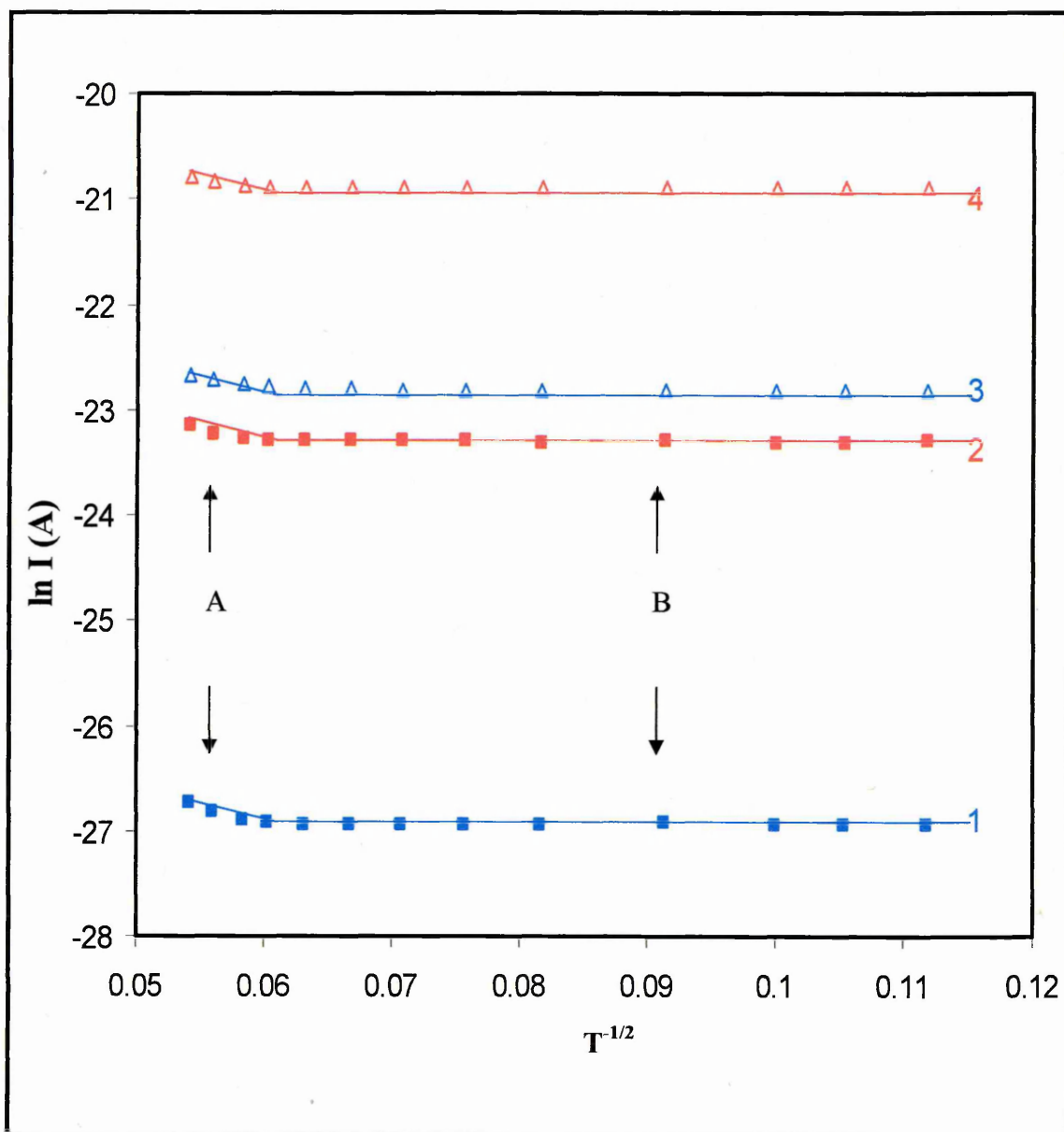


Figure 7.19. Temperature dependence of I-V Characteristics of CA LB films: (1) after  $H_2S$  at 0.5 V, (2) after  $H_2S$  at 2.5 V, (3) before  $H_2S$  at 0.5 V, (4) before  $H_2S$  at 2.5 V.

In Sugi's model the conductivity through multilayered LB films can be described by a combination of two mechanisms: (i) electron tunnelling through each LB bilayer, and (ii) thermally activated hopping within the plane of carboxylic head groups. Such behaviour is schematically described in Figure 7.20. The rate of charge transfer is given by Equation (7.15), which is

$$\lambda = \lambda_0 (2\alpha d)^2 \exp \left[ -(2\alpha d) - \left( \frac{4\alpha}{\pi N_t dkT} \right)^{\frac{1}{2}} \right], \text{ where } \lambda_0 \approx 10^{-13} \text{ s}^{-1} \text{ is a frequency factor,}$$

$$\alpha = \frac{2\pi}{h} (2m\Phi)^{\frac{1}{2}}, \text{ } m \text{ is the electron mass, and } \Phi \text{ is the height of a rectangular potential}$$

barrier. The first exponential term describes tunnelling through the barrier, while the second one reflects Mott's electron variable-range hopping [Mott *et al*, 1979] between localised states with the concentration of  $N_t \approx 10^{19} \text{ m}^{-2} \text{ eV}^{-1}$  [Sugi, 1985]. It should be stressed that in this case the number of LB bilayers does not affect the tunnelling current. It is believed that this model associated to the features of DC electrical conductivity through LB films above the room temperature (region A observed in Figure 7.18 and 7.19).

Further investigation of the temperature dependence of conductivity was carried out in order to evaluate the effect of the formation of CdS nanoparticles within the LB films in their electrical properties. The interface states density,  $N_t$  can be calculated from the slope of  $\ln I$  v.s.  $T^{-1/2}$  plot which is equal to  $\frac{4\alpha}{\pi N_t dk}$  (see Equation (7.15)). For this

Al/LB films/Al junctions, the tunnelling coefficient  $\alpha = 8 \times 10^9 \text{ m}^{-1}$  was taken from Polymeropoulos [1977]. Table 7.1 gives values of the interface states density for both types of LB films (treated and untreated samples). As can be seen, the exposure of H<sub>2</sub>S gas to the LB films reduces the  $N_t$  value of about 16 % and 12.5 % for SA and CA LB

films, respectively. This decreasing of  $N_i$  can be associated with film disordering due to the formation of CdS nanoparticles inside the LB films.

The increase of film thickness,  $d$  of about 5 % from 2.43 to 2.55 nm for SA LB films and around 4 % from 1.35 to 1.405 nm for CA LB films obtained from SPR and ellipsometry measurements (Chapter 6) can also affect tunnelling. The thickness dependence of conductivity of LB is given by the term  $\exp(-2\alpha d)$  in Equation (7.15). The calculation showed that the conductivity of SA films decreases in more than one order of magnitude (exponential term decreases from  $1.3 \times 10^{-17}$  to  $1.9 \times 10^{-18}$ ) as a result of  $H_2S$  treatment, while in CA LB films the decreasing from  $4.2 \times 10^{-10}$  to  $1.73 \times 10^{-10}$  gives a smaller reduction of conductivity. In addition to that, the increase in dispersion of film thickness as a result of  $H_2S$  treatment may also affect electron tunneling and thus gives further current reduction.

Despite the fact that LB films of SA have a larger bilayer spacing than that of CA films, the conductivity of SA LB films is much larger. It is most likely because of much higher layer-by-layer periodicity compared to CA LB films. This is supported by the results of Low Angle X-ray Diffraction study [Nabok *et al*, 1998], which also showed a significant decrease in the periodicity of SA LB films after the exposure to  $H_2S$  gas.

The weak temperature dependence of conductivity (line B in Figure 7.18 and 7.19) observed at low temperatures can be described by an inelastic tunnelling. Figure 7.21 shows the schematic diagram of this process. Electrons move through LB films by tunnelling through the hydrocarbon barriers and dissipate their energy in the head group planes by emitting phonons.

The effect of the applied voltage can be encountered by using the effective barrier height in Equation (7.15)  $(\Phi^*)^{1/2} = \frac{\Phi^{3/2} - (\Phi - V)^{3/2}}{V}$  for the tunnelling through the series of trapezium barrier (see Figure 7.21). Therefore, the observed changes in both the conductivity and slope of the linear part of I-V curves, shown in Figure 7.19 in logarithmic coordinates, can be interpreted in terms of changes in either bilayer thickness ( $2l$ ) or barrier height ( $\Phi$ ).

*Table 7.1. Interface density of states and exponential term of conductivity of treated and untreated LB films*

Samples		Interface density state, $N_i$ ( $\text{m}^{-2} \text{eV}^{-1}$ )		Exponential term, $\exp(-2\alpha d)$
		at 0.5 Volt bias	at 2.5 Volt bias	
SA films	Initial sample	$6.402 \times 10^{19}$	$6.396 \times 10^{19}$	$1.3 \times 10^{-17}$
	After $\text{H}_2\text{S}$	$5.419 \times 10^{19}$	$5.325 \times 10^{19}$	$1.9 \times 10^{-18}$
CA films	Initial sample	$5.484 \times 10^{19}$	$5.468 \times 10^{19}$	$4.2 \times 10^{-10}$
	After $\text{H}_2\text{S}$	$5.067 \times 10^{19}$	$5.077 \times 10^{19}$	$1.7 \times 10^{-10}$

Several conduction mechanisms, such as Schottky, Poole-Frenkel and Tunneling, were attempted to fit the experimental data. These conduction mechanisms should give a linear dependence on semi-logarithmic scale ( $\ln I$  versus  $V$ ). The experimental data described previously show clearly three major facts: (1) the conductivity has a weak dependence on temperature, (2) the conductivity does not depend on the film thickness (number of LB layer), and (3) the effect of the formation of CdS particles in the LB films decreases the conductivity. These three major experimental facts can only be described properly by Sugi's model at room temperature.

In contrast, other conduction mechanisms (Poole-Frenkel and Schottky) have a temperature dependence of conductivity. The film thickness affects the values of current (conductivity) in such mechanisms. These mechanisms also expect that inclusion of CdS particles in LB films will increase conductivity.

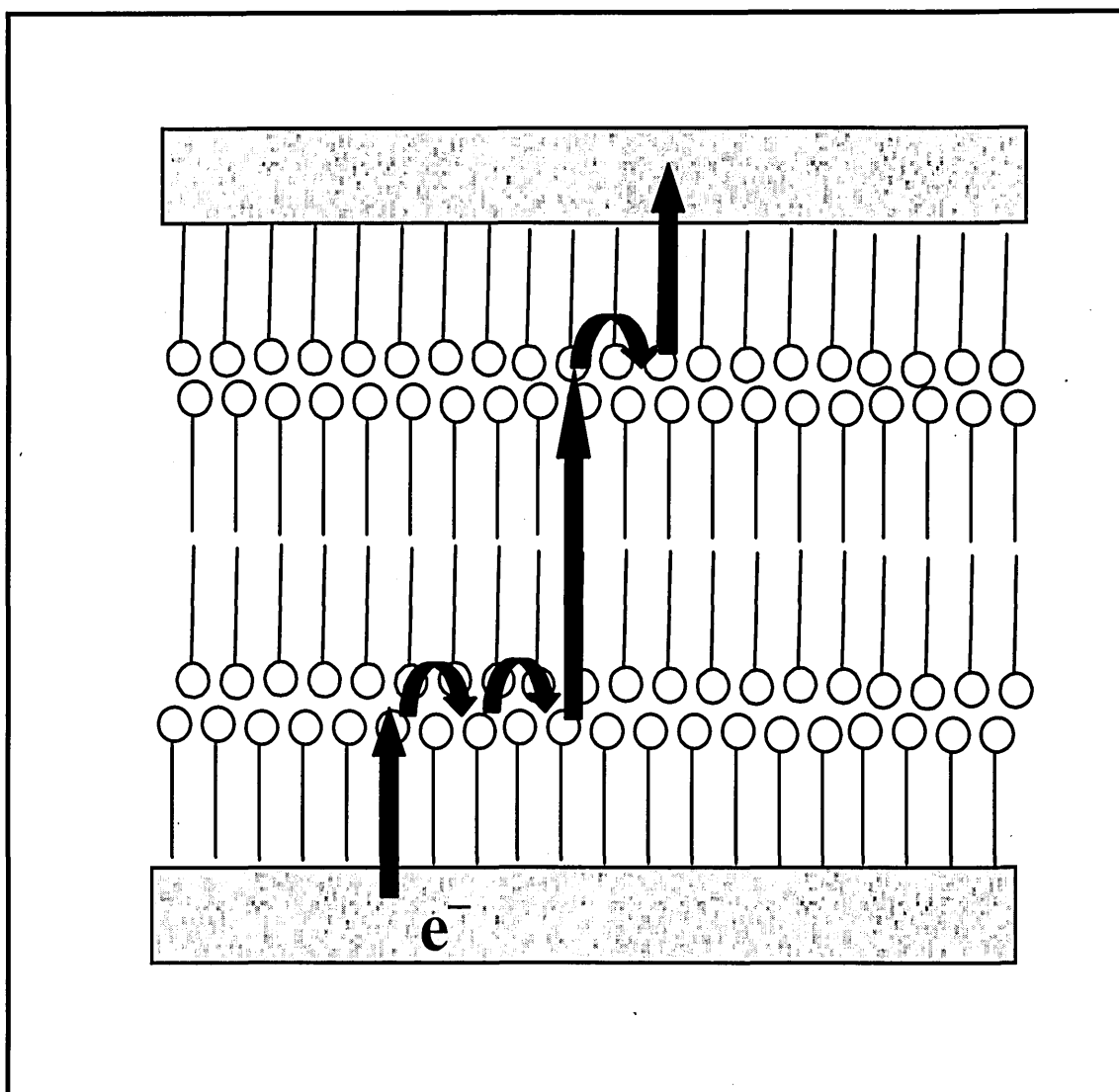


*Figure 7.20. Schematic diagram of the physical process of the electron transfer through a multilayered LB film according to Sugi's mechanism*

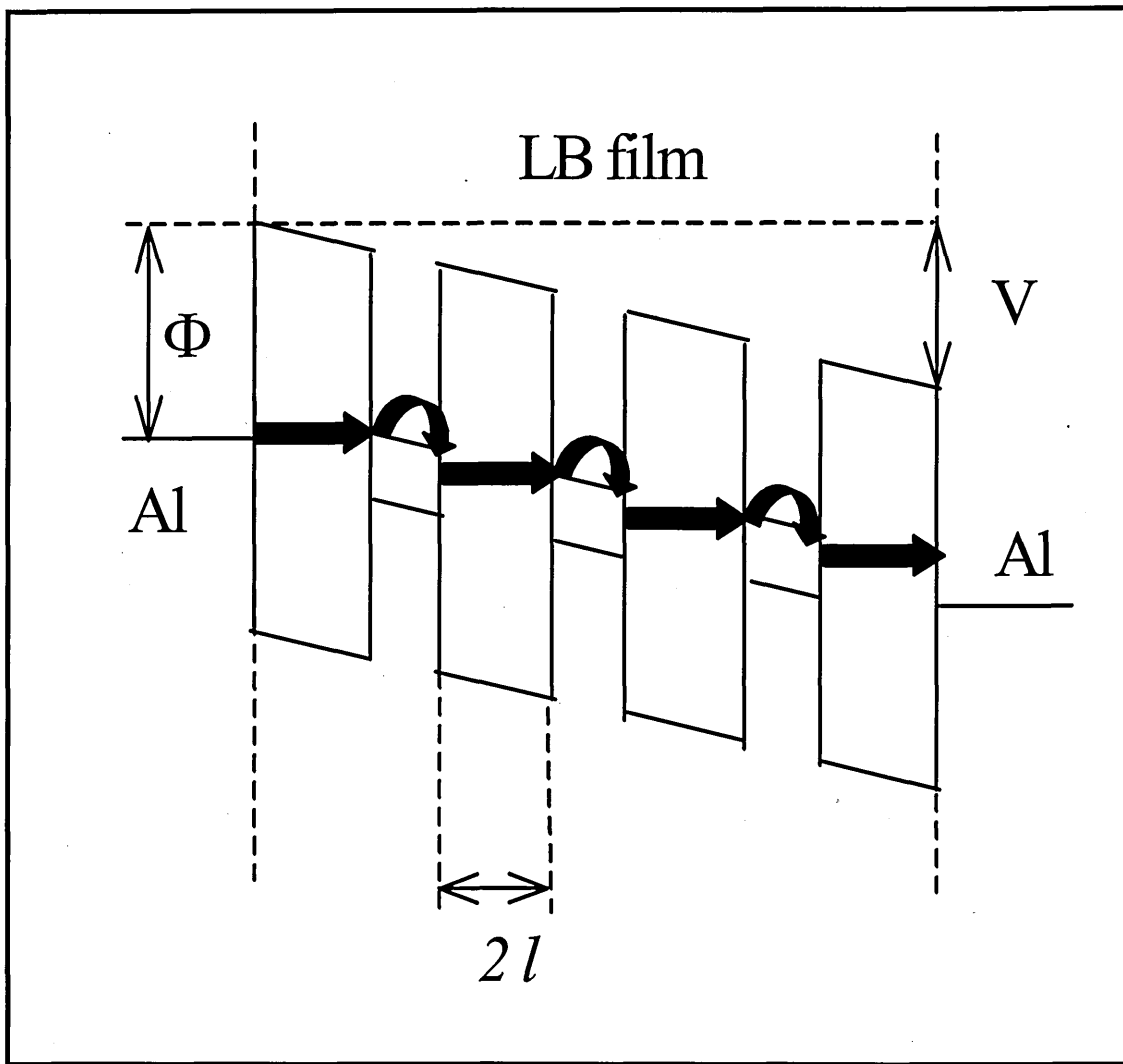


Figure 7.21. Schematic diagram of the inelastic electron tunnelling through a multilayered LB film

## 7.4.2. AC Measurements

Figure 7.22 shows typical results of the AC measurements of sandwich structures (Al/LB film/Al) as frequency dependencies of the capacitance for both treated with H<sub>2</sub>S gas and untreated samples. Figure 7.23 demonstrates their AC conductance as a function of frequency. These two kinds of measurement results represent a traditional insulating behaviour for all films studied. Similar AC characteristics have been previously reported for different types of LB films [Roberts *et al*, 1980; Geddes, *et al*, 1992].

As can be seen from Figure 7.22, the capacitance of the CA LB films is practically independent of frequency over the range of 10<sup>2</sup> –10<sup>6</sup> Hz. On the other hand, the capacitance of the SA LB films is found to decrease dramatically at frequencies higher than 10<sup>5</sup> Hz. It is also observed from the figure that the value of capacitance is higher for the SA films in comparison to that of the CA films. This is believed due to a larger thickness of the SA films compared to that for the CA LB films.

If the system is considered as a plane capacitor  $C = \frac{\epsilon_r \epsilon_0 A}{d_r}$ , the dielectric permittivity ( $\epsilon_r$ ) of closely packed LB films of SA is much higher than that of nanoporous CA LB films. Exact evaluation of dielectric constant  $\epsilon_r$  was difficult without knowing precisely the film thickness (the later is also affected by the film swelling due to H<sub>2</sub>S treatment). The calculations of the electric permittivity with the film thickness of 2.43 nm and 2.55 nm (for SA films before and after H<sub>2</sub>S treatment, respectively) obtained from ellipsometry and SPR measurements yield the values of 3.05 for the films before H<sub>2</sub>S treatment and 1.76 for after the exposure H<sub>2</sub>S. In the case of CA LB films, the values of 2.97 and 1.55 found for the sample before and after H<sub>2</sub>S treatment, respectively.

The formation of CdS nanoparticles within LB films disorders their structure and may cause the decrease in the dielectric permittivity ( $\epsilon_r$ ) and increase in the film thickness ( $d_r$ ). Previously reported swelling of calix[8]arene LB films of up to 5% of their thickness [Nabok et al, 1999] as a result of H<sub>2</sub>S treatment can not explain the observed 30 - 50% drop in capacitance. Therefore, formation of CdS nanoparticles in LB films must be accompanied by a decrease in  $\epsilon_r$ . Similar behaviours are also observed in this current result. Simple inclusion of CdS material, having a higher  $\epsilon_r$  value than that for organic film matrix, would yield an opposite effect. The most reasonable explanation of the observed decreasing in  $\epsilon_r$  lies in disorientation of amphiphilic molecules and the resulting reduction in the polarisability of LB films.

Figure 7.23 presents typical AC conductivity as a function of frequency of both SA and CA LB films. The observed monotonic increase of the AC conductivity with frequency ( $\sigma \approx \omega^n$ ,  $n < 1$ ) for both SA and CA compounds is a typical characteristic of LB films [Roberts *et al*, 1980; Geddes, *et al*, 1992]. As can be seen, the SA LB films have a higher conductivity compared to that of the CA LB films (similar data have been obtained from I-V DC measurements). The flattening of the conductance,  $G(\omega)$  curve, appeared at frequencies higher than 10<sup>5</sup> Hz, corresponds well to the drop of the capacitance in the AC capacitance measurements (Figure 7.22 and 7.23). It can be associated with some characteristic times of polarisation in LB films, so that at frequencies higher than 10<sup>5</sup> Hz the polarisation cannot follow the AC signal.

The attempts of fitting of AC experimental results to an equivalent circuit showed that the sandwich structures Al/ LB film/ Al cannot be modelled with a simple parallel RC circuit. The best fit, although not perfect, was achieved by introducing an extra series resistor, which can be associated with the contact, and substituting the capacitor with a constant phase element. Both AC and DC conductivity measurements

showed weak temperature dependence, a fact which verifies the tunnelling mechanism for the conductivity in the LB films. DC and AC electrical measurements were also performed on the planar structures of SA and CA films. The value of DC electric current between interdigitated electrodes with a spacing of 60  $\mu\text{m}$  is very small and close to the lower limit of the electrometer. Polarisation effects in the planar structure are also small and could not be registered with the LCR meter.

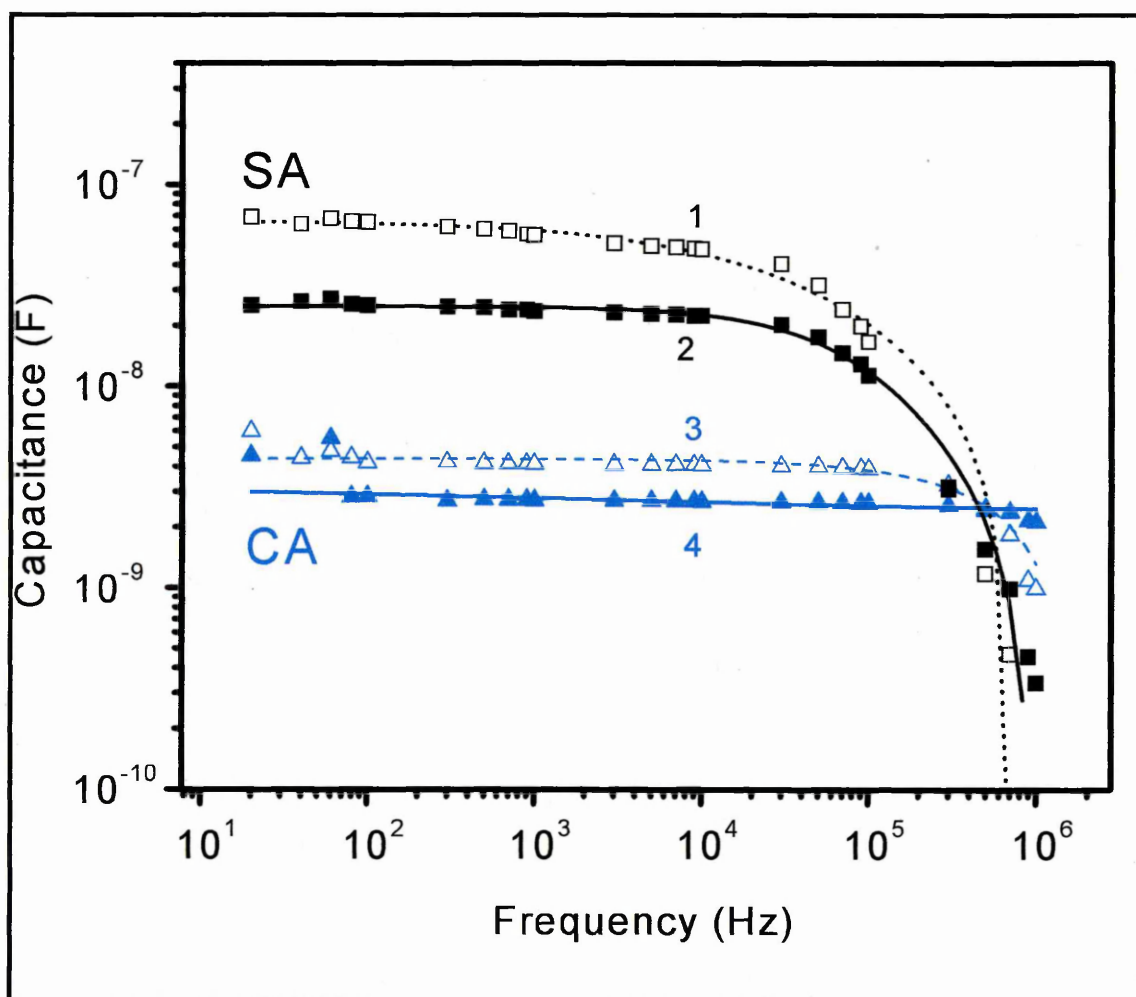
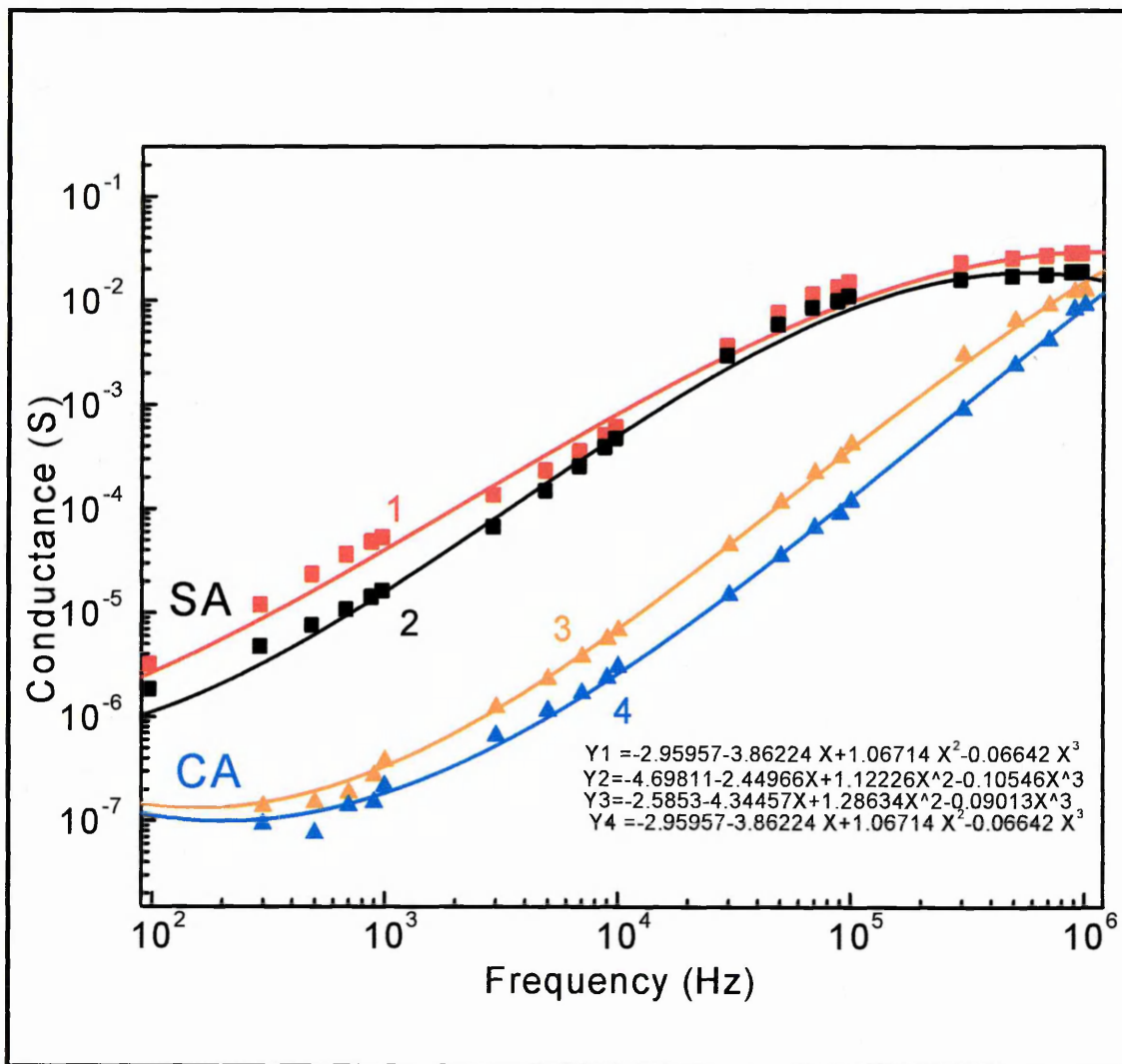


Figure 7.22. AC capacitance of the sandwich structures containing LB films (33 layers) of SA (1,2) and 37 layers of CA (3,4) before (1,3) and after (2,4)  $\text{H}_2\text{S}$  treatment



7.23. AC conductance of the sandwich structures containing LB films (33 layers) of SA (1,2) and 37 layers CA (3,4) before (1,3) and after (2,4) H<sub>2</sub>S treatment

## 7.5. Summary

The study of the DC and AC electrical characteristics of LB films of stearic acid and calix[8]arene in sandwich structures shows a traditional dielectric AC behaviour. Temperature dependence of conductivity indicated the conductivity mechanism of the LB films, which is a combination of electron tunnelling through the periodic LB film structure and thermally activated hopping within the plane of carboxylic head groups. The presence of CdS clusters in the film matrix did not result in either an enhancement of the electron transfer or an additional polarisation at a small (50 mV) AC signal. Most likely, the observed changes in DC conductivity and AC impedance are caused by the film disorder introduced by CdS nanoparticles.

# CHAPTER 8

## CONCLUSIONS AND FUTURE WORK

### 8.1. Thesis Conclusions

The formation and characterisation of CdS nanoparticles within organic films of different compounds (stearic acid and calixarene) is the subject of study in this thesis. This research concentrates on the Langmuir-Blodgett (LB) technique as the main method to produce the samples of CdS nanoparticles. Characterisation of the samples was carried out by using a variety of experimental techniques including AFM, SPR, ellipsometry, UV-visible spectroscopy, photoluminescence, DC and AC electrical measurements.

The LB films of Cd-salt stearic acids and Cd-salt calix[8]arene were successfully deposited on different solid substrates. The surface pressures of 25 mN/m and 28 mN/m were selected for LB deposition of calixarene and stearic acid, respectively. The  $\pi$ -A isotherm of stearic acid monolayer demonstrates the area per molecule of about 21 Å<sup>2</sup>, while calix[8]arene derivatives shows it's increasing, as the length of the substituting alkyl chain on the lower rim increases. CdS nanoparticles were formed by exposure the Cd-salt LB films to dihydrogen sulphide (H<sub>2</sub>S) gas at room temperature.

AFM (tapping mode) study of the treated in H<sub>2</sub>S gas cadmium stearate LB films demonstrates CdS clusters with lateral dimensions in the range of 20-30 nm. The amphiphiles retain their positions over the CdS particles resembling the particle shape. The actual size of CdS particles may therefore be smaller than the values determined from AFM studies. Additionally, the tip broadening and limited resolution of AFM instrument are likely to contribute to the uncertainties associated with the particle sizes. These clusters are faceted to hexagonal shape. Similar but slightly smaller CdS clusters of about 10-15 nm were found in CA LB films.

It should be emphasized that the size of 2-3 nm for CdS particles, obtained previously from UV-visible absorption spectra measurements, is 10 times less than that from the AFM study. It is believed that CdS particles in stearic acid LB films are pseudo two-dimensional and have a shape of hexagonal platelets with the lateral dimensions of 20-30 nm and 2-3 nm in thickness. Additionally, the hexagonal shape gives clear indication of wurzite structure of CdS nanoparticles.

Photoluminescence excitation spectra of CdS in LB films resemble respective UV-visible absorption spectra, and yield similar size of CdS nanoclusters formed inside the LB films. Calculations of the cluster thickness  $L_z$  yield the value of 2 nm (PLE) and 1.9 nm (UV-vis) for CdS clusters in SA matrix and two values of 1.2 nm and 1.6 nm (PLE) and 1.08 nm and 1.42 nm (UV-vis) for CA LB films. The photoluminescence emission spectra demonstrate a very large Stokes shift, which can be attributed to the formation of “dark excitons” in the platelet-shaped CdS clusters.

The transformations of the absorption spectra caused by ageing were monitored as time dependencies of the CdS nanoparticles size. A monotonic increase in size with the tendency of saturation was observed in all cases, although the changes in size are much more pronounced for SA films compared to those in CA films. The observed

spectral features and the changes in size of CdS clusters can be explained by the model of two-dimensional diffusion. According to this model, CdS molecules in the SA films, initially evenly distributed within each LB bilayer, aggregate and form "large" clusters having Lifshitz-Slezoff type size distribution with an average size of 1.9 nm.

The aggregation of CdS molecules in LB layers, and thus the size of the nano-clusters formed, can be controlled by using organic cavitand compounds instead of fatty acids. In particular, much smaller CdS nanoparticles (as compared to those formed in fatty acid LB films) have been formed in calixarene LB films. Moreover, apart from the shift of the absorption band edge, the UV-visible absorption spectra of these films show two well-resolved peaks at room temperature, which can be associated with two different sizes of CdS clusters, 1.2 nm and 1.4 nm. The size distribution is similar to that in SA films. Smaller size of CdS particles in CA films is because of the restriction of two-dimensional diffusion by calixarene cavities.

The SPR measurements performed before the exposure of H<sub>2</sub>S gas give an average thickness of  $2.44 \pm 0.034$  nm and  $1.33 \pm 0.058$  nm per-monolayer for SA and CA LB films, respectively. This value is in good agreement with the result obtained from ellipsometry measurements, which gives the average value of  $2.42 \pm 0.090$  nm and  $1.37 \pm 0.007$  nm for SA LB films and CA LB films, respectively. Meanwhile, the refractive index has been found to slightly increase as the number of films increases with the value of refractive index of SA LB films slightly higher than that of CA LB films.

The formation of CdS nanoparticles inside LB films was monitored *in-situ* with SPR measurements at a fixed angle of incidence during the flow of H<sub>2</sub>S gas into the gas cell. The results demonstrate both the resonance shift and broadening of SPR curves due to formation of light absorbing CdS clusters. It can be concluded that the formation of

CdS clusters happened relatively fast within a few minutes and almost reaches saturation in about 30 minutes.

The fitting of the ellipsometry and SPR data obtained for samples after H<sub>2</sub>S treatment, shows that both thickness and refractive index of the LB films increase due to formation of CdS nanoparticles inside. In case of CA LB films, smaller changes have been found compared to those of SA LB films. This may be caused by smaller size of CdS nanoparticles compared to that of SA LB films.

The DC I-V characteristics of the sandwich structures (MIM) of Aluminium/LB films/Aluminium show exponential behaviour and weak temperature dependence. Such behaviour is typical for electron tunnelling through multi-layered LB films. The formation of CdS nanoparticles in the LB films of both stearic acid and calixarene decreases the conductivity value, which is believed to be caused by the reduction of layer-by-layer film order. AC measurements show a traditional insulating behaviour for all kind of films studied. Formation of CdS clusters in the LB films resulted in the decrease in both the capacitance and AC conductivity, which can be interpreted by the drop in the polarisability in disordered LB films.

## 8.2. Suggestion for Future Work

Realisation of real applications in nanoelectronics and optoelectronics of CdS nanoparticles needs improvement of the production quality and the knowledge of electrical and optical properties of these materials. In order to obtain a better understanding of the electrical, morphological and optical properties of CdS nanoparticles, further measurements need to be done.

1. Further photoluminescence experiments, particularly at low temperature and luminescence kinetics are needed to exclude luminescence of impurities and confirm large Stokes spectral shift.
2. In order to evaluate optical parameters of CdS nanoparticles in LB films (SA and CA), further spectroscopic ellipsometry measurements are required.
3. AFM and STM measurements with improved resolution (presumably down to atomic level) need to be done in order to study CdS particles in more detail.
4. Further DC and AC electrical measurements, such as impedance measurements in a wider frequency range stretched down to DC need to be done in order to further explore their electrical properties.
5. The work should be expanded by using other metal salts and thus other metal sulphide nanoclusters. It would be extremely interesting to study II-VI semiconductor layers formed after washing out the organic molecules.

## REFERENCES

- Abdulkhadar, A., and Thomas, B., 1998, *Nanostructured Materials*, 10 (4), p593
- Alkuhaimi, S. A., 2000, *Energy*, 25, 8, p731
- Allais, M., and Gandais, M., 1992, *Philos. Magazine Letters*, 65, p243
- Andryushin, E. A., and Silin, A. P., 1980, *Soviet Physics Solid St.*, 22, p1562
- Arakawa, Y., Nishioka, M., Nakayama, H., and Kitamura, M., 1996, *IEICE Trans. Electron.*, E79-C, p1487
- Aramoto, T., Adurodija, F., Nishiyama, Y., Arita, T., Hanafusa, A., Omura, K., and Morita, A., 2003, *Solar energy Materials & Solar Cells*, 75, p211
- Asai H., Yamada S. and Fukui T., 1987, *Applied Physics Letters*, 51, p1518
- Aven, M., and Prener, J. S., 1967, *Physics and Chemistry of II-VI Compounds*, North-Holland Publishing Company, Amsterdam, the Netherland
- Azzam, R. M. A., and Bashara, N. M., 1977, *Ellipsometry and Polarized Light*, North-Holland, Amsterdam, the Netherland
- Babaev, N. A., Bagaev, V. S., Gaponov, S. V., Kopylovskii, B. D., Salashchenko, N. N., and Stopachinskii, V. B., 1983, *JETP Letters*, 37, p624
- Babaev, N. A., Bagaev, V. S., Gavin, F. V., Kochemasov, A. V., Paramonov, L. V. Poyarkov, A. G., Salashchenko, N. N., and Stopachinskii, V. B., 1984, *JETP Letters*, 40, p952
- Bawendi, M. G., Wilson, W. L., Rothberg, L., Carroll, P. J., Jedju, T. M., Steigerwald, M., L., and Brus, L. E., 1990, *Physics Review Letters*, 65, p1623
- Birman et al., 1961 in: Aven, M., and Prener, J. S., 1967, *Physics and Chemistry of II-VI Compounds*, North-Holland Publishing Company, Amsterdam, the Netherland
- Bonnell, D. A., 2001, *Scanning probe microscopy and spectroscopy: theory, techniques, and applications*, Wiley-VCH, New York, USA
- Borrelli, N. F., Hall, D. W., Holland, H. J., and Smith, D. W., 1987, *Journal of Applied Physics*, 61, p5399
- Brasil, M. J. S. P., Bernussi, A. A., Cotta, M. A., Marquezini, M. V., Brum, J. A., Hamm, R. A., Chu, S. N. G., Harriott, L. R., and Temkin, H., 1994, *Applied Physics Letter*, 65, p857
- Brus, L. E., 1983, *Journal of Chemical Physics*, 79, p5566
- Brus, L. E., 1984, *Ibid.*, 80, p4403
- Brus, L. E., 1986, *IEEE Journal of Quant. Electron.*, QE-22, p1909

- Bykov, V.A., 1996, *Biosensors & Bioelectronics*, Vol. 11, No. 9, p923
- Chadderton, L. T., Fitzgerald, A. G., and Yoffe, A. D., 1964, *Journal of Applied Physics*, 35, p1582
- Chaimowicz, J. C. A., 1989, *Optoelectronics: an introduction*, Butterworth-Heinemann Ltd., Oxford, UK
- Chestony, N., Harris, T. D., Hull, R., and Brus, L. E., 1986, *Journal of Physical Chemistry*, 90, p3393
- Chevreau, A., Phillips, B., Higgins, B.G., and Risbud, S.H., 1996, *Journal of Material Chemistry*, 6(10), p1643
- Chikyow, T., and Koguchi, N., 1992, *Applied Physics Letters*, 61, p2431
- Colvin, V. L., and Alivisatos, A. P., 1992, *Journal of Chemical Physics*, 97, p730
- D'Andrea, A., Del Sole, R., and Cho, K., 1990, *Euro Physics Letters*, 11, p169
- De Bruijn, H.E., Altenburg, B. S. F., Kooyman, R. P. H., and Greve, J., 1991, *Optical Communication*, 82, p425
- Dean, P. J., 1982, *Progress in Crystal Growth and Characterisation*, Vol. 5, p89
- Desnica, U.V., Gamulin, O., Tonejc, A., Ivanda, M., White, C.W., Sonder, E., and Zuhr, R.A., 2001, *Materials Science and Engineering C*, 15, p105
- Desnica, U.V., Desnica-Frankovic, I.D., Gamulin, O., White, C.W., Sonder, E., and Zuhr, R.A., 2002, *Journal of Non-crystalline Solids*, 299-302, p1100
- Dharmadasa, I. M., 1998, *Prog. Crystal Growth and Charact.*, Vol. 36, No. 4, p249
- Dingle, R., 1976, *Proceeding of 13<sup>th</sup> International Conference on the Physics of Semiconductors*, Rome, 1976, edited by F. G. Fumi, p965
- Edelstein, A. S. and Cammarata, R. C., 1998, *Nanomaterials: Synthesis, Properties and Applications*, Institute of Physics Publishing, Bristol, UK
- Efros, Al. L., and Efros, A. L., 1982, *Soviet Phys. Semicond.*, 16, p772
- Efros, Al. L., Ekimov, A. I., Kozlowski, F., Petrova-Koch, V., Schmidbaur, H., and Shumilov, S., 1991, *Solis State Communications*, 78, p853
- Einevoll, G. T., 1992, *Physics Review B*, 45, p3410
- Ekimov, A. I., and Onushchenko, A. A., 1981, *JETP Letters*, 34, p345
- Ekimov, A. I., Efros, Al. L., and Onushchenko, A. A., 1985, *Solid State Communications*, 56, p921
- Ekimov, A. I., Efros, Al. L., Shubina, T. V., and Skvortsov, A. P., 1990, *Journal of Luminescence*, 46, p97
- Ekimov, A. I., 1991, *Phys. Scrip. T.*, 39, p217

**Elliot, D.J., Furlog, D.N., Grieser, F., 1999, *Colloids and Surfaces A: Physicochemical and Engineering Aspects*, 155, p101**

**Elliot, R. J., 1957, *Phys. Rrv.*, 108, p1384**

**Erokhin V., Carrara, S., Amenitch, H., Bernstroff, S., and Nicolini, C., November 5-8 1997, *Proceeding of the fifth Foresight Conference on Molecular Nanotechnology*, Palo Alto Research Center, CA, USA**

**Erokhin V., Paddeu, S., Paternolli, C., Leotti, A., and Nicolini, C., November 12-15 1998, *Proceeding of the sixth Foresight Conference on Molecular Nanotechnology*, the Westin Hotel in Santa Clara, CA, USA**

**Erokhin, V., Facci, P., Gobbi, L., Dante, S., Rustichelli, F., and Nicolini, C., 1998, *Thin Solid Films*, 327-329, p503**

**Erokhin, V., Facci, P., Carrara, S., and Nicolini, C., 1996, *Thin Solid Films*, p284**

**Erokhin, V., Facci, P., Carrara, S., and Nicolini, C., 1995, *Journal of Physics D: Applied Physics*, 28, p2534**

**Erokhin, V., Facci, P., Tronin, and Nicolini, C., 1994, *Journal of Physical Chemistry*, 98, p13323**

**Erokhin, V., Feigin, L., Ivakin, G., Klechkovskaya, V., Yu Lvov, Stiopina, N, 1991, *Makromol. Chem. Makromol. Symo*, 46, p359**

**Evans, B. L., and Young, P. A., 1968, *Phys. Stat. Sol.*, 25, p417**

**Facci, P., Erokhin, V., Carrara, S., and Nicolini, C., 1996, *Proc. Nat. Acad. Sci. USA*, 93, p10556**

**Facci, P., Erokhin, V., Tronin, A., and Nicolini, C., 1994, *Journal of Physical Chemistry*, Vol. 98 no. 50, p13323**

**Fontana, E., Pantell, R. H., and Strober, S., 1990, *Applied Optics*, Vol. 29, No. 31, p4694**

**Fukui, T., and Ando, S., 1989, *Electronics letters*, 25, p410**

**Galeuchet, Y. D., Rothuizen, H., and Roentgen, P., 1991, *Applied Physics Letters*, 58, p2423**

**Geddes, N.J., Sambles, J.R., D.J.Jarvis, D.J., Parker, W.G., and Sandman, D.J., 1992, *Journal of Applied Physics*, 71(2), p756**

**Gordon, J. G., and Swalen, J. D., 1977, *Optics Communications*, Vol. 22, No. 3, p374**

**Greene, R. L., and Bajaj, K. K., 1983, *Solid State Communications*, 45, p831**

**Gupta, P., Pal, R., Bhattacharyyya, D., Chaudhuri, S., and Pal, A. K., 1995, *Phys. Stat. Sol.*, 148, p459**

**Hanamura, E., Nagaosa, N., Kumagai, M., and Takagahara, T., 1988, *Material Science and Engineering B*, 1, p255**

**Hara, S., Motohisa, J., and Fukui, T., 1998, *Solid State Electronics*, 42, p1233**

**Hassan, A.K., Ray, A.K., Nabok, A.V., and Wilkop, T., 2001, *Applied Surface Science*, 182, p49**

**Hassan, A.K., Ray, A.K., Nabok, A.V., and Davis, F., 2001, *Sensors and Actuators B*, 77, p638**

**Hassan, A.K., Ray, A.K., Nabok, A.V., Lucke, A., Smith, K., Stirling, C.J.M., and Davis, F., 1999, *Materials Science and Engineering C*, 8-9, p251**

**Isshiki, H., Aoyagi, Y., Sugano, T., Iwai, S., and Meguro, T., 1993, *Applied Physics Letters*, 63, p1528**

**Iwantono, 1999, *Optical Spectroscopic Study of the Electronic Properties of III-V Nitrides and Phosphides Semiconductors*, M.Phil thesis, the University of Sheffield, U.K.**

**Jacak, L., Hawrylak, P., and Wojs., A., 1998, *Quantum dots*, Springer-Verlag, Berlin**

**Jin, J., Li, L. S., Tian, Y. Q., Zhang, Y. J., Liu, Y., Zhao, Y. Y., Shi, T. S., and Li, T. J., 1998, *Thin Solid Films*, 327-329, p559**

**Jonscher, A. K., 1992, *IEEE Transactions on Electrical Insulation*, Vol. 27, No. 3, p407**

**Jonscher, A. K., 1990, *Solid State Electronics*, Vol. 33, p737**

**Jonscher, A. K., 1983, *Dielectric Relaxation in Solids*, Chelsea Dielectrics Press, London**

**Kapon, E., Hwang, D. M., and Bhat, R., 1989, *Physics Review Letters*, 63, p430**

**Kasap, S. O., 2001, *Optoelectronics and Photonics: Principles and Practices*, Prentice Hall, New Jersey, USA**

**Kasap, S. O., 1997, *Principles of Electrical Engineering Materials and Devices*, McGraw-Hill, New York, USA**

**Kawabe, M., Chun, Y. J., Nakajima, S., and Akahane, K., 1997, *Japanese Journal of Applied Physics*, 36, p4078**

**Kayanuma, Y., 1986, *Solid State Communications*, 59, p405**

**Kayanuma, Y., 1988, *Physics Review B*, 38, p9797**

**Keldysh, L. V., 1979, *JETP Letters*, 29, p659**

**Kim, S. J., Asahi, H., Takemoto, M., Asami, K., Takeuchi, M., and Gonda, S., 1996, *Japanese Journal of Applied Physics*, 35, p4225**

- Kittel, C., 1996, *Introduction to Solid State Physics*, seventh edition, John Wiley & Sons, Inc., New York, USA
- Kojima, K., Mitsunaga, K., and Kyuma, K., 1990, *Applied Physics Letters*, 56, p154
- Kortan, A.R., Hull, R., Opila, R.L., Bawendi, M.G., Steigergerwald, M.L. Carrol, P.J., and Brus, L.E., 1990, *J. Am. Chem. Soc.*, 112, p1327
- Kuhn, H., 1967, *Naturwissenschaften*, 54, p429
- Lakowicz, J. R., 1999, *Principles of Fluorescence Spectroscopy*, Plenum Publishers, New York, USA
- Landsberg, P. T., 1991, *Recombination in Semiconductors*, Cambridge University Press, Cambridge
- Liedberg, B., Nylander, C., and Lundstrom, I., 1995, *Biosensens. Bioelectron.*, 10, R1
- Liedberg, B., Nylander, C., and Lundstrom, I., 1983, *Sensors and Actuators B*, 4, p299
- Li, H., Mao, G., and Simon Ng, K. Y., 2000, *Thin Solid Films*, 358, p62
- Li, L. S., Qu, L., Lu, R., Peng, X., Zhao, Y., and Li, T. J., 1998, *Thin Solid Films*, 327-329, p408
- Li, L. S., Jin, J., Tian, Y. Q., Zhao, Y. Y., Li, T. J., Jiang, S. M., Du, Z. L., Ma, G. H., and Zheng, N., 1998, *Supramolecular Science*, 5, p475
- Li, L. S., Qu, L., Wang, L., Lu, R., Peng, X., Zhao, Y., and Li, T. J., 1997, *Langmuir*, 13, p6183
- Li, L.S., Jin, J., Tian, Y.Q., Zhao, Y.Y., Li, T.J., Jiang, S.M., Du, Z.L., Ma, G.H., and Zheng, N., 1998, *Supramolecular Science*, 5, p475
- Li, S. S., 1993, *Semiconductor Physical Electronics*, Plenum Press, New York
- Liang, E. Z., Lin, C. F., Shih, S. M., and Su, W. F., 2001, *Proceeding of IEEE-NANO 2001 Conference*, p363
- Lifshitz, I. M., and Slezov, V. V., 1959, *Soviet Phys., JETP*, 8, p331
- Lippens, P. E., and Lannoo, M., 1989, *Physics Review B.*, 39, p10935
- Lippens, P. E., and Lannoo, M., 1990, *Ibid.*, 41, p6079
- Lippens, P. E., and Lannoo, M., 1991, *Semiconductor Science and Technology*, 6, A157
- Mandal, S. K., Maity, A. B., Dutta, J., Pal, R., Chaudhuri, S., and Pal, A. K., 1997, *Phys. Stat. Sol.*, 163, p433
- Mann, B., and Kuhn, H., 1971, *Journal of Applied Physics*, 42, p4398

**Martin P., and Szablewski, M., 1999, *Tensiometers and Langmuir-Blodgett Troughs; Operating Manual*, Nima technology Ltd., Coventry, England**

**Masumoto, Y., 1994, *Journal of Luminescence*, 60-1, p256**

**McCartney, C.M., Richardson, T., Greenwoog, M.B., Cowlam, N., Davis, F., Stirling, C.J.M., 1997, *Supramolecular Science*, 4, p385**

**Mews, A., Eychmuller, A., Giersig, M., Schooss, D., and Weller, H., 1994, *J. Phys. Chem.*, 98, p934**

**Mikhailov, G. V., Panfilov, A. G., and Razbirin, B. S., 1990, *Journal of Cryst. Growth*, 101, p739**

**Misawa, K., Yao, H., Hayashi, T., and Kobayashi, T., 1991, *Journal of Luminescence*, 48-49, p269**

**Moriguchi, I., Nii, H., Hanai, K., Nagaoka, H., Teraoaka, Y., and Kagawa, S., 1995, *Colloids and Surfaces A: Physicochemical and Engineering Aspects*, 103, p173**

**Moriguchi, I., Tanaka, I., Teraoaka, Y., and Kagawa, S., 1991, *Journal of Chem. Soc. Chem. Commun.*, 1401**

**Nabok, A. V., Iwantono, B., Hassan, A. K., Ray, A. K., and Wilkop, T., 2002, *Materials Science and Engineering C*, 22, p355**

**Nabok, A. V., Iwantono, Ray, A. K., Larkin, I., Richardson, T., 2002, *Journal of Physics D*, Vol. 35, p1512**

**Nabok, A. V., Ray, A. K., Hassan, A. K., 2000, *Journal of Applied Physics*, Vol. 88, No. 3, p1333**

**Nabok, A. V., Hassan, A. K., and Ray, A. K., 2000, *Journal of Material Chemistry*, 10, p189**

**Nabok, A.V., Ray, A.K., Hassan, A.K., Titchmarsh, J.M., Davis, J., Richardson, T., Starovoitov, A., Bayliss, S., 1999, *Materials Science & Engineering C*, 8-9, p171**

**Nabok, A.V., Richardson, T., McCartney, C., Cowlamb, N., Davis, F., Stirling, C.J.M., Ray, A.K., Gacem, V., and Gibaud, A., 1998, *Thin Solid Films*, 327-329, p510**

**Nabok, A. V., Ray, A. K., Hassan, A. K., Omar, O., Taylor, R., Richardson, T., and Pavier, M., 1998, *Thin Solid Films*, 327-329, p104**

**Nabok, A.V., Richardson, T., Davis, and F., Stirling, 1997, *Langmuir*, 13, p3198**

**Nabok, A. V., Hassan, A. K., Ray, A. K., Omar, O., Kalchenko, V. I., 1997, *Sensors and Actuators B*, 45, p115**

**Nakamura, K., Gotoh, M., Fujihara, T., Toyama, T., and Okamoto, H., 2003, *Solar Energy Materials & Solar Cells*, 75, p185**

- Nakata, Y., Ueda, O., Tacheuchi, A., Nakamura, S., and Muto, S., 1995, *J. Cryst. Growth*, 150, p341
- Nanda, K. K., Sarangi, S. N., and Sahu, S. N., 1998, *NanoStructured Materials*, Vol. 10, No. 8, p1401
- Nanda, K.K., and Sahu, S.N., 1999, *Solid State Communications*, 111, p671
- Nirmal, M., Dabbousi, B. O., Bawendi, M. G., Macklin, J. J., Trautman, J. K., Harris, T. D., and Brus, L. E., 1996, *Nature*, 383, p802
- Nötzel, R., Temmyo, J., and Tamamura, T., 1994, *Nature*, 369, p131
- Okada, H., Fujikura, H., Hashizume, T., and Hasegawa, H., 1997, *Japanese Journal of Applied Physics*, 36, p1672
- O’Niel, M., Marohn, J., and McLendon, G., 1990, *Journal of Physical Chemistry*, 94, p4356
- Oshinowo, J., Nishioka, M., Ishida, S., and Arakawa, Y., 1994, *Applied Physics Letters*, 65, p1421
- Pankove, J.I., 1971, *Optical Processes in Semiconductors*, Prentice-Hall, Inc., New Jersey
- Pearah, P. J., Chen, A. C., Moy, A. M., Hsieh, K. C., and Cheng, K. Y., 1993, *Applied Physics Letters*, 62, p729
- Peng, X. G., Lu, R., Zhao, Y. Y., Qu, L. H., Chen, H. Y., and Li, T. J., 1994, *Journal of Physical Chemistry*, 98, p7052
- Petroff, P. M., Lorke, A., and Imamoglu, A., May 2001, *Physics Today*, p46
- Petty, M. C., 1996, *Langmuir-Blodgett Films: An Introduction*, Cambridge University Press, Cambridge, UK
- Petty, M. C., Bryce, M. R., and Bloor, D., 1995, *Introduction to Molecular Electronics*, Edward Arnold, London, UK
- Pokatilov, E. P., Beril, S. I., Fomin, V. M., and Kalinovskii, V. V., 1990, *Phys. Stat. Sol.*, 161, p603
- Polymeropoulos, E. E., 1977, *Journal of Applied Physics*, 48, p2404
- Pozina, G. R., Kavokin, A. V., Kochereshko, V. P., Uraltsev, I. N., Yakovlev, D. R., Landwehr, G., Bicknell-Tassius, R. N., and Waag, A., 1992, *Solid State Communications*, 81, p639
- Rama Krishna, M. V., and Friesner, R. A., 1 December 1991, *Journal of Chemical Physics*, 95 (11), p8309
- Ralph, R. I., 1965, *Solid State Communications*, 3, p303
- Ray, B., 1969, *II-VI Compounds*, Pergamon, Oxford

- Roberts, G. G., 1985, *Advances in Physics*, Vol. 34, No. 4, p475
- Roberts, G.G., McGinnity, T.M., Barlow, W.A., and Vincett, P.S., 1980, *Thin Solid Films*, 68, p223
- Roberts, G. G., Vincent, P. S., and Barlow, W. A., 1978, *Journal of Physics C*, 11, p2077
- Rogers, A., 1997, *Essentials of Optoelectronics*, Chapman & Hall, London, UK
- Ruauudel-Teixier, A., Leloup, J., and Barraud, A., 1986, *Mol. Cryst. Liq. Cryst.*, 134, p347
- Sah, C. T., 1991, *Fundamentals of Solid-State Electronics*, World Scientific Publishing Co. Pte. Ltd., Singapore
- Sajinovic, D., Saponjic, Z. V., Cvjeticanin, N., Cincovic, M. M., and Nedeljkovic, J. M., 2000, *Chemical Physics Letters*, 329, p168
- Salata, O.V., Dobson, P.J., Sabesan, S., Hull, P.J., and Hutchison, J.L., 1996, *Thin Solid Films*, 288, p235
- Seeger, K., 1985, *Semiconductor Physics*, Springer-Verlag, Berlin
- Segall, B., in: Aven, M., and Prener, J. S., 1967, *Physics and Chemistry of II-VI Compounds*, North-Holland Publishing Company, Amsterdam, the Netherland
- Seto, C. T. and Whitesides, 1993, *J. Am. Chem. Soc.*, 115, p905
- Shinada, M., and Sugano, S., 1966, *Journal of Phys. Soc. Japan*, 20, p1274
- Shoji, H., Mukai, K., Ohtsuka, N., Sugawara, M., Uchida, T., and Ishikawa, H., 1995, *IEEE Photon. Technol. Lett.*, 12, p1385
- Singh, J., 1999, *Modern Physics for Engineers*, John Wiley & Sons, Inc., New York.
- Smith, S. D., 1995, *Optoelectronic Devices*, Prentice Hall, International Series in Optoelectronics, London, UK
- Smotkin, E.S., Lee, C., Bard, S., Campion, A., Fox, M.A., Mallouk, T.E., Webber, S.E., and White, J.M., 1988, *Chem. Phys. Lett.*, 152, p265
- Solymar, L. and Walsh, D., 1998, *Electrical properties of Materials*, sixth edition, Oxford University Press, Oxford.
- Streetman, B. G. and Banerjee, S., 2000, *Solid State Electronic Devices*, fifth edition, Prentice Hall, New Jersey
- Streetman, B. G., 1995, *Solid State Electronic Devices*, Prentice-Hall International inc., New Jersey
- Stroud, D., 1998, *Superlattices and Microstructures*, Vol. 23, no. 314, p567
- Sugi, M., 1985, *Journal of Molecular electronics*, 1, p3

- Sugi, M., Fukui, T., and Iizima, S., 1979, *Mol. Cryst. Liq. Cryst.*, 50, p183
- Sugi, M., and Iizima, S., 1979, *Physics Review B*, 15, p574
- Sugi, M., Fukui, T., and Iizima, S., 1977, *Chemical Physics Letters*, 45, p163
- Swalen, J. D., 1986, *Journal of Molecular Electronics*, Vol. 2, p155
- Sze, S. M., 1985, *Semiconductor Devices: Physics and Technology*, John Wiley & Sons, Singapore
- Tanaka, M., and Masumoto, Y., 2001, *Solid State Communications*, 120, p7
- Tanaka, M., Qi, J., and Masumoto, Y., 2000, *Journal of Crystal Growth*, 214/215, p410
- Tanaka, M., and Masumoto, Y., 2001, *Solid State Communications*, 120, p7
- Tattabi, M., and Uchil, J., 2000, *Solar energy Materials & Solar Cells*, Vol. 63, p309
- Tomasulo, A., and Rama Krishna, M. V., 1 September 1996, *Journal of Chemical Physics*, 105 (9), p3612
- Tsukamoto, S., Nagamune, Y., Nishioka, M., and Arakawa, Y., 1993, *Applied Physics Letters*, 62, p49
- Tyagi, M. S., 1991, *Introduction to Semiconductor Materials and Devices*, John Wiley & Sons, Singapore
- Vincett, P.S., and Roberts, G.G., 1980, *Thin Solid Films*, 68, p135
- Wang, X. L., Ogura, M., and Matsuhata, H., 1995, *Applied Physics Letters*, 66, p1506
- Wang, Y., and Herron, N., 1991, *Ibid.*, 95, p525
- Wang, Y., and Herron, N., 1990, *Physics Review B*, 42, p7253
- Weller, H., 1998, *Angew. Chem. Int. Ed.*, 37(12), p1658
- Wiesendanger, R., 1994, *Scanning probe microscopy and spectroscopy: methods and applications*, Cambridge University Press, UK
- Wilson, J. and Hawkes, J., 1998, *Optoelectronics: an introduction*, third edition, Prentice Hall Europe, Hertfordshire
- Wu, J., Zeng, Y. P., Cui, L. J., Zhu, Z. P., Wang, B. X., and Wang, Z. G., 2002, *International Journal of Modern Physics B*, Vol. 16, No. 28&29, p4423
- Wu, F., Zhang, J. Z., Kho, R., and Mehra, R. K., 2000, *Chemical Physics Letters*, 330, p237
- Yang, X. M., Wang, G. M., and Lu, Z. H., 1998, *Supramolecular Science*, 5, p549

**Yao T. and Woo J. C.**, 2001, *Physics and Applications of Semiconductor Quantum Structures*, Proceeding of the International Workshop on Physics and Applications of Semiconductor Quantum Structures (Asian Science Seminar), Cheju Island, Korea, October 18-23, 1998, Institute of Physics Publishing, Bristol

**Yoffe, A. D.**, 1993, *Advances in Physics*, Vol. 42, No. 2, p173

**Yoffe, A. D.**, 2001, *Advances in Physics*, Vol. 50, No. 1, p1

**Yu, Z., Degang, F., Xin, W., Juzheng, L., and Zuhong, L.**, 2001, *Colloids and Surfaces A: Physicochemical and engineering Aspects*, 181, p145

**Zhang, P., Kim, P. S., and Sham, T. K.**, 2001, *Journal of Electron Spectroscopy and Related Phenomena*, 119, p229

**Zhao, J., Dou, K., Chen, Y., Jin, C., Sun, L., Huang, S., Yu, J., Xiang, W., and Ding, Z.**, 1996, *Journal of Luminescence*, 66&67, p332

**Zorman, B., Rama Krishna, M. V., and Friesner, R. A.**, 1995, *Journal of Physical Chemistry*, 99, p7649

**Zylberajch, G., Ruaudel-Teixier, A., and Barraud, A.**, 1989, *Thin Solid Films*, 179, p9

**Zylberajch, G., Ruaudel-Teixier, A., and Barraud, A.**, 1989, *Thin Solid Films*, 178, p535

**Zylberajch, G., Ruaudel-Teixier, A., and Barraud, A.**, 1998, *Synth. Met.*, 27, B609